

ROSELLE (HIBISCUS SABDARIFFA) ANTHOCYANIN USE IN MONITORING MEAT FRESHNESS

ARTICLES FOR FACULTY MEMBERS

Title/Author	A double-layer smart film based on gellan gum/modified anthocyanin and sodium carboxymethyl cellulose/starch/Nisin for application in chicken breast / Wu, Y., & Li, C.
Source	<p><i>International Journal of Biological Macromolecules</i> Volume 232 (2023) 123464 Pages 1-16 https://doi.org/10.1016/J.IJBIOMAC.2023.123464 (Database: ScienceDirect)</p>
Title/Author	A visual bi-layer indicator based on roselle anthocyanins with high hydrophobic property for monitoring griskin freshness / Zhang, J., Huang, X., Shi, J., Liu, L., Zhang, X., Zou, X., Xiao, J., Zhai, X., Zhang, D., Li, Y., & Shen, T.
Source	<p><i>Food Chemistry</i> Volume 355 (2021) 129573 Pages 1-8 https://doi.org/10.1016/J.FOODCHEM.2021.129573 (Database: ScienceDirect)</p>
Title/Author	Characterization of Natural Anthocyanin Indicator Based on Cellulose Bio-Composite Film for Monitoring the Freshness of Chicken Tenderloin / Boonsiriwit, A., Itkor, P., Sirieawphikul, C., & Lee, Y. S.
Source	<p><i>Molecules</i> Volume 27 Issue 9 (2022) 2752 Pages 1-16 https://doi.org/10.3390/molecules27092752 (Database: MDPI)</p>

ROSELLE (HIBISCUS SABDARIFFA) ANTHOCYANIN USE IN MONITORING MEAT FRESHNESS

ARTICLES FOR FACULTY MEMBERS

<p>Title/Author</p>	<p>Halochromic smart packaging film based on montmorillonite/polyvinyl alcohol-high amylose starch nanocomposite for monitoring chicken meat freshness / Sharaby, M. R., Soliman, E. A., & Khalil, R.</p>
<p>Source</p>	<p><i>International Journal of Biological Macromolecules</i> Volume 258 Part 2 (2024) 128910 Pages 1-12 https://doi.org/10.1016/j.ijbiomac.2023.128910 (Database: ScienceDirect)</p>
<p>Title/Author</p>	<p>Inkjet-printed pH-sensitive QR code labels for real-time food freshness monitoring / Xu, Y., Liu, Z., Liu, R., Luo, M., Wang, Q., Cao, L., & Ye, S.</p>
<p>Source</p>	<p><i>Journal of Materials Science</i> Volume 56 Issue 33 (2021) Pages 18453–18462 https://doi.org/10.1007/s10853-021-06477-x (Database: Springer Nature)</p>
<p>Title/Author</p>	<p>Intelligent food tag: A starch-anthocyanin-based pH-sensitive electrospun nanofiber mat for real-time food freshness monitoring / Lv, H., Wang, C., He, D., Zhao, H., Zhao, M., Xu, E., Jin, Z., Yuan, C., Guo, L., Wu, Z., Liu, P., & Cui, B.</p>
<p>Source</p>	<p><i>International Journal of Biological Macromolecules</i> Volume 256 Part 1 (2024) 128384 Pages 1-12 https://doi.org/10.1016/j.ijbiomac.2023.128384 (Database: ScienceDirect)</p>

ROSELLE (HIBISCUS SABDARIFFA) ANTHOCYANIN USE IN MONITORING MEAT FRESHNESS

ARTICLES FOR FACULTY MEMBERS

<p>Title/Author</p>	<p>Multifunctional halochromic packaging materials: Saffron petal anthocyanin loaded-chitosan nanofiber/methyl cellulose matrices / Alizadeh-Sani, M., Tavassoli, M., McClements, D. J., & Hamishehkar, H.</p>
<p>Source</p>	<p><i>Food Hydrocolloids</i> Volume 111 (2021) 106237 Pages 1-13 https://doi.org/10.1016/J.FOODHYD.2020.106237 (Database: ScienceDirect)</p>
<p>Title/Author</p>	<p>Smart packaging for food spoilage assessment based on hibiscus sabdariffa l. anthocyanin-loaded chitosan films / Khezerlou, A., Tavassoli, M., Alizadeh Sani, M., Ehsani, A., & McClements, D. J.</p>
<p>Source</p>	<p><i>Journal of Composites Science</i> Volume 7 Issue 10 (2023) 404 Pages 1-14 https://doi.org/10.3390/JCS7100404 (Database: MDPI)</p>
<p>Title/Author</p>	<p>The highly stable indicator film incorporating roselle anthocyanin co-pigmented with oxalic acid: Preparation, characterization and freshness monitoring application /Huang, J., Hu, Z., Li, G., Chin, Y., Pei, Z., Yao, Q., Li, D., & Hu, Y.</p>
<p>Source</p>	<p><i>Food Research International</i> Volume 173 Part 2 (2023) 113416 Pages 1-10 https://doi.org/10.1016/j.foodres.2023.113416 (Database: ScienceDirect)</p>

ARTICLES FOR FACULTY MEMBERS

ROSELLE (HIBISCUS SABDARIFFA) ANTHOCYANIN USE IN MONITORING MEAT FRESHNESS

Title/Author	A double-layer smart film based on gellan gum/modified anthocyanin and sodium carboxymethyl cellulose/starch/Nisin for application in chicken breast / Wu, Y., & Li, C.
Source	<i>International Journal of Biological Macromolecules</i> Volume 232 (2023) 123464 Pages 1-16 https://doi.org/10.1016/j.ijbiomac.2023.123464 (Database: ScienceDirect)



A double-layer smart film based on gellan gum/modified anthocyanin and sodium carboxymethyl cellulose/starch/Nisin for application in chicken breast

Yanglin Wu, Chunwei Li*

College of Engineering and Technology, Northeast Forestry University, Harbin 150040, PR China

ARTICLE INFO

Keywords:
Anthocyanins
Roselle
Nisin
CMC
Bilayer

ABSTRACT

In order to overcome this challenge of poor stability of natural anthocyanins in intelligent packaging materials, roselle anthocyanin (RA) was first modified by acetic acid, and then a double-layer smart indication antimicrobial film was developed using modified roselle anthocyanin (MRA)-gellan gum (GG) as the inner layer and sodium carboxymethyl cellulose (CMC)-starch (ST)-Nisin as the outer layer. UV spectra revealed that acetic acid was successfully grafted onto RA, which dramatically improved their thermal stability, antioxidant capabilities, photostability, and pH stability. The bilayer films were successfully prepared, as revealed by scanning electron microscopy, Fourier-transform infrared spectroscopy, and X-ray diffraction measurements. In comparison to GG-MRA and CMC-ST-Nisin films, the water content, water solubility, mechanical characteristics, water vapor barrier, oxygen barrier, and hydrophobicity of GG-MRA@CMC-ST-Nisin films were significantly enhanced. The presence of the outer layer films significantly enhanced the UV-vis light barrier, opacity, antioxidant and antibacterial properties of the inner layer films. When the films were applied to chicken breast, it was found that the indicator films not only monitored the freshness of the chicken in real-time but also that the GG-MRA film and the double-layer film were effective in extending the shelf life of the chicken by 1 and 2 days, respectively, compared to the control group.

1. Introduction

Protein-rich meats are prone to spoilage during storage and transportation due to microbial and enzymatic effects; therefore, the development of biodegradable intelligent and active packaging films has received increasing attention in the food industry [1]. Numerous studies have shown that anthocyanins in natural plants such as purple kale, mulberry, purple potato, and roselle are sensitive to pH and are important indicators for assessing food spoilage [2,3]. However, anthocyanins are prone to degradation and discoloration during storage and processing, severely affecting their application in intelligent packaging [4]. It has been shown that acylated anthocyanins are superior to non-acylated anthocyanins in terms of stability and lipophilicity [5–7]. This is because it reduces the polarity of anthocyanins, creating a spatial site-blocking effect that reduces the sensitivity of anthocyanins to nucleophilic attack as well as an effectual physical hindrance to nucleophilic attack through intramolecular co-pigmentation [8]. Therefore, researchers have often used acetic acid to acylate anthocyanins to

improve their stability, and in addition, binding them to hydrocolloids can also enhance their stability, such as carrageenan gum [9], tapioca starch [10] and gelatin [11], etc. Among them, gellan gum (GG) is a water-soluble anionic polysaccharide produced by the bacterium *Sphingomonas* spp. It is widely used as a thickener, emulsifier and stabilizer. Its texture is not subject to time and temperature changes during storage, with good thermal stability and significant temperature hysteresis [12].

For food packaging materials, antimicrobial properties are a prerequisite to prevent bacterial and fungal contamination of food products. However, the antimicrobial activity of pure biopolymer films is usually weak and to some extent does not meet the demand for freshness preservation. Therefore, active packaging containing natural antibiotics is attracting attention as one of the most novel food packaging technologies. Starch (ST) has received increasing attention among natural polymers as an edible, inexpensive, and readily available biopolymer [13]. However, starch films without modifiers suffer from poor mechanical properties and high hydrophilicity. Several studies have shown

* Corresponding author.

E-mail address: lcwnefu@126.com (C. Li).

<https://doi.org/10.1016/j.ijbiomac.2023.123464>

Received 1 November 2022; Received in revised form 24 January 2023; Accepted 25 January 2023

Available online 30 January 2023

0141-8130/© 2023 Elsevier B.V. All rights reserved.

that starch blended with other biopolymers, such as polyvinyl alcohol, chitosan, etc., can improve their properties [14]. Sodium carboxymethyl cellulose (CMC) is an anionic derivative of cellulose with good thickening properties and film-forming properties. It is recognized as a safe (GRAS) material, often used as a carrier for active ingredients (e.g., antioxidants, antimicrobial agents, and color indicators) [15]. Nisin is a highly effective, non-toxic, safe, and side-effect-free natural food preservative and is widely used as a potential entity for constructing antimicrobial films for food packaging due to its broad range of antimicrobial properties and biosafety [16]. Sun et al. [17] prepared antibacterial nanocomposite films by incorporating Nisin and ϵ -polylysine into corn distarch phosphate/nanocrystalline cellulose-based films by casting. Yang et al. [18] developed a nanocellulose-based hybrid film with antimicrobial properties using sugarcane bagasse and lactic acid streptococin. However, there are no studies on incorporating Nisin into a dual network film matrix as a physical protective layer to improve the antimicrobial properties of intelligent indication films.

Therefore, developing a pH-responsive antimicrobial bilayer film based on improved anthocyanin stability is an excellent choice to make the intelligent film more widely used in meat foods. This is the first time that acetic acid-modified roselle anthocyanins (RA) were added to low-acylated GG to form an internal indicator layer. Nisin was then added to a double network structure of CMC and starch to form an external antibacterial physical protection layer. They were ultimately forming a complete double-layer structure of the packaging film. SEM, FT-IR, and X-ray characterized the structural and microscopic properties of the films, and the films' mechanical properties, water resistance and optical properties were discussed. In addition, the films were evaluated for antioxidant activity, antimicrobial properties, pH sensitivity, ammonia responsiveness, and their potential application in chicken breasts.

2. Materials and methods

2.1. Materials and reagents

Roselle, chicken breast was purchased from the Harbin Bijut Supermarket (Harbin, China). Glacial acetic acid (analytical grade, CH₃COOH, $\geq 99.5\%$) was purchased from Tianjin Fuyu Fine Chemical Co., Ltd. (Tianjin, China), GG (CAS: 71010-52-1) was purchased from Beijing Boaltoda Technology Co., Ltd. (Beijing, China). CMC (food grade) was provided by Beijing Runfa Biotechnology Co., Ltd. (Beijing, China). Starch (analytical grade, pH 6.0–7.5) was purchased from Tianjin Hengxing Chemical Reagent Manufacturing Co., Ltd. (Tianjin, China). Nisin (food grade) was obtained from Zhejiang Xinyinxiang Bioengineering Co., Ltd. (Taizhou, China).

2.2. Extraction of anthocyanins from roselle

The roselle was dried, crushed and preserved in a brown bottle by passing through a 60 mesh sieve. The 50 % ethanol solution was used as the extracting solution and mixed at a material-liquid ratio of 1:40 g/mL and stirred at 500 r/min in a water bath at 30 °C for 3 h. The filtrate was collected with a vacuum filtration device, and then the rotary evaporated at 50 °C in a dark environment to obtain the anthocyanin concentrate.

2.3. Determination of anthocyanin content in roselle

The total anthocyanin content of roselle was tested by the pH difference method [19].

2.4. Preparation and determination of acylated roselle anthocyanins

The anthocyanin concentrate was mixed with an acetic acid solution (1 mol/L) in a ratio of 2:1, and the acylated roselle anthocyanin was obtained after heating it in a water bath at 90 °C for 30 min. The

acylated and unacylated anthocyanin solutions were then diluted to the same concentration and analyzed by scanning from 280 to 600 nm with a Cary100 UV-Vis spectrophotometer (Agilent, California, USA). The acylation results were judged by the difference in absorption peaks in the chromatograms.

2.5. Color response of roselle anthocyanins to different pH changes before and after acylation

The anthocyanin solutions before and after acylation were dissolved in 15 mL of different buffer solutions (pH 2–13) and analyzed by scanning from 450 to 700 nm with a Cary100 UV-Vis spectrophotometer (Agilent, California, USA).

2.6. Investigation of the stability of roselle anthocyanins before and after acylation

According to Lambert Beer's law, the preservation rate of anthocyanins was calculated by the change of absorbance under certain conditions. Before and after modification, anthocyanins' maximum absorption wavelength and absorbance were measured using a Cary100 UV-Vis spectrophotometer (Agilent, California, USA).

$$\text{Retention rate} = \frac{A}{A_0} \times 100\% \quad (1)$$

where A was the absorbance after modification, A_0 was the absorbance before modification.

2.6.1. Temperature stability

The anthocyanin solutions before and after acylation were heated in a constant temperature water bath at 45 °C, 60 °C, 75 °C and 90 °C for 2 h under a dark environment, and then the absorbance values were measured to calculate the retention rate.

2.6.2. Oxidation stability

Hydrogen peroxide (1 %, w/v) was added to the anthocyanin solutions before and after acylation, and the absorbance values were measured at 1 h intervals under dark conditions.

2.6.3. Light stability

The anthocyanin solutions before and after acylation were placed under light and dark conditions for 7 d, and the absorbance values were measured every day.

2.6.4. pH stability

The anthocyanin solutions before and after acylation were placed in buffer pH 1, 3, 5, 7, 9 and 11 under a dark environment, and the absorbance values were measured daily.

2.7. Preparation of GG-RA, GG-MRA, CMC-ST-Nisin and GG-MRA@CMC-ST-Nisin films

GG solution was obtained by dissolving 1 g of GG in 100 mL of deionized water at 70 °C and stirring with glycerol (0.8 %, w/v) for 1 h. Subsequently, when the temperature was cooled to 40 °C, appropriate amounts of roselle anthocyanin solution were added to the GG solution, and 20 mL of the film solution was poured into the Petri dishes ($d = 9$ cm) immediately after stirring for 1 h. The film solution forms firm GG-RA and GG-MRA hydrogels after cooling at room temperature.

CMC solution (2 %, w/v) was obtained by dissolving 2 g of CMC in 100 mL of deionized water at 60 °C with magnetic stirring for 2 h. Secondly, 2 g of ST were dissolved in 100 mL of deionized water at 80 °C and stirred for 30 min to obtain the ST solution (2 %, w/v). Subsequently, the two solutions were mixed in a ratio of 1:1 (v/v). Glycerol (40 wt%, based on solute mass) and Nisin (5 wt%, based on solute mass)

were added and stirred at 50 °C for 1 h to obtain the CMC-ST-Nisin solution. 15 mL of the film solution was poured into Petri dishes (d = 9 cm) and dried at room temperature for 60 h.

The prepared CMC-ST-Nisin solution was cast onto the GG-MRA hydrogel and dried at room temperature for 60 h to obtain GG-MRA@CMC-ST-Nisin films. The prepared films were stored in a constant temperature and humidity chamber at 25 °C and 50 % relative humidity until equilibrium before analysis.

2.8. Characterization of GG-RA, GG-MRA, CMC-ST-Nisin and GG-MRA@CMC-ST-Nisin films

2.8.1. Scanning electron microscope (SEM)

The surface and cross-sectional morphology of the films were observed using a JSM-7500F scanning electron microscope (JEOL, Japan).

2.8.2. Fourier transform infrared (FT-IR) spectroscopy

The samples were scanned using a Spectrum 400 Fourier transform infrared spectrometer (PerkinElmer Inc., MA, USA) in the wavelength range of 4000 cm^{-1} to 600 cm^{-1} .

2.8.3. X-ray diffraction (XRD)

The sample films were scanned with an X' Pert3 Powder X-ray diffractometer (PANalytical, The Netherlands) in the range of $2\theta = 5^\circ\text{--}90^\circ$ at a scanning rate of $5^\circ/\text{min}$.

2.8.4. Film thickness and mechanical properties

Thicknesses were measured at different film positions by a GKB-4 variable pressure thickness gauge (Yue Ming Small Testing Machine Co., Ltd., Changchun, China).

Tensile strength (TS) and elongation at break (EB) of film samples (100 mm \times 10 mm) were measured on an LD-05 tensile tester (Yue Ming Small Testing Machine Co., Ltd., Changchun, China) using an initial clamping distance of 4 cm and a crosshead speed of 10 mm/min.

$$TS(\text{MPa}) = \frac{F}{x \times W} \quad (2)$$

$$EB(\%) = \frac{\Delta L}{L_0} \times 100 \quad (3)$$

where F was the fracture stress of the film (N), x was the film thickness (mm), W was the film width (mm), ΔL and L_0 were the elongation and original length of the film sample (mm), respectively.

2.8.5. Moisture content and water solubility

Film samples (40 mm \times 40 mm) were dried at 105 °C until constant weight. The moisture content (MC) of each film was calculated.

$$MC = \frac{W_1 - W_2}{W_1} \times 100 \quad (4)$$

where W_1 and W_2 were the weight of the film before and after drying, respectively.

Water solubility was determined by referring to the method of Alizadeh et al. [20] with slight modifications. Film samples (40 mm \times 40 mm) were dried to constant weight (W_2) in a desiccator at 105 °C and then immersed in 50 mL of buffer solution (pH 7.0) and shaken for 24 h at room temperature. The films were then dried again in a drying oven at 105 °C to determine the final weight of dry matter (W_3), and the water solubility (WS) of the films was calculated as follows:

$$WS(\%) = \frac{W_2 - W_3}{W_2} \times 100 \quad (5)$$

2.8.6. Water vapor permeability (WVP) and water contact angle (WCA)

According to ASTM E96-95 standard method, 40 g of silica were

packed into WVP cups (8.5 cm deep, 3.5 cm diameter), covered with film samples (6 cm \times 6 cm) and sealed with tape, then placed in a constant temperature and humidity chamber (25 °C, 75 % relative humidity). The weight of the WVP cups was measured every hour for 8 h [21], and the WVP ($\text{g}\cdot\text{m}/\text{m}^2\cdot\text{Pa}\cdot\text{s}$) of the films was calculated as follows:

$$WVP = \frac{\Delta m \times x}{S \times \Delta P \times t} \quad (6)$$

where x (mm) was the average thickness of the film, Δm (g) was the increased weight of the test vessel, S (m^2) was the permeable area of the film, t (s) was the time for weight increase, and ΔP (3169 Pa, 25 °C) was the vapor partial pressure.

Smart films' surface wettability was tested using an OCA-20 WCA analyzer (Dataphysics, Stuttgart, Germany) and measured three times at different locations on the same film sample.

2.8.7. Oxygen permeability (OP)

The oxygen permeability was measured in continuous mode at 23 °C, 0 % RH by an Ox-Tran apparatus (BSG-33, Guangzhou Xi Tang Electromechanical Technology Co., Ltd., Guangzhou, China) according to the Chinese national standard (GB/T1038-2000).

2.8.8. Optical properties

The transmission spectra of the film samples were measured by UV-Vis spectrophotometer in the range of 200 to 800 nm. The opacity of the film samples was calculated according to the following equation [22]:

$$Opacity = \frac{A_{600}}{x} \quad (7)$$

where A_{600} was the absorbance of the film sample at 600 nm and x was the film thickness (mm).

2.9. Release of anthocyanin

Tests were performed according to the method of Alizadeh-Sani et al. [20] with slight modifications. Film samples (2 cm \times 2 cm) were immersed in 25 mL of food simulant (water, 50 % and 95 % ethanol solutions) and gently shaken at room temperature. Three milliliter samples were taken at predetermined time intervals (30, 60, 90, 120, 180, 240 min), and the absorbance at 520 nm (λ_{max}) was measured using a Cary100 UV-Vis spectrophotometer (Agilent, California, USA).

2.10. Antioxidant capacity

Referring to the method of Liu et al. [23] with slight modifications. Briefly, 1 mL of film sample leachate was added to 3 mL of 100 $\mu\text{mol}/\text{L}$ DPPH solution. The absorbance values of the mixed solutions were measured at 517 nm using a UV spectrophotometer after 30 min of protection from light. Anhydrous ethanol was used as the blank group, and the free radical scavenging rate (Y_{DPPH}) was calculated according to Eq. (8).

$$Y(\%) = \frac{A_2 - (A_1 - A_3)}{A_2} \times 100 \quad (8)$$

A_1 was the absorbance value of the film solution and the free radical solution, A_2 was the absorbance value of anhydrous ethanol and the free radical solution, and A_3 was the absorbance value of anhydrous ethanol and film solution.

2.11. Antimicrobial properties

The antibacterial properties of the films were tested according to the method of Liu et al. [3] with slight modifications. First, 6 mm diameter films were irradiated under UV for 15 min, and then 100 μL of *S. aureus*

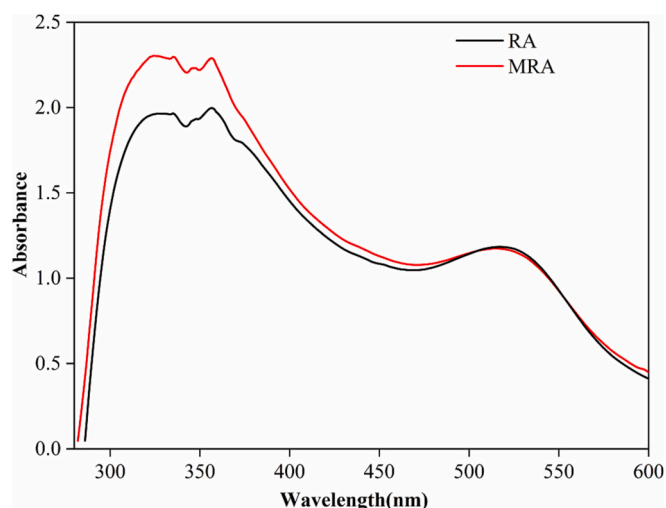


Fig. 1. UV-Vis spectra of roselle anthocyanins before and after modification (280–600 nm).

or *E. coli* suspension was uniformly distributed in a solid medium. Then the film samples were placed in Petri dishes with sterilized forceps and incubated in a biochemical incubator at 37 °C for 24 h. Finally, the diameter of the inhibition circle was measured.

2.12. Color responsiveness

2.12.1. pH sensitivity

The film samples (2 × 2 cm) were immersed in different buffer

solutions (pH 2 to 13), and then the color change of the films were recorded.

2.12.2. Ammonia responsiveness

The ammonia responsiveness of the films was tested according to the method of Huang et al. [24] with slight modifications. The films (2 cm × 2 cm) were placed 1 cm above an 8 mmol/L ammonia solution for 30 min. The color change of the color-indicating film was recorded every 5 min. The color change of the color indicator film was recorded every 5 min. The total color difference (ΔE) was calculated as follows:

$$\Delta E = \sqrt{(L - L_0)^2 + (a - a_0)^2 + (b - b_0)^2} \tag{9}$$

where L , a , and b were the values after the color change, while L_0 , a_0 , and b_0 were the initial values.

2.13. Application in chicken breast

Each round plastic box (d = 95 mm) was filled with 70 g of chicken breast, and then the film was fixed on the inner lid of the box and stored at 4 °C for 10 days. Each index of chicken breast and film color change was measured every 2 days. Total volatile basic nitrogen (TVB-N) values were determined according to Chinese standard 5009.228-2016, “Determination of volatile salt nitrogen in foodstuffs”. The pH was determined by placing the chicken breast in a beaker containing distilled water at a ratio of 1:10 (g/mL), homogenizing and crushing it, and then measuring it with a PHS-3E precision pH meter (Shanghai Electric Scientific Instruments Co., Ltd., Shanghai, China). The thiobarbituric acid (TBARS) value was determined by weighing 2 g of chopped chicken in 7.5 mL of trichloroacetic acid solution (7.5 wt%), filtering and adding 7.5 mL of 0.02 mol/L thiobarbituric acid (TBA) solution, heating at

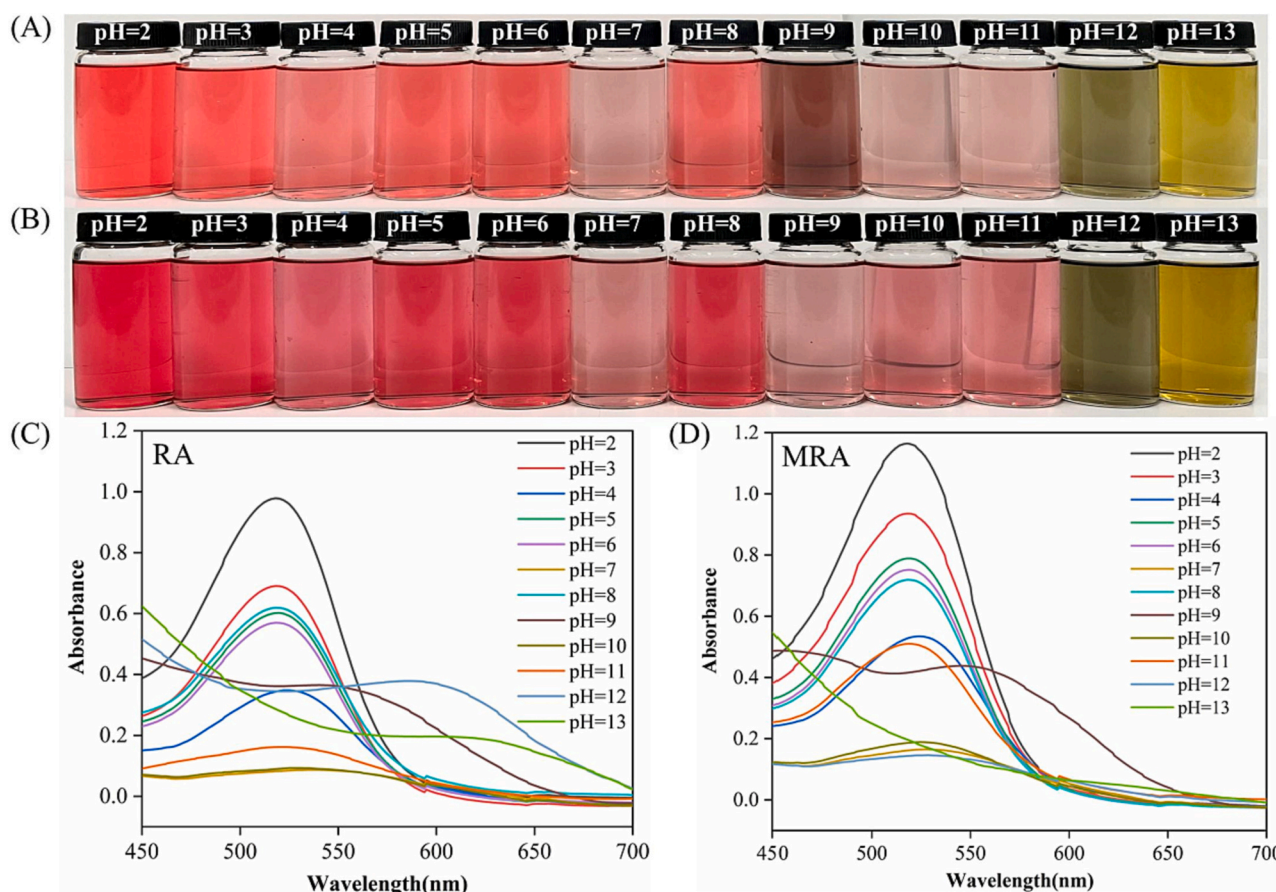


Fig. 2. Color variations of RA (A) and MRA (B) in different buffer solutions (pH 2–13), UV-vis spectra of RA (C) and MRA (D) from 450 to 700.

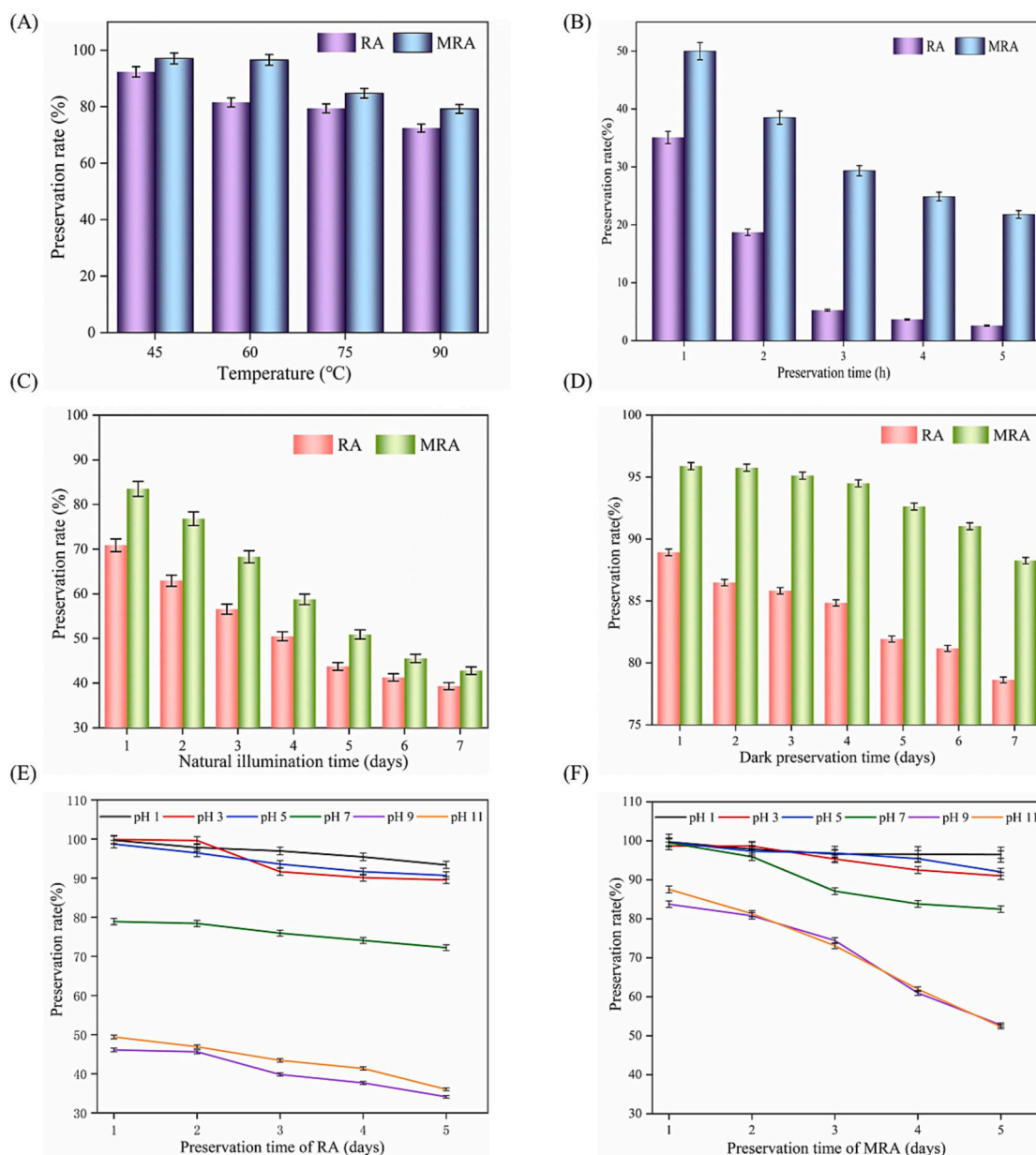


Fig. 3. (A) Stability of RA and MRA at different temperatures, (B) oxidative stability of RA and MRA, (C–D) stability of RA and MRA under natural light and dark environment, (E–F) stability of RA and MRA in different buffer solutions.

100 °C for 30 min, then centrifuged at 1600 r/min for 5 min after cooling. Finally, the UV absorbance of the supernatant was measured at 532 nm.

2.14. Statistical analysis

Graphs were drawn using Origin 9.5 software (Origin Lab Corporation, USA). SPSS software (IBM SPSS Statistics 22, Chicago) was used to analyze the statistical data.

3. Results and discussion

3.1. UV absorption spectra of roselle anthocyanins before and after modification

Harborne [25,26] already reported in 1958 that the shoulder peak of anthocyanin at 300 to 350 nm on the UV–Vis spectrum was caused by an acyl group and that the ratio of its absorbance at this point to the

maximum absorption intensity in the visible region indicated the degree of acylation of the anthocyanin. As shown in Fig. 1, the shoulder peak at 346 nm of the modified roselle anthocyanin indicated that acetic acid was grafted onto the anthocyanin molecule by the acylation reaction. In addition, there were absorption peaks at 324 nm and 356 nm for roselle anthocyanins before and after the modification, which indicated that roselle anthocyanins themselves had a certain degree of acylation, and the acylation degree of roselle anthocyanins after acetic acid modification was higher.

3.2. Characterization of roselle anthocyanins before and after modification in different pH buffer solutions

The total anthocyanin content in roselle was 225.01 ± 3.99 mg/L as measured by the pH difference method. As shown in Fig. 2(A) and (B), RA and MRA showed the same trend of color change at pH 2–8 and pH 12–13, and MRA presented as a slightly darker color than RA at the same pH value. It was red at pH 2–3, dark pink at pH 4, red at pH 5–6, light

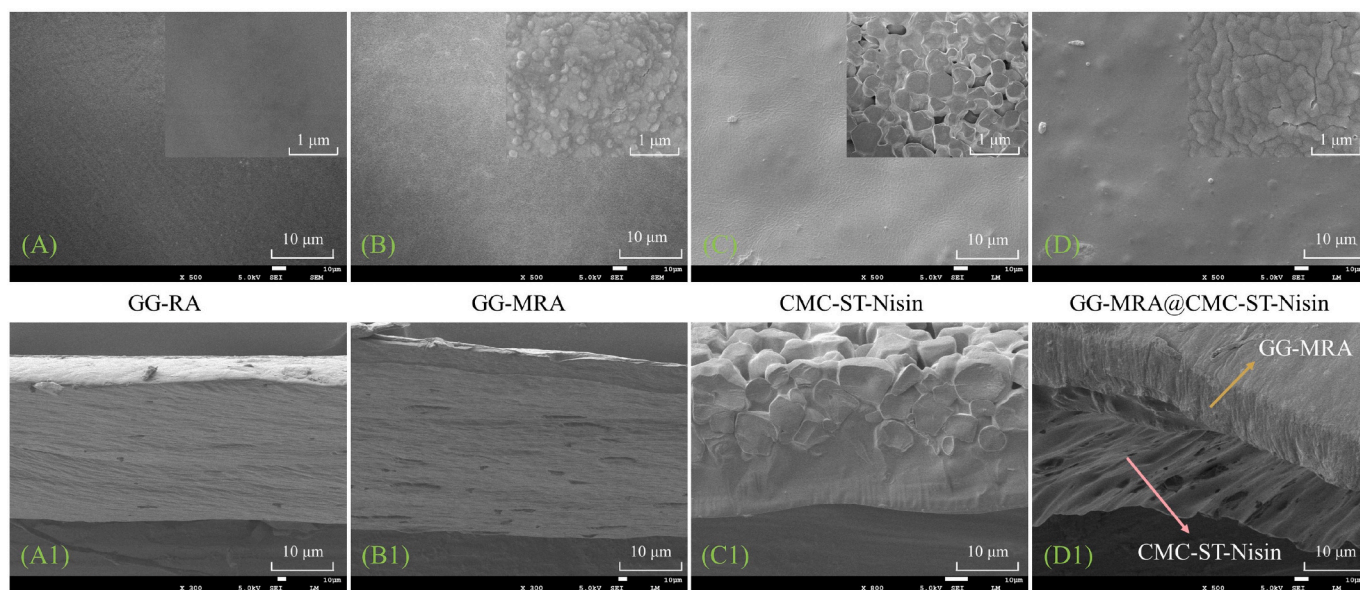


Fig. 4. SEM micrographs of the surfaces and cross sections of films.

pink at pH 7, red at pH 8, dark green at pH 12, and yellow-green at pH 13. It is worth noting that at pH 9, RA and MRA exhibited two distinct colors, RA was dark brown and MRA was light pink, and at pH 10–11, RA was light pink and MRA was pink. As shown in Fig. 2(C) and (D), the UV absorption peaks of MRA were higher than those of RA, which was consistent with the observation that MRA presented a slightly darker color than RA at the same pH, probably because acylation makes anthocyanins more stable in aqueous solution through intramolecular co-pigmentation, protecting the flavin chromophore from nucleophilic attack by water and creating spatial site resistance [27,28]. It was evident that the maximum UV absorption peaks of anthocyanins before and after acylation were significantly red-shifted as the pH of the buffer solution increased. The maximum absorption peak of RA was shifted from 518 nm to 614 nm. In comparison, the maximum absorption peak of MRA was shifted from 518 nm to 548 nm, indicating that the acylated anthocyanins' molecular structure was changed, further verifying that the acetic acid modification achieved the acylation of roselle anthocyanins.

3.3. Anthocyanin stability before and following acylation

As presented in Fig. 3(A), the stability of anthocyanins before and after acylation gradually decreased with increasing temperature. However, the preservation rate of anthocyanins after acylation was higher than that of anthocyanins before acylation at different temperatures, indicating that the heat resistance of roselle anthocyanins improved after acylation. The thermal stability of acylated anthocyanins can be explained by the phenomenon of intramolecular co-pigmentation, where hydrophobic interactions between the anthocyanin backbone and acyl groups and the overlap of off-domain p-electron clouds protect the anthocyanin molecule from nucleophilic water molecules and prevent the formation of colorless methanol [7]. As shown in Fig. 3(B), the antioxidant capacity of post-acylation anthocyanins was significantly higher than that of pre-acylation anthocyanins. The retention rate of post-acylation anthocyanins was still higher than 20 % at 5 h. In comparison, the retention rate of pre-acylation anthocyanins was <5 %. The grafting of acetic acid inhibited the oxidation and decomposition of anthocyanins, and this protective effect may be reflected in two aspects. On the one hand, as a good antioxidant, acetic acid prevents the oxidation of anthocyanins at the cost of its oxidation. On the other hand, acetic acid may accumulate on the benzene ring of anthocyanins,

hindering the hydrolysis of anthocyanins and inhibiting their conformational conversion and color fading. Matsufuji et al. [29] also found that all acylated anthocyanins exhibited more vigorous antioxidant activity at different pH values. As shown in Fig. 3(C) and (D), the preservation rate of acylated anthocyanins was significantly higher than that of pre-acylated anthocyanins under the same light and dark environment, which indicated that acetic acid-modified roselle anthocyanins could effectively improve anthocyanin photostability. This was because the aromatic acyl groups in acylated anthocyanins acted as filters when photons were absorbed by the molecule and caused bond breakage, absorbing photons and reducing the sensitivity of the acylated anthocyanins to light stress [30]. It was worth noting that the preservation rate of anthocyanins before and after acylation was higher in the dark environment than in the light environment, which indicated that acylated anthocyanins were highly stable in dark environments. The same conclusion was reached by Escher et al. [31]. As shown in Fig. 3(E) and (F), the retention rates of anthocyanins before and after acylation was in the range of 30–50 % under weak alkaline (pH = 9) and alkaline conditions (pH = 11), while the retention of anthocyanins after acylation was in the range of 50–90 %, indicating that acetic acid modification could improve the pH stability of roselle anthocyanins under neutral and alkaline conditions, which echoed the results of different color changes of anthocyanins at pH 9, 10 and 11 before and after acylation in Fig. 2.

3.4. Characterization of GG-RA, GG-MRA, CMC-ST-Nisin and GG-MRA@CMC-ST-Nisin films

3.4.1. SEM

As shown in Fig. 4(A), (B), (C) and (D), the GG-RA films exhibited a uniform, dense and flat surface, which indicated that the roselle anthocyanins were uniformly distributed in the film matrix with good compatibility. Compared with the GG-RA films, the GG-MRA film showed a uniform distribution of particles on the compact film surface observed at 1 μm, which might be formed by the intra-molecular hydrophobic interaction between the benzopyran ring and aromatic acyl group when the acylated anthocyanins were co-mixed with the film matrix solution. CMC-ST-Nisin films were observed to have a uniform and dense film surface at 10 μm. However, the presence of honeycomb-like blocks could be observed at 1 μm, which could be formed due to the inability of Nisin to dissolve entirely in the film matrix. Some aggregates were also observed in the films doped with ZnO nanoparticles by Liu

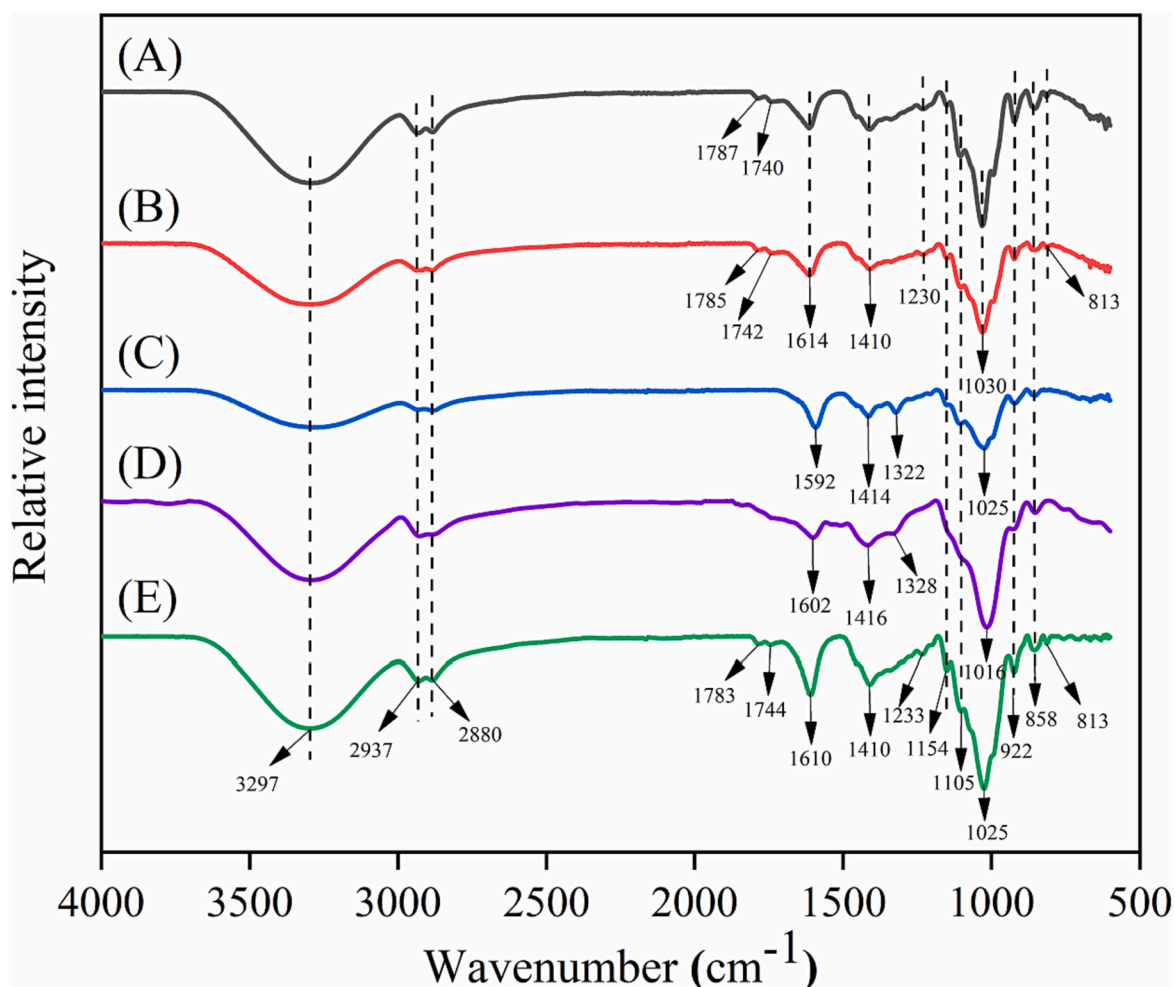


Fig. 5. FT-IR spectra of GG-RA (A), GG-MRA (B), CMC-ST-Nisin (C), GG-MRA@CMC-ST-Nisin-1 (CMC-ST-Nisin facing up) (D) and GG-MRA@CMC-ST-Nisin-2 (GG-MRA facing up) (E) films.

et al. [32]. Notably, GG-MRA@CMC-ST-Nisin films were found to have a chain-like structure on the film surface under the observation of 1 μm . This may be because during the preparation of the bilayer film, when the CMC-ST-Nisin film solution was cast onto the GG-MRA film, some of the MRA underwent dissolution and penetration into the CMC-ST-Nisin film, promoting the compatibility of Nisin with the CMC-ST film matrix. In addition, complexes may be formed between the flavonoid cation of MRA and CMC through electrostatic interactions, which enhances the stability of the particle dispersion system and thus exhibits self-assembly behavior [33].

The cross-sectional morphologies of GG-RA, GG-MRA, CMC-ST-Nisin and GG-MRA@CMC-ST-Nisin films are shown in Fig. 4(A1), (B1), (C1) and (D1). Compared with the dense and compact cross-section of GG-RA film, the cross-section of GG-MRA films exhibited micro-pores of different sizes, which may be due to the spatial site resistance imposed by GG as well as the aromatic acyl groups of acylated anthocyanins causing intramolecular co-pigmentation, thus creating an effective physical hindrance to the nucleophilic attack of water molecules [34]. The cross-section of the CMC-ST-Nisin film showed that although many particles appear in the upper truncation of the film, CMC and ST closely surround Nisin, exhibiting a compact structure. It is worth noting that the double-layer structure could be seen in the GG-REM@CMC-ST-Nisin film, which was because after GG dissolved in water, the molecules would automatically gather to form a double helix structure. The double helix could further gather to form a three-dimensional mesh structure, which was convenient for trapping water molecules and producing a

stable gelation phenomenon [12]. In addition, there was no apparent gap between the films, which indicated that a well-integrated continuous structure was formed between the inner and outer layers. These results indicated that well-complete bilayer-indicative bacteriostatic films were successfully developed.

3.4.2. FT-IR spectroscopy

FTIR spectroscopy can be used not only to determine the functional groups of the film components but also to determine whether intermolecular interactions occur between them [35]. Both sides of GG-MRA@CMC-ST-Nisin were tested separately by FTIR, where the outer film (CMC-ST-Nisin) was tested as the contact surface called GG-MRA@CMC-ST-Nisin-1 film, and the inner film (GG-MRA) was tested as the contact surface called GG-MRA@CMC-ST-Nisin-2 film. As presented in Fig. 5, similar characteristic peaks were observed around 3200–3500 cm^{-1} for all films, which were caused by the —OH stretching vibrations in the film matrix. The peaks at 2880 cm^{-1} and 2937 cm^{-1} correspond to the symmetric and antisymmetric methylene, respectively. The GG-RA film showed relatively weak peaks at 1787 cm^{-1} and 1740 cm^{-1} , indicating the presence of aryl ketones (five-membered cyclic ketones), which was related to the C=O stretching of the pyran ring of flavonoids [24]. Notably, the peak positions of the GG-MRA films were shifted to 1785 cm^{-1} and 1742 cm^{-1} , respectively, indicating intermolecular interactions (such as hydrogen bonding) occurred between the anthocyanin and the film matrix after acylation. Both GG-RA and GG-MRA films showed moderate intensity absorption peaks at 1614

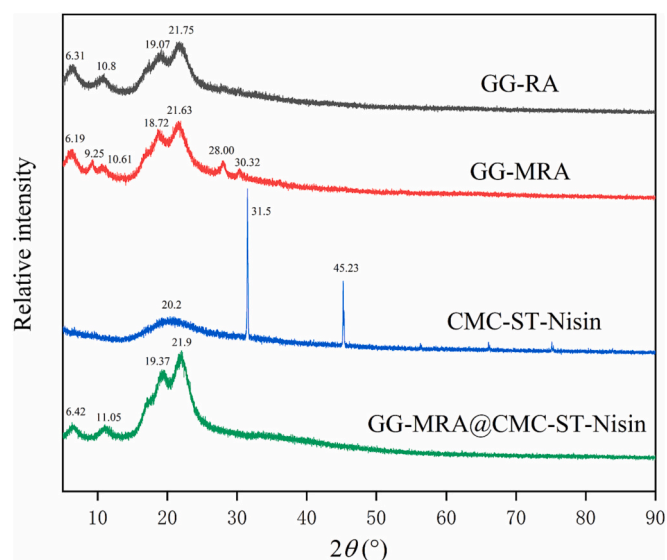


Fig. 6. XRD patterns of films.

cm^{-1} , which was caused by the C=C vibration of the anthocyanin aromatic ring, while the GG-MRA@CMC-ST-Nisin-2 film shifted the peak at 1614 cm^{-1} to 1610 cm^{-1} and the peak intensity increased, indicating the existence of physical interactions between the bilayers (van der Waals forces and hydrogen bonds). The peak at 1410 cm^{-1} was a C—O specific angular deformation of phenols and the absorption band at 1230 cm^{-1} was a C—O—C symmetric stretching vibration, indicating that oxygen was linked to the aromatic ring. The peaks at 1592 cm^{-1} and 1414 cm^{-1} in the CMC-ST-Nisin film were —COO asymmetric and symmetric stretching vibrations of CMC, and the in-plane bending vibrations of C—H at 1322 cm^{-1} , which were consistent with that observed by Liang et al. [33]. Unlike CMC-ST-Nisin, the GG-MRA@CMC-ST-Nisin-1 films shifted the peaks to 1602 cm^{-1} and 1328 cm^{-1} , respectively, indicating intermolecular interactions occurred between the CMC-ST-Nisin films and the GG-MRA films. The absorption peaks at 922 cm^{-1} and 858 cm^{-1} were attributed to the C—O of 3,6-anhydrous-D-galactose and C—O—SO₃ of D-galactose-4-sulfate [36]. The absorption peak at 1030 cm^{-1} is the C=O stretching vibration of the dehydrated glucose ring in flavonoids [2], and the weaker absorption peak of GG-MRA compared to the GG-RA film further confirmed the formation of new hydrogen bonds between the acylated anthocyanins and the film matrix. The absorption peaks of GG-MRA@CMC-ST-Nisin films became stronger. They gradually shifted to lower wave numbers (1025 cm^{-1}), which might be due to the formation of complexes between the carboxyl groups of CMC and the flavonoid cation of anthocyanin through electrostatic interactions during the preparation process. A good and complete continuous structure was formed between the bilayer films through the compatibility of anthocyanins and intermolecular interactions. A similar phenomenon was reported by Liang et al., who found that red kale and CMC modified the complex spatial and crystalline structure between Artemisia Sphaerocephala Krasch gum and CMC through electrostatic interactions [33]. Jamroz et al. also reported that the interaction between lingonberry extract and film components promoted the compatibility between the furfuranose layer and the CMC+ gelatin layer [37]. Therefore, the FT-IR results indicated that the bilayer films were successfully prepared.

3.4.3. X-ray diffraction (XRD)

As illustrated in Fig. 6, the diffraction peak at $2\theta = 21.7^\circ$ was the characteristic peak of the cold junctional gel caused by its double-helical crystal structure [38]. Notably, GG-MRA showed microscopic absorption peaks at 9.25° , 28° , and 30.3° compared to GG-MA, indicating the formation of tiny crystals between the acylated anthocyanins and the

Table 1

Thicknesses, TS, EB of films.

Films	Thickness (mm)	TS (MPa)	EB (%)
GG-RA	0.056 ± 0.004^c	36.15 ± 4.40^a	45.02 ± 14.8^a
GG-MRA	0.059 ± 0.006^c	29.72 ± 1.86^b	25.81 ± 3.69^b
CMC-ST-Nisin	0.067 ± 0.003^b	10.92 ± 0.70^c	8.63 ± 1.44^c
GG-MRA@CMC-ST-Nisin	0.092 ± 0.003^a	33.17 ± 4.34^{ab}	19.00 ± 5.25^{bc}

Values are expressed as mean \pm SD ($n = 10$ for film thickness, and $n = 3$ for TS, EB). Different letters in the same column indicate significantly different ($p < 0.05$).

film matrix, which was consistent with the results observed by SEM. The CMC-ST-Nisin film exhibited a weak broad peak at 20.2° . In comparison, the XRD diffraction peaks of CMC (22°) and ST (20°) are non-overlapping amorphous states according to the relevant literature [10,39], where the amorphous state of ST was due to the destruction of the original semi-crystalline structure during the pasting process. The CMC-ST-Nisin film showed only one diffraction peak at 20.2° , indicating that CMC and ST were completely miscible and formed an amorphous complex by new hydrogen bonding. The relatively sharp peaks at 31.5° and 45.2° confirmed the highly crystalline nature of the partially immiscible formation of Nisin [40], which was consistent with the observed microstructure. Notably, the GG-MRA@CMC-ST-Nisin film exhibited a different XRD pattern from that of the GG-MRA and CMC-ST-Nisin films, which may be due to the formation of new hydrogen bonds between the anthocyanins and the polymer matrix, thus disrupting the original interactions and promoting the spatial reorganization of the biopolymer chains [3].

3.4.4. Film thickness and mechanical properties

As seen in Table 1, no significant thickness difference was observed between GG-RA films and GG-MRA films, indicating that anthocyanins could be well distributed in GG before and after acylation. The thickness of CMC-ST-Nisin films was about 0.067 mm , and the thickness of GG-MRA@CMC-ST-Nisin films was about 0.092 mm , indicating that the structure of the bilayer was dense and compact. The GG-RA films had the highest TS and EB values, indicating good compatibility between RA and GG. Chen et al. [2] also showed good compatibility and mechanical properties by adding red kale anthocyanins to the films. The TS and EB values of GG-MRA films were slightly decreased compared to GG-RA films, which was consistent with the observed SEM and XRD results. The formation of microcrystals on the film's surface and micropores in the cross-section causes structural discontinuities, leading to a decrease in mechanical properties. The TS and EB of CMC-ST-Nisin were the worst due to the insolubility of Nisin particles disrupting the film's denseness, reducing the film matrix's cohesion and restricting the film matrix's movement chain segments. A similar situation occurred with the addition of insoluble beet residue powder to the gelatin film by Iahnke et al. [41]. Notably, the GG-MRA@CMC-ST-Nisin films showed a significant increase in TS and a slight improvement in EB compared to the monolayer GG-MRA and CMC-ST-Nisin films. This may be due to the inter-solubility of anthocyanins in MRA with the bilayers enhanced the intermolecular interactions between the bilayers, increasing the mobility of the polymer chains and moderately filling the voids in the film matrix, which was consistent with the observed microstructure, FTIR and XRD results.

3.4.5. Moisture content and water solubility

As summarized in Table 2, the water content of GG-MRA films was slightly reduced compared to GG-RA films due to the hydrophobic groups in MRA that resisted the attack of nucleophilic water molecules. Notably, the CMC-ST-Nisin film showed the highest water content, which could be attributed to two reasons: the non-dense particle structure of Nisin allowing the film to adsorb water and the other being the strong interaction between the hydrophilic hydroxyl groups of CMC and

Table 2
Moisture contents, water solubility, WVP, OP and opacity of films.

Films	Moisture content (%)	Water solubility (%)	WVP ($\times 10^{-11}$ g m ⁻¹ s ⁻¹ Pa ⁻¹)	OP ($\times 10^{-16}$ cm ³ cm ⁻² s ⁻¹ Pa ⁻¹)	Opacity (mm ⁻¹)
GG-RA	16.12 \pm 0.86 ^b	34.44 \pm 0.71 ^b	7.05 \pm 0.64 ^b	2.88 \pm 0.13 ^{ab}	3.25 \pm 0.37 ^c
GG-MRA	15.66 \pm 1.00 ^b	32.61 \pm 0.65 ^b	6.45 \pm 0.45 ^c	2.66 \pm 0.18 ^b	4.21 \pm 0.22 ^c
CMC-ST-Nisin	19.55 \pm 0.98 ^a	46.60 \pm 1.74 ^a	9.18 \pm 0.36 ^a	3.17 \pm 0.12 ^a	14.92 \pm 1.33 ^a
GG-MRA@CMC-ST-Nisin	13.18 \pm 0.94 ^c	28.59 \pm 1.38 ^c	5.52 \pm 0.47 ^d	1.40 \pm 0.17 ^c	5.48 \pm 0.26 ^b

Values are expressed as mean \pm SD (n = 3 for moisture content, water solubility, WVP and OP). Different letters in the same column indicate significantly different (p < 0.05).

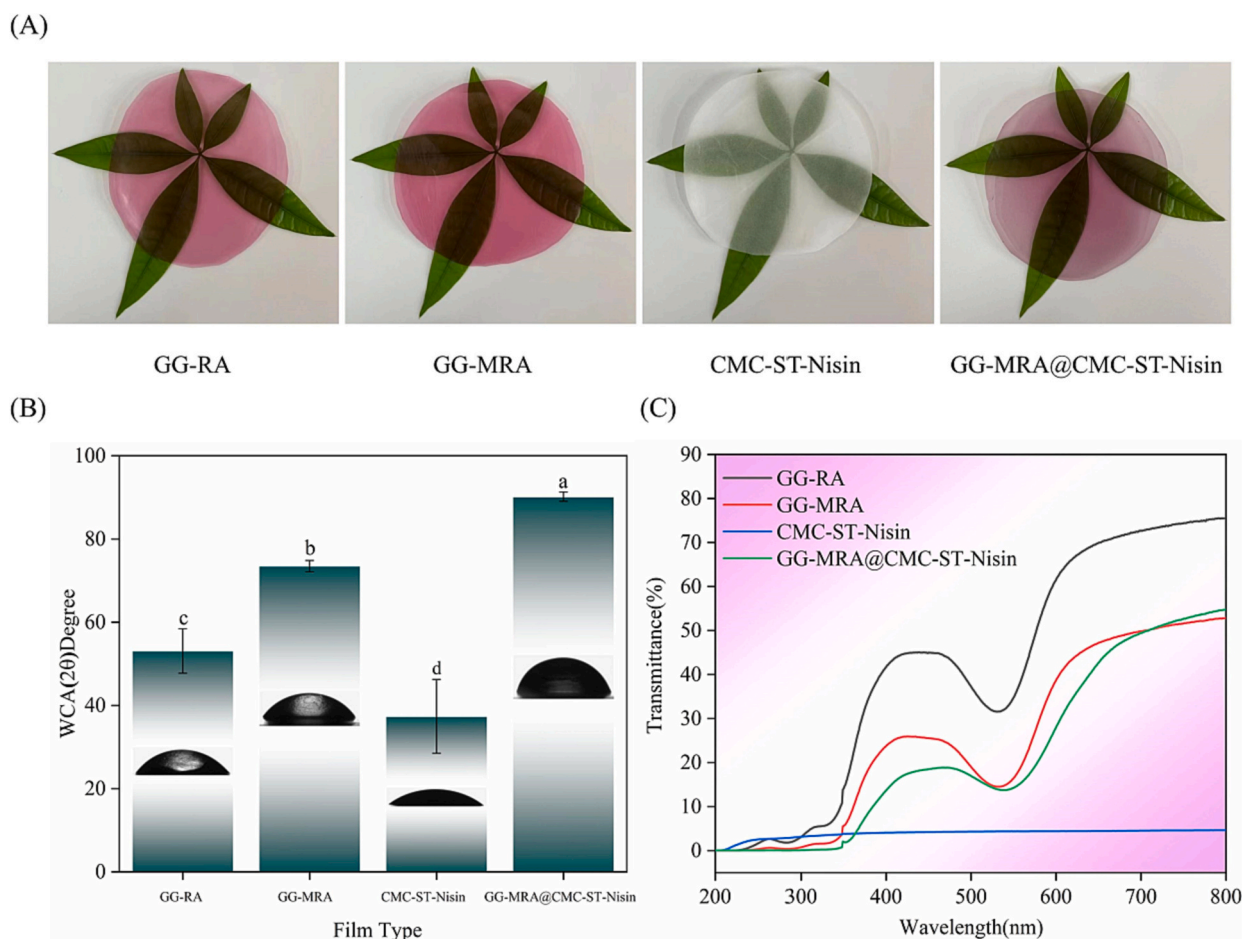


Fig. 7. Physical appearances (A), WCA (B) and UV-vis light transmittance (C) of films.

ST and water molecules. The water content of GG-MRA@CMC-ST-Nisin film was significantly reduced because some of the acylated anthocyanins were dissolved in the CMC-ST-Nisin film, which promoted the compatibility of Nisin with the film, resulting in a dense and continuous film structure, and a sound and complete continuous structure between the bilayers through intermolecular interactions.

Water solubility reflects the water resistance of the film. Due to the hydrophilic nature of anthocyanins in RA, GG-RA films exhibited moderate water solubility, which was similarly found by Huang et al. [24] in PVA/hydroxypropylmethylcellulose incorporating roselle anthocyanins. The slightly reduced water solubility of GG-MRA films compared to GG-RA films was attributed to the fact that acylated anthocyanins make anthocyanins more stable in aqueous solutions through intramolecular co-pigmentation [28]. Furthermore, the results by SEM, XRD, and FTIR showed that tiny crystals were formed on the surface of GG-MRA, indicating that the reduction of available hydroxyl groups on the surface of the film limits the ability of water molecules to penetrate the polymer structure, thus delaying the swelling behavior [42]. The

water solubility of CMC-ST-Nisin films was significantly increased, which may be related to the hydrophilicity of starch and CMC, Goodarzi et al. [43] and Michelin et al. [15] also showed the same finding. GG-MRA@CMC-ST-Nisin films exhibited the lowest water solubility due to the incorporation of hydrophobic groups of acylated anthocyanins into the bilayer structure, forming intermolecular hydrogen bonds with hydrophilic hydroxyl groups in the film matrix, which significantly reduced the number of hydrophilic hydroxyl groups available in the film matrix and thus greatly reduced the hydrophilicity of the bilayer, similar reports were found in films with added black carrot and red kale anthocyanins [44,45].

3.4.6. WVP and WCA

As presented in Table 2, GG-RA films exhibited moderate WVP values. Compared with the GG-RA films, the WVP of the GG-MRA films was significantly lower because the “sandwich structure” formed between anthocyanin backbone and acyl groups in MRA effectively hinders the nucleophilic attack of water molecules and generates spatial

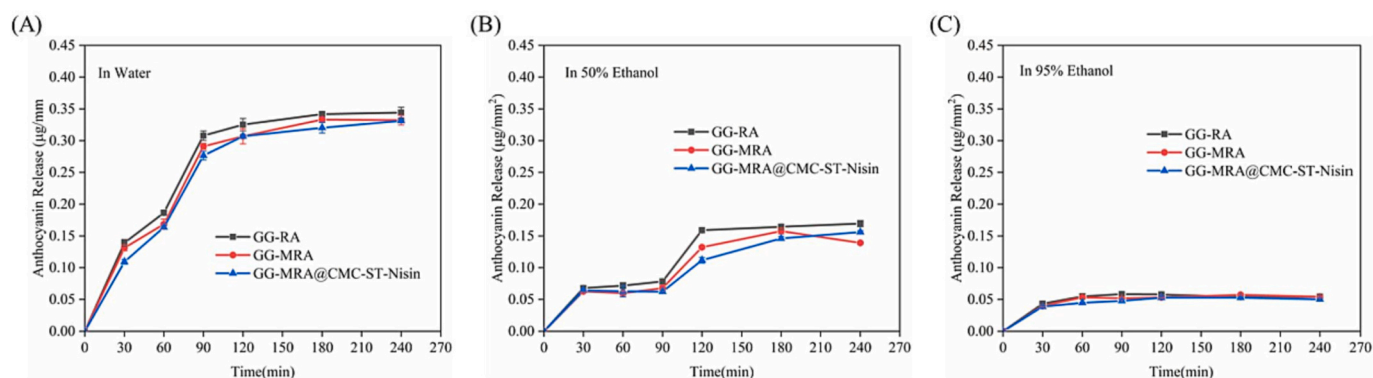


Fig. 8. Release of anthocyanins from indicator films in different food simulated solutions (in water (A), 50 % ethanol (B), 95 % ethanol (C)). Data are mean \pm SD ($n = 3$).

resistance [27]. The CMC-ST-Nisin films had the most significant WVP values due to the pore structure formed on the film surface (Fig. 4), which reduced the barrier to water vapor transmission while increasing the possibility of water adsorption by hydrophilic hydroxyl groups in the film matrix. It is worth noting that the GG-MRA@CMC-ST-Nisin films had the smallest WVP values due to the long and circuitous pathway created by the increased film thickness that makes it difficult for water vapor to pass through [46]. In addition, the partial dissolution of MRA allowed the polyphenols and flavonoids in anthocyanins to act as a bridge between the bilayer films through intermolecular hydrogen bonds, forming a tight and continuous network structure that reduced the water absorption and thus lowering the WVP value [47].

The contact angle values can measure the wettability of the film surface, and film surfaces with contact angles $<65^\circ$ and $>65^\circ$ are considered hydrophilic and hydrophobic, respectively [48]. As shown in Fig. 7(B), the GG-RA film was hydrophilic, which may be related to the fact that RA has extreme hydrophilic hydroxyl groups on its molecular chain that enhanced the hydrophilicity of the film. In contrast, the GG-MRA film was hydrophobic due to the change in the molecular structure of the acylated anthocyanins. It is evident from the microstructure and XRD results that uniform, dense microcrystals were formed on the surface of GG-MRA films. According to Crouvisier-Urien et al. [49], the higher contact angle values may be related to the hydrophobicity or roughness of the film surface. The CMC-ST-Nisin film had the lowest WCA and was highly hydrophilic, which was consistent with the microstructure observed on the film surface, where the non-dense and continuous pore surface would allow water molecules to be in complete contact with the hydrophilic groups in the film and reduced the water resistance. Notably, the GG-MRA@CMC-ST-Nisin film had an enormous WCA value, which was consistent with the results of WVP.

3.4.7. OP

Packaging with an excellent oxygen barrier can maintain food quality and extend food shelf life. The oxygen permeability of GG-RA, GG-MRA, CMC-ST-Nisin and GG-MRA@CMC-ST-Nisin films are shown in Table 2. GG-RA films exhibited moderate OP values due to forming a dense structure between the phenolic compounds present in RA and GG through intermolecular forces as shown in SEM images (Fig. 4(A, A1)), which resulted in a film with a particular barrier to oxygen. The lower OP value of GG-MRA was attributed to the bulky aromatic and pyranic rings in the MRA backbone structure that promoted the cross-linked network effect of the GG film, thus limiting the movement of oxygen molecules and reducing the oxygen transmission rate [50]. CMC-ST-Nisin exhibited the largest OP value ($p < 0.05$), which was consistent with the results exhibited by WVP (Table 2) and WCA (Fig. 7). The GG-MRA@CMC-ST-Nisin films exhibited the best oxygen barrier, probably due to the difficulty of oxygen transmission due to the increased film thickness on the one hand, and the partial dissolution of anthocyanins

on the other hand, probably because the interfacial adhesion between the bilayers delayed the chain mobility, thus providing a lower vacant-free volume for oxygen transport [51].

3.4.8. Optical properties

The appearance of all films is shown in Fig. 7(A). The GG-RA film was pink, the GG-MRA film was rosy red, the CMC-ST-Nisin film was creamy white, and the GG-MRA@CMC-ST-Nisin film was reddish purple. As predicted, due to the modification of anthocyanins, the color of GG-MRA film is slightly darker than that of GG-RA film. As shown in Fig. 7(C), the transmittance of GG-RA film was $<5\%$ in the range of 200–310 nm and $<50\%$ in the range of 310–580 nm, which was attributed to the UV absorption capacity of the phenolic compounds in RA. Compared to GG-RA films, GG-MRA films prevented UV light transmission below 300 nm due to the selective light absorption of polyphenolic compounds in plant extracts occurring at lower wavelengths, which was associated with red color in the films [52]. In contrast, the molecular structure of the acylated anthocyanin was transformed, and the color of the resulting film became more intense, thus enhancing UV-blocking properties, as also concluded by Jamroz et al. [53]. It is noteworthy that the CMC-ST-Nisin film had a light transmission of $<5\%$ in all wavelength ranges, which was due to the white color of the starch itself and the incomplete dissolution of Nisin forming particles that block UV-Vis light by reflection and scattering, which was consistent with the appearance of CMC-ST-Nisin film, so the outer film had perfect light shielding properties. The light transmission of GG-MRA@CMC-ST-Nisin film was almost 0 in the range of 200–350 nm, which indicated that it had the most excellent UV-blocking property compared with other films. Besides, the bilayer film had lower light transmission in the entire wavelength range than both GG-RA and GG-MRA films, which indicated that CMC-ST-Nisin film was used in the outer layer of the bilayer film, which hindered light transmission and enhanced the stability of the inner layer to a certain extent, which could improve the UV-visible light blocking performance of the bilayer film, so the bilayer film has excellent potential for UV-blocking packaging materials.

In addition to light transmittance, opacity is also an effective way to evaluate the optical properties of films. As shown in Table 2, the order of opacity of the films was: CMC-ST-Nisin $>$ GG-MRA@CMC-ST-Nisin $>$ GG-MRA $>$ GG-RA. Compared with the GG-MRA film, the opacity of the bilayer film was significantly increased, which was consistent with the UV-Vis blocking performance results, indicating that the outer film had good light barrier properties. Therefore, the bilayer films not only mitigated the oxidation and degradation of anthocyanins in the inner layer but also protected food from UV-visible light-induced nutrient loss, discoloration, and off-flavors, Liu et al. [54] and Sun, Zhang, Adhikari, Devahastin and Wang [55] prepared bilayer films also reached similar conclusions.

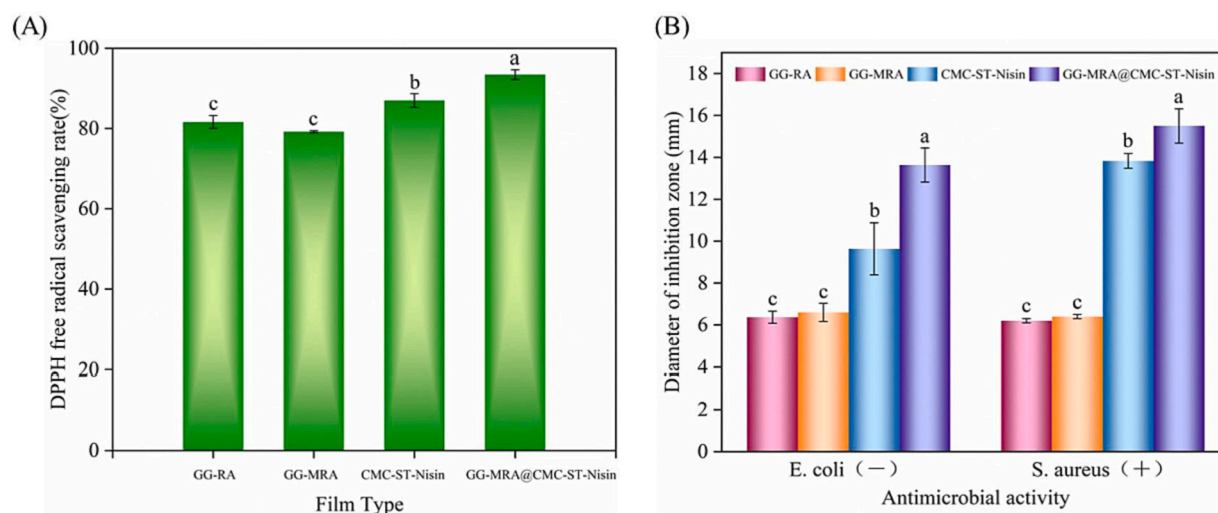


Fig. 9. The antioxidant and antimicrobial activity of films.

3.5. Release of anthocyanin

In general, the releasing rate of functionally active ingredients from the polymer films depends on factors such as the type of food simulant solution, solubility, and swelling properties of the polymer [39]. As shown in Fig. 8, the three films showed the fastest release rate in water, followed by 50 % ethanol and then 95 % ethanol, which was mainly attributed to the extreme hydrophilic hydroxyl groups on the molecular chains of roselle anthocyanins, which enhanced their solubility in aqueous solutions. It is evident from Fig. 8(A) and (B) that the rate of anthocyanin release from GG-MRA films was lower than that from GG-RA films because acylation decreased the polarity of anthocyanins, creating a spatial site-blocking effect and an effective physical hindrance to nucleophilic attack through intramolecular co-pigmentation [8], which was consistent with the WCA results (Fig. 7(B)). Collectively, the lowest anthocyanin release rate was observed in the GG-MRA@CMC-ST-Nisin films, which was attributed to the partial solubilization of MRA that allowed the polyphenols and flavonoids in anthocyanins to bind the bilayer films through covalent and non-covalent intermolecular interactions to form a more compact and continuous network structure resulting in a slower release of anthocyanins, which was consistent with the WVP results (Table 2).

3.6. Antioxidant capacity of films

As shown in Fig. 9(A), all films exhibited excellent DPPH radical scavenging ability, and GG-RA films showed good free radical scavenging ability due to the abundant phenolic compounds in RA. Anthocyanins can trap free radicals by providing phenolic hydrogen atoms [24]. Various reports have shown that biopolymeric films prepared by adding anthocyanins, such as black bean seed coat [22], red kale [2],

purple and black eggplant [56], have antioxidant activity. In contrast, GG-MRA films exhibited slightly poorer DPPH scavenging ability due to the fact that during the acylation process, acetic acid attacks the —OH on the benzene ring of anthocyanins to form —COOH, and with the reduction of phenolic hydroxyl groups, the antioxidant activity of acylated anthocyanins decreased along with it [4]. The free radical scavenging ability of CMC-ST-Nisin was attributed to Nisin, and Fan et al. [16] found an increase in radical scavenging activity with the increase of Nisin. This antioxidant mechanism may depend on its physical properties and chemical composition. Notably, GG-MRA@CMC-ST-Nisin films exhibited the highest free radical scavenging capacity, possibly due to MRA and Nisin's coordinated action.

3.7. Antimicrobial properties of films

As shown in Fig. 9(B), all films exhibited growth inhibition against *E. coli* and *S. aureus*. GG-RA and GG-MRA films exhibited antimicrobial properties due to the high content of phenolic compounds in the films, which disrupt the bacterial cell membrane and its metabolism, leading to the release of bacterial contents and decomposition, resulting in a significant reduction in bacterial activity [57]. The CMC-ST-Nisin films exhibited higher antimicrobial activity ($p < 0.05$), which was attributed to two aspects, on the one hand, it may be because Nisin binding to precursors of peptidoglycan and phospholipids inhibits cell wall biosynthesis and then forms pores within the cell membrane through which essential ions are released, ultimately leading to cell death [58]. On the other hand, it may be because electrostatic interaction between positively charged Nisin and negatively charged microbial cell membrane disrupts the cytoplasmic membrane, interferes with the essential energy transfer in the cytoplasmic membrane, loses the ATP transport system, and inhibits cell wall biosynthesis and bacterial growth, thus

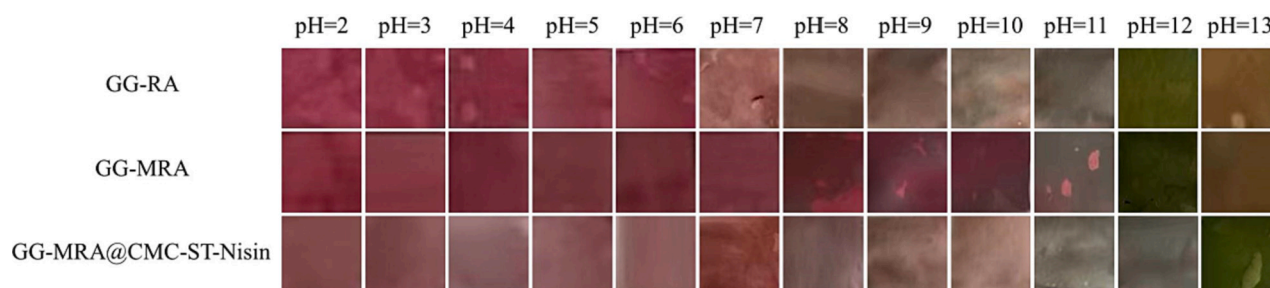


Fig. 10. Color changes of GG-RA, GG-MRA and GG-MRA@CMC-ST-Nisin films.

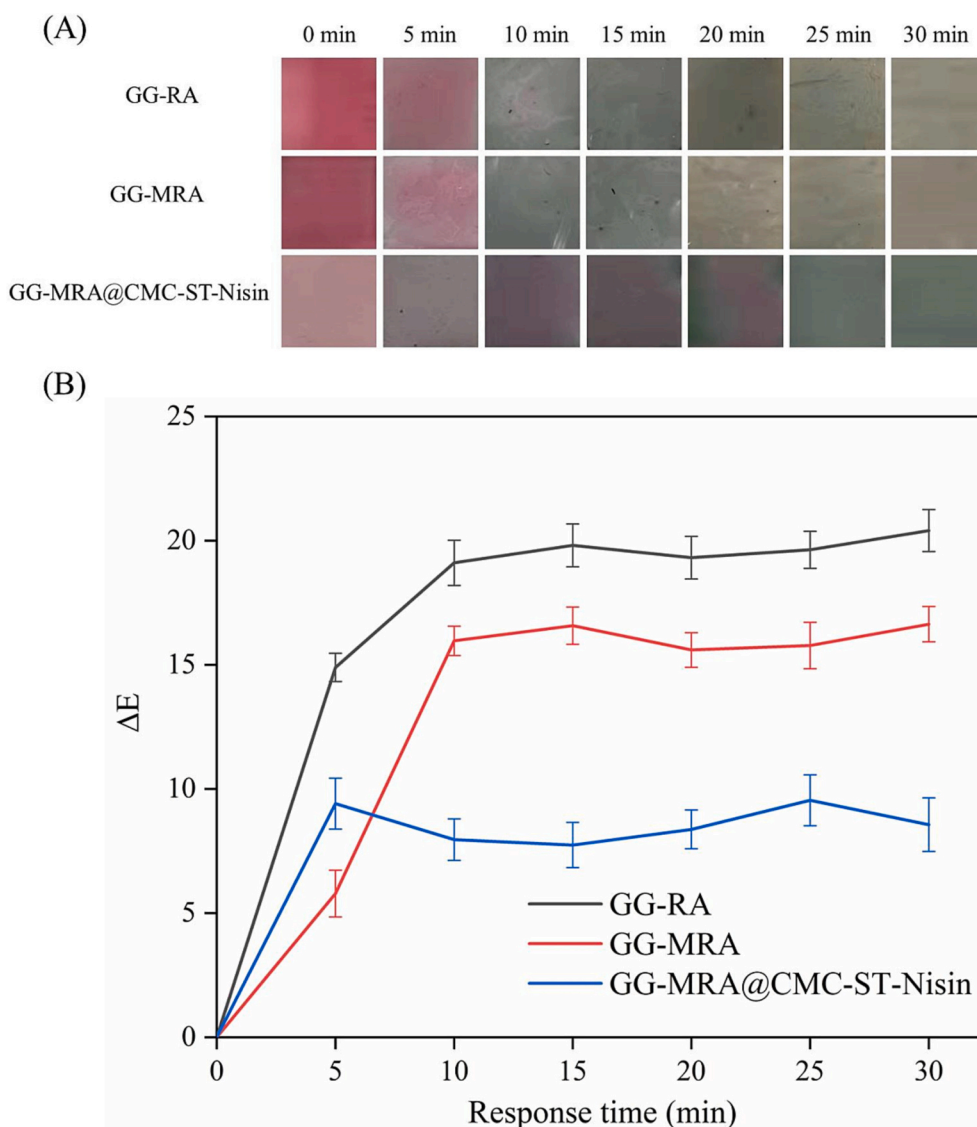


Fig. 11. Color changes (A) and sensitivity (B) of GG-RA, GG-MRA and GG-MRA@CMC-ST-Nisin films.

killing the cells [17]. Notably, GG-MRA@CMC-ST-Nisin films exhibited the most vigorous antibacterial activity ($p < 0.05$), which may be due to the synergistic effect of Nisin and anthocyanins.

3.8. Color responsiveness of films

3.8.1. pH sensitivity

As shown in Fig. 10, the GG-RA, GG-MRA and GG-MRA@CMC-ST-Nisin films all showed significant color changes at different pH (2–13), which were associated with the structural transformation of anthocyanins from flavonium cations to quinone-type bases and eventually chalcone. Among them, GG-RA films were cinnabar red at pH 2–6, pink at pH 7, slowly changed from grayish-teal to gray at pH 8–11, mossy green at pH 12, and yellowish brown at pH 13. GG-MRA films were cinnabar red at pH 2–7, dark red at pH 8–10, light green at pH 11, dark green at pH 12, and brown at pH 13. GG-MRA@CMC-ST-Nisin films were beige at pH 2–6, diaphanous at pH 7, grayish teal at pH 8–10, changing from gray to thin ink at pH 11–12, and green at pH 13. Compared to GG-RA films, GG-MRA films had higher color stability under weak alkaline conditions (pH 8–10). Notably, the bilayer films exhibited higher sensitivity than GG-MRA films, which may be because Nisin particles could enhance the color rendering of the indicator films.

Liu et al. [54] also found that bilayer films exhibited higher sensitivity than monolayer films, and the added TiO_2 could enhance the color rendering of the indicator films. Therefore, these films have great potential in intelligent food packaging applications due to their easy visualization of color changes.

3.8.2. Ammonia responsiveness

As shown in Fig. 11, all films showed high ammonia sensitivity and discernible color changes since volatile NH_3 could combine with H_2O in the films to form $\text{NH}_3\text{-H}_2\text{O}$, which was hydrolyzed to produce NH_4^+ and OH^- , and NH_4^+ stimulated the film surface in an alkaline state, leading to structural changes in anthocyanins and thus color responses [59]. The GG-RA films changed from the initial red color to beige at the 5th minute, and their ΔE increased significantly; from the 10th minute onwards, the films turned gray-green and slowly changed to yellow-green at 30 min, and the ΔE values remained within a specific fluctuation range (19.11–20.41). The GG-MRA films changed from the initial cinnabar red to light pink at the 5th minute. Its ΔE value also increased significantly, changing to gray-green at the 10th and 15th minutes, then to yellow-green at the 20th min, and remaining until the 30th minute, during which the ΔE value fluctuated within a specific range (15.6–16.6). The GG-MRA@CMC-ST-Nisin film changed from its initial

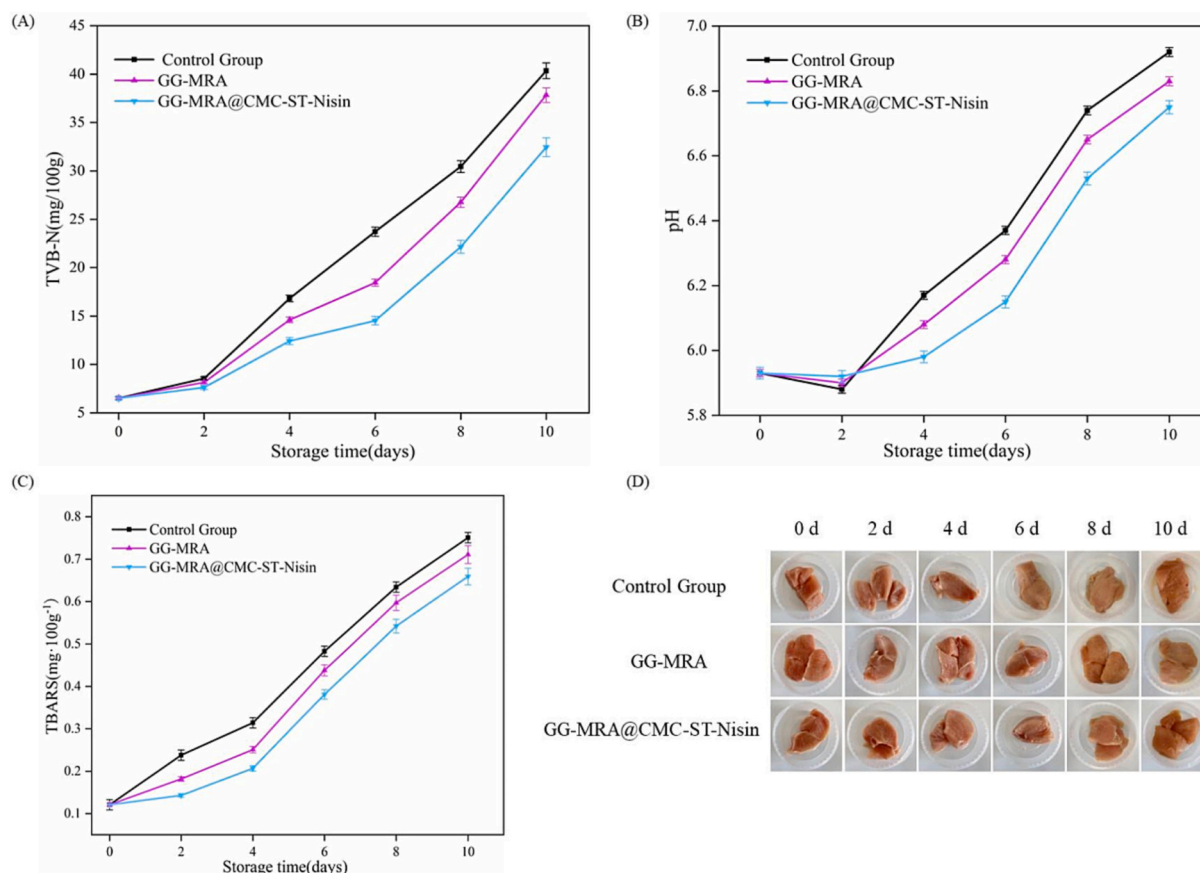


Fig. 12. (A) TVB-N, (B) pH, (C) TBARS values and (E) freshness of chicken breast were stored at 4 °C for 10 days.

peach color to light ink at the 5th min. Its ΔE value increased significantly, changing to an inky red color at the 10th minute and remaining there until the 20th minute, and changing to dark green color at the 25th and 30th minute, with the ΔE value fluctuating within a specific range (7.7–9.5) between the 10th and 30th minute. Generally, excellent indicators should have the properties of real-time monitoring and sensitive response, and all three of our films could provide the appropriate color response in a short time. Therefore, GG-RA, GG-MRA and GG-MRA@CMC-ST-Nisin films can monitor volatile nitrogenous compounds in meat products.





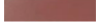
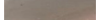






3.9. Application of GG-MRA and GG-MRA@CMC-ST-Nisin films in chicken breast

As shown in Fig. 12, we recorded pictures of the freshness of chicken breasts packed with GG-MRA and GG-MRA@CMC-ST-Nisin films at a 4 °C storage environment and measured three essential indicators to evaluate the degree of spoilage of chicken breasts: TVB-N content, pH value and TBARS, due to the excellent antioxidant, antimicrobial and color sensitivity of GG-MRA and GG-MRA@CMC-ST-Nisin films. In addition, a blank control group was established for freshness comparison. The total volatile salt nitrogen (TVB-N) value is one of the most critical indicators of the freshness of meat and seafood. According to the relevant standards, chicken meat with TVB-N values below 15 mg/100 g was considered fresh, between 15 and 30 mg/100 g was considered sub-fresh, and >30 mg/100 g was considered spoiled. As shown in Fig. 12 (A), the initial TVB-N content of chicken breasts was (6.51 ± 0.13) mg/100 g. The TVB-N content of the control, GG-MRA and GG-MRA@CMC-ST-Nisin film-packed chicken breasts on day 8 were (30.45 ± 0.61) mg/100 g, (26.78 ± 0.54) mg/100 g and (22.16 ± 0.54) mg/100 g, respectively. At this time, the chicken breasts in the control group were

already spoiled, while the other film-wrapped chicken breasts were in a sub-fresh state, and all the chicken breasts were spoiled by the 10th day. As shown in Fig. 12(B), the initial pH of chicken breasts was 5.93; however, the pH value suddenly decreased on day 2, which was attributed to the breakdown of protein ATP and the production of lactic acid in chicken breasts [2]. With the prolonged storage time, the pH values of chicken breasts in the control group, GG-MRA and GG-MRA@CMC-ST-Nisin film-packed were 6.74, 6.65 and 6.53, respectively, on the eighth day. At this time, the control packaged chicken breasts were spoiled, while the GG-MRA and GG-MRA@CMC-ST-Nisin film-packed chicken breasts were in a sub-fresh state, and both were spoiled by day 10. TBARS content is a reliable indicator of lipid oxidation, and consumers can usually detect off-flavors in meat when the TBARS value is above the threshold of 0.5 mg MDA/kg [60]. As shown in Fig. 12(C), the initial TBARS value of the chicken breasts was 0.121, and at day 8, the TBARS values of the chicken breasts in the control group, GG-MRA and GG-MRA@CMC-ST-Nisin film-packed were 0.634, 0.597 and 0.542, respectively, at which point the chicken had all produced peculiar smell. The freshness photographs of chicken breasts under different packaging are shown in Fig. 12(D). Chicken breasts in the control group were bright red with uniform color at 0–4 days; the luster of chicken breasts decreased at day 6 but still had elasticity, and the external edges of chicken breasts became slightly moist and sticky at day 8. On day 10, the color became dark red, the elasticity disappeared, and the secreted mucus was visible. The GG-MRA and GG-MRA@CMC-ST-Nisin film-packed chicken breasts were red meat with a transparent texture and a typical slightly bloody smell at 0–6 days. On day 8, the surface of the chicken breasts started to turn yellow. However, the muscle color was still uniform, and the texture was clear, maintaining an excellent sensory state. On day 10, the chicken breasts were soft and inelastic, with mucus exuding and producing an unpleasant taste. It can

Table 3

The color response of GG-MRA and GG-MRA@CMC-ST-Nisin films at different storage times.

Films	Storage time (days)	L	a	b	ΔE	Photographs
GG-MRA	0	39.67 \pm 0.60 ^d	46.33 \pm 0.58 ^a	16.67 \pm 1.15 ^a	0.00 \pm 0.00 ^d	
	2	38.33 \pm 0.58 ^{de}	45.00 \pm 1.73 ^a	16.00 \pm 1.00 ^a	2.40 \pm 1.83 ^c	
	4	37.00 \pm 1.00 ^e	45.33 \pm 0.60 ^a	17.70 \pm 1.16 ^a	3.45 \pm 1.48 ^c	
	6	46.67 \pm 0.57 ^b	46.67 \pm 0.58 ^a	12.00 \pm 1.00 ^b	22.04 \pm 1.58 ^b	
	8	43.00 \pm 1.00 ^c	25.00 \pm 0.00 ^b	12.00 \pm 1.00 ^b	22.14 \pm 0.67 ^b	
GG-MRA@CMC-ST-Nisin	10	52.33 \pm 0.57 ^a	2.33 \pm 0.57 ^c	8.00 \pm 1.73 ^c	46.92 \pm 0.29 ^a	
	0	63.00 \pm 2.00 ^a	26.66 \pm 0.57 ^{ab}	3.67 \pm 1.53 ^d	0.00 \pm 0.00 ^e	
	2	62.33 \pm 0.57 ^{bc}	24.67 \pm 2.31 ^b	5.70 \pm 0.58 ^{cd}	2.20 \pm 1.93 ^{de}	
	4	62.00 \pm 2.00 ^{bc}	26.67 \pm 1.50 ^{ab}	7.33 \pm 2.08 ^c	3.89 \pm 0.50 ^{cd}	
	6	59.67 \pm 2.08 ^b	27.70 \pm 0.58 ^a	6.00 \pm 1.00 ^{cd}	4.56 \pm 0.56 ^c	
	8	50.67 \pm 0.58 ^c	18.33 \pm 1.16 ^c	12.04 \pm 0.96 ^b	17.21 \pm 1.85 ^b	
	10	56.66 \pm 0.57 ^b	2.00 \pm 0.00 ^d	16.67 \pm 1.52 ^a	28.70 \pm 0.50 ^a	

Values are expressed as mean \pm SD (n = 3). Different letters in the same column indicate significantly different (p < 0.05).

be seen that the chicken breasts in the control group showed higher TVB-N, pH and TBARS values during storage, indicating that the films added with anthocyanins or Nisin destroyed the suitable environment for the growth and reproduction of the bacteria to a certain extent, delaying the decomposition of chicken proteins. It is noteworthy that the bilayers consistently showed the lowest TVB-N, pH and TBARS values during storage. The reason for this situation could be, on the one hand, that the outer CMC-ST-Nisin film resisted the harsh external environment and protected the stability of the inner anthocyanin layer, allowing it to develop its biological activity fully. On the other hand, it may be that the partial dissolution of anthocyanins promoted the compatibility between Nisin and the film matrix, facilitating the spatial reorganization of the biopolymer chains, and the synergistic effect of Nisin and anthocyanins gave the best antibacterial performance of the bilayer film. The rich phenolic compounds in anthocyanins and the high antibacterial activity of Nisin can effectively inhibit the growth of spoilage microorganisms. In particular, the circuitous path of the bilayer film limited the oxygen utilization capacity for microbial growth, effectively preventing lipid autoxidation during chicken storage and delaying the decomposition of proteins in chicken meat. [60]. Comprehensively considering the results of TVB-N, pH, TBARS and sensory quality, at 4 °C, GG-MRA effectively prolonged the shelf life of chicken breasts by 1 day and GG-MRA@CMC-ST-Nisin film prolonged the shelf life of chicken breasts by 2 days compared with the control group.

The film color also changed depending on the spoilage of the chicken breast packed in the film. As shown in Table 3, GG-MRA films were red on days 0–4, reddish-brown on days 6–8 and grayish-green on days 10. The bilayer films were pink on days 0–6, reddish-brown on days 8 and yellowish-brown on days 10. The ΔE values of the GG-MRA and GG-MRA@CMC-ST-Nisin films gradually increased with time, which was consistent with the color change of the films. Notably, the color changes of GG-MRA and GG-MRA@CMC-ST-Nisin films during the storage of chicken breasts at 4 °C reflected the freshness of the chicken. That is, GG-MRA film was red for fresh meat, reddish brown for second fresh meat, grayish green for spoiled meat, and GG-MRA@CMC-ST-Nisin film was pink for fresh, reddish brown for second fresh meat and yellowish brown for spoiled meat. Therefore, GG-MRA and GG-MRA@CMC-ST-Nisin films have great potential as freshness indicators for real-time monitoring of chicken breasts. In conclusion, our results showed that GG-MRA and GG-MRA@CMC-ST-Nisin films could not only extend the shelf life of chicken breasts by 1–2 days but also monitor the freshness in real-time.

4. Conclusion

To address the issue of poor stability of roselle anthocyanins in

intelligent packaging materials, this study started from both microscopic and macroscopic perspectives, enhancing the stability of roselle anthocyanins by acylation with acetic acid on the one hand, and providing physical protection by the outer antibacterial composite film on the other hand. The bilayer pH-sensitive antimicrobial films were successfully developed based on an inner indicator film made of GG and MRA and an outer inhibitory film made of CMC, starch and Nisin. The acylated anthocyanins enhanced the water vapor barrier, hydrophobicity, UV-vis light barrier, and pH color stability of GG films in comparison to GG-MRA films. Notably, the water content, water solubility, mechanical properties, water vapor and oxygen barrier, and hydrophobicity of GG-MRA@CMC-ST-Nisin were significantly improved compared to GG-MRA and CMC-ST-Nisin films. In addition, the outer layer considerably improved the inner layer's UV-vis light barrier, opacity, oxidation resistance, and antibacterial properties. All of the indicator films showed outstanding pH sensitivity and ammonia responsiveness. When the films were applied to chicken breast, it was observed that the indicator films not only monitored the chicken's freshness in real-time but also that the GG-MRA film and the double-layer film extended the chicken breast's shelf life by 1 and 2 days, respectively, compared to the control group. Considering all the physical and functional properties, GG-MRA@CMC-ST-Nisin film has excellent potential as novel multifunctional food packaging material.

CRedit authorship contribution statement

Yanglin Wu: Conceptualization, Methodology, Formal analysis, Writing – original draft, Writing – review & editing. **Chunwei Li:** Conceptualization, Funding acquisition, Supervision.

Declaration of competing interest

The authors declare that they have no known competing financial interests or personal relationships that could have appeared to influence the work reported in this paper.

Data availability

The data that has been used is confidential.

Acknowledgements

This work was financed by Fundamental Research Funds for the Central Universities (2572018BL09), Heilongjiang Provincial Natural Science Foundation Project (LH2019E001), and China Postdoctoral Science Foundation Funded Project (2016M590273). We would like to

sincerely acknowledge the support from the Analysis and Testing Center of Northeastern Forestry University.

References

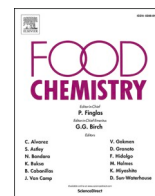
- P. Cazon, G. Velazquez, J.A. Ramirez, M. Vazquez, Polysaccharide-based films and coatings for food packaging: a review, *Food Hydrocoll.* 68 (2017) 136–148.
- M.Y. Chen, T.Y. Yan, J.Y. Huang, Y.Q. Zhou, Y.Q. Hu, Fabrication of halochromic smart films by immobilizing red cabbage anthocyanins into chitosan/oxidized-chitin nanocrystals composites for real-time hairtail and shrimp freshness monitoring, *Int. J. Biol. Macromol.* 179 (2021) 90–100.
- Y. Wu, C. Li, A smart film incorporating anthocyanins and tea polyphenols into sodium carboxymethyl cellulose/polyvinyl alcohol for application in mirror carp, *Int. J. Biol. Macromol.* 223 (2022) 404–417.
- P. Fei, F.S. Zeng, S.Y. Zheng, Q.L. Chen, Y.H. Hu, J. Cai, Acylation of blueberry anthocyanins with maleic acid: improvement of the stability and its application potential in intelligent color indicator packing materials, *Dyes Pigments* 184 (2021), 108852.
- J. Cai, F.S. Zeng, S.Y. Zheng, X.X. Huang, J.Y. Zhang, P. Zhang, P. Fei, Preparation of lipid-soluble bilberry anthocyanins through acylation with cinnamic acids and their antioxidant activities, *J. Agric. Food Chem.* 68 (28) (2020) 7467–7473.
- S. Oancea, A review of the current knowledge of thermal stability of anthocyanins and approaches to their stabilization to heat, *Antioxidants* 10 (9) (2021) 1337.
- P. Sari, A. Setiawan, T.A. Siswoyo, Stability and antioxidant activity of acylated jambolan (*Syzygium cumini*) anthocyanins synthesized by lipase-catalyzed transesterification, *Int. Food Res. J.* 22 (2) (2015) 671–676.
- J.H. Xie, X. Hao, Y.Q. Shang, W. Chen, Improvement of stability and lipophilicity of pteralgonidin-3-glucoside by enzymatic acylation with aliphatic dicarboxylic acid, *Food Chem.* 389 (2022), 133077.
- Y.P. Liu, Y. Qin, R.Y. Bai, X. Zhang, L.M. Yuan, J. Liu, Preparation of pH-sensitive and antioxidant packaging films based on kappa-carrageenan and mulberry polyphenolic extract, *Int. J. Biol. Macromol.* 134 (2019) 993–1001.
- Y. Qin, Y.P. Liu, H.M. Yong, J. Liu, X. Zhang, J. Liu, Preparation and characterization of active and intelligent packaging films based on cassava starch and anthocyanins from *Lycium ruthenicum* murr, *Int. J. Biol. Macromol.* 134 (2019) 80–90.
- Y.S. Musso, P.R. Salgado, A.N. Mauri, Gelatin based films capable of modifying its color against environmental pH changes, *Food Hydrocoll.* 61 (2016) 523–530.
- L.T. Wu, L.L. Tsai, Y.C. Ho, Y.H. Hang, C. Lin, M.L. Tsai, F.L. Mi, Active and intelligent gellan gum-based packaging films for controlling anthocyanins release and monitoring food freshness, *Carbohydr. Polym.* 254 (2021), 117410.
- S. Naghdi, M. Rezaei, M. Abdollahi, A starch-based pH-sensing and ammonia detector film containing betacyanin of paperflower for application in intelligent packaging of fish, *Int. J. Biol. Macromol.* 191 (2021) 161–170.
- Y. Qin, Y.P. Liu, X. Zhang, J. Liu, Development of active and intelligent packaging by incorporating betalains from red pitaya (*Hylocereus polyrhizus*) peel into starch/polyvinyl alcohol films, *Food Hydrocoll.* 100 (2020), 105410.
- M. Michelin, A.M. Marques, L.M. Pastrana, J.A. Teixeira, M.A. Cerqueira, Carboxymethyl cellulose-based films: effect of organosolv lignin incorporation on physicochemical and antioxidant properties, *J. Food Eng.* 285 (2020), 110107.
- L. Fan, J. Hu, Z. Hu, M. Peng, H. Wen, Y. Li, T. Wang, Preparation and characterization of aminoethyl hydroxypropyl methyl cellulose modified with nisin, *Int. J. Biol. Macromol.* 89 (2016) 62–69.
- H. Sun, X. Shao, M. Zhang, Z. Wang, J. Dong, D. Yu, Mechanical, barrier and antimicrobial properties of corn distarch phosphate/nanocrystalline cellulose films incorporated with nisin and ϵ -polylysine, *Int. J. Biol. Macromol.* 136 (2019) 839–846.
- Y. Yang, H. Liu, M. Wu, J. Ma, P. Lu, Bio-based antimicrobial packaging from sugarcane bagasse nanocellulose/nisin hybrid films, *Int. J. Biol. Macromol.* 161 (2020) 627–635.
- Z.R. Wang, Y. Li, L. Chen, X.L. Xin, Q.P. Yuan, A study of controlled uptake and release of anthocyanins by oxidized starch microgels, *J. Agric. Food Chem.* 61 (24) (2013) 5880–5887.
- M. Alizadeh-Sani, M. Tavassoli, E. Mohammadian, A. Ehsani, G.J. Khaniki, R. Priyadarshi, J. Rhim, PH-responsive color indicator films based on methylcellulose/chitosan nanofiber and barberry anthocyanins for real-time monitoring of meat freshness, *Int. J. Biol. Macromol.* 166 (2021) 741–750.
- S. Roy, H. Kim, J. Rhim, Effect of blended colorants of anthocyanin and shikonin on carboxymethyl cellulose/agar-based smart packaging film, *Int. J. Biol. Macromol.* 183 (2021) 305–315.
- X. Wang, H. Yong, L. Gao, L. Li, M. Jin, J. Liu, Preparation and characterization of antioxidant and pH-sensitive films based on chitosan and black soybean seed coat extract, *Food Hydrocoll.* 89 (2019) 56–66.
- J. Liu, S. Liu, Q.Q. Wu, Y.Y. Gu, J. Kan, C.H. Jin, Effect of protocatechuic acid incorporation on the physical, mechanical, structural and antioxidant properties of chitosan film, *Food Hydrocoll.* 73 (2017) 90–100.
- J. Huang, J. Liu, M. Chen, Q. Yao, Y. Hu, Immobilization of roselle anthocyanins into polyvinyl alcohol/hydroxypropyl methylcellulose film matrix: study on the interaction behavior and mechanism for better shrimp freshness monitoring, *Int. J. Biol. Macromol.* 184 (2021) 666–677.
- J.B. Harborne, Spectral methods of characterizing anthocyanins, *Biochem. J.* 70 (1) (1958) 22–28.
- J.B. Harborne, The natural distribution in angiosperms of anthocyanins acylated with aliphatic dicarboxylic acids, *Phytochemistry* 25 (8) (1986) 1887–1894.
- C. Zhao, Y. Yu, Z. Chen, G. Wen, F. Wei, Q. Zheng, C. Wang, X. Xiao, Stability-increasing effects of anthocyanin glycosyl acylation, *Food Chem.* 214 (2017) 119–128.
- P. Trouillas, J.C. Sancho-Garcia, V. De Freitas, J. Gierschner, M. Otyepka, O. Dangles, Stabilizing and modulating color by copigmentation: insights from review theory and experiment, *Chem. Rev.* 116 (9) (2016) 4937–4982.
- H. Matsufuji, H. Kido, H. Misawa, J. Yaguchi, T. Otsuki, M. Chino, M. Takeda, K. Yamagata, Stability to light, heat, and hydrogen peroxide at different pH values and DPPH radical scavenging activity of acylated anthocyanins from red radish extract, *J. Agric. Food Chem.* 55 (9) (2007) 3692–3701.
- M. Dyrby, N. Westergaard, H. Stapelfeldt, Light and heat sensitivity of red cabbage extract in soft drink model systems, *Food Chem.* 72 (4) (2001) 431–437.
- G.B. Escher, M. Wen, L. Zhang, N.D. Rosso, D. Granato, Phenolic composition by UHPLC-Q-TOF-MS/MS and stability of anthocyanins from *Clitoria ternatea* L. (Butterfly pea) blue petals, *Food Chem.* 331 (2020), 127341.
- J.L. Liu, J.Y. Huang, Y.B. Ying, L.P. Hu, Y.Q. Hu, PH-sensitive and antibacterial films developed by incorporating anthocyanins extracted from purple potato or roselle into chitosan/polyvinyl alcohol/nano-ZnO matrix: comparative study, *Int. J. Biol. Macromol.* 178 (2021) 104–112.
- T. Liang, G. Sun, L. Cao, J. Li, L. Wang, A pH and NH₃ sensing intelligent film based on *Artemisia sphaerocephala* Krasch. Gum and red cabbage anthocyanins anchored by carboxymethyl cellulose sodium added as a host complex, *Food Hydrocoll.* 87 (2019) 858–868.
- S. Passamonti, U. Vrhovsek, F. Mattivi, The interaction of anthocyanins with biltranslocase, *Biochem. Biophys. Res. Commun.* 296 (3) (2002) 631–636.
- Y. Qin, D. Yun, F. Xu, C. Li, D. Chen, J. Liu, Impact of storage conditions on the structure and functionality of starch/polyvinyl alcohol films containing *Lycium ruthenicum* anthocyanins, *Food Packag. Shelf Life* 29 (2021), 100693.
- S.F. Uy, A.J. Eastal, M.M. Farid, R.B. Keam, G.T. Conner, Seaweed processing using industrial single-mode cavity microwave heating: a preliminary investigation, *Carbohydr. Res.* 340 (7) (2005) 1357–1364.
- E. Jamróz, J. Tkaczewska, L. Juszczak, M. Zimowska, A. Kawecka, P. Krzyściak, M. Skóra, The influence of lingonberry extract on the properties of novel, double-layered biopolymer films based on furcellaran, CMC and a gelatin hydrolysate, *Food Hydrocoll.* 124 (2022), 107334.
- Y.C. Wei, C.H. Cheng, Y.C. Ho, M.L. Tsai, F.L. Mi, Active gellan gum/purple sweet potato composite films capable of monitoring pH variations, *Food Hydrocoll.* 69 (2017) 491–502.
- P. Ezati, J.W. Rhim, M. Moradi, H. Tajik, R. Molaei, CMC and CNF-based alizarin incorporated reversible pH-responsive color indicator films, *Carbohydr. Polym.* 246 (2020), 116614.
- D.X. Qi, Y.W. Xiao, L. Xia, L.L. Li, S.W. Jiang, S.T. Jiang, H.L. Wang, Colorimetric films incorporated with nisin and anthocyanins of pomegranate/*Clitoria ternatea* for shrimp freshness monitoring and retaining, *Food Packag. Shelf Life* 33 (2022), 100898.
- A. Iahnke, T. Costa, A.D. Rios, S.H. Flores, Antioxidant films based on gelatin capsules and minimally processed beet root (*Beta vulgaris* L. Var. *Conditiva*) residues, *J. Appl. Polym. Sci.* 133 (10) (2016).
- N. Bumbudsanpharoke, S. Kwon, W. Lee, S. Ko, Optical response of photonic cellulose nanocrystal film for a novel humidity indicator, *Int. J. Biol. Macromol.* 140 (2019) 91–97.
- M.M. Goodarzi, M. Moradi, H. Tajik, M. Forough, P. Ezati, B. Kuswandi, Development of an easy-to-use colorimetric pH label with starch and carrot anthocyanins for milk shelf life assessment, *Int. J. Biol. Macromol.* 153 (2020) 240–247.
- M. Moradi, H. Tajik, H. Almasi, M. Forough, P. Ezati, A novel pH-sensing indicator based on bacterial cellulose nanofibers and black carrot anthocyanins for monitoring fish freshness, *Carbohydr. Polym.* 222 (2019), 115030.
- L. Prietto, T.C. Mirapalhete, V.Z. Pinto, J.F. Hoffmann, N.L. Vanier, L. Lim, A. R. Guerra Dias, E. Da Rosa Zavarze, PH-sensitive films containing anthocyanins extracted from black bean seed coat and red cabbage, *LWT* 80 (2017) 492–500.
- D. Fu, Y. Ding, R. Guo, J. Zhang, H. Wang, B. Niu, H. Yan, Poly(lactic acid)/poly(vinyl alcohol)-quaternary ammonium chitosan double-layer films doped with novel antimicrobial agent CuO@ZIF-8 NPs for fruit preservation, *Int. J. Biol. Macromol.* 195 (2022) 538–546.
- T. Gasti, S. Dixit, O.J. D'Souza, V.D. Hiremani, S.K. Vootla, S.P. Masti, R. B. Chougale, R.B. Malabadi, Smart biodegradable films based on chitosan/methylcellulose containing Phyllanthus reticulatus anthocyanin for monitoring the freshness of fish fillet, *Int. J. Biol. Macromol.* 187 (2021) 451–461.
- E.A. Vogler, Structure and reactivity of water at biomaterial surfaces, *Adv. Colloid Interf. Sci.* 74 (1) (1998) 69–117.
- K. Crouvisier-Urien, P.R. Bodart, P. Wincler, J. Raya, R.D. Gougou, P. Cayot, S. Domenek, F. Debeaufort, T. Karbowiak, Biobased composite films from chitosan and lignin: antioxidant activity related to structure and moisture, *ACS Sustain. Chem. Eng.* 4 (12) (2016) 6371–6381.
- X. Zhang, Y. Liu, H. Yong, Y. Qin, J. Liu, J. Liu, Development of multifunctional food packaging films based on chitosan, TiO₂ nanoparticles and anthocyanin-rich black plum peel extract, *Food Hydrocoll.* 94 (2019) 80–92.
- X. Zhai, X. Zou, J. Shi, X. Huang, Z. Sun, Z. Li, Y. Sun, Y. Li, X. Wang, M. Holmes, Y. Gong, M. Povey, J. Xiao, Amine-responsive bilayer films with improved illumination stability and electrochemical writing property for visual monitoring of meat spoilage, *Sensors Actuators B Chem.* 302 (2020), 127130.
- M.J. Fabra, I. Falco, W. Randazzo, G. Sanchez, A. Lopez-Rubio, Antiviral and antioxidant properties of active alginate edible films containing phenolic extracts, *Food Hydrocoll.* 81 (2018) 96–103.

- [53] E. Jamroz, J. Tkaczewska, L. Juszcak, M. Zimowska, A. Kawecka, P. Krzysciak, M. Skora, The influence of lingonberry extract on the properties of novel, double-layered biopolymer films based on furcellaran, CMC and a gelatin hydrolysate, *Food Hydrocoll.* 124 (2022), 107334.
- [54] L. Liu, J. Zhang, J. Shi, X. Huang, X. Zou, D. Zhang, X. Zhai, Z. Yang, Z. Li, Y. Li, Preparation and comparison of two functional nanoparticle-based bilayers reinforced with a κ -carrageenan–anthocyanin complex, *Int. J. Biol. Macromol.* 165 (2020) 758–766.
- [55] Y. Sun, M. Zhang, B. Adhikari, S. Devahastin, H. Wang, Double-layer indicator films aided by BP-ANN-enabled freshness detection on packaged meat products, *Food Packag. Shelf Life* 31 (2022), 100808.
- [56] H. Yong, X. Wang, X. Zhang, Y. Liu, Y. Qin, J. Liu, Effects of anthocyanin-rich purple and black eggplant extracts on the physical, antioxidant and pH-sensitive properties of chitosan film, *Food Hydrocoll.* 94 (2019) 93–104.
- [57] E. Genskowsky, L.A. Puente, J.A. Pérez-álvarez, J. Fernandez-Lopez, L.A. Muñoz, M. Viuda-Martos, Assessment of antibacterial and antioxidant properties of chitosan edible films incorporated with maqui berry (*Aristotelia chilensis*), *LWT Food Sci. Technol.* 64 (2) (2015) 1057–1062.
- [58] I. Khan, D. Oh, Integration of nisin into nanoparticles for application in foods, *Innov. Food Sci. Emerg.* 34 (2016) 376–384.
- [59] L. Liu, J. Zhang, X. Zou, M. Arslan, J. Shi, X. Zhai, J. Xiao, X. Wang, X. Huang, Z. Li, Y. Li, A high-stable and sensitive colorimetric nanofiber sensor based on PCL incorporating anthocyanins for shrimp freshness, *Food Chem.* 377 (2022), 131909.
- [60] E. Hernández-García, M. Vargas, A. Chiralt, Starch-polyester bilayer films with phenolic acids for pork meat preservation, *Food Chem.* 385 (2022), 132650.

ARTICLES FOR FACULTY MEMBERS

ROSELLE (HIBISCUS SABDARIFFA) ANTHOCYANIN USE IN MONITORING MEAT FRESHNESS

Title/Author	<p>A visual bi-layer indicator based on roselle anthocyanins with high hydrophobic property for monitoring griskin freshness / Zhang, J., Huang, X., Shi, J., Liu, L., Zhang, X., Zou, X., Xiao, J., Zhai, X., Zhang, D., Li, Y., & Shen, T.</p>
Source	<p><i>Food Chemistry</i> Volume 355 (2021) 129573 Pages 1-8 https://doi.org/10.1016/J.FOODCHEM.2021.129573 (Database: ScienceDirect)</p>



A visual bi-layer indicator based on roselle anthocyanins with high hydrophobic property for monitoring griskin freshness

Junjun Zhang^a, Xiaowei Huang^{a,*}, Jiyong Shi^{a,*}, Li Liu^a, Xinai Zhang^a, Xiaobo Zou^{a,*}, Jianbo Xiao^{a,b}, Xiaodong Zhai^a, Di Zhang^a, Yanxiao Li^a, Tingting Shen^a

^a Agricultural Product Processing and Storage Lab, School of Food and Biological Engineering, Jiangsu University, Zhenjiang, Jiangsu 212013, China

^b Nutrition and Bromatology Group, Department of Analytical Chemistry and Food Science, Faculty of Food Science and Technology, University of Vigo - Ourense Campus, E-32004, Ourense, Spain

ARTICLE INFO

Keywords:

PVDF film
Hydrophobic property
Bi-layer indicator
WCA
WVP
Freshness

ABSTRACT

This study designed a new type indicator with hydrophobic Polyvinylidene Fluoride (PVDF) film as a moisture prevent-layer. And the sensor layer was provided based on polyvinyl alcohol/Sodium alginate (PS) and Roselle anthocyanins (RAs). Physical properties, microstructure, and color stability of the bi-layer indicator have been investigated. The Water contact angle (WCA) of PS/RAs/ PVDF film (PSRF) was 108.85°, which can be considered as an excellent hydrophobic surface. The lowest Water Vapor Permeability (WVP) value of PSRF exhibited a good barrier property for moisture. Therefore, PSRF film was used to monitor the griskin freshness. The Total volatile basic nitrogen (TVB-N) level was increased to 18.02 mg/100 g at 72 h, and the color of the indicator presented visible color changes. The acquired results revealed a good correlation between TVB-N, pH and color change of the indicator. The research indicated that PSRF indicator has increasing potential application on food intelligent packaging.

1. Introduction

The food products spoiled easily during storage time due to the enzymatic reaction and extrinsic microbial contamination. Generally, the spoilage products lead to the generation of volatile amines and carboxylic acids, which can cause harmful effects on human health. Therefore, the assessment of pork freshness is essential for both consumers and the food industry. The colorimetric indicators reflect the quality of the product through the visible color changes with the naked eye (Huang et al., 2019b; Zhai, Li, Zhang, Shi, & Povey, 2018)

In recent years, natural pH-sensitive dyes have drawn attention, because of their eco-friendly nature, lower power consumption and toxicity to food products and environment. Anthocyanins are natural dyes that exhibit visible color from red in an acidic environment to yellow in an alkaline condition (Senem, Esra, Charlotte, & John, 2015). Zhai extracted red radish anthocyanins as a sensor to indicate milk and fish freshness (Zhai et al., 2017). Another pH indicator incorporated the purple sweet potato anthocyanins into agar/starch and was used as a diagnostic media for monitoring food spoilage (Choi, Lee, Lacroix, & Han, 2017). Roselle anthocyanins have attracted the attention of

worldwide scientists, and studies have demonstrated that they mainly take the form of cyanin and delphinine-like anthocyanin (Hashemi & Shahani, 2019). Particularly, roselle anthocyanins possess the properties of pH sensitivity, antioxidant activity, and antibacterial activity (Zou et al., 2017). It can be used to develop pH sensors for intelligent packaging of food quality.

Generally, the pH indicators are composed of two parts: one is the pH dyes, and the other is a solid matrix for immobilizing the dyes. The solid matrix supporters are mostly made of synthetic and biodegradable polymers such as polysaccharide (Coma, & Véronique, 2012), PVA (Liu et al., 2017), chitosan (Mannozi et al., 2018), and sodium alginate (Koray et al., 2014). Polyvinyl alcohol (PVA), carrying a suitable mechanical propriety is widely used in food packaging (Zhang et al., 2017). Previously, sodium alginate (SA), a linear polysaccharide extracted from brown algae, was used as an excellent natural edible film material (Ibrahim & Salmawi, 2013). Various researches have also combined with PVA and SA as the matrix of the pH indicators (Eghbalifam, Frounchi, & Dadbin, 2015).

However, the hydrophilicity of anthocyanin affects itself weeping out biopolymers matrix and the biopolymers matrix is easy to dissolve in

* Corresponding authors.

E-mail addresses: huangxiaowei@ujs.edu.cn (X. Huang), shi_jiyong@ujs.edu.cn (J. Shi), zou_xiaobo@ujs.edu.cn (X. Zou).

an aqueous solution in the previous study (Huang, Chen, Zhou, Li, & Hu, 2020; Zhai et al., 2017; Zhang et al., 2019). These problems have been ignored such as the intelligent packaging is water-solubility then the pH dyes is easy to leak out from the packaging systems. So it is the need of the hour to prepare a bi-layer film. One of the layers (sensor layer) works as the pH indicator and the other layer (prevent-layer) serves as a protective barrier to moisture. The Polyvinylidene fluoride (PVDF) film is a crystalline polymer that possesses better chemical stability, heat resistance, antimicrobial and mechanical properties (Tang, Wang, & Han, 2019). Up to now, no research work has been reported that PVDF layer serves as a protective barrier to moisture for food freshness indicators. The fabrication of the bi-layer through coating on PVDF film surface with a smart sensor layer enables to increase the hydrophobicity of the packaging film.

The overarching objective of the current study was to develop the bilayer indicator to monitor the griskin freshness. One layer was prepared by incorporating roselle anthocyanins into polyvinyl alcohol/sodium alginate solution and defined as sensor layer. The other layer was prepared by using PVDF film and defined as a moisture prevent-layer. The filter paper (a typical hydrophilic film) was used to prepare as the negative control of the moisture prevent-layer. Moreover, scanning electron microscopy (SEM), Fourier transform infrared (FT-IR) spectroscopy, physical properties, color sensitivity and color stability were characterized and investigated.

2. Material and methods

2.1. Material

Roselle calyx and griskin were purchased from the local supermarket. The Polyvinylidene fluoride (PVDF) and filter paper (#1, Wood pulp, diameter: 90 mm) were purchased from Millipore Co., Ltd. Polyvinyl alcohol (MW: 1750 ± 50), Sodium alginate and Glycerin were purchased from Shanghai Natural Wild-insect Kingdom Co. Ltd. Ammonia hydroxide (NH₃-H₂O), potassium chloride solution and sodium acetate were obtained from Jiangsu Thorpe Group Co. Ltd. Buffers solution were prepared with potassium chloride/sodium acetate and their pH values were measured by using a digital pH meter. Plastic Petri dishes were purchased from Sinopharm Chemical Reagent Co., Ltd.

2.2. Detection and identification of roselle anthocyanins

2.2.1. Extraction of roselle anthocyanins

Roselle anthocyanins were extracted according to the previous literature (Zhang et al., 2019). Firstly, the roselle calyx was dried by using an oven at 50 °C for 3 h. Then, the dried roselle calyx was crushed with a small pulverizer (JIUYANG M01, China) to get Roselle powders. Thereafter, approximately 100 g roselle powders were macerated with 1 L of 80% ethanol for 3 h at 45 °C. The roselle extraction was filtered through Whatman filter paper (#1) to get the roselle anthocyanins solvent extraction solution. After that, the ethanol solvent was removed to obtain the roselle anthocyanins concentrated solution (RACs) with a rotary evaporator (SY-2000A, Shang Hai Yarong Biochemistry Instrument Factory, China) at 50 °C for 1 h. Finally, the anthocyanins concentrated solution was stored at 4 °C until further analyzed.

2.2.2. Detection of total anthocyanins content (TAC) in roselle extraction

The total anthocyanins content (TAC) in RACs was determined according to the pH differential quantitative detection method (Hashemi & Shahani, 2019). Firstly, 1 mL of RACs was diluted in 10 mL potassium chloride solution (pH = 1) and 10 mL sodium acetate buffer solution (pH = 4.5), respectively. The samples were incubated away from light at 25 °C for an hour. Then, the absorbance of samples was measured at 520 and 700 nm by using Agilent CARY 100 UV-Vis spectrophotometer (Varian Corporation, USA). TAC was calculated according to the following equation:

$$TAC(\text{mg/L}) = \frac{A \times Mw \times DF \times 10^3}{\epsilon \times L} \quad (1)$$

where: A was calculated as $(A = [\text{Abs}_{510\text{nm}} - \text{Abs}_{700\text{nm}}]_{\text{pH}_{1.0}} - [\text{Abs}_{510\text{nm}} - \text{Abs}_{700\text{nm}}]_{\text{pH}_{4.5}})$ and Mw was 449.2 g/mol (cyanidin-3-O-glucoside); DF is the dilution factor; ϵ is the molar extinction coefficient; L is the diameter of the cuvette, 1 cm.

2.2.3. Identification of anthocyanins in roselle extraction by HPLC-MS (High performance liquid chromatography-mass spectrometer)

Before the identification of RACs, the sugar impurities in the concentrated solution were removed by macroporous resins. The resins (AB-8) were activated in the glass column (10 cm × 60 cm) by sequential 95% ethanol elution and then washed by deionized water. Next, 5% hydrochloric acid was used for resin and then rinsed again by deionized water making resin until neutral. Lastly, 5% sodium hydroxide was further utilized for resin and eluted by deionized water until the pH value reached 7 (Eghbalifam et al., 2015). The roselle anthocyanins concentrated solution was filled in the AB-8 macroporous resin column for 2 h. Then water-soluble impurities such as sugars were washed and then rinsed by a 95% ethanol solution until the column was colorless (5 column volume; flow rate: 2 mL/min).

The HPLC-MS, which was used to qualitative analysis of RACs, included a Thermo Electron Surveyor MS pump and a Surveyor auto sampler injector (Thermo Electron, San Jose, CA) The sample was prepared by dissolving 50 µL RACs in 5 mL deionized water. ZORBAX SB-C18 column (lichrospher5-C18, 150 mm, 4.6 mm, 5 µm, Agilent Technologies, Santa Clara, CA) was performed for HPLC-MS. A binary gradient elution of mobile phase A (100% acetonitrile) B (5% formic acid in deionized water) were used for anthocyanin separation at a flow rate of 1 mL/min. The gradient elution conditions was used as follows: 0–15 min, 10–30% B; 15–25 min, 30–50% B; 25–30 min, 50–30% B; 30–35 min, 30–10% B; 35.01 min, 10% B. The wavelength was set at 530 nm and column oven temperature was set at 35 °C. The capillary voltage was 3.0 kV for positive (ESI+) mode

2.3. Preparation of bi-layer pH indicator

The bi-layer pH indicator was prepared by dissolving and coating process (Liu et al., 2020). Firstly, 100 mL of deionized water containing 1.6 g SA and 0.4 g PVA (PS) were heated and stirred with a magnetic stirrer (F-101S, YUHUA, China) at 60 °C for 60 min. Afterwards, the RACs, which was established as 1% of the PS solution, was incorporated into the PS solution (PSR). The mixed film-forming solution was stirred until it was completely homogenized at 40 °C and degassed for 5 min. After that, the PVDF film was cut into plastic petri dish size (9 cm × 9 cm) to form a moisture prevent-layer. The filter paper was also put into plastic petri dish as the negative comparison. The bi-layer pH indicator was prepared by the coating on PVDF film or filter paper with 10 g of the PSR solution which denoted as PSRFor PSRP. All the indicators were dried at 37 °C in an incubator with 50% relative humidity for 12 h.

2.4. Characterization of films

2.4.1. Fourier transform infrared (FT-IR) spectroscopy and scanning electron microscopy (SEM)

FT-IR spectrum of samples was detected on a Nicolet50 spectrometer (Perkin Elmer 16 PC spectrometer, Boston, USA) using attenuated total reflectance accessory (ATR) mode in a range of 4000–650 cm⁻¹. After being sputtered with a gold layer on the bi-layer film, the film was investigated using a JSM-7800F scanning electron microscopy (SEM, Hitachi, High-Technologies Corporation, Japan).

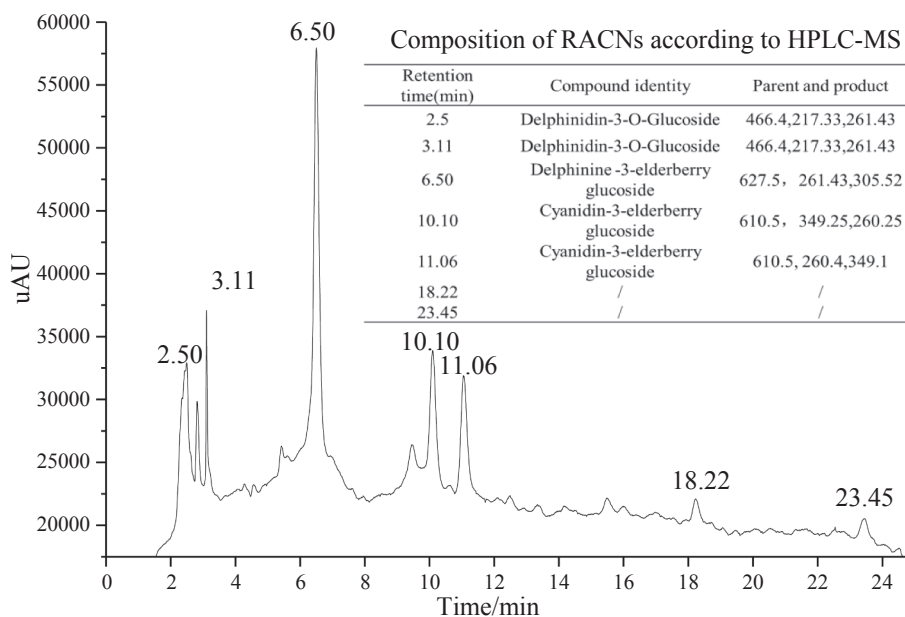


Fig. 1. HPLC chromatogram of RACNs recorded at 530 nm and the illustration was the composition of RACNs.

2.4.2. Moisture content (MC), swelling index (SI) and water solubility (WS)

For analyzing the moisture content (MC), the films were cut into a square shape 30×30 mm (M_0) and dried at 105°C in an oven until reached an equipoise (M_1). For analyzing the swelling index (SI) and water solubility (WS), each dried piece was immersed into deionized water for 24 h at room temperature (Homez-Jara et al., 2018). Later, the deionized water was discarded and films pieces were dried with a filter paper (M_2). Then, the pieces were re-dried in the oven at 105°C (M_3). SI, WS and MC were calculated according to the following equations:

$$MC(\%) = \frac{M_0 - M_1}{M_0} \times 100 \quad (2)$$

$$SI(\%) = \frac{M_2 - M_1}{M_1} \times 100 \quad (3)$$

$$WS(\%) = \frac{M_1 - M_3}{M_1} \times 100 \quad (4)$$

2.4.3. Thickness and mechanical properties

The thickness of the indicators was measured from six different random points with a digital micrometer on a precision of $0.1 \mu\text{m}$. Tensile strength (TS) and elongation break (EB) were measured according to the ASTM standard method D882-97. Before test, the indicators were cut into rectangular pieces (60×20 mm) and fixed on TA96 texture analyzer (Food Technology Co., VA, USA). The initial distance was set to 40 mm and crosshead speed of 0.6 mm/s (Zhang et al., 2021).

2.4.4. Water vapor permeability (WVP) and water contact angle (WCA)

The measurement of WVP was determined gravimetrically in accordance with ASTM E96-05 standard (Hudoklin, Šetina, & Drnovšek, 2012). Each film sample was sealed on a 50 mL beaker containing 20 mL deionized water. The beaker was then put in a desiccator (0% RH). The beaker was periodically taken out from the desiccator after 12 h of intervals and weighed for 3 days, and WVP was calculated according to the following equations:

$$WVP = \frac{\Delta m \times x}{S \times \Delta P \times t} \quad (5)$$

where m is the increasing weight of beaker (g), x is film thickness (m), and t is the time (s), S is the exposed area (m^2), and ΔP stands for partial water vapor pressure difference across the film (2339 Pa at 20°C).

The water contact angle (WCA) of the films was determined by using a WCA analyzer (KSV CAM20, Instruments Co., Ltd., Finland). Prior to analysis, each film was cut into a square shape ($20 \text{ mm} \times 20 \text{ mm}$) and placed on the horizontal stage. A drop of deionized water ($5 \mu\text{L}$) dropped on the film surface and then recorded by the camera (Zhang et al., 2019). Three measurements were performed to obtain the average values by using the Image software.

2.4.5. Colorimetric response

The colorimetric response of each indicator toward volatile ammonia was measured to evaluate the indicators efficiency. The indicator was fixed in a crisper containing 1 mL of 100 mM ammonia solution for 24 min at 25°C with 75%RH (Zhang et al., 2021). A white paper was added on the inner surface of PSR film as a white board. The color of the indicator was captured and photographed every 2 min. The photos were analyzed using Matlab R2010 software (Mat works Inc., Natick, MA, USA). The colorimetric response of the indicators was expressed as the response sensitivity (S_{RGB}) according to the following equation:

$$\begin{aligned} \Delta R &= |R_a - R_b| \\ \Delta G &= |G_a - G_b| \\ \Delta B &= |B_a - B_b| \end{aligned} \quad (6)$$

2.4.6. Color Stability

In order to determine the color stability, all indicators were stored at a plastic case in incubators at 4 and 25°C under a relative humidity of 50% (Zhang et al., 2021). Briefly, the color changes of these indicators were captured at 2 d intervals for 14 days by using a portable spectrophotometer (CM2300d, Konica Minolta Holding, Inc. Japan). Before the analysis, portable spectrophotometer was calibrated with a white ceramic plate. The acquired results were expressed as color values: L^* (lightness), a^* (red to green), and b^* (yellow to blue) for the evaluation of the total color changes (ΔE):

$$\Delta E = \sqrt{(L^* - L_0^*)^2 + (a^* - a_0^*)^2 + (b^* - b_0^*)^2} \quad (7)$$

where L_0^* , a_0^* and b_0^* were the initial gray values of the films.

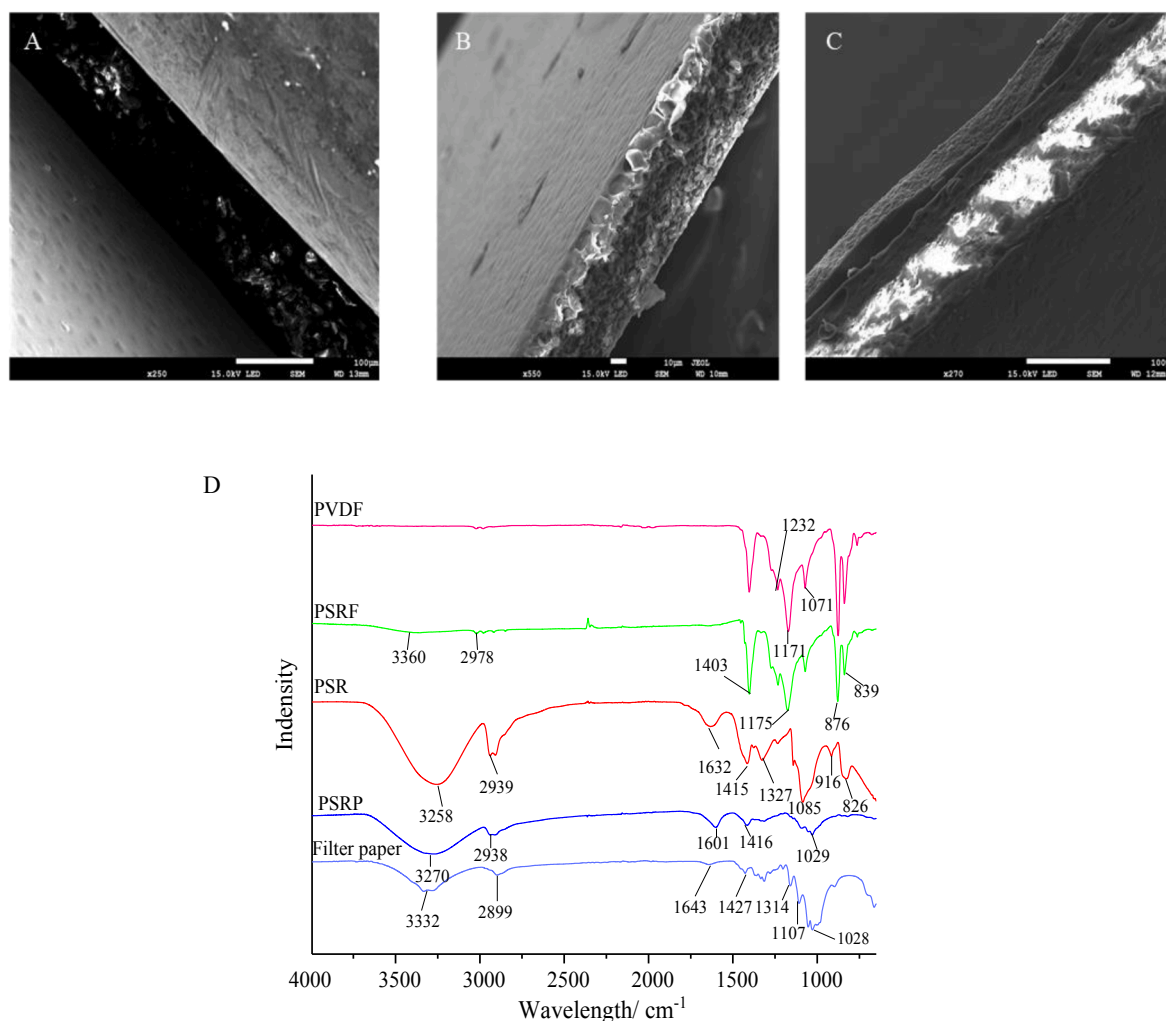


Fig. 2. SEM images of the indicator films: PSR (A), PSRP (B), and PSRF (C) and FTIR spectra of the indicator films (D).

2.5. The griskin freshness trial of indicator film

Finally, the PSRF was applied to evaluate the griskin freshness. Firstly, PVDF-film (2×2 cm) was fixed on the sealed crispier (350 mL) containing 20 g of fresh griskin. They were placed in the industrial container at 10°C and 50% RH. The color parameter value of indicator was determined with a portable CM2300d spectrophotometer every 24 h for four days. During the test period, the pH of the griskin samples was measured using a digital pH meter, and the total volatile basic nitrogen (TVB-N) was monitored according to the method reported previously (semi-micro Kjeldahl method) (Zhang et al., 2019).

2.6. Statistical analysis

All the analysis was performed in triplicate independent experiments and reported as average \pm std. The acquired data and mean differences were analyzed for statistical significance ($p < 0.05$) using DPS software with Duncan's multiple range tests.

3. Results and discussion

3.1. The characterization of roselle anthocyanins

According to the pH differential method, the RACs content was 120.50 ± 0.84 mg/L. Combined with the HPLC-MS images of the RACs, the fragment ions provide information regarding the parent nucleus and

substituents in the molecules; subsequently, the approximate structural information of the anthocyanins can be inferred (Guzmán-Figueroa, Ortega-Regules, Bautista-Ortín, Gómez-Plaza, & Anaya-Berrios, 2016; Lourith & Kanlayavattanukul, 2013). As shown in the Fig. 1, the main pigments found in the calyx of Roselle were delphinidin-3-glucoside, cyanidin-3-glucoside, delphinidin-3-sambubioside, and cyanidin-3-sambubioside. And these phenolic compounds are responsible for Roselle's red color and the bioactive properties (Liu, Fu, & Si, 2014).

3.2. The microstructure of bilayer indicators

3.2.1. FT-IR spectra of indicators

The FT-IR spectra of PSR, filter paper, PVDF film, PSRP and PSRF films were shown in Fig. 2D. In the spectrum of PSR, the broad band at 3258 cm^{-1} was assigned to the stretching vibrations of O—H (Hong, Chen, Zeng, & Han, 2016). The band at 2939 cm^{-1} represented the C—H bending and $-\text{CH}_2$ stretching of a methyl group (Sukhtezari, Almasi, Pirsá, Zandi, & Pirouzfard, 2017). The bands at 1632 cm^{-1} and 1415 cm^{-1} presented prominent absorption peaks and attributed to stretching vibrations of C=C aromatic ring in flavonoid compounds. The band at 1327 cm^{-1} was a characteristic peak corresponding to C—H deformation (Zhang et al., 2019). Another major band at 1085 cm^{-1} was associated with the stretching vibrations of C—C rings. Compare to filter paper and the PSR, no new structural peak appeared in PSRP spectra. Meanwhile, two low shifts of peaks for O—H stretching (3323 cm^{-1} (filter paper), 3258 cm^{-1} (PSR) \rightarrow 3270 cm^{-1} (PSRP)) and C=O

Table 1

Summary of the physical properties of the films.

Film	Thickness/ μm	MC/%	WS/%	SI/%	TS/MPa	EB/%	WCA/ $^\circ$	WVP/ 10^{-4} ($\text{g m}^{-1} \text{s}^{-1} \text{Pa}^{-1}$)
PSR	60.50 \pm 2.85 ^a	7.50 \pm 1.98 ^b	67.61 \pm 2.59 ^{bc}	94.33 \pm 2.59 ^{bc}	10.63 \pm 3.21 ^a	49.09 \pm 0.33 ^a	56.09 \pm 1.73 ^b	5.07 \pm 0.31 ^b
PSRP	74.63 \pm 3.64 ^b	2.88 \pm 0.35 ^a	35.06 \pm 2.21 ^a	177.35 \pm 2.21 ^a	11.52 \pm 3.39 ^c	14.62 \pm 0.24 ^c	47.79 \pm 1.31 ^a	4.74 \pm 0.15 ^a
PSRF	84.82 \pm 3.13 ^{ab}	3.55 \pm 0.68 ^a	28.71 \pm 2.61 ^a	77.75 \pm 2.61 ^a	6.08 \pm 1.51 ^b	29.40 \pm 0.98 ^c	108.85 \pm 1.76 ^c	1.42 \pm 0.15 ^a

Notes: Data with the same superscript letter in the same column indicate that statistically different ($p < 0.05$).

stretching (1643 cm^{-1} (filter paper), 1632 cm^{-1} (PSR) \rightarrow 1601 (PSRP) cm^{-1}) indicated the presence of hydrogen bonds interaction between sensor layer and filter paper (Mohammadinejad, Almasi, & Moradi, 2020). The peak at 1601 cm^{-1} and 1416 cm^{-1} in PSRP could also be ascribed to roselle anthocyanin structure (C=C aromatic ring). Notably, the spectra showed that the sensor layer were successfully immobilized on the filter paper. The spectra of PSRF and PVDF film presented the obvious similar structure. PSRF film exhibited strong bands at 1403 cm^{-1} and 1175 cm^{-1} corresponding to $-\text{CF}_2$ deformation and stretching vibration in PVDF, respectively. The band at 876 cm^{-1} was main typical spectra of PVDF amorphous phase (Hudoklin et al., 2012). And the band at 3360 cm^{-1} in PSRF confirms that the formation of intermolecular hydrogen bonds between the PVDF layer and sensor layer (Moradi, Tajik, Almasi, Forough, & Ezati, 2019). The above results can prove that sensor layer was formed successfully on the surface of filter paper and PVDF films

3.2.2. Morphology and structure of indicators

As shown in Fig. 2A, the PSR film displayed the smoothest cross-section without any wrinkles, suggesting that the incorporation of RAs was uniformly uniform into the PVA and sodium alginate matrix (Hernández, Pérez, Genesca, Gómez, & Covelo, 2020). Fig. 2B. exhibited a typical image of filter paper with coarse and porous network structure of fibrils. The results confirmed that the PSR solution was distributed on filter paper uniformly. PSRF was a typical hydrophobic layer with coarse, proliferous and more interconnected chemical crosslink morphology structures. The microstructure of PSRF could decrease water vapor permeability and improve the moisture barrier property of the indicator. The microstructure results were consistent with the physical properties.

3.3. Physical properties of the bilayer indicators

As shown in Table 1, the SI, WS, MC, TS, EB, WCA and WVP results of indicators were significantly different from each other. The thickness of PSR film was the smallest, with an amount of $60.50 \mu\text{m}$. The thickness of the bi-layer indicators was increased due to the existence of outer layer. The SI is substantially evaluated to the stability and water absorption of films and it is noted that the film with high swelling properties decreases structural integrity (Abdollahi, Rezaei, & Farzi, 2012). As shown in Table 1, the SI of PSRP film was the highest, with a value of 177.35%. The PVDF indicator had the lowest swelling degree, which reduced to 77.75%. In fact, the change of the SI was dependent on the different outer layer materials. The negative control layer of PSRP was filter paper, which was known as the media for filtering water with porous structure (Hu et al., 2020). However, PVDF as hydrophobic material, possessed an excellent barrier to water and reduced the swelling of film. Moreover, WS reflects the integrity of films to water (Lian, Shi, Zhang, & Peng, 2020). The PVA and SA were hydrophilic substances, which results in the highest WS values of PSR film. Thus, the WS of bi-layers film decreased due to the outer layer which was industrial products that contain almost no water. The similar changes in MC were also observed (Table 1).

TS and EB are the typical parameters to characterize mechanical properties. As shown in Table 1, there were obvious changes of mechanical properties between three indicators ($p > 0.05$) because of their different polymer matrices. The highest TS (11.52 MPa) but the lowest

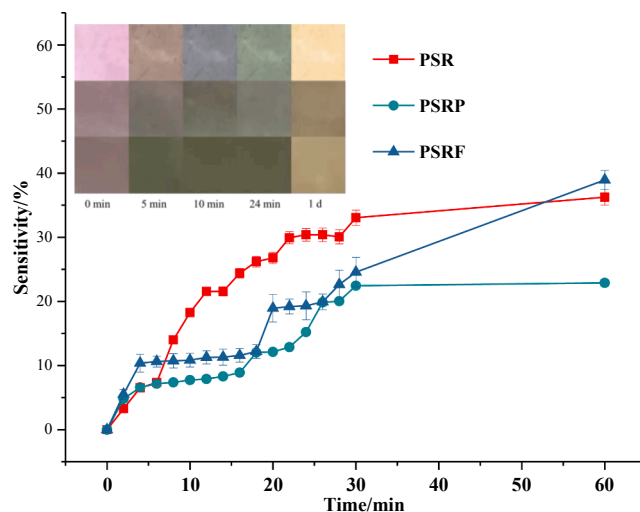


Fig. 3. The color response of the indicator films toward ammonia gas and the illustration is the color changes of films.

EB (14.62%) of PSRP film was attributed to coarse and porous network structure of filter paper (Fig. 2B). In comparison, relatively higher TS (10.63 MPa) and the highest EB (49.09%) of PSR film was a normal plasticizing effect with compact structure (Koray et al., 2014) The EB value (29.40%) of PSRF film indicated the flexible structure, which can be used an indicator.

WCA is commonly defined as an essential parameter for determining the film surface hydrophobicity and the WCA value above 90° is generally considered as well hydrophobic property (Pizarro et al., 2020). The WCA of the PSR film was 56.09° , indicating that the PSR film had a hydrophilic surface. Meanwhile, WCA of the PSRP film was slightly lower with a value of 47.79° , which is attributed to the porous network structure of filter paper. The phenomenon is consistent with the microstructure results. However, the WCA value of the PSRF film was increased to 108.85° , which can be considered as an excellent hydrophobic surface. The statistically significant ($p > 0.05$) increase in WCA of the PSRF film was due to the C-F bonds and presence of no-hydrophilic groups in PVDF crystalline phase structure (Shah et al., 2020).

The WVP is evaluated to their barrier property against water vapor, and it is noted that a lower WVP was generally required for food packaging (Huang et al., 2019a). The PSR film exhibited the highest WVP, with a value of $5.07 \times 10^{-4} \text{ g}/(\text{m}\cdot\text{s}\cdot\text{pa})$. The existence of outer-layer increased the diffusion path and decreased the WVP values of bi-layer indicator. Furthermore, the decrease in WVP could due to the hydrophilic group interactions which reduced sorption of free volume (Moschakis, Murray, & Biliaderis, 2010). The PSRF layer increased hydrophobicity with the lowest WVP value ($1.42 \times 10^{-10} \text{ g}/(\text{m}\cdot\text{s}\cdot\text{pa})$) because of the C-F bands and the tortuosity chemical crosslink morphology structure (Li, Ren, Shao, Tu, & He, 2019) (Fig. 2C). Therefore, PSRF indicator exhibited an excellent barrier property for moisture.

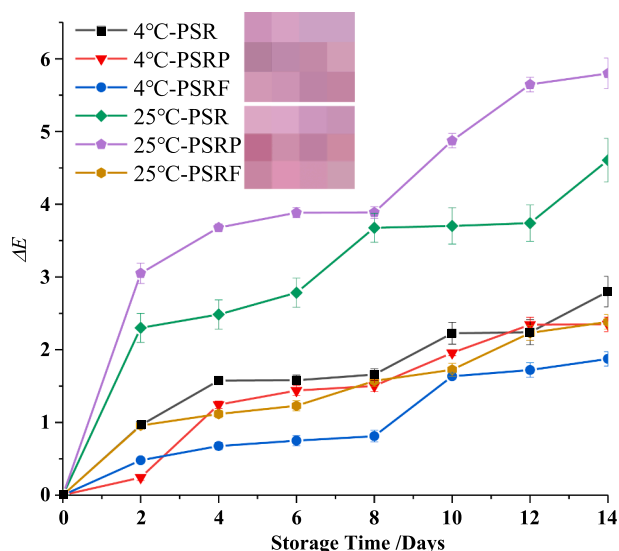


Fig. 4. The color stability (ΔE values) of the indicator films stored at 4 and 25 °C for 14 days and the illustration is the color changes of films.

3.4. Colorimetric response efficiency of the films

To evaluate the color response performance, the indicators were exposed to volatile ammonia, and the indicators sensitivity were illustrated in Fig. 3. The color of the films changed significantly from pink to bluish, then green to yellow in an ammonia environment. Over the first 6 min, PSR and PSRP film turned to a slight reduction of color variation. In comparison, the color of PSRF film turned appreciable change from pink-red to green and the color sensitivity (S_{RGB}) of the film was 10.62% at that time. With the reaction time increasing, the PSR film showed obvious color changes at 18 min. Meanwhile, the PSRP and PSRF film increased to a platform. The bilayer indicator increased the diffusion

path which could be a barrier to ammonia. After one day, the yellowness degree of the PSRF film gradually deepened and exhibited the highest color variation which S_{RGB} value was 38.93%. The color variation mechanism was demonstrated in the formation of phenolic oxygen anions. The volatilized ammonia was firstly diffused into the smart film and combined with the water to form hydrated ammonia which then hydrolyzed to hydroxyl ions and ammonium ions. The hydroxyl ions made an alkaline environment that changed the anthocyanins structure and caused the color changes (Alizadeh-Sani, Tavassoli, McClements, & Hamishehkar, 2020). The results indicate that the film was considered to be a useful indicator for the protein-rich meat freshness.

3.5. Color stability of indicator films

The color stability plays a vitally important role in relation to the freshness evaluation mechanism. As shown in Fig. 4, the color stability was evaluated at 4 and 25 °C for 14 days. Generally, the PSRF indicator showed the best color stability at 4 °C, which ΔE value was 2.92. When ΔE value is no more than 5, the color change is not visually perceptible by naked eyes. The hydrophobic indicator acted as a barrier for the moisture and then showed higher color stability. However, the PSRP film performed the relatively highest color changes at 25 °C because of the porous structure of filter paper. The moisture could decrease the color stability of anthocyanins (Zhao et al., 2017). Compared to the film stored at 25 °C, the films stored at 4 °C showed higher stability. The results indicated that anthocyanins were partially oxidized and then rapidly degraded at the high temperature. This phenomenon has also been reported in previous studies (Huang et al., 2019b; Zhang et al., 2019). The above results indicated that the better color stability of PSRF indicator at 4 °C could be the best choice for the application.

3.6. The application in monitoring griskin spoilage

The PSRF indicator was used to monitor the griskin freshness due to its suitable hydrophobic property and high color stability. The PSRF film

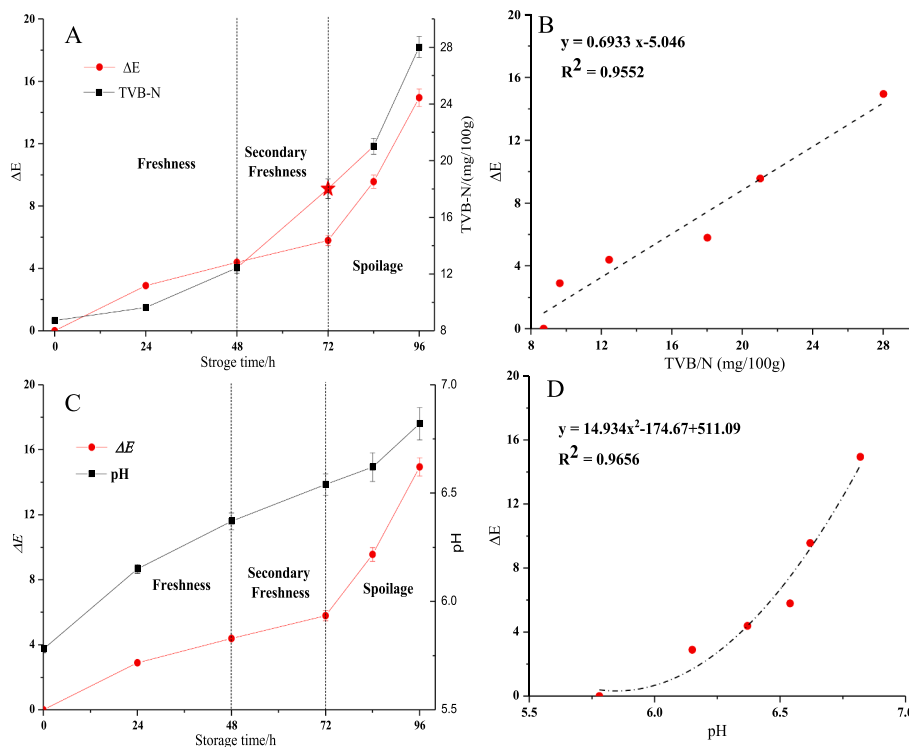


Fig. 5. ΔE values of the PSRF indicator and the TVB-N (A), pH (C) of the griskin at the storage time; The correlation between TVB-N (B), pH (D) and ΔE values of PSRF indicator.

showed visible color changes during the storage time. As shown in Fig. 5, the TVB-N and pH values of griskin followed a similar trend with increased ΔE value over time. In the first 48 h, the TVB-N value increased from 8.72 to 12.24 mg/100 g, and the pH increased gradually from 5.78 to 6.37. The indicator color shown no significant changes, which ΔE value was 4.38. According to the Chinese standard (GB2707-2016), the legislative limit of TVB-N level in pork is 15 mg/100 g. The results indicated that the griskin sample was in an edible state at 48 h (Liao, Fan, & Fang, 2012). The TVB-N value was increased to 18.02 mg/100 g and the ΔE value was increased to 5.79 at 72 h, suggesting that the griskin was decomposed and not suitable for consumption after 72 h. The correlation between ΔE and TVB-N of griskin samples was evaluated by the linear model with a high correlation coefficient ($R^2 = 0.9552$). Similarly, linear polynomial model was estimated between the ΔE and pH value with a coefficient of correlation 0.9656 (the precision of the mode). Hence, the PSRF indicator could be an entirely suitable medium for monitoring the griskin freshness in real-time.

4. Conclusions

This study has fabricated a new type of indicator by coating the film-forming solution on PVDF film. The FT-IR spectra and SEM results confirmed that sensor layer was formed successfully on the surface of the prevent-layer. The results of WVP and WCA indicated that the PSRF indicator was a typical hydrophobic film. The PSRF indicator showed visible color changes to ammonia gas. The PVDF film was first reported on the food freshness indicator as a moisture prevent-layer. Finally, the PSRF was used as an indicator for distinguishing griskin freshness/spoilage process: the results revealed good correlations between TVB-N, pH and color changes, respectively. Future studies should focus on multifunctional intelligent packaging for keeping and indicating food freshness.

CRedit authorship contribution statement

Junjun Zhang: Writing - original draft, Conceptualization, Methodology, Software. **Xiaowei Huang:** Conceptualization, Methodology, Software. **Jiyong Shi:** Validation, Resources, Data curation, Funding acquisition. **Li Liu:** Software, Validation, Data curation. **Xinai Zhang:** Visualization, Investigation. **Xiaobo Zou:** Validation, Resources, Data curation, Funding acquisition. **Jianbo Xiao:** Formal analysis. **Xiaodong Zhai:** Visualization, Investigation. **Di Zhang:** Visualization, Investigation. **Yanxiao Li:** Visualization, Investigation. **Tingting Shen:** Writing - review & editing.

Declaration of Competing Interest

The authors declare that they have no known competing financial interests or personal relationships that could have appeared to influence the work reported in this paper.

Acknowledgement

The authors gratefully acknowledge the Project supported by Science Foundation for Distinguished Young Scholars of Jiangsu Province (Grant No. BK20200103), Project supported by National Natural Science Foundation of China (Grant No. 31671844). Project supported by Graduate Student Innovation Training Project of Jiangsu Province (Grant No. KYCX20_3046). Project supported by National Key research and Development Program of China (Grant No. 2018YFD 0400800), Project supported by the Natural Science Foundation of Jiangsu province, China (Grant No. BK20180865). Project of Faculty of Agricultural Equipment of Jiangsu University. We also would like to thank our colleagues in School of Food and Biological Engineering who provided assistance in this study.

Appendix A. Supplementary data

Supplementary data to this article can be found online at <https://doi.org/10.1016/j.foodchem.2021.129573>.

References

- Abdollahi, M., Rezaei, M., & Farzi, G. (2012). A novel active bionanocomposite film incorporating rosemary essential oil and nanoclay into chitosan. *Journal of Food Engineering*, *111*(2), 343–350.
- Alizadeh-Sani, M., Tavassoli, M., McClements, D. J., & Hamishehkar, H. (2020). Multifunctional halochromic packaging materials: Saffron petal anthocyanin loaded-chitosan nanofiber/methyl cellulose matrices. *Food Hydrocolloids*, *111*, Article 106237.
- Choi, I., Lee, J. Y., Lacroix, M., & Han, J. (2017). Intelligent pH indicator film composed of agar/potato starch and anthocyanin extracts from purple sweet potato. *Food Chemistry*, *218*, 122–128.
- Coma, & Véronique. (2012). Polysaccharide-based biomaterials with antimicrobial and antioxidant properties. *Polímeros*, *23*(3), 287–297.
- Eghbalifam, N., Frounchi, M., & Dabbini, S. (2015). Antibacterial silver nanoparticles in polyvinyl alcohol/sodium alginate blend produced by gamma irradiation. *International Journal of Biological Macromolecules*, *80*, 170–176.
- Guzmán-Figueroa, M. d. P., Ortega-Regules, A. E., Bautista-Ortín, A. B., Gómez-Plaza, E., & Anaya-Berrios, C. (2016). New pyranoanthocyanins synthesized from roselle (*Hibiscus sabdariffa* L.) anthocyanins. *Journal of the Mexican Chemical Society*, *60*(1), 13–18.
- Hashemi, A., & Shahani, A. (2019). Effects of salt stress on the morphological characteristics, total phenol and total anthocyanin contents of Roselle (*Hibiscus sabdariffa* L.). *Plant Physiology Reports*, *24*(2), 210–214.
- Hernández, M., Pérez, L., Genesca, J., Gómez, K. K., & Covelo, A. (2020). Evaluation of the biocompatibility of a PVA/SA scaffold with a human gingival fibroblast (HGF) by using electrochemical impedance spectroscopy. *Bioelectrochemistry*, *131*, 107386.
- Homez-Jara, Angie, Daniel, Daza, Luis, Marcela, ... Munoz. (2018). Characterization of chitosan edible films obtained with various polymer concentrations and drying temperatures. *International Journal of Biological Macromolecules*, *113*, 1233–1240.
- Hong, J., Chen, R., Zeng, X.-A., & Han, Z. (2016). Effect of pulsed electric fields assisted acetylation on morphological, structural and functional characteristics of potato starch. *Food Chemistry*, *192*, 15–24.
- Hu, S., Zeng, S., Li, X., Jiang, J., Yang, W., Chen, Y., ... Zheng, J. (2020). Flexible and high performance of n-type thermoelectric PVDF composite film induced by nickel nanowires. *Materials & Design*, *188*, 108496.
- Huang, J., Chen, M., Zhou, Y., Li, Y., & Hu, Y. (2020). Functional characteristics improvement by structural modification of hydroxypropyl methylcellulose modified polyvinyl alcohol films incorporating roselle anthocyanins for shrimp freshness monitoring. *International Journal of Biological Macromolecules*, *162*, 1250–1261.
- Huang, S., Xiong, Y., Zou, Y., Dong, Q., Ding, F., Liu, X., & Li, H. (2019a). A novel colorimetric indicator based on agar incorporated with *Arnebium* euchroma root extracts for monitoring fish freshness. *Food Hydrocolloids*, *90*(MAY), 198–205.
- Huang, X., Li, Z., Zou, X., Shi, J., Elrasheid Tahir, H., Xu, Y., ... Hu, X. (2019b). A low cost smart system to analyze different types of edible Bird's nest adulteration based on colorimetric sensor array. *Journal of Food and Drug Analysis*, *27*(4), 876–886.
- Hudoklin, D., Šetina, J., & Drnovšek, J. (2012). Uncertainty evaluation of the new setup for measurement of water-vapor permeation rate by a dew-point sensor. *International Journal of Thermophysics*, *33*(8–9), 1595–1605.
- Ibrahim, S. M., & Salmawi, K. M. E. (2013). Preparation and properties of carboxymethyl cellulose (CMC)/sodium alginate (SA) blends induced by gamma irradiation. *Journal of Polymers & the Environment*, *21*(2), 520–527.
- Koray, Gurkan, Shokat, Sarmad, Seda, & Bekin. (2014). Dielectric, thermal, and swelling properties of calcium ion-crosslinked sodium alginate film. *Polymer Engineering & Science*, *54*(6), 1372–1382.
- Li, J., Ren, L. F., Shao, J., Tu, Y., & He, Y. (2019). Fabrication of triple layer composite membrane and its application in membrane distillation (MD): Effect of hydrophobic-hydrophilic membrane structure on MD performance. *Separation & Purification Technology*, *234*, Article 116087.
- Lian, H., Shi, J., Zhang, X., & Peng, Y. (2020). Effect of the added polysaccharide on the release of thyme essential oil and structure properties of chitosan based film. *Food Packaging & Shelf Life*, *23*, 100467.
- Liao, Y., Fan, Y., & Fang, C. (2012). On-line prediction of pH values in fresh pork using visible/near-infrared spectroscopy with wavelet de-noising and variable selection methods. *Journal of Food Engineering*, *109*(4), 668–675.
- Liu, B., Xu, H., Zhao, H., Liu, W., Zhao, L., & Li, Y. (2017). Preparation and characterization of intelligent starch/PVA films for simultaneous colorimetric indication and antimicrobial activity for food packaging applications. *Carbohydrate Polymers*, *157*, 842–849.
- Liu, L., Zhang, J., Shi, J., Huang, X., Zou, X., Zhang, D., ... Li, Y. (2020). Preparation and comparison of two functional nanoparticle-based bilayers reinforced with a κ -carrageenan–anthocyanin complex. *International Journal of Biological Macromolecules*, *165*, 758–766.
- Liu, S., Fu, Y., & Si, N. (2014). Buffering colour fluctuation of purple sweet potato anthocyanins to acidity variation by surfactants. *Food Chemistry*, *162*(nov.1), 16–21.
- Lourith, N., & Kanlayavattanakul, M. (2013). Antioxidant activity and stability of natural colour recovered from Roselle juice production. *Agro Food Industry Hi Tech*, *24*(5), 40–42.

- Mannozi, C., Tylewicz, U., Chinnici, F., Siroli, L., Rocculi, P., Dalla Rosa, M., & Romani, S. (2018). Effects of chitosan based coatings enriched with procyanidin by-product on quality of fresh blueberries during storage. *Food Chemistry*, *251*, 18–24.
- Mohammadinejad, S., Almasi, H., & Moradi, M. (2020). Immobilization of Echinium amoenum anthocyanins into bacterial cellulose film: A novel colorimetric pH indicator for freshness/spoilage monitoring of shrimp. *Food Control*, *113*, 107169.
- Moradi, M., Tajik, H., Almasi, H., Forough, M., & Ezati, P. (2019). A novel pH-sensing indicator based on bacterial cellulose nanofibers and black carrot anthocyanins for monitoring fish freshness. *Carbohydrate Polymers*, *222*, 115030.
- Moschakis, T., Murray, B. S., & Biliaderis, C. G. (2010). Modifications in stability and structure of whey protein-coated o/w emulsions by interacting chitosan and gum arabic mixed dispersions. *Food Hydrocolloids*, *24*(1), 8–17.
- Pizarro, G. d. C., Marambio, O. G., Jeria-Orell, M., Sánchez, J., Oyarzún, D. P., Martín-Trasanco, R., & Novio, F. (2020). Morphological, optical and wettability characterization of honeycomb patterned films based on self-assembling copolymer under thermal annealing. *Chemical Physics*, *533*, 110715.
- Senem, K., Esra, C., Charlotte, G., & John, V. C. (2015). Anthocyanin absorption and metabolism by human intestinal Caco-2 Cells—A review. *International Journal of Molecular Sciences*, *16*(9), 21555–21574.
- Shah, A. A., Cho, Y. H., Nam, S.-E., Park, A., Park, Y.-I., & Park, H. (2020). High performance thin-film nanocomposite forward osmosis membrane based on PVDF/bentonite nanofiber support. *Journal of Industrial and Engineering Chemistry*, *86*, 90–99.
- Sukhtezari, S., Almasi, H., Pirs, S., Zandi, M., & Pirouzifard, M. (2017). Development of bacterial cellulose based slow-release active films by incorporation of Scrophularia striata Boiss. extract. *Carbohydrate Polymers*, *156*, 340–350.
- Tang, E. L., Wang, L., & Han, Y. F. (2019). Space debris positioning based on two-dimensional PVDF piezoelectric film sensor. *Advances in Space Research*, *63*(8), 2410–2421.
- Zhai, X., Li, Z., Zhang, J., Shi, J., & Povey, M. (2018). Natural biomaterial-based edible and pH-sensitive films combined with electrochemical writing for intelligent food packaging. *Journal of Agricultural and Food Chemistry*, *66*(48), 12836–12846.
- Zhai, X., Shi, J., Zou, X., Wang, S., Jiang, C., Zhang, J., ... Holmes, M. (2017). Novel colorimetric films based on starch/polyvinyl alcohol incorporated with roselle anthocyanins for fish freshness monitoring. *Food Hydrocolloids*, *69*, 308–317.
- Zhang, J., Huang, X., Zou, X., Shi, J., Zhai, X., Liu, L., ... Xiao, J. (2021). A visual indicator based on curcumin with high stability for monitoring the freshness of freshwater shrimp, *Macrobrachium rosenbergii*. *Journal of Food Engineering*, *292*, 110290.
- Zhang, J., Zou, X., Zhai, X., Huang, X., Jiang, C., & Holmes, M. (2019). Preparation of an intelligent pH film based on biodegradable polymers and roselle anthocyanins for monitoring pork freshness. *Food Chemistry*, *272*, 306–312.
- Zhang, L., Wang, H., Jin, C., Zhang, R., Li, L., Li, X., & Jiang, S. (2017). Sodium lactate loaded chitosan-polyvinyl alcohol/montmorillonite composite film towards active food packaging. *Innovative Food Science & Emerging Technologies*, *42*, 101–108.
- Zhang, R., Wang, W., Zhang, H., Dai, Y., Dong, H., & Hou, H. (2019). Effects of hydrophobic agents on the physicochemical properties of edible agar/maltodextrin films. *Food Hydrocolloids*, *88*, 283–290.
- Zhao, C. L., Yu, Y. Q., Chen, Z. J., Wen, G. S., Wei, F. G., Zheng, Q., ... Xiao, X. L. (2017). Stability-increasing effects of anthocyanin glycosyl acylation. *Food Chemistry*, *214*, 119–128.
- Zou, X., Zhang, J., Shi, J., Jiang, C., Zhai, X., Wang, S., ... Liang, N. (2017). Development of intelligent indicator films based on roselle anthocyanins for monitoring pork freshness. *Food Science*, *38*(23), 243–248.




ARTICLES FOR FACULTY MEMBERS

ROSELLE (HIBISCUS SABDARIFFA) ANTHOCYANIN USE IN MONITORING MEAT FRESHNESS

Title/Author	Characterization of Natural Anthocyanin Indicator Based on Cellulose Bio-Composite Film for Monitoring the Freshness of Chicken Tenderloin / Boonsiriwit, A., Itkor, P., Sirieawphikul, C., & Lee, Y. S.
Source	<i>Molecules</i> Volume 27 Issue 9 (2022) 2752 Pages 1-16 https://doi.org/10.3390/molecules27092752 (Database: MDPI)

Article

Characterization of Natural Anthocyanin Indicator Based on Cellulose Bio-Composite Film for Monitoring the Freshness of Chicken Tenderloin

Athip Boonsiriwit ^{1,2} , Pontree Itkor ¹ , Chanutwat Sirieawphikul ² and Youn Suk Lee ^{1,*} 

¹ Department of Packaging, Yonsei University, Wonju 220-710, Korea; athip8266@gmail.com (A.B.); pontree.itkor@gmail.com (P.I.)

² Rattanakosin International College of Creative Entrepreneurship (RICE), Rajamangala University of Technology Rattanakosin, Nakhon Pathom 73170, Thailand; chanutwatgus@gmail.com

* Correspondence: leeyouns@yonsei.ac.kr; Tel.: +82-33-760-2395

Abstract: Intelligent packaging with indicators that provide information about the quality of food products can inform the consumer regarding food safety and reduce food waste. A solid material for a pH-responsive indicator was developed from hydroxypropyl methylcellulose (HPMC) composited with microcrystalline cellulose (MCC). MCC at 5%, 10%, 20%, and 30% *w/w* was introduced into the HPMC matrix and the physical, barrier, thermal, and optical properties of the HPMC/MCC bio-composite (HMB) films were analyzed. At 5, 10, and 20% MCC, improved mechanical, transparency, and barrier properties were observed, where HMB with 20% of MCC (H20MB) showed the best performance. Therefore, H20MB was selected as the biodegradable solid material for fabricating Roselle anthocyanins (RA) pH sensing indicators. The performance of the RA-H20MB indicator was evaluated by monitoring its response to ammonia vapor and tracking freshness status of chicken tenderloin. The RA-H20MB showed a clear color change with respect to ammonia exposure and quality change of chicken tenderloin; the color changed from red to magenta, purple and green, respectively. These results indicated that RA-H20MB can be used as a biodegradable pH sensing indicator to determine food quality and freshness.

Keywords: anthocyanin; bio-composite film; hydroxypropyl methylcellulose; microcrystalline cellulose; pH sensing indicator; chicken tenderloin



Citation: Boonsiriwit, A.; Itkor, P.; Sirieawphikul, C.; Lee, Y.S. Characterization of Natural Anthocyanin Indicator Based on Cellulose Bio-Composite Film for Monitoring the Freshness of Chicken Tenderloin. *Molecules* **2022**, *27*, 2752. <https://doi.org/10.3390/molecules27092752>

Academic Editors: Mihai Brebu and Elena Stoleru

Received: 10 April 2022

Accepted: 23 April 2022

Published: 25 April 2022

Publisher's Note: MDPI stays neutral with regard to jurisdictional claims in published maps and institutional affiliations.



Copyright: © 2022 by the authors. Licensee MDPI, Basel, Switzerland. This article is an open access article distributed under the terms and conditions of the Creative Commons Attribution (CC BY) license (<https://creativecommons.org/licenses/by/4.0/>).

1. Introduction

Intelligent packaging can monitor quality changes in food products; therefore, it has garnered significant attention for application in food packaging. It can provide information on the direct quality of the food products within the package and indirectly inform the consumer of food safety, thereby protecting the consumer from food poisoning and reducing food wastage [1,2]. Based on the function of the detection indicators, intelligent packaging can be divided into three types: time–temperature, gas, and freshness indicators [3]. pH sensing indicators are one of the indicators for freshness, which change colors with respect to the pH of the environment [4]. Recently, a variety of colorimetric dyes from natural resources, such as anthocyanins, are increasingly being used in pH sensing indicator applications for monitoring food freshness [4–6]. Compared to the several synthetic dyes, anthocyanin presents a wide range in responding to the pH (Table S1 in the Supplementary Materials). The fabrication of anthocyanin-based pH sensing indicators require the incorporation of the anthocyanins in a solid material, for which biodegradable materials, such as chitosan, gelatin, and agar, are generally used [7].

However, these materials exhibit their own specific colors, which may directly affect the color of anthocyanin. Therefore, a colorless biomaterial is preferable for fabricating pH sensing indicators. As such, hydroxypropyl methylcellulose (HPMC), a biodegradable

material, is a good candidate for fabricating pH sensing indicators because it consists of nonionic cellulose ethers, and it is colorless, odorless, tasteless, and flexible [8,9]. It does not interfere with the chemical structure and color of anthocyanin. Moreover, it is suitable for integration with a highly water-soluble substrate [8,10]. However, HPMC is transparent, has high water sensitivity, and exhibits inferior gas-barrier properties. Therefore, composite HPMC films with cellulose fibers have been recommended to improve these properties [11].

Microcrystalline cellulose (MCC), which is derived from high-quality wood pulp by removing the amorphous regions of cellulose by acid hydrolysis, can be a cellulosic reinforcement for polymers. MCC can also serve as a binder and disintegrating agent, facilitating film formation [8]. Several studies have reported that introducing MCC into polymers can improve their physical, optical, and barrier properties [12–14]. Therefore, this study aimed to develop biodegradable solid materials composed of HPMC with various concentrations of MCC. The physical, chemical, and barrier properties of the HPMC/MCC bio-composites (HMB) were analyzed. The optimum ratio of HMB was selected for fabricating an anthocyanin pH sensing indicator and its performance was evaluated by monitoring the color change after exposure to volatile ammonia and tracking the freshness status of chicken tenderloin.

This study will provide a better understanding of cellulose bio-composite and intelligent packaging application with natural anthocyanin pH sensing indicator, where it is sensitive to the gases occurred by spoiled chicken tenderloin.

2. Results and Discussion

2.1. HMB Film Characterization

2.1.1. Morphological Analysis

The morphology of the HPMC (control) and HMB films was observed by FE-SEM. The SEM images of the cross-section and surface of the films are shown in Figure 1. The cross-section of the HPMC film (Figure 1A) was smooth, where no stacking or cracking of the layers was observed. In contrast, introducing MCC into the HPMC structure (Figure 1B–D) showed a packed and homogenous layer between MCC and HPMC. Moreover, the surface images of HPMC (Figure 1F), H5MB (Figure 1G), H10MB (Figure 1H), and H20MB (Figure 1I) showed smooth areas without holes and agglomeration of MCC. These results indicated that 5–20% of the MCC content was successfully incorporated within the HPMC matrix. Several studies have previously reported that a polymer matrix can be improved by introducing an optimum concentration of MCC [12,14]. The high specific area and a large number of –OH groups in the MCC structure may facilitate the interaction with the polymer via hydrogen bonding [11,13]. However, further increasing the MCC content in the HPMC matrix significantly increased the stacked area and roughness of the surface cross-section, as observed in H30MB (30% MCC) (Figure 1E). The agglomeration effect is also particularly apparent for H30MB (Figure 1J). Excess MCC results in the disruption of the HPMC matrix, yielding a non-uniform film.

2.1.2. Optical Properties

The images and transparency values of the HPMC and HMB films are shown in Figure 2. A high transparency value denotes a less transparent film [15]. The transparency value of the HPMC film was 0.94 ± 0.31 Abs/mm. The introduction of MCC into the HPMC matrix increased the transparency values, with the transparency values of the H5MB, H10MB, H20MB, and H30MB were 1.96 ± 0.38 , 2.81 ± 0.50 , 5.12 ± 0.53 , and 6.76 ± 0.45 Abs/mm, respectively. These results were consistent with the increase in the intensity of the white color of the HMB films (Figure 2A). This is in agreement with the results obtained by Hermawan, et al. [16], who reported that loading 7% of MCC into a seaweed film increased the transparency values up to 28.5%.

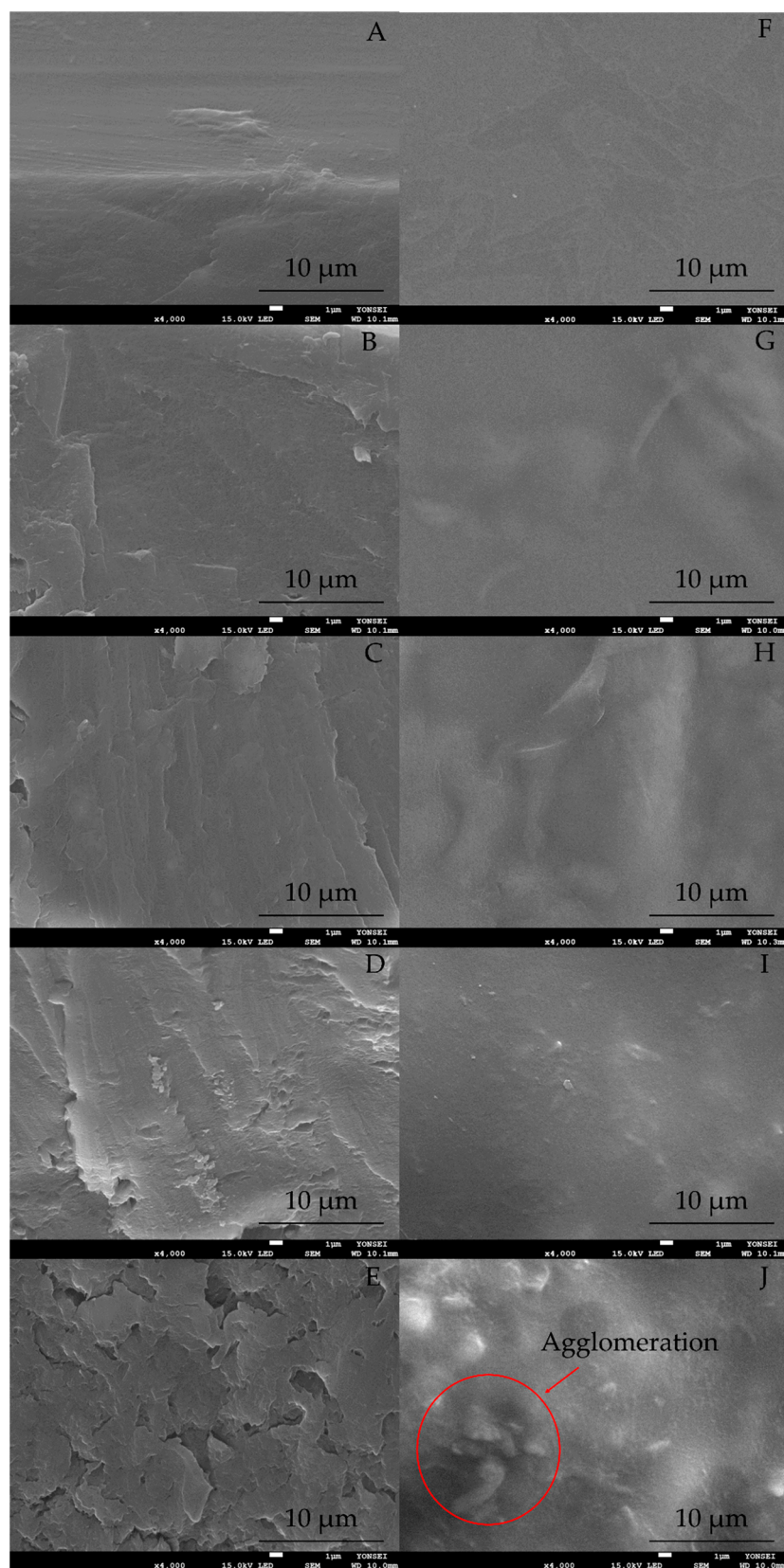


Figure 1. Field emission scanning electron microscopy images of the cross-section of the pure hydroxypropyl methylcellulose (HPMC) (A), 5% microcrystalline cellulose (MCC) (H5MB) (B), 10% MCC (H10MB) (C), 20% MCC (H20MB) (D), and 30% MCC (H30MB) (E) films and the surface of the HPMC (F), H5MB (G), H10MB (H), H20MB (I), and H30MB (J) films.

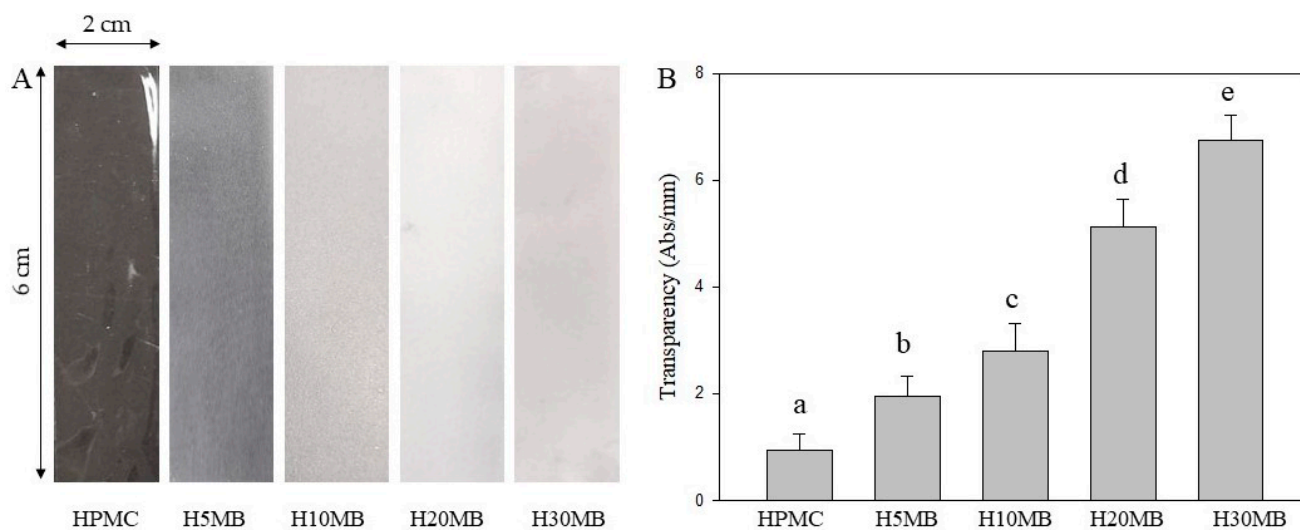


Figure 2. Image (A) and transparency values (B) of the hydroxypropyl methylcellulose (HPMC), 5% microcrystalline cellulose (MCC) (H5MB), 10% MCC (H10MB), 20% MCC (H20MB), and 30% MCC (H30MB) films. a–e letters indicate significant differences ($p < 0.05$).

2.1.3. Physical Properties

The thickness of the composite film is an important factor because it directly affects the mechanical, barrier, and optical properties. The thicknesses of the control and composite films were between 73.62 ± 2.38 and 76.98 ± 3.57 μm (Table 1) with no significant differences.

Table 1. Characteristics of the hydroxypropyl methylcellulose (HPMC), 5% microcrystalline cellulose (MCC) (H5MB), 10% MCC (H10MB), 20% MCC (H20MB), and 30% MCC (H30MB) films.

Sample	Thickness (μm)	Tensile (MPa)	Elongation (%)	OTR ($\text{cc}^2/\text{m}^2/\text{day}$)	WVTR ($\text{g}/\text{m}^2/\text{day}$)
HPMC	74.59 ± 1.48 ^{ns}	24.08 ± 3.51 ^a	33.19 ± 3.19 ^c	51.97 ± 1.35 ^d	48.17 ± 3.97 ^{bc}
H5MB	73.62 ± 2.38 ^{ns}	28.17 ± 3.73 ^{ab}	28.17 ± 2.79 ^{bc}	20.37 ± 1.02 ^c	45.00 ± 1.37 ^{ab}
H10MB	75.84 ± 3.64 ^{ns}	31.34 ± 2.86 ^{bc}	25.23 ± 3.41 ^{ab}	14.00 ± 1.49 ^b	43.31 ± 2.19 ^{ab}
H20MB	74.48 ± 3.48 ^{ns}	35.99 ± 1.88 ^c	24.96 ± 2.37 ^{ab}	6.85 ± 0.47 ^a	42.16 ± 3.21 ^a
H30MB	76.98 ± 3.57 ^{ns}	26.12 ± 2.84 ^{ab}	21.29 ± 3.36 ^a	22.44 ± 0.96 ^c	51.93 ± 1.33 ^c

Data represented means \pm SD ($n = 5$), ^{ns} means not significantly different, ^{a–d} means with same superscript in a column do not vary significantly ($p < 0.05$) with respect to each other.

Table 1 also lists the tensile strength and elongation at break values of the composite films. The tensile strength of HPMC was 24.08 ± 3.51 MPa. Introducing MCC into the HPMC matrix significantly increased the tensile strength of the HMB films, where the tensile strengths of the H10MB and H20MB films were 30.14 and 49.46% higher than that of HPMC, respectively. However, above 20% MCC, the tensile strength decreased, as observed in H30MB. As compared to H20MB, H30MB (a 10% increase in the MCC concentration) witnessed a 27.42% decrease in the tensile strength. These results indicate that 20% MCC was the optimum concentration for improving the mechanical properties of HPMC. The high specific area of the MCC fiber facilitates the formation of an adhesion net between the composite polymer and MCC during the film dehydration process, resulting in the improved tensile strength [17]. However, an excessive amount of MCC leads to a discontinuous microstructure, as observed in the SEM image, thereby decreasing the tensile strength.

The elongation at break of the HMB film gradually decreased compared to HPMC. This is frequently observed in bio-composite films that use cellulose fiber as a reinforcing element [14]. The elongation at break of HMB decreased from 33.19 ± 3.19 (control) to 28.17 ± 2.79 , 25.23 ± 3.41 , 24.96 ± 2.37 , and 21.29 ± 3.36 for H5MB, H10MB, H20MB, and

H30MB, respectively. This decreasing trend may be attributed to the stiffness of MCC, which directly hinders the mobility of the polymer strand [18]. These results were in agreement with the study conducted by Mathew, Oksman and Sain [12], who reported that introducing MCC into poly lactic acid (PLA) leads to a decrease in the elongation of the MCC/PLA composite films.

The gas barrier properties of the HMB films were determined by calculating the OTR and WVTR (Table 1). The OTR values of the control, H5MB, H10MB, H20MB, and H30MB were 51.97 ± 1.35 , 20.37 ± 1.02 , 14.00 ± 1.49 , 6.85 ± 0.47 , and 22.44 ± 0.96 cc²/m²/day, respectively, suggesting that MCC improved the gas barrier properties of HPMC. At 20% MCC, the film was least permeable to oxygen, which decreased the OTR value by 86.81% compared to the control, whereas above 20% MCC, the OTR value increased. This may be because at low concentrations, the MCC is well-dispersed within the HPMC matrix and acts as an effective barrier, slowing down the diffusion of gas molecules. However, increasing the MCC concentration leads to the formation of aggregates that generate voids within the HMB film, thereby facilitating the fast permeation of gases. These results were confirmed by SEM images of the cross-section and surface of the HMB film (Figure 1E,J).

The WVTR of the HPMC film was 48.17 g/m²/day. At 5 and 10% MCC, the moisture barrier properties did not improve, but at 20% MCC, the WVTR value reduced to 42.16 ± 3.21 g/m²/day (approximately by 12%), indicating an improvement in the moisture barrier properties. The presence of MCC in the polymer matrix increases the hydrophobicity of the composite films, thereby providing protection against moisture [19]. However, increasing the MCC content to 30% compromised the moisture barrier properties. This may be because at higher loadings, MCC aggregates formed voids within the film that allowed the fast permeation of gases, negating the barrier effect.

2.1.4. XRD Analysis

XRD is a very useful technique for characterizing crystalline materials. XRD diffractograms of the composite films and CrI are shown in Figure 3. The main diffraction peaks of MCC were observed at 15° (110) and 22.5° (200), representing the crystalline polymorph I cellulose, which is the dominant form of cellulose in nature [20]. The CrI of MCC was 65.45%, which is within the range previously reported (65–83%) [21]. Increasing the MCC content leads to a significant increase in the diffraction peak at 22.5° and the CrI of the HMB films. The CrI of the HMB films ranged from 6.66 to 18.97% depending on the MCC concentration. As expected, the lowest and highest values of the CrI were exhibited by H5MB and H30MB, respectively. These results confirmed the presence of MCC, which was successfully incorporated into the HPMC matrix. Additionally, the CrI directly relates to the hydrophobicity of the material; a high value of CrI is indicative of higher hydrophobicity [22]. An increase in the CrI also relates to the brittleness of the composite film, which was confirmed by the results of the elongation at break (Table 1) as previously discussed.

2.1.5. Thermal Properties

The thermal degradation of the HMB films was determined by TGA in terms of percentage weight loss (Figure 4). All TGA curves (Figure 4A) of the HMB films showed a similar pattern to that of the HPMC film (control). The decomposition behavior of the HMB films observed in the DTG curves (Figure 4B) can be divided into two stages; the first stage begins at approximately 130 °C, which is attributed to the evaporation and degradation of glycerol in the composite films [16]; the second stage is observed at approximately 310 °C, representing the degradation of HPMC and MCC.

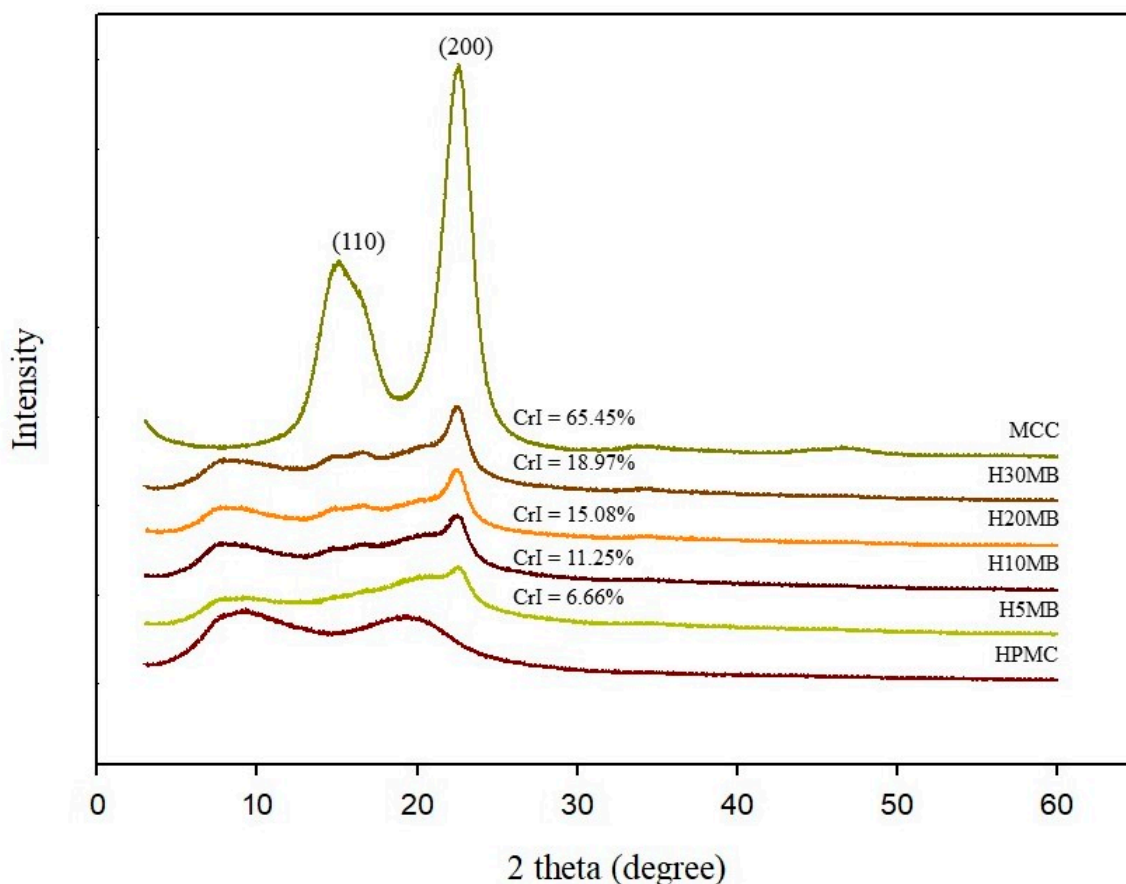


Figure 3. X-ray diffraction spectra of the hydroxypropyl methylcellulose (HPMC), 5% microcrystalline cellulose (MCC) (H5MB), 10% MCC (H10MB), 20% MCC (H20MB), and 30% MCC (H30MB) films.

Generally, the weight loss at 10% ($T_{10\%}$) and 50% ($T_{50\%}$) are used for comparing film stability [23]. There was no significant difference in the percent weight loss between the control and HMB films until $T_{10\%}$. However, an increase in the MCC content significantly decreased the degradation temperature of the composite films. The $T_{50\%}$ values of the control, H5MB, H10MB, H20MB, and H30MB films were 352.42 ± 1.45 , 346.33 ± 1.15 , 345.84 ± 1.26 , 344.80 ± 0.99 , and 337.83 ± 1.18 °C, respectively; there were no observed differences in the $T_{50\%}$ values of H5MB, H10MB, and H20MB. The decrease in thermal stability of the HMB may be due to the incompatibility and weak interfacial bonding between the polymer and fibers [24]. Similarly, Xian, Wang, Zhu, Guo, and Tian [14] reported a decrease in the thermal degradation temperature upon loading MCC in a PLA matrix.

Based on the characterization results, the H20MB film showed the best physical and barrier properties and better optical properties than the control. Therefore, H20MB was selected for the subsequent fabrication of the RA anthocyanins pH sensing indicator. The performance of the RA-H20MB indicator was evaluated by monitoring the color change after exposure to volatile ammonia. In addition, the RA-H20MB indicator was applied in packaging for tracking the freshness status of chicken tenderloin.

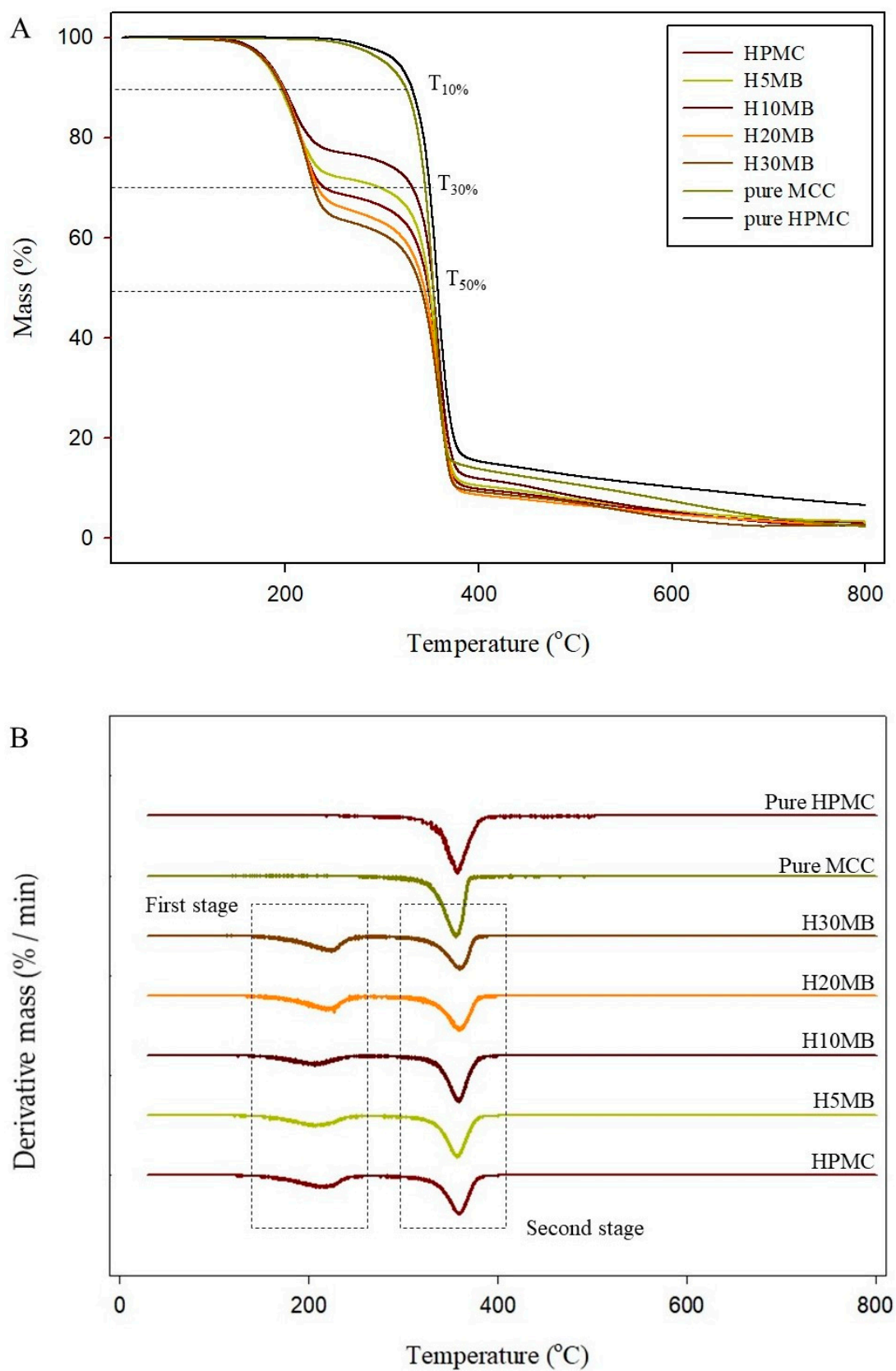


Figure 4. Thermogravimetry (A) and differential thermogravimetry (B) curves of the hydroxypropyl methylcellulose (HPMC), 5% microcrystalline cellulose (MCC) (H5MB), 10% MCC (H10MB), 20% MCC (H20MB), and 30% MCC (H30MB) films.

2.2. RA and RA-H20MB Indicator Characterization

2.2.1. Color Response to pH of RA Anthocyanins

The color change of RA solution in the pH range of 1–12 is displayed in Figure 5A. RA solution exhibited a red shade which the intensity gradually decreased with the increase of pH at pH 1–4 and changed to light coral red at pH 5–6, magenta at pH 7–8, maroon at pH 9, grey at pH 10, brown at pH 11 and yellow at pH 12. The corresponding absorption spectra change of the RA in the pH range from 1 to 12 are shown in Figure 5B.

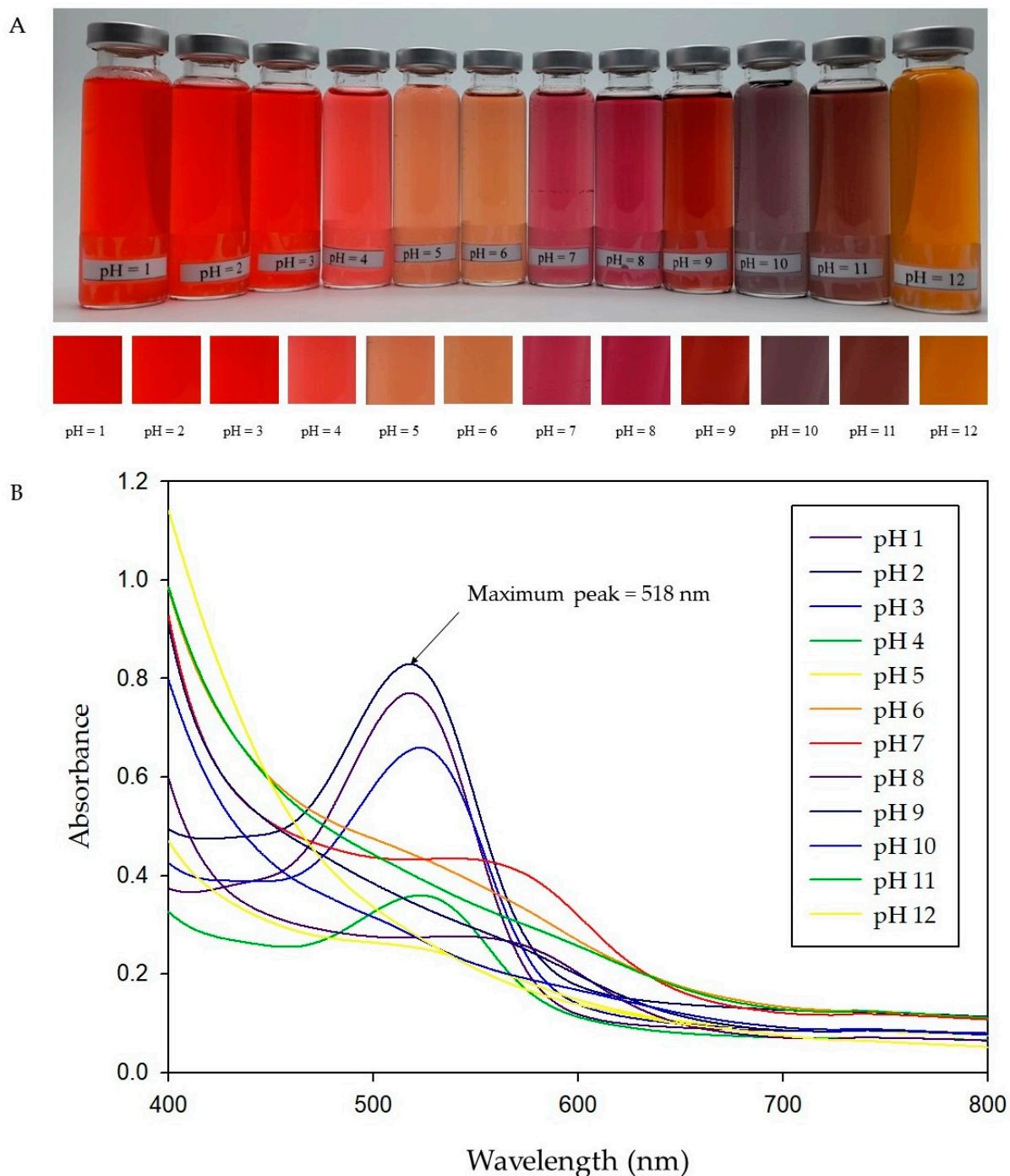


Figure 5. Changes in colors of RA solution (A) and UV-vis spectra of RA solutions in the pH range of 1–12 (B).

The maximum absorbance peak was obtained at approximately 518 nm of pH = 2; then, it gradually decreased and shifted to 579 nm when the pH was increased to 7. The change in absorbance peaks of RA solution is directly related to changes in the structures of anthocyanins [25]. This is because the molecular structure of anthocyanins has an ionic nature [26]. Generally, anthocyanins exist in the form of red flavylium cations at lower pH, which gradually change to colorless hemiketal and chalcones with an increase in pH, slowly transform into a blue quinoidal base under neutral and weakly alkaline conditions, and then turn to yellow chalcone under strongly alkaline conditions [27]. These results indicated that RA has the potential to be applied for the development of pH-sensing indicators due to it shows clear changes to a wide range of colors in response to variations in pH, which can be distinguished by the naked eye.

2.2.2. RA-H20MB Indicator

In order to evaluate the performance of the RA-H20MB indicator, NH₃ at 0.8 M was employed as a representative of spoilage nitrogen compound in fresh meat. Figure 6 exhibits the change in color and ΔE value of H20MB and RA-H20MB indicator upon exposure to volatile NH₃. Clearly, the color of RA-H20MB turned from red to magenta, purple, purple-blue, and green after 30 min of exposure. The ΔE values increased with exposure time which were 6.96–13.98 for magenta, 14.17–22.54 for purple, 35.54–36.80 for purple-blue, and 43.28–46.71 for green. The highest ΔE value of RA-H20MB was found at 28 min which value was 46.71 ± 1.90 . In addition, the ΔE values of RA-H20MB were significantly higher than H20MB for all exposure times which confirmed that the change in color of the indicator originates from RA only. These results indicate that the RA-H20MB indicators were successfully developed and can be applied as freshness indicators for intelligent food packaging.

2.2.3. Application of RA-H20MB Indicator for Tracking Freshness of Chicken Tenderloin

The freshness of chicken meat reduces with time, and the main factor for the reduction in freshness deals with the activity of various microorganisms [28]. The growth of microorganisms increases protein degradation which leads to an increase in the volatile nitrogen and pH of the packaging. According to this behavior, the freshness of chicken tenderloin can be tracked by monitoring the change of pH in the headspace gas.

Figure 7 shows the parameters related to the freshness of chicken tenderloin and the ΔE value of the RA-H20MB. The initial TPC of chicken tenderloin was 3.90 ± 0.14 log CFU/g (Figure 7A), which gradually increased with the storage time to 8.20 ± 0.25 log CFU/g at 15 days of storage. According to, the TPC at 7 logs CFU/g was employed at the end of the microbiological shelf-life of fresh poultry [29]. Therefore, chicken tenderloin was marked as spoilage since 12 days of storage due to the TPC exceeded the acceptable limit.

TVB-N at 40 mg/100 g has been used as the rejection limit for fresh chicken [30]. The TVB-N results of chicken tenderloin are presented in Figure 7A. The pattern of the TVB-N graph was similar to TPC results, increasing with the storage time. It increased from 8.43 ± 0.35 to 36.13 ± 0.35 mg/100 g at the end of storage period. However, there were no TVB-N results of chicken tenderloin that exceeded the rejection limit during the storage at 4 °C for 15 days.

The initial pH of chicken tenderloin was 6.13 ± 0.10 (Figure 7B), which increased with the storage time. At 15 days, the pH of chicken tenderloin reaches 7.00 ± 0.12 . The higher pH at the end of storage is attributed to the accumulation of volatile compounds including ammonia, which originated from protein degradation owing to microbial activity [31].

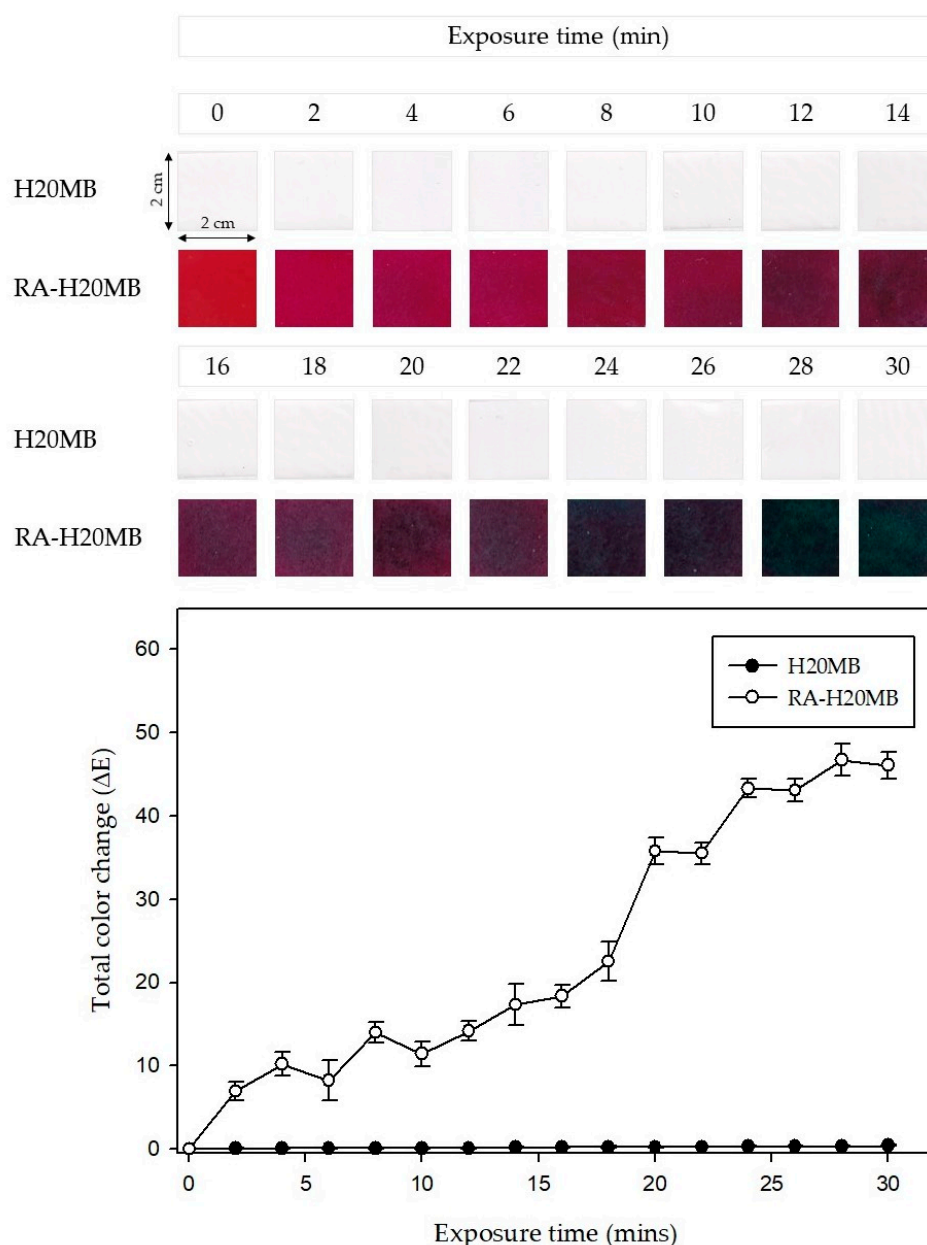


Figure 6. Total color change (ΔE) of the RA-H20MB indicators upon exposure to NH_3 vapors.

The color change and ΔE values of RA-H20MB indicator are presented in Figure 7B. The RA-H20MB at the initial was red and turned to magenta at 6 days, red-wine at 9 days, purple at 12 days, and green at 15 days of storage period. The red color of RA-H20MB on the initial day was used as a reference to calculate ΔE values. The ΔE value increased with an increase in spoilage factors. It increased from 0 to 8.46 ± 1.6 on day 3, and gradually increased to 42.49 ± 1.80 at the end of the storage period. In addition, the empty PET tray (without chicken tenderloin) embedded with RA-H20MB was used as a control of the RA-H20MB indicator during the storage test. The result showed that there was no observed difference in the color change of the control indicator during 15 days of storage. Thus, these results indicated that the color of the RA-H20MB indicator changed according to the changes in the quality of chicken tenderloin.

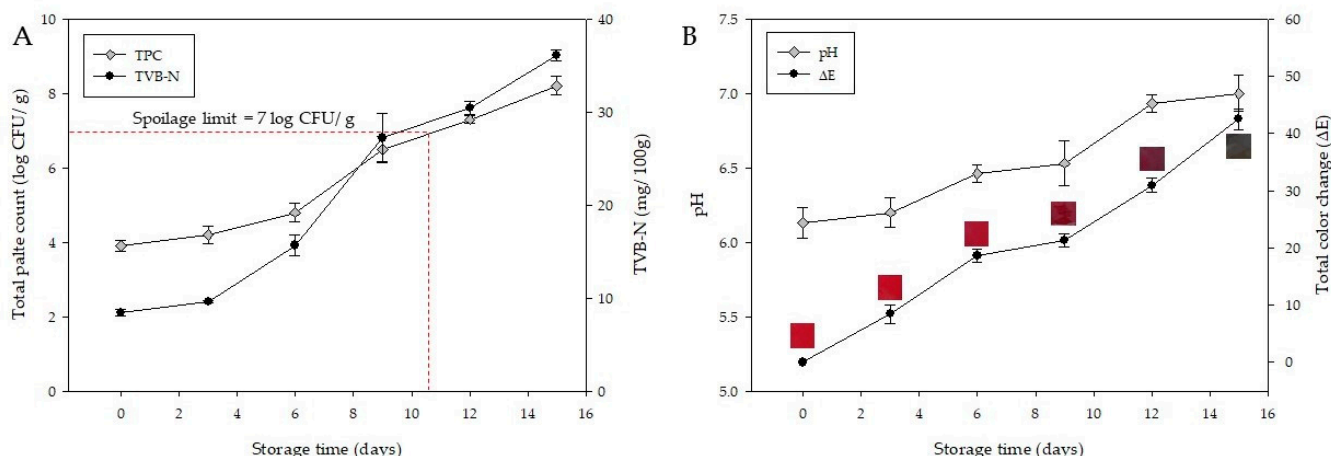


Figure 7. The changes of TPC and TVB-N of chicken tenderloin (A) and the change of pH of chicken tenderloin and the total color change (ΔE) of the RA-H20MB indicator (B) during stored at 4 °C.

Images of chicken tenderloin packaging and changes in the color of the RA-H20MB indicator are presented in Figure 8. According to the changes in the color of the RA-H20MB indicator and spoilage results of chicken tenderloin including the standard of fresh chicken, each color of the RA-H20MB indicator could be interpreted as follows: red color demonstrated that chicken tenderloin was fresh; magenta and red wine demonstrated that chicken tenderloin was good to eat; purple and green revealed that chicken tenderloin was spoilage. These indicated that the RA-H20MB indicator can be used as a freshness indicator due to its performance and ability to change its color regarding the spoilage status of the chicken tenderloin sample.

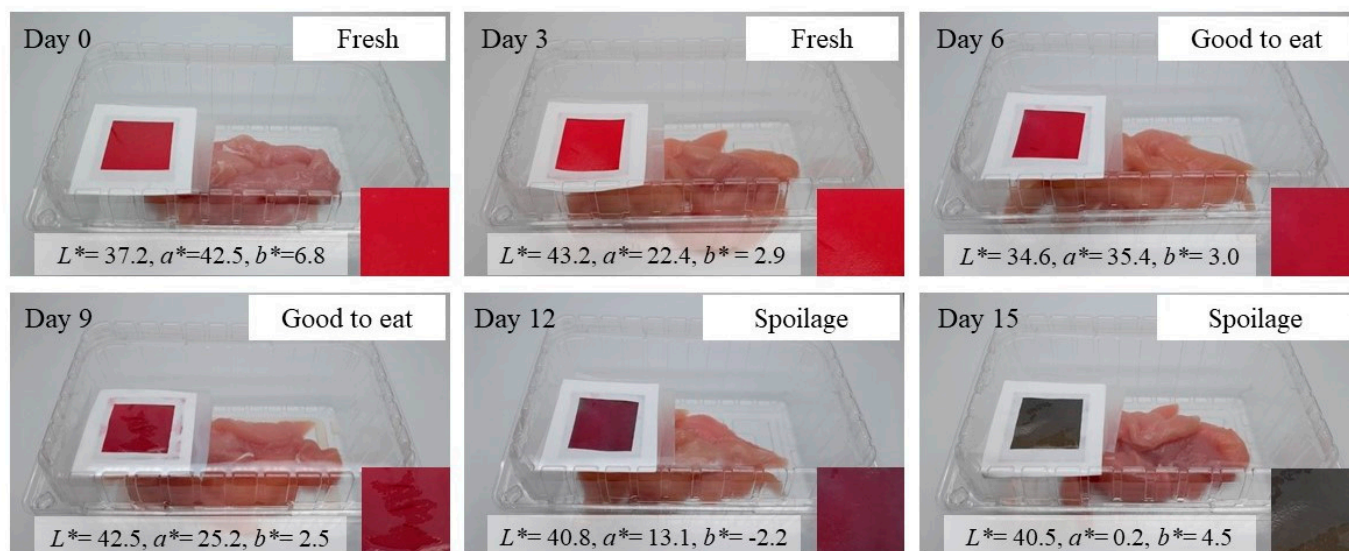


Figure 8. The color change of the RA-H20MB indicator and freshness/spoilage status of chicken tenderloin stored at 4 °C.

3. Materials and Methods

3.1. HMB Film Preparation

The HMB film was prepared according to a previously reported procedure [28] with some modifications. Briefly, the MCC (Sigma-Aldrich, St. Louis, MO, USA) suspension was prepared at 8% *w/w*. HPMC (Alfa Aesar, Haverhill, MA, USA) and was dissolved in DI water at 80 °C to obtain an HPMC solution at 5% *w/w*. Thereafter, the HPMC solution was mixed into the MCC suspension at different final ratios of HPMC: MCC = 100:0, 90:5,

90:10, 80:20, and 70:30 (dried basis), denoting HPMC (control), H5MB, H10MB, H20MB, and H30MB, respectively. Afterward, 6 g of glycerol was added to 400 mL of each HMB mixture. The mixture was heated at 80 °C, followed by homogenization using an IKA T-18 Ultra Turrax Digital Homogenizer (IKA, Wertheim, BW, Germany) at 10,000× *g* for 20 min. Subsequently, the temperature was reduced to 50 °C under the same homogenization conditions for 10 min, and the HMB solutions were degassed using a sonicator at 50 °C for 30 min. Finally, 30 mL of the HMB solutions were cast into a polystyrene petri dish (12 cm × 12 cm) and evaporated at 30 °C for 24 h to obtain HMB films. The dried films were wrapped with aluminum foil and stored in a desiccator at room temperature (25 °C) until further study.

3.2. Characterization of HMB

3.2.1. Field Emission Scanning Electron Microscopy (FE-SEM)

FE-SEM of the composite films was conducted using a Leica 360-S setup (Leica Microsystems Ltd., Cambridge, UK) at an acceleration voltage of 15 kV under high vacuum. A thin layer of Au was sputter-coated on the fractured surface of the composite films to avoid charging upon their exposure to an electron beam during SEM analysis.

3.2.2. Mechanical Properties

The thickness of each film was measured using a micrometer (Mitutoyo, Kawasaki, Japan). The tensile strengths and elongations of the films were tested using a universal texture meter according to GB 13022-1991. Before testing, the films were cut into rectangular strips of 6.0 cm × 2.0 cm and placed in the desiccator at room temperature (25 °C) for 24 h. The load cell and initial clamp distance were 150 kgf and 4.0 cm, respectively. The test speed was fixed at 0.06 mm/s. Each sample was analyzed five times at room temperature.

3.2.3. Barrier Properties

The oxygen transmission rate (OTR) of the films was evaluated with an 8001 Oxygen Permeation Analyzer (Illinois Instruments, Inc., Johnsburg, IL, USA). The oxygen gas permeability tests were performed at 23 °C and 0% relative humidity (RH) using high-purity nitrogen and oxygen as the carrier and testing gases, respectively. The water vapor transmission rate (WVTR) of the films was determined using a 7000 Water Vapor Permeation Analyzer (Illinois Instruments, Inc., Johnsburg, IL, USA). Measurements were performed at 38 °C and 90% RH.

3.2.4. Optical Property

The transparency of the HMB films was measured according to the method proposed by Gutiérrez [32] at 600 nm and calculated using the following equation:

$$\text{Transparency} = \frac{A_{600}}{e} \quad (1)$$

where A_{600} is the absorbance at 600 nm, and e is the film thickness (mm).

3.2.5. X-ray Diffraction (XRD) Measurement

XRD tests were carried out using a Bruker AXS D8 Advance X-ray diffractometer (Bruker Inc., Ettlingen, Germany) accompanied by Ni-filtered Cu K α radiation ($\lambda = 0.154$ nm) at a voltage of 40 kV and an electric current of 40 mA. The XRD profiles were obtained by scanning from 3 to 60° (2θ) at a rate of 3°/min. The crystallinity index (CrI) was calculated according to the Terinte, Ibbett and Schuster [21] method using the following Equation (2)

$$\text{CrI} = \frac{I_{200} - I_{\text{non-cr}}}{I_{200}} \times 100 \quad (2)$$

where I_{200} refers to the maximum intensity of the peak corresponding to the plane having a miller index of 200 ($2\theta = 22.5$), while I_{non-cr} represents the intensity of diffraction of the non-crystalline material.

3.2.6. Thermal Properties

Thermogravimetric analysis (TGA) of the indicators was performed using a TGA 4000 system (PerkinElmer Co., Groningen, The Netherlands). TGA curves were obtained by heating the indicators from 30 to 800 °C at a rate of 10 °C/min under a N₂ gas flow.

3.3. Application of HMB Film for Roselle Anthocyanin (RA) Indicator Fabrication

3.3.1. Extraction and Characterization of RA

Roselle (*Hibiscus sabdariffa*) was selected as a source of natural anthocyanins for fabricating the indicators due to the rich in effective anthocyanins and low cost. The freeze dried Roselle was purchased from a Happy Organic farm (Chiangmai, Thailand). RA was extracted following the method proposed by Zhang, Zou, Zhai, Huang, Jiang, and Holmes [25]. Briefly, 100 g of Roselle powder were added into 1500 mL of 80% ethanol, and pH of the mixture was adjusted to 2 using 1 M HCl. Then, the mixture was heated in a water bath at 50 °C for 1 h, filtered with Whatman No. 1 filter paper. Thereafter, the solvent was removed using a rotary evaporator (IKA Rotary evaporator RV 10 auto V, IKA, Staufen, Germany) at 50 °C in the dark. Finally, the RA extract was frozen and dried to obtain RA powder. The concentration of RA was determined according to the procedure demonstrated by Çam, et al. [33]. Briefly, RA solutions with pH = 1 and 4.5 was measured at 510 and 700 nm using a UV-Vis spectrophotometer (V-650 Spectrophotometer, JASCO Inc., Hachioji, Japan). The total anthocyanins content was determined as mg cyanidin/100 mL of RA using Equations (3) and (4):

$$A = (A_{510} - A_{700})_{pH=1} - (A_{510} - A_{700})_{pH=4.5} \quad (3)$$

$$\text{total anthocyanin content} = \frac{A \times M_w \times 100}{M_A} \quad (4)$$

where M_w = molecular weight of cyanidin (449.2 Da) and M_A = molar absorptivity of cyanidin (26,900).

The pH response of the RA was evaluated by changing the spectra. The RA powder was separately diluted with buffer solution (pH = 1–12) to obtain 3.75 mg of anthocyanins/100 mL of solution. Thereafter, the RA-HMB indicators at various pH values were scanned in the wavelength range of 400–800 nm using a UV-Vis spectrophotometer.

3.3.2. Preparation of RA-HMB

To fabricate the RA-HMB indicator, 60 mg of RA was dissolved into 400 mL of HMB solution, homogenized at 5000 × g for 5 min, and degassed for 30 min at 40 °C to obtain the RA-HMB solution. Thereafter, 30 mL of the RA-HMB solution was cast into a petri dish and dried at 30 °C for 24 h.

3.3.3. Color Response of RA-HMB to Ammonia

The sensitivity of the indicators to volatile NH₃ was determined based on a procedure formulated by Jiang, et al. [34] with some modifications. Briefly, the square (2 cm × 2 cm) RA-HMB indicators were placed in a 100 mL flask, 1 cm above an NH₃ solution (60 mL, 0.8 M). Thereafter, at 2 min intervals, the changes in the colors of the indicators were recorded using a digital camera (Canon EOD 450D, Yokohama, Japan) and measured using a CR-400 Chroma Meter (Konica Minolta Sensing, Inc., Tokyo, Japan) to obtain L^* , a^* , and b^* values of the indicators at specific time intervals after exposure to NH₃. The total color difference (ΔE) was calculated using Equation (5):

$$\Delta E = \sqrt{(L^* - L_0^*)^2 + (a^* - a_0^*)^2 + (b^* - b_0^*)^2} \quad (5)$$

where L_0^* , a_0^* , and b_0^* are initial color parameters of the indicators and L^* , a^* , and b^* are those at a given time.

3.3.4. Application of RA-HMB Indicator for Tracking Freshness of Chicken Tenderloin

The performance of RA-HMB was evaluated by tracking the spoilage of chicken tenderloin which were purchased from local market in Wonju, Korea. For the packaging preparation, RA-HMB indicator ($3 \times 3 \text{ cm}^2$) was attached under the cover of polyethylene terephthalate (PET) clamshell tray ($250 \text{ mm} \times 150 \text{ mm} \times 90 \text{ mm}$). Thereafter, approximately 300 g of fresh chicken tenderloins were placed in prepared tray. Each packed tray was hot-sealed (ISS 350–5, Gasungpak Co., Busan, South Korea) in a linear low-density polyethylene pouch (thickness = $60 \text{ }\mu\text{m}$) and stored at $4 \text{ }^\circ\text{C}$ in the dark for 15 days.

Samples were subjected to be analyzed in 3 day intervals. The images and the color parameters of the RA-HMB indicator were determined according to a previously mentioned method. The spoilage parameter, total bacterial count (TPC), and total volatile basic nitrogen (TVB-N) of chicken tenderloin were performed at room temperature according to method suggested by Baltić, Ćirić, Velebit, Petronijević, Lakićević, Đorđević and Janković [30]. The results of TPC and TVB-N were expressed as $\log_{10} \text{ CFU/g}$ and $\text{mg}/100 \text{ g}$ of chicken meat, respectively. The pH values of the samples were evaluated by a digital pH meter (AB15pH, Fisher Scientific Co., Pittsburgh, PA, USA) after mixing 10 g of the chicken tenderloin in 90 mL of distilled water.

3.4. Statistical Analysis

All experiments were conducted at least in triplicates. The experimental data were analyzed using Statistical Package for the Social Sciences (SPSS) (SPSS 25 for Windows, SPSS Inc., Chicago, IL, USA) and analysis of variance (ANOVA). Statistical significance of the difference in the mean values was established by $p \leq 0.05$, and Duncan's new multiple range test was utilized for all statistical analyses.

4. Conclusions

A biodegradable solid material by compositing HPMC and MCC was successfully developed. Introducing 5%, 10%, and 20% of MCC into the HPMC matrix improved the physical, barrier, and optical properties of HPMC. H20MB exhibited the best physical and barrier properties and better optical properties as compared to the control. Therefore, H20MC was selected for fabricating the RA pH sensing indicator. The RA-H20MB indicator exhibited a clear change in color in response to various pH conditions and ammonia vapor exposure times. Moreover, the RA-H20MB was applied to track the freshness of chicken tenderloin. It was found that the color change of RA-H20MB was easy to distinguish and related to the change in quality parameters of chicken tenderloin. These results indicated that the novel anthocyanin pH sensing indicator synthesized in this study could be a potential candidate for the environment-friendly pH sensing indicators, which can provide consumers with valuable information regarding food quality.

Supplementary Materials: The following supporting information can be downloaded at: <https://www.mdpi.com/article/10.3390/molecules27092752/s1>. Table S1: The overview of type of biopolymer for anthocyanin bio-composite film fabrication [35–45].

Author Contributions: Conceptualization, A.B. and Y.S.L.; methodology, A.B.; validation, A.B. and Y.S.L.; formal analysis, A.B., P.I. and C.S.; investigation, A.B. and P.I.; data curation, A.B.; writing—original draft preparation, A.B.; writing—review and editing, Y.S.L.; supervision, Y.S.L. All authors have read and agreed to the published version of the manuscript.

Funding: This research received no external funding.

Institutional Review Board Statement: Not applicable.

Informed Consent Statement: Not applicable.

Data Availability Statement: The data supporting the findings of this study are included in this article.

Acknowledgments: This work has been partially supported by BK21+ program funded by the Ministry of Education, Republic of Korea.

Conflicts of Interest: The authors declare no conflict of interest.

Sample Availability: Samples of the compounds are not available from the authors.

References

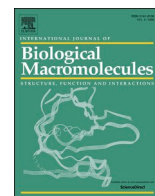
1. Lu, P.; Yang, Y.; Liu, R.; Liu, X.; Ma, J.; Wu, M.; Wang, S. Preparation of sugarcane bagasse nanocellulose hydrogel as a colourimetric freshness indicator for intelligent food packaging. *Carbohydr. Polym.* **2020**, *249*, 116831. [[CrossRef](#)] [[PubMed](#)]
2. Cheng, H.; Xu, H.; McClements, D.J.; Chen, L.; Jiao, A.; Tian, Y.; Miao, M.; Jin, Z. Recent advances in intelligent food packaging materials: Principles, preparation and applications. *Food Chem.* **2021**, *375*, 131738. [[CrossRef](#)]
3. Ghaani, M.; Cozzolino, C.A.; Castelli, G.; Farris, S. An overview of the intelligent packaging technologies in the food sector. *Trends Food Sci. Technol.* **2016**, *51*, 1–11. [[CrossRef](#)]
4. Moradi, M.; Tajik, H.; Almasi, H.; Forough, M.; Ezati, P. A novel pH-sensing indicator based on bacterial cellulose nanofibers and black carrot anthocyanins for monitoring fish freshness. *Carbohydr. Polym.* **2019**, *222*, 115030. [[CrossRef](#)] [[PubMed](#)]
5. Alizadeh-Sani, M.; Tavassoli, M.; Mohammadian, E.; Ehsani, A.; Khaniki, G.J.; Priyadarshi, R.; Rhim, J.-W. pH-responsive color indicator films based on methylcellulose/chitosan nanofiber and barberry anthocyanins for real-time monitoring of meat freshness. *Int. J. Biol. Macromol.* **2021**, *166*, 741–750. [[CrossRef](#)]
6. Kang, S.; Wang, H.; Xia, L.; Chen, M.; Li, L.; Cheng, J.; Li, X.; Jiang, S.; Kang, S.; Wang, H.; et al. Colorimetric film based on polyvinyl alcohol/okra mucilage polysaccharide incorporated with rose anthocyanins for shrimp freshness monitoring. *Carbohydr. Polym.* **2020**, *229*, 115402. [[CrossRef](#)]
7. Dong, H.; Ling, Z.; Zhang, X.; Zhang, X.; Ramaswamy, S.; Xu, F. Smart colorimetric sensing films with high mechanical strength and hydrophobic properties for visual monitoring of shrimp and pork freshness. *Sens. Actuators B Chem.* **2020**, *309*, 127752. [[CrossRef](#)]
8. Saeidipour, F.; Mansourpour, Z.; Mortazavian, E.; Rafiee-Tehrani, N.; Rafiee-Tehrani, M. New comprehensive mathematical model for HPMC-MCC based matrices to design oral controlled release systems. *Eur. J. Pharm. Biopharm.* **2017**, *121*, 61–72. [[CrossRef](#)]
9. Deshmukh, K.; Basheer Ahmed, M.; Deshmukh, R.R.; Khadheer Pasha, S.K.; Bhagat, P.R.; Chidambaram, K. 3-Biopolymer composites with high dielectric performance: Interface engineering. In *Biopolymer Composites in Electronics*; Sadasivuni, K.K., Ponnamma, D., Kim, J., Cabibihan, J.-J., AlMaadeed, M.A., Eds.; Elsevier: Amsterdam, The Netherlands, 2017; pp. 27–128. [[CrossRef](#)]
10. Siepman, J.; Peppas, N.A. Modeling of drug release from delivery systems based on hydroxypropyl methylcellulose (HPMC). *Adv. Drug Deliv. Rev.* **2012**, *64*, 163–174. [[CrossRef](#)]
11. Bilbao-Sáinz, C.; Avena-Bustillos, R.J.; Wood, D.F.; Williams, T.G.; McHugh, T.H. Composite Edible Films Based on Hydroxypropyl Methylcellulose Reinforced with Microcrystalline Cellulose Nanoparticles. *J. Agric. Food Chem.* **2010**, *58*, 3753–3760. [[CrossRef](#)] [[PubMed](#)]
12. Mathew, A.P.; Oksman, K.; Sain, M. Mechanical properties of biodegradable composites from poly lactic acid (PLA) and microcrystalline cellulose (MCC). *J. Appl. Polym. Sci.* **2005**, *97*, 2014–2025. [[CrossRef](#)]
13. Siró, I.; Plackett, D. Microfibrillated cellulose and new nanocomposite materials: A review. *Cellulose* **2010**, *17*, 459–494. [[CrossRef](#)]
14. Xian, X.; Wang, X.; Zhu, Y.; Guo, Y.; Tian, Y. Effects of MCC Content on the Structure and Performance of PLA/MCC Biocomposites. *J. Polym. Environ.* **2018**, *26*, 3484–3492. [[CrossRef](#)]
15. Jridi, M.; Boughriba, S.; Abdelhedi, O.; Nciri, H.; Nasri, R.; Kchaou, H.; Kaya, M.; Sebai, H.; Zouari, N.; Nasri, M. Investigation of physicochemical and antioxidant properties of gelatin edible film mixed with blood orange (*Citrus sinensis*) peel extract. *Food Packag. Shelf Life* **2019**, *21*, 100342. [[CrossRef](#)]
16. Hermawan, D.; Lai, T.K.; Jafarzadeh, S.; Gopakumar, D.A.; Hasan, M.; Owolabi, F.A.T.; Aprilia, N.A.S.; Rizal, S.; Khalil, H.P.S.A. Development of seaweed-based bamboo microcrystalline cellulose films intended for sustainable food packaging applications. *BioResources* **2019**, *14*, 3389–3410. [[CrossRef](#)]
17. Hazrati, K.; Sapuan, S.; Zuhri, M.; Jumaidin, R. Preparation and characterization of starch-based biocomposite films reinforced by *Dioscorea hispida* fibers. *J. Mater. Res. Technol.* **2021**, *15*, 1342–1355. [[CrossRef](#)]
18. Wang, X.; Tang, Y.; Zhu, X.; Zhou, Y.; Hong, X. Preparation and characterization of polylactic acid/polyaniline/nanocrystalline cellulose nanocomposite films. *Int. J. Biol. Macromol.* **2020**, *146*, 1069–1075. [[CrossRef](#)] [[PubMed](#)]
19. Chen, Q.; Shi, Y.; Chen, G.; Cai, M. Enhanced mechanical and hydrophobic properties of composite cassava starch films with stearic acid modified MCC (microcrystalline cellulose)/NCC (nanocellulose) as strength agent. *Int. J. Biol. Macromol.* **2019**, *142*, 846–854. [[CrossRef](#)] [[PubMed](#)]
20. Bumbudsanpharoke, N.; Lee, W.; Chung, U.; Ko, S. Study of humidity-responsive behavior in chiral nematic cellulose nanocrystal films for colorimetric response. *Cellulose* **2018**, *25*, 305–317. [[CrossRef](#)]
21. Terinte, N.; Ibbett, R.; Schuster, K.C. Overview on native cellulose and microcrystalline cellulose I structure studied by X-ray diffraction (WAXD): Comparison between measurement techniques. *Lenzing. Ber.* **2011**, *89*, 118–131.

22. Hamdan, M.A.; Ramli, N.A.; Othman, N.A.; Amin, K.N.M.; Adam, F. Characterization and property investigation of microcrystalline cellulose (MCC) and carboxymethyl cellulose (CMC) filler on the carrageenan-based biocomposite film. *Mater. Today Proc.* **2021**, *42*, 56–62. [[CrossRef](#)]
23. Olewnik, E.; Garman, K.; Czerwiński, W. Thermal properties of new composites based on nanoclay, polyethylene and polypropylene. *J. Therm. Anal.* **2010**, *101*, 323–329. [[CrossRef](#)]
24. Khouaja, A.; Koubaa, A.; Ben Daly, H. Dielectric properties and thermal stability of cellulose high-density polyethylene bio-based composites. *Ind. Crop. Prod.* **2021**, *171*, 113928. [[CrossRef](#)]
25. Zhang, J.; Zou, X.; Zhai, X.D.; Huang, X.W.; Jiang, C.P.; Holmes, M. Preparation of an intelligent pH film based on biodegradable polymers and roselle anthocyanins for monitoring pork freshness. *Food Chem.* **2019**, *272*, 306–312. [[CrossRef](#)] [[PubMed](#)]
26. Khoo, H.E.; Azlan, A.; Tang, S.T.; Lim, S.M. Anthocyanidins and anthocyanins: Colored pigments as food, pharmaceutical ingredients, and the potential health benefits. *Food Nutr. Res.* **2017**, *61*, 1361779. [[CrossRef](#)] [[PubMed](#)]
27. Sun, G.; Chi, W.; Xu, S.; Wang, L. Developing a simultaneously antioxidant and pH-responsive κ -carrageenan/hydroxypropyl methylcellulose film blended with *Prunus maackii* extract. *Int. J. Biol. Macromol.* **2020**, *155*, 1393–1400. [[CrossRef](#)] [[PubMed](#)]
28. Zhang, T.; Ding, H.; Chen, L.; Zhang, S.; Wu, P.; Xie, K.; Pan, Z.; Zhang, G.; Dai, G.; Wu, H.; et al. Characterization of chilled chicken spoilage using an integrated microbiome and metabolomics analysis. *Food Res. Int.* **2021**, *144*, 110328. [[CrossRef](#)]
29. Balamatsia, C.C.; Patsias, A.; Kontominas, M.G.; Savva, I.N. Possible role of volatile amines as quality-indicating metabolites in modified atmosphere-packaged chicken fillets: Correlation with microbiological and sensory attributes. *Food Chem.* **2007**, *104*, 1622–1628. [[CrossRef](#)]
30. Baltić, T.; Ćirić, J.; Velebit, B.; Petronijević, R.; Lakićević, B.; Đorđević, V.; Janković, V. Changes in total viable count and TVB-N content in marinated chicken breast fillets during storage. In Proceedings of the IOP Conference Series: Earth and Environmental Science, Zlatibor, Serbia, 1–4 October 2017; p. 012073.
31. Ramezani, Z.; Zarei, M.; Raminnejad, N. Comparing the effectiveness of chitosan and nanochitosan coatings on the quality of refrigerated silver carp fillets. *Food Control* **2015**, *51*, 43–48. [[CrossRef](#)]
32. Gutiérrez, T.J. Surface and nutraceutical properties of edible films made from starchy sources with and without added blackberry pulp. *Carbohydr. Polym.* **2017**, *165*, 169–179. [[CrossRef](#)]
33. Çam, M.; Hışıl, Y.; Durmaz, G. Classification of eight pomegranate juices based on antioxidant capacity measured by four methods. *Food Chem.* **2009**, *112*, 721–726. [[CrossRef](#)]
34. Jiang, G.; Hou, X.; Zeng, X.; Zhang, C.; Wu, H.; Shen, G.; Li, S.; Luo, Q.; Li, M.; Liu, X.; et al. Preparation and characterization of indicator films from carboxymethyl-cellulose/starch and purple sweet potato (*Ipomoea batatas* (L.) lam) anthocyanins for monitoring fish freshness. *Int. J. Biol. Macromol.* **2020**, *143*, 359–372. [[CrossRef](#)]
35. Talukder, S.; Mendiratta, S.; Kumar, R.; Agrawal, R.; Soni, A.; Luke, A.; Chand, S. Jamun fruit (*Syzygium cumini*) skin extract based indicator for monitoring chicken patties quality during storage. *J. Food Sci. Technol.* **2020**, *57*, 537–548. [[CrossRef](#)] [[PubMed](#)]
36. Kim, S.; Baek, S.-K.; Song, K.B. Physical and antioxidant properties of alginate films prepared from *Sargassum fulvellum* with black chokeberry extract. *Food Packag. Shelf Life* **2018**, *18*, 157–163. [[CrossRef](#)]
37. Nogueira, G.F.; Fakhouri, F.M.; Velasco, J.I.; de Oliveira, R.A. Active edible films based on arrowroot starch with microparticles of blackberry pulp obtained by freeze-drying for food packaging. *Polymers* **2019**, *11*, 1382. [[CrossRef](#)]
38. Mohammadlinejad, S.; Almasi, H.; Moradi, M. Immobilization of Echium amoenum anthocyanins into bacterial cellulose film: A novel colorimetric pH indicator for freshness/spoilage monitoring of shrimp. *Food Control* **2020**, *113*, 107169. [[CrossRef](#)]
39. Zepón, K.M.; Martins, M.M.; Marques, M.S.; Heckler, J.M.; Morisso, F.D.P.; Moreira, M.G.; Ziulkoski, A.L.; Kanis, L.A. Smart wound dressing based on κ -carrageenan/locust bean gum/cranberry extract for monitoring bacterial infections. *Carbohydr. Polym.* **2019**, *206*, 362–370. [[CrossRef](#)] [[PubMed](#)]
40. Yun, D.; Cai, H.; Liu, Y.; Xiao, L.; Song, J.; Liu, J. Development of active and intelligent films based on cassava starch and Chinese bayberry (*Myrica rubra* Sieb. et Zucc.) anthocyanins. *RSC Adv.* **2019**, *9*, 30905–30916. [[CrossRef](#)]
41. Ebrahimi Tirtashi, F.; Moradi, M.; Tajik, H.; Forough, M.; Ezati, P.; Kuswandi, B. Cellulose/chitosan pH-responsive indicator incorporated with carrot anthocyanins for intelligent food packaging. *Int. J. Biol. Macromol.* **2019**, *136*, 920–926. [[CrossRef](#)] [[PubMed](#)]
42. Koosha, M.; Hamed, S. Intelligent Chitosan/PVA nanocomposite films containing black carrot anthocyanin and bentonite nanoclays with improved mechanical, thermal and antibacterial properties. *Prog. Org. Coat.* **2019**, *127*, 338–347. [[CrossRef](#)]
43. Prietto, L.; Mirapalhete, T.C.; Pinto, V.Z.; Hoffmann, J.F.; Vanier, N.L.; Lim, L.-T.; Dias, A.R.G.; da Rosa Zavareze, E. pH-sensitive films containing anthocyanins extracted from black bean seed coat and red cabbage. *LWT* **2017**, *80*, 492–500. [[CrossRef](#)]
44. Jamróz, E.; Kulawik, P.; Guzik, P.; Duda, I. The verification of intelligent properties of furcellaran films with plant extracts on the stored fresh Atlantic mackerel during storage at 2 °C. *Food Hydrocoll.* **2019**, *97*, 105211. [[CrossRef](#)]
45. Ge, W.; Zhao, Y.; Kong, X.; Sun, H.; Luo, M.; Yao, M.; Wei, B.; Ji, S. Combining salicylic acid and trisodium phosphate alleviates chilling injury in bell pepper (*Capsicum annuum* L.) through enhancing fatty-acid desaturation efficiency and water retention. *Food Chem.* **2020**, *327*, 127057. [[CrossRef](#)] [[PubMed](#)]

ARTICLES FOR FACULTY MEMBERS

ROSELLE (HIBISCUS SABDARIFFA) ANTHOCYANIN USE IN MONITORING MEAT FRESHNESS

Title/Author	Halochromic smart packaging film based on montmorillonite/polyvinyl alcohol-high amylose starch nanocomposite for monitoring chicken meat freshness / Sharaby, M. R., Soliman, E. A., & Khalil, R.
Source	<i>International Journal of Biological Macromolecules</i> Volume 258 Part 2 (2024) 128910 Pages 1-12 https://doi.org/10.1016/j.ijbiomac.2023.128910 (Database: ScienceDirect)



Halochromic smart packaging film based on montmorillonite/polyvinyl alcohol-high amylose starch nanocomposite for monitoring chicken meat freshness

Muhammed R. Sharaby^{a,b,*}, Emad A. Soliman^c, Rowaida Khalil^b

^a Basic and Applied Sciences (BAS) Institute, Egypt-Japan University of Science and Technology (E-JUST), New Borg El-Arab city, Alexandria 21934, Egypt

^b Botany and Microbiology Department, Faculty of Science, Alexandria University, Alexandria 21511, Egypt

^c Polymeric Materials Research Department, Advanced Technology and New Materials Research Institute (ATNMRI), City of Scientific Research and Technological Applications (SRTA-City), New Borg El-Arab City, Alexandria 21934, Egypt

ARTICLE INFO

Keywords:

Anthocyanins
Halochromic
High amylose starch
Meat spoilage
Montmorillonite
Smart packaging

ABSTRACT

Polyvinyl alcohol (PVA) was blended with high amylose starch (HAS) at a ratio of 3:1, and reinforced with montmorillonite (MMT K10) at different concentrations (1, 2, 5, and 7 % w/w of polymers) and anthocyanins (ANT) to develop an active and smart packaging film. MMT addition enhanced the film's mechanical, barrier, thermal, and water resistance properties. Incorporating ANT extracted from roselle calyx into the optimal nanocomposite film (MMT/PVA-HAS II) increased the films' antioxidant, pH-response, and antibacterial properties. FTIR, XRD, and SEM confirmed the intermolecular interactions and even distribution of ANT and MMT in the film matrix. Release rate of ANT was dependent on type of simulant, with higher rate in aqueous solutions compared to alcoholic/fatty food simulants, and cytotoxicity evaluation proved safety of films for food packaging applications. Storage experiments confirmed the potential applicability of the novel halochromic smart film as a promising candidate for monitoring chicken spoilage under abusive storage conditions.

1. Introduction

Smart packaging has emerged as a new type of food packaging systems that can monitor the quality of foods through generating signals that food consumers can read in response to real-time changes of food products [1]. For instance, pH-sensitive films containing colorimetric indicators change their colors when proteinaceous food (meat and fish) decompose releasing basic volatile organic amines [2]. Synthetic dyes used as indicators such as bromocresol blue, cresol red, chlorophenol, and xylene blue, may pose a risk to consumers due to their possible toxicity, and thus their incorporation in edible films for monitoring food quality is constrained [3]. Anthocyanins (ANT), a group of plant flavonoids, have emerged as an eco-friendly, safe alternative to synthetic dyes. ANT are abundant where they can be extracted from berries, purple sweet potato, red cabbage, purple carrot, and roselle [4]. They possess strong antioxidant and antimicrobial properties and many health benefits. Besides, ANT have the ability to change their chemical structure and color in response to different pH conditions, justifying

their use as colorimetric indicators in smart packaging applications [5].

Starch is composed of amylose and amylopectin, and their ratio greatly influence the properties of starch-based materials. Different types of starch have been utilized for packaging films preparations, such as high amylose (HAS), normal-amylose starch, and modified starch [6]. Starch films have moderate oxygen barrier, poor moisture barrier, thermal and mechanical properties, limiting their applicability despite their biocompatibility and safety as packaging materials. Nevertheless, starch films prepared with HAS tend to have better mechanical, thermal, barrier and water-resistance properties [7–9]. Polyvinyl alcohol (PVA) is a biodegradable, semi-crystalline, non-toxic, and water-soluble synthetic polymer. PVA-based films have high transparency and good mechanical and gas barrier properties [10], however, their use is limited by their low moisture sensitivity and subsequently, low moisture barrier properties. To overcome this limitation, PVA blending with other polymers such as chitosan, gelatin, and starch enhances its physicochemical, barrier, thermal, and moisture sensitivity properties [11]. Many studies reported the efficient blending between PVA and starch

* Corresponding author at: Basic and Applied Sciences (BAS) Institute, Egypt-Japan University of Science and Technology (E-JUST), New Borg El-Arab city, Alexandria 21934, Egypt.

E-mail addresses: muhammed.sharaby@ejust.edu.eg, muhammedsharaby@alexu.edu.eg (M.R. Sharaby).

<https://doi.org/10.1016/j.ijbiomac.2023.128910>

Received 21 June 2023; Received in revised form 10 December 2023; Accepted 18 December 2023

Available online 21 December 2023

0141-8130/© 2023 Elsevier B.V. All rights reserved.

resulting in films with better properties [12,13]. To the best of our knowledge, based on literature survey, there are no studies on the blending of PVA with HAS for active or smart films preparation for food packaging applications. Montmorillonite (MMT) is the most commonly used layered silicate filler in packaging film preparations due to its environmental safety, abundance, non-toxicity, low cost, and chemical and thermal stability [14,15]. It has been reported to enhance mechanical properties and decrease water vapor permeability (WVP) in different polymer matrices when used at the appropriate concentration [16].

Meat spoilage is a metabolic process that changes meat sensorial attributes rendering it unacceptable for consumption. Microbial growth and enzymatic action are the main reasons for meat deterioration, emitting some volatile compounds and gases such as ammonia (NH₃), dimethylamine, and trimethylamine into the package headspace, causing an alteration in the pH of the gas environment [17]. Traditional quality assessment techniques such as determination of total volatile basic nitrogen (TVBN) and total microbial counts can provide sufficient quantitative data as indicators of meat freshness. However, such techniques are time-consuming and require handling skills, making them unfavorable for commercial application, especially with large samples number [18]. On the contrary, colorimetric pH sensing films can provide real-time and accurate freshness information for consumers through visual color changes for monitoring meat freshness [19].

With this background, we aimed to develop a novel active and smart ANT-loaded/MMT/PVA-HAS nanocomposite film with strong antimicrobial, antioxidant and pH-sensing properties, to monitor the freshness of chicken meat. The fabricated films' structural, morphological, barrier, mechanical, thermal, and optical properties were studied. The release behavior of ANT from films was also investigated using different food simulants, and the cytotoxic activity of films and films' ingredients were tested against normal WI-38 cell lines. We hypothesize that the smart film has potential for real-time monitoring of chicken freshness stored at different storage conditions providing better communication between the product and the consumer.

2. Materials and methods

2.1. Materials

Roselle calyx (*Hibiscus sabdariffa* L.) was purchased from a local market in Alexandria, Egypt. PVA (M.wt ~ 115,000 g/mol, CAS No. 9002-89-5) was obtained from Loba Chemie, India. Corn starch (high amylose content, 70 %) was provided by Park Scientific Limited, UK. MMT-K10 and 2,2-diphenyl-1-picryl-hydrazyl-hydrate (DPPH), and all cytotoxicity assay chemicals were supplied by Sigma-Aldrich (St. Louis, MO, USA). Tryptic Soy Broth (TSB), Mueller-Hinton Agar (MH), and agar-agar were provided by HiMedia (India). All other chemicals and solvents were of analytical grade and obtained from recognized chemical suppliers.

2.2. Extraction and characterization of ANT

Dried roselle calyx was ground and macerated with 75 % ethanol (1:15 w/v) at 25 °C for 24 h in a light-protected bottle and filtered using Whatman filter paper No. 1. The filtrate was then concentrated using a rotary evaporator (Kayoto, RE-2000A), freeze-dried and ground into fine powder [20]. Total anthocyanins content (TAC) was determined using pH differential method [21]. Briefly, ANT powder was dispersed in DW (1:10 w/v), mixed with 9 mL of potassium chloride buffer (pH 1.0) and 9 mL of sodium acetate buffer (pH 4.5), then incubated in the dark at RT for 20 min. Then, the absorbance of the reaction mixtures were read at 520 and 700 nm, respectively, using an ELISA reader (Epoch microplate reader, Agilent, CA USA). TAC results were calculated according to equation (Eq. (1)) and expressed as mg cyanidin-3-glucoside/g of dried powder.

$$\text{TAC} = (\text{A}^* \text{MW} * \text{DF} * \text{V} * 1000) / (\epsilon * \text{L} * \text{M}) \quad (1)$$

where A = (A₅₂₀ - A₇₀₀)pH1 - (A₅₂₀ - A₇₀₀)pH4, MW is the molecular weight (449.2 g/mol for cyanidin-3-O-glucoside), DF is the dilution factor, V is the volume of solvent, ε is the molar absorptivity (26,900 L. mol⁻¹.cm⁻¹), and L is the light path through the quartz cell (1 cm), and M is the weight of dry roselle calyx.

To determine the pH response, 2 mg of ANT powder was dissolved in 2 mL of different buffer solutions. Citric acid/sodium hydroxide/hydrogen chloride buffer; pH 2 & 4, citric acid/sodium hydroxide buffer; pH 5 & 6, di-sodium hydrogen phosphate/potassium dihydrogen phosphate buffer; pH 7, and boric acid/potassium chloride/sodium hydroxide buffer; pH 10 (Certipur®, Merck, Germany) and sodium hydroxide/potassium chloride buffer; pH 13. UV-vis spectra were measured using a UV-visible spectrophotometer (Hitachi U-3900, Japan) in the range of 400–800 nm, and the solution's color was photographed [22].

2.3. Film preparation

PVA and HAS were dissolved independently (5 % w/v) in distilled water (DW) at 95 °C for 2 h, mixed at a ratio of 3:1 (PVA: HAS, based on preliminary studies on mechanical and barrier properties), and glycerol was added as a plasticizer (25 % w/w of polymers) with stirring for 30 min (SMHS-3, Daihan Scientific Co., Korea) to obtain PVA-HAS neat film-forming solution (FFS). MMT/PVA-HAS nanocomposite films were prepared by adding different concentrations (1, 2, 5, and 7 % w/w of polymers) of previously sonicated MMT solutions to the PVA-HAS FFS, followed by stirring at 500 rpm for 30 min before subsequent ultrasonication (WUC-D06H, Daihan Scientific Co., Korea) at 25 kHz for an additional 30 min [23]. To prepare the smart nanocomposite film, ANT was added at concentration of 6.25 mg/mL of FFS, (double the MIC value; 3.12 mg/mL) to the MMT/PVA-HAS FFS (optimal film). All prepared formulations (Table S1) were degassed for 10 min in a water bath sonicator, cast on polystyrene plates, left to dry at 25 °C for 48 h, then peeled and stored in a desiccator (RH = 54 %) until further use.

2.4. Films characterization

2.4.1. FTIR spectroscopy

FTIR spectra of ANT, MMT powders was determined by mixing the samples individually with 250 mg of dry KBr crystals and compressing under vacuum to form a pellet prior to measurement. The FTIR spectra of the functional groups were identified in the frequency region 4000–400 cm⁻¹ using a Bruker VERTEX 70v FTIR spectrometer with a resolution of 4 cm⁻¹. While, film samples were placed directly on the reading surface and measured with the same parameters [24].

2.4.2. XRD analysis

XRD patterns of the films and ingredients were analyzed by Shimadzu XRD-6100 diffractometer (Japan) operated at 40 kV using CuKα radiation (λ = 1.54060 Å) in the 2θ range between 5° and 90° and a scan rate of 2°/min.

2.4.3. Thickness and mechanical properties

The thickness of the prepared films was determined using a digital micrometer (REXBETI, China). 10 random readings were taken per film, and the mean thickness value was recorded. Tensile strength (TS) and elongation at break (E%) were measured using a universal strength tester (Tensolab 5000, Mesdan, Italy) according to the standard method D882–12 [25]. Sample films were cut into 2 cm × 8 cm strips, with an initial grip separation of 4 cm and a crosshead speed of 1 mm/s. TS was calculated by dividing the force by the cross-sectional area of the film, and E% was calculated by the machine's software. An average of five readings was recorded per sample. Young's modulus (YM) was obtained

from the slope of the resulting stress vs strain curve of each film.

2.4.4. Hydration and water vapor barrier properties

Moisture content (MC), moisture absorption (MA) and water solubility (WS) were determined by the gravimetric method [26]. Film specimens (2 cm × 2 cm) were weighed (W_1), oven-dried at 105 °C for 24 h, weighed again (W_2), and MC was determined by the following equation (Eq. (2)):

$$MC\% = (W_1 - W_2)/W_1 \times 100 \quad (2)$$

Pre-dried film specimens (W_1) were placed in a desiccator with saturated NaCl solution (RH = 75 %) to determine the MA, and weighed daily until a constant weight was reached (W_2). Films moisture absorption was calculated from the following equation (Eq. (3)):

$$MA\% = (W_2 - W_1)/W_1 \times 100 \quad (3)$$

Dried and weighed samples (W_1) were put in 50 mL of distilled water under constant agitation for 6 h at 25 °C, filtered using filter paper, where residues dried at 105 °C for 24 h until constant weight (W_2). Films solubility was calculated using the following equation (Eq. (4)):

$$WS\% = (W_1 - W_2)/W_1 \times 100 \quad (4)$$

Water vapor permeability (WVP) was determined gravimetrically at 25 °C according to ASTM E96-00 [27] with slight modifications. Film specimens were mounted on porcelain cups containing 8 g anhydrous calcium chloride and completely sealed with molten wax. Cups were weighed, stored in a desiccator containing saturated magnesium nitrate solution (RH = 53 ± 1), and the weight gain of cups was monitored every 12 h for 5 days using a four digits balance (AXIS ACE220, Poland). WVTR was calculated from the slope of the straight line obtained by plotting the rate of sample weight change versus time (t), divided by the transfer area (m^2). WVTR ($g \cdot m^2 \cdot s^{-1}$) and WVP ($g \cdot m^{-1} \cdot s^{-1} \cdot Pa^{-1}$) values were calculated using the respective equations (Eqs. (5) and (6)):

$$WVTR = \frac{w}{t \cdot A} \quad (5)$$

$$WVP = \frac{WVTR \cdot x}{P_o \cdot (RH_1 - RH_2)} \quad (6)$$

where w/t is the slope of the weight gain line as a function of time (g/s) (calculated by linear regression with $R^2 > 0.99$), A is the area of the cup opening (m^2), x is the average thickness of the film (m), P_o is the partial pressure of water vapor at 25 °C (3169 Pa), and $(RH_1 - RH_2)$ is the relative humidity difference between the two sides of the film.

2.4.5. Scanning electron microscopy (SEM)

Surface morphology of the films was examined using SEM (JEOL, JSM-6010LV) under vacuum conditions at an acceleration voltage of 20 kV. Film samples were sputter-coated (JEOL, JEC-3000FC) with gold before analysis.

2.4.6. Thermogravimetric analysis

The thermal stability of MMT and studied films were analyzed by thermogravimetric analyzer (Universal V4.5A TA, USA) from 40 to 700 °C and a rate of 10 °C/min under a nitrogen flow of 40 mL/min.

2.4.7. Antioxidant and antimicrobial activity

The DPPH radical scavenging assay was used to analyze the antioxidant activity of ANT and films [4]. Equal-weight film samples (30 mg) were immersed in 4 mL DPPH methanol solution (100 μM), solution was stored in the dark at 25 °C for 1 h, and the absorbance was measured at 517 nm. Radical scavenging activity was calculated according to the equation (Eq. (7)):

$$\text{Scavenging activity (\%)} = (A_o - A)/A_o \times 100 \quad (7)$$

where A_o is the absorbance of the blank, and A is the absorbance of the reaction mixture.

The antimicrobial activity of prepared films was evaluated using the disc diffusion method [28] against seven different pathogenic strains (*E. coli* O157:H7, *Klebsiella pneumonia* ATCC 13883, *Proteus mirabilis*, *Pseudomonas aeruginosa*, *Salmonella enterica*, *Staphylococcus aureus* ATCC 12598, and *Candida albicans* ATCC 10231). 100 μL of each bacterial suspension (1.5×10^7 CFU/mL) were spread onto MH plates, onto which film discs (8 mm in diameter) were placed. Plates were incubated at 37 °C for 24 h, and the mean of inhibition zone diameters (IZD) were determined.

2.4.8. Color parameters and pH response

Color parameters of film samples (L^* , a^* , and b^*) were measured, and the total color difference (ΔE) was calculated using a hunter lab colorimeter (Miniscan EZ 4500 L, HunterLab, USA), where the color values of the standard color plate were $L = 99.54$, $a = -0.1$, and $b = 0.14$. For pH response analysis, the colored film samples were soaked in a series of buffer solutions with different pH values (pH 2–13), at room temperature for 10 min, then dried on filter paper to remove the excess solution. and color parameters were calculated by the device using the untreated film as a control [29], according to the following equation (Eq. (8)):

$$\Delta E = \sqrt{(L^* - L_o)^2 + (a^* - a_o)^2 + (b^* - b_o)^2} \quad (8)$$

where, values of L^* , a^* and b^* are color values of indicator film in different pH values, L_o , a_o and b_o are color values of the control smart film.

To estimate the response time of the smart film in the buffer solutions with different pHs, photographs of films were taken every 2 min interval.

2.4.9. Release of ANT

Film samples (2 cm × 2 cm) were immersed in 20 mL of three different food simulants; distilled water (simulant for aqueous foods), 50 % ethanol (simulant for oil-in-water emulsions and alcoholic foods), and 95 % ethanol (simulant for fatty foods), and gently shaken at 37 °C. 1 mL of each solution was taken at predetermined time intervals (15, 30, 60, 90, 120, 150, 180, 210, 240 and 270 min), and the absorbance was measured at 520 nm using a UV-vis spectrophotometer, and the cumulative release percentage was calculated as follows (Eq. (9)):

$$\text{Cumulative release (\%)} = \frac{Mt}{M_o} \times 100 \quad (9)$$

where Mt (mg) is the amount of ANT released (calculated from the standard curve) from films at time t and M_o (mg) is the total amount of ANT incorporated in films [30].

2.4.10. Cytotoxicity evaluation

Cytotoxicity of ANT, MMT, PVA-HAS FFS, and ANT/MMT/PVA-HAS FFS were evaluated using the MTT (3-(4, 5 Dimethylthiazol-2-yl)-2, 5-diphenyltetrazolium bromide) colorimetric assay against normal lung fibroblasts (WI-38, CCL-75) obtained from the American Type Culture Collection (ATCC, Rockville, MD), according to method of Sharaby, et al. [31]. The cells were seeded in flat-bottom 96 well plate (Corning, USA) at a density of 1×10^4 cell/well (100 μL) in high glucose DMEM culture medium (Biosera, France) supplemented with 10 % fetal bovine serum albumin (Sigma-Aldrich, USA) and 1 % Penicillin streptomycin (Sigma Aldrich, USA). Plates were incubated at 37 °C for 18 h in a humidified 5 % CO₂ incubator (Memmert, UK) to allow cells attachment. ANT, MMT and FFSs were serially two-fold diluted, added in triplicate in each well, and incubated for 48 h under the previously mentioned culture conditions. Supernatants from each well were replaced with fresh medium (100 μL/well) containing MTT reagent with a final concentration of 0.5 mg/mL, and plates were re-incubated at 37 °C for 4 h. Media over the cells were removed, and dimethyl sulfoxide (Merck, Germany)

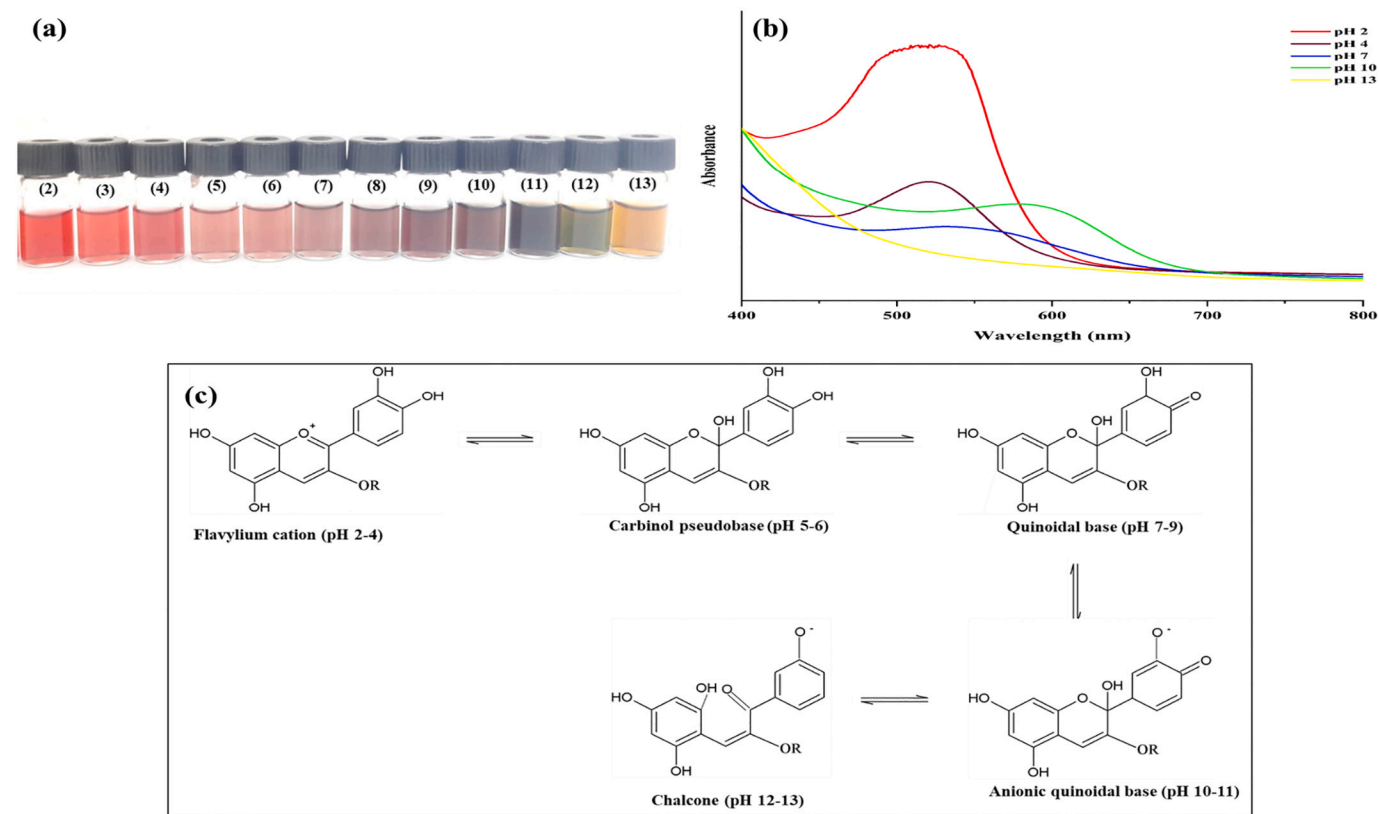


Fig. 1. Visual color changes (a); UV-vis spectra (b); and structural transformations of ANT in different pH buffers. (For interpretation of the references to color in this figure legend, the reader is referred to the web version of this article.)

was added (100 μL /well), plates were shaken for 15 min, and the absorbance was measured at 570 nm using an Epoch microplate reader (Agilent, CA USA). The cell viability was calculated as follows (Eq. (10)):

$$\text{Cell Viability (\%)} = \frac{\text{Absorbance of sample}}{\text{Absorbance of control}} \times 100 \quad (10)$$

2.5. Chicken freshness monitoring

The smart film was cut (2 cm \times 2 cm) and affixed to the inner surface of the lid of a petri dish (diameter 9 cm) containing 10 g of fresh chicken breasts. The aim of this experiment was to monitor the color response of the film to the volatile nitrogen compounds present in the head space of the petri dish without direct contact with samples. Accordingly, petri dishes were sealed with plastic wrap and stored at different conditions; 25 $^{\circ}\text{C}$ for 3 days, 7 $^{\circ}\text{C}$ for 5 days, and -20 $^{\circ}\text{C}$ for 7 days. Chicken samples were daily analyzed for total bacterial population counts (TPC), homogenized in a stomacher (Seward 400, UK) with sterile peptone water (0.1 % w/v) at 260 rpm for 2 min. Homogenates were serially ten-fold diluted, spread plated on tryptic soy agar (TSA) medium, plates were incubated at 37 $^{\circ}\text{C}$ for 24 h, and counts were presented as mean (log CFU/g) of three independent experiments. pH values of the homogenates were determined using a pH meter (Hanna, Romania), and TVBN content were measured according to Cao, et al. [32] by steam distillation method. Where, 10 g of homogenized chicken samples was mixed with 250 mL DW in a 500 mL round bottom flask, to which 2 g of magnesium oxide was added, and the mixture was distilled. The distillate was collected in a flask containing 3 % (w/v) aqueous solution of boric acid and a drops of mixed indicator (0.1 g of methyl red and 0.05 g methylene blue to 100 mL ethanol). The boric acid solution turned green when the distilled TVBN made it alkaline. Finally, the obtained solution was titrated with a 0.01 N HCl solution until it turned pink. TVBN was calculated from the following equation (Eq. (11)) and results were

expressed as mg/100 g of sample.

$$\text{TVBN} = (V \times 0.01 \times 14 \times 100) / W \quad (11)$$

where, V is titrated volume of HCl, and W is the sample weight.

2.6. Statistical analysis

Statistical analysis was performed with analysis of variance (ANOVA) using OriginPro 2021 (Northampton, USA) software. All results were presented as means of at least two replicates from three independent experiments (unless otherwise stated) \pm standard deviation (SD), where Tukey's test was used to determine the significance of differences among the mean values at $p < 0.05$ level.

3. Results and discussion

3.1. Characterization of ANT

According to the pH differential assay, the TAC value was 9.33 mg/g, which close to results (11 mg/g) of Huang et al. [33], but lower than values (36 mg/g) reported by Amer et al. [34], due to differences in extraction methods and cultivars of hibiscus. Color changes of the ANT at different pH buffers were tested to validate its use as a colorimetric indicator. As shown in Fig. 1a, a red color was obtained at pH 2–3, pink at pH 4–6, shades of purple at pH 7–10 and green-yellow at pH 11–13. The corresponding maximum absorption spectra shifted in response to increasing pH value (Fig. 1b), besides, all spectra showed single peak curve. The maximum absorption peak around 515 nm at pH 2 was due to the presence red colored flavylium cation (Fig. 1c). At pH 7, the maximum absorption peak moved to a higher wavelength (550 nm) with a noticeable decrease in absorption intensity, likely due to the deprotonation of flavylium cation leading to the formation of quinoidal base

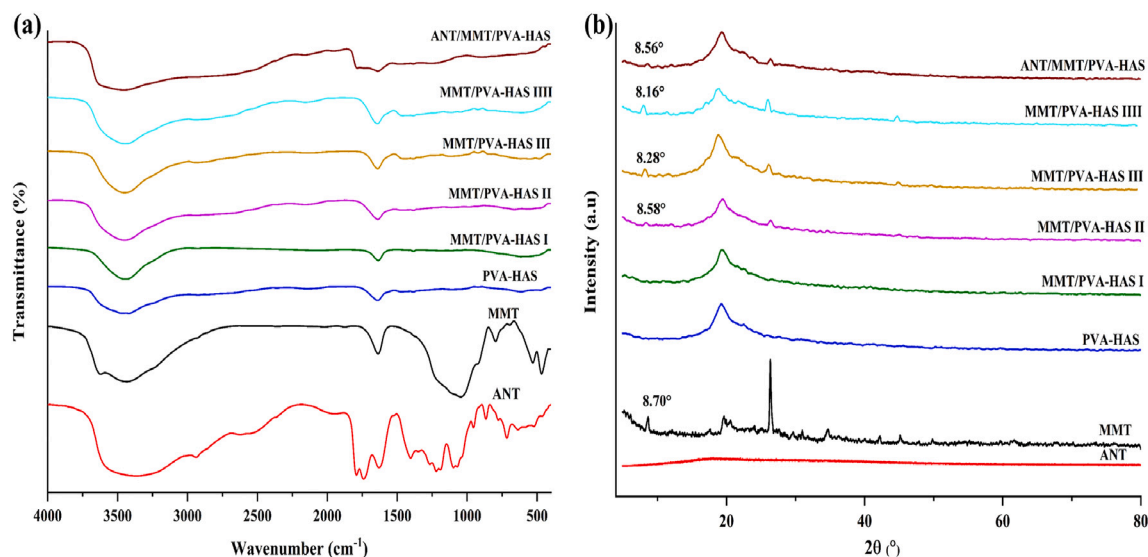


Fig. 2. FTIR spectra (a) and XRD diffractograms (b) of ANT, MMT, and the PVA-HAS-based films.

(blue-purple hue). As the pH increased to 10, the maximum absorption peak continued shifting to 580 nm, but with an increase in absorption intensity, may be due to the formation of a further deprotonated blue anionic quinone base. The absorption at 580 nm decreased at strong alkalinity (pH 13), and ANT were degraded and the central ring cracked forming a pale yellow chalcone [35,36].

3.2. Characterization of films

3.2.1. FTIR analysis

Fig. 2a shows absorption bands of ANT at 3356 and 2938 cm^{-1} corresponding to —OH and —CH , respectively. Peaks at 1740, 1630, and 1097 cm^{-1} were assigned to stretching vibration of C=O , C=C , and C—O , respectively. Additionally, the peak at 1791 cm^{-1} was due to the pyran ring stretching of flavonoid compounds [33,37]. MMT absorption bands at 3433 and 1636 cm^{-1} were related to —OH stretching and bending, respectively [38]. Characteristic peaks at 3627, 1045, 530, and 467 cm^{-1} were ascribed to —OH stretching in Al—OH and Si—OH , Si—O—Si symmetric stretching, SiO—Al linkages and deformation of Si—O—Si bonds, respectively [39,40]. For the PVA-HAS film, intense peaks at 3419 and 1639 cm^{-1} were attributed to the stretching and bending vibration of the —OH group due to intermolecular and intramolecular hydrogen bonding [41]. Peaks at 2924, 1468, and 1385 cm^{-1} were due to C—H stretching, and deformation vibrations of CH_2 and

C—H , respectively. The presence of ether linkages between aldehyde and —OH groups of the polymers (crosslinking of PVA and HAS) was confirmed by the peak at 1106 cm^{-1} [42].

No MMT characteristic peaks were detected in the spectrum of MMT/PVA-HAS films, likely due to the low concentration of incorporated filler in the film, aside from an overlap of MMT with those of PVA-HAS film [43]. Increased intensity and a slight shift in the —OH group was observed from 3419.14 to 3449.50, 3449.73, 3450.97, and 3452.96 cm^{-1} in spectra of films with MMT concentrations of 1, 2, 5, and 7 %, respectively, related to hydrogen bonding between components [40]. The smart film showed a broad —OH band due to the abundance of hydroxyl groups in ANT extract, in addition to a shift to 3455.83 cm^{-1} , suggesting possible intermolecular interactions [22].

3.2.2. XRD diffractograms

The crystalline nature of nanocomposite films and structural changes upon fillers addition was investigated using XRD (Fig. 2b). The absence of obvious diffraction peaks confirmed the amorphous nature of ANT, where a broad peak was detected at $2\theta = 21.32^\circ$. On the contrary, MMT displayed a high crystalline nature, as identified by peaks at 2θ of 8.70, 17.62, 19.67, and 34.78° corresponding to lattice planes of (001), (002), (110), and (101), respectively [44], according to the Joint Committee on Powder Diffraction Standards (JCPDS) card numbers 003-0010 and 29-1498 [45,46]. Furthermore, other peaks at 26.34° (101) and 45.30°

Table 1

Mechanical, barrier, and hydration properties of PVA-HAS-based films.

Films	Thickness (mm)	TS (MPa)	YM (MPa)	E (%)	WVP $\times 10^{-11}$ ($\text{g}\cdot\text{m}^{-1}\cdot\text{s}^{-1}\cdot\text{Pa}^{-1}$)	WS (%)	MC (%)	MA (%)
PVA-HAS	0.069 \pm 0.002 ^c	18.97 \pm 0.34 ^b	42.64 \pm 1.89 ^c	356.66 \pm 8.02 ^a	7.69 \pm 0.17 ^a	11.62 \pm 0.40 ^a	15.91 \pm 0.32 ^a	22.32 \pm 0.37 ^a
MMT/PVA-HAS I	0.076 \pm 0.001 ^{bc}	19.56 \pm 0.34 ^b	47.18 \pm 1.62 ^c	318.0 \pm 7.14 ^b	4.43 \pm 0.14 ^b	10.66 \pm 0.08 ^b	14.24 \pm 0.21 ^b	20.52 \pm 0.08 ^b
MMT/PVA-HAS II	0.081 \pm 0.002 ^{bc}	21.87 \pm 0.41 ^a	53.66 \pm 0.36 ^b	291.12 \pm 3.60 ^c	3.75 \pm 0.05 ^c	9.87 \pm 0.04 ^c	13.0 \pm 0.49 ^c	17.56 \pm 0.50 ^c
MMT/PVA-HAS III	0.096 \pm 0.003 ^{ab}	14.72 \pm 0.31 ^c	66.23 \pm 2.46 ^a	160.33 \pm 7.50 ^d	4.10 \pm 0.08 ^{bc}	7.14 \pm 0.22 ^d	10.36 \pm 0.14 ^e	15.06 \pm 0.16 ^c
MMT/PVA-HAS IIII	0.12 \pm 0.014 ^a	12.03 \pm 0.78 ^d	68.82 \pm 0.72 ^a	96.62 \pm 2.08 ^e	7.25 \pm 0.53 ^a	6.16 \pm 0.12 ^e	9.90 \pm 0.06 ^e	13.14 \pm 0.11 ^d
ANT/MMT/PVA-HAS	0.083 \pm 0.002 ^{bc}	22.51 \pm 0.38 ^a	55.52 \pm 0.93 ^b	311.19 \pm 2.31 ^b	3.54 \pm 0.06 ^c	9.84 \pm 0.15 ^c	11.89 \pm 0.54 ^d	17.49 \pm 0.18 ^c

Values are given as means \pm SD ($n = 3$). Different lowercase letters in the same column indicate significantly different values ($P < 0.05$).

TS: Tensile strength; YM: Young's modulus; E: Elongation at break; WVP: Water vapor permeability; WS: Water solubility; MC: Moisture content; MA: Moisture absorption.

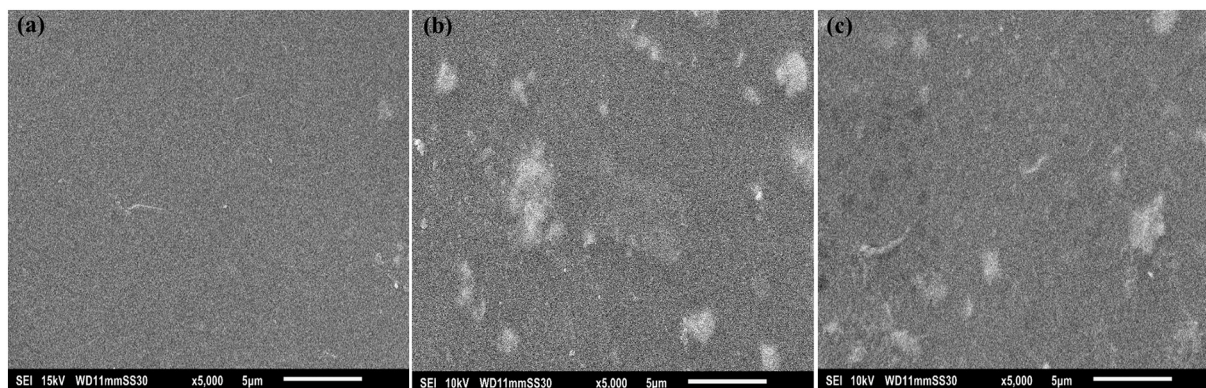


Fig. 3. SEM micrographs of surface microstructure of PVA-HAS (a), MMT/PVA-HAS II (b), and ANT/MMT/PVA-HAS (c) films.

(112) confirmed the presence of quartz in the sample. XRD spectra of films showed a semi-crystalline nature, with a strong peak at $2\theta = 19.45^\circ$ corresponding to (101) crystallographic plane owing to physical interaction or hydrogen bonding between —OH groups of PVA and starch [41]. According to Kong, et al. [42], crystallinity of films was associated with PVA rather than HAS. HAS tend to form dense molecular structures during heat treatment where micro-crystalline domains remain in swollen granules of HAS, in addition to reassociation of glucan chains may occur during the gelatinization process [47].

MMT characteristic peaks were absent in the diffractogram of MMT/PVA-HAS nanocomposite containing 1 % MMT, due to the formation of exfoliated structure of MMT, which was disordered and not detectable in the XRD pattern [48,49]. Increasing the concentration of MMT from 2 to 7 % resulted in a gradual appearance of MMT peaks. The characteristic peak at lattice plane (001) slightly shifted to 8.58° , 8.28° , and 8.16° for nanocomposites containing 2, 5 and 7 % (w/w) MMT, respectively, attributed to intercalation of polymers into the layers of MMT, which increases the interplanar spaces [23,50]. Notably, the smart film exhibited similar peaks and pattern to that of MMT/PVA-HAS II film, suggesting that the crystal structure of film was not greatly affected by ANT incorporation, possibly due to the low concentration of ANT [51].

3.2.3. Mechanical properties

The incorporation of MMT and ANT had an impact on films thickness and mechanical properties (Table 1). The thickness of films containing MMT varied from 0.069 to 0.12 mm, related to the incorporated solids content, however, the addition of ANT had no significant effect ($P > 0.05$) on thickness. The PVA-HAS neat film showed tensile TS of 18.97 MPa, which was higher than those reported for PVA-Starch blends in previous studies [52–54] likely due to the differences in PVA: starch ratio, type of starch, and plasticizer used. The TS of films increased at MMT concentrations up to 2 %, which is related to the good dispersion of the MMT in the polymer matrix and the formation of intermolecular hydrogen bonds. Furthermore, the MMT nanometric size and high surface area facilitate the formation of an effective interface for transferring tensile stresses [55]. On the contrary, films with high MMT concentrations (5 and 7 % MMT) showed a decline in TS values due to incomplete dispersion of clay in the film matrix, agglomeration of MMT layers limiting the load transfer and causing early ruptures of the films under tension [43,49].

The neat film exhibited the maximum E% of 356.66 %, which was reduced by adding increasing concentrations of MMT reaching the lowest value of 96.62 % in MMT/PVA-HAS III film. On the contrary, films' stiffness (YM) improved proportionally with increasing MMT concentration. The highest YM value was recorded in MMT/PVA-HAS III film (68.82 MPa), which was 62 % more than YM value of the neat film. This increase is attributed to the rigid nature of MMT that constrain segmental chain mobility in the polymer matrix, which is consistent with a previous report [56]. For the smart film, hydrogen

bonding and interfacial interactions between ANT and the film components may be the reason for the increase in TS, E% and YM values [57], in corroboration with FTIR results (Fig. 2a). Overall, the TS and E% of the smart film exceeded those of some commercially used polymers such as LDPE, polystyrene and cross-linked polyethylene [58,59].

3.2.4. Hydration and water vapor barrier properties

Water sensitivity is a crucial factor determining the potential feasibility of films for food packaging applications. Therefore, MC, MA, WS, and WVP of films were evaluated (Table 1). PVA-HAS film showed the highest MC, MA, and WS values due to the hydrophilic nature of both PVA and starch. The WS of the neat film (11.62 %) was lower than that reported by Huang, et al. [33] and Wu, et al. [60], attributed to the high amylose content starch used in our study [8]. The low MC, MA, and WS values of 9.90, 13.14 and 6.16 %, respectively, recorded in MMT/PVA-HAS III film compared to 14.24, 20.52 and 10.72 % for MMT/PVA-HAS I film provided evidence for the inverse correlation between the studied hydration properties and MMT concentration. These findings denote a strong hydrogen bonding between hydroxyl groups of MMT and the polymer matrix components, increasing the polymer cohesiveness and lowering WS and water diffusion into the polymer matrix, and in turn, reducing MA [14,15,61]. The smart film contained less moisture (MC) compared to MMT/PVA-HAS II; WS and MA values were also reduced with no significant difference ($P > 0.05$), may be associated with the interactions between ANT and film components which lead to the formation of tighter network between ANT and film matrix and limited the availability of free hydroxyl groups [33,35,36].

Lower WVP of packaging films is preferred to hinder moisture passage and consequently retard microbial spoilage and prolong the shelf life of foods. The WVP value of the neat film was $7.69 \times 10^{-11} \text{ g}\cdot\text{m}^{-1}\cdot\text{s}^{-1}\cdot\text{Pa}^{-1}$, which decreased upon MMT addition at 1–2 % concentrations. The WVP value recorded in 2 % MMT-containing film ($3.75 \times 10^{-11} \text{ g}\cdot\text{m}^{-1}\cdot\text{s}^{-1}\cdot\text{Pa}^{-1}$) was reduced by 50 % compared to the neat film, attributed to prolonged tortuous path created by the nanoclay, in addition to the hydrophobic nature of MMT [62]. Incorporating higher MMT concentrations (5 and 7 % w/w) increased the WVP of films, due to MMT agglomeration and voids formation, making passage for moisture through the film matrix [23,50]. The smart film had the lowest WVP value ($3.54 \times 10^{-11} \text{ g}\cdot\text{m}^{-1}\cdot\text{s}^{-1}\cdot\text{Pa}^{-1}$) as a consequence of the intermolecular interactions between the film components and ANT, reducing the availability of free hydroxyl groups, resulting in reducing the affinity of the films towards moisture [63]. The improved hydration properties of the smart film reflect the films ability to maintain the quality and integrity of high moisture content food products.

3.2.5. Surface morphology

PVA-HAS film exhibited a smooth continuous surface with no cracks or phase separation (Fig. 3a), confirming the good homogeneity and compatibility of both polymers [41]. The MMT/PVA-HAS II film surface

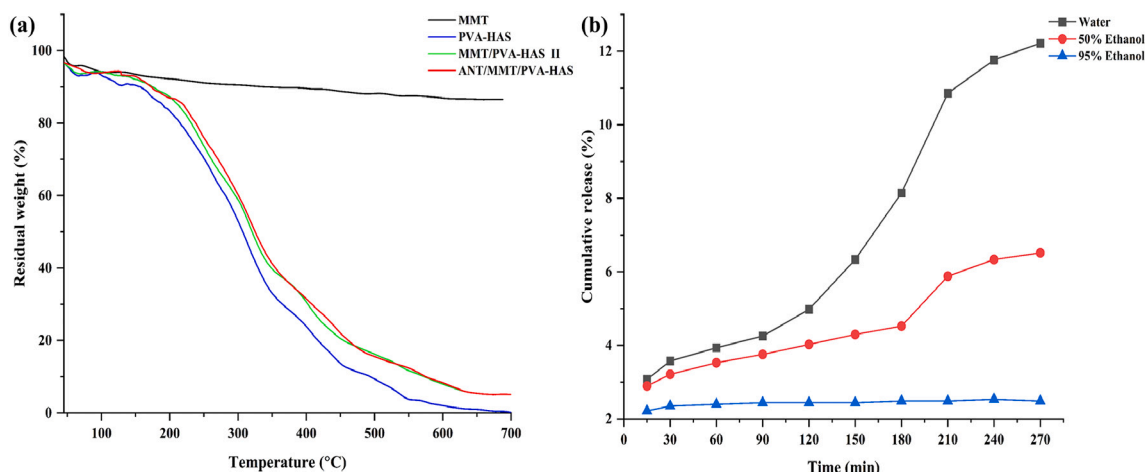


Fig. 4. TGA thermograms of MMT and the PVA-HAS-based films (a); cumulative release of ANT from ANT/MMT/PVA-HAS film in different food simulants (b).

Table 2
Antioxidant and antimicrobial properties of PVA-HAS-based films.

	PVA-HAS	MMT/PVA-HAS I	MMT/PVA-HAS II	MMT/PVA-HAS III	MMT/PVA-HAS IIII	ANT/MMT/PVA-HAS
DPPH scavenging activity (%) of films	2.80 ± 0.43 ^b	4.25 ± 0.82 ^b	4.38 ± 0.62 ^b	4.45 ± 0.85 ^b	4.73 ± 1.02 ^b	63.51 ± 5.13 ^a
Antimicrobial activity (IZD mm) of films						
<i>S. aureus</i>	0 ^b	0 ^b	0 ^b	0 ^b	0 ^b	25 ± 1.0 ^a
<i>E. coli</i> O157:H7	0 ^b	0 ^b	0 ^b	0 ^b	0 ^b	21 ± 1.50 ^a
<i>P. mirabilis</i>	0 ^b	0 ^b	0 ^b	0 ^b	0 ^b	15 ± 1.50 ^a
<i>P. aeruginosa</i>	0 ^b	0 ^b	0 ^b	0 ^b	0 ^b	15 ± 2.5 ^a
<i>S. enterica</i>	0 ^b	0 ^b	0 ^b	0 ^b	0 ^b	18 ± 1.25 ^a
<i>K. pneumonia</i>	0 ^b	0 ^b	0 ^b	0 ^b	0 ^b	12 ± 0.5 ^a
<i>C. albicans</i>	0 ^b	0 ^b	0 ^b	0 ^b	0 ^b	20 ± 1.5 ^a

Values are given as mean ± SD ($n = 3$). Different lowercase letters in the same row indicated significant differences ($p < 0.05$).

was rough, and heterogeneous with small MMT agglomerates that were uniformly distributed in the film matrix (Fig. 3b), in agreement with similar reports for alginate, chitosan, *Ocimum basilicum* seed mucilage nanocomposites [49,50,64]. The surface of the smart film had fewer agglomerates compared to the surface of MMT/PVA-HAS II film (Fig. 3c), related to the concurrent addition of ANT and MMT to the blend, which increased potential interactions between the components of the polymer matrices, and thus diminished coalescence of MMT particles [20,36].

3.2.6. Thermal stability

The TGA thermogram (Fig. 4a) of MMT depicted a mass loss of 4.3 % at a temperature of 45–120 °C, due to dehydration of water bound to the surface and interlayer space of MMT. Another mass loss of 7.37 % occurring at 120–700 °C was related to MMT dehydroxylation [65]. TGA curves of films demonstrated a four-degradation stage pattern. In all studied films, the first degradation stage (45–190 °C) corresponds to the loss of moisture content, while the second stage is assigned to glycerol

breakdown at a temperature range of 200–280 °C [55]. PVA and starch depolymerization occurred in the third (major degradation step). The degradation temperature in the neat film ranged from 280 to 380 °C with a T_{max} of 310 °C and a mass loss of 32.64 % [13]. T_{max} and T_{50} values were more by 15 °C for the MMT/PVA-HAS II film (Fig. S1), indicating a more thermally stable film as a result of MMT addition. MMT could maintain its structure in the matrix even at high temperatures, which insulates the underlying material and delays the escape of the products generated during decomposition [62]. The fourth degradation step (>400 °C) was marked by the thermal decomposition of high-molar-mass polyenes formed during the third stage and their subsequent conversion to char [57,66]. The final residues for the neat and MMT/PVA-HAS II films were 0.45 and 5.13 %, respectively. ANT incorporation showed no significant effect on the thermal stability of the

Table 3
Color parameters and total color difference (ΔE) of PVA-HAS-based films and pH response of the smart film.

Film	Color parameters			
	L^*	a^*	b^*	ΔE
PVA-HAS	94.26 ± 0.41 ^a	-0.91 ± 0.01 ^b	1.45 ± 0.05 ^f	6.16 ± 0.12 ^c
MMT/PVA-HAS I	92.17 ± 0.22 ^b	-0.98 ± 0.01 ^b	2.01 ± 0.14 ^e	7.58 ± 0.10 ^d
MMT/PVA-HAS II	90.33 ± 0.45 ^c	-1.19 ± 0.07 ^b	2.64 ± 0.22 ^d	7.99 ± 0.03 ^d
MMT/PVA-HAS III	88.18 ± 0.22 ^d	-1.69 ± 0.08 ^b	4.3 ± 0.19 ^c	12.08 ± 0.07 ^c
MMT/PVA-HAS IIII	85.89 ± 0.28 ^e	-1.93 ± 0.04 ^b	4.96 ± 0.01 ^b	14.54 ± 0.27 ^b
ANT/MMT/PVA-HAS	27.27 ± 0.57 ^f	23.27 ± 1.13 ^a	6.72 ± 0.21 ^a	76.07 ± 0.76 ^a
pH response of ANT/MMT/PVA-HAS film				
pH 2	40.06 ± 0.24 ^f	24.94 ± 0.08 ^a	7.69 ± 0.20 ^c	12.67 ± 1.20 ^f
pH 4	67.79 ± 1.44 ^e	21.38 ± 0.62 ^b	6.42 ± 0.19 ^c	41.45 ± 0.49 ^e
pH 5	79.56 ± 0.31 ^c	8.48 ± 0.92 ^c	3.9 ± 0.09 ^d	54.60 ± 1.9 ^c
pH 6	82.19 ± 0.28 ^b	1.89 ± 0.12 ^c	2.9 ± 0.15 ^c	59.05 ± 1.39 ^b
pH 7	72.70 ± 1.08 ^d	1.27 ± 0.02 ^c	-1.49 ± 0.49 ^f	48.98 ± 2.20 ^d
pH 10	78.42 ± 0.74 ^c	4.19 ± 0.10 ^d	10.15 ± 0.52 ^b	53.68 ± 1.26 ^c
pH 13	86.73 ± 0.48 ^a	0.42 ± 0.04 ^f	13.41 ± 0.50 ^a	63.61 ± 2.78 ^a

Values are given as means ± SD ($n = 3$). Different lowercase letters in the same column indicate significantly different values ($P < 0.05$).

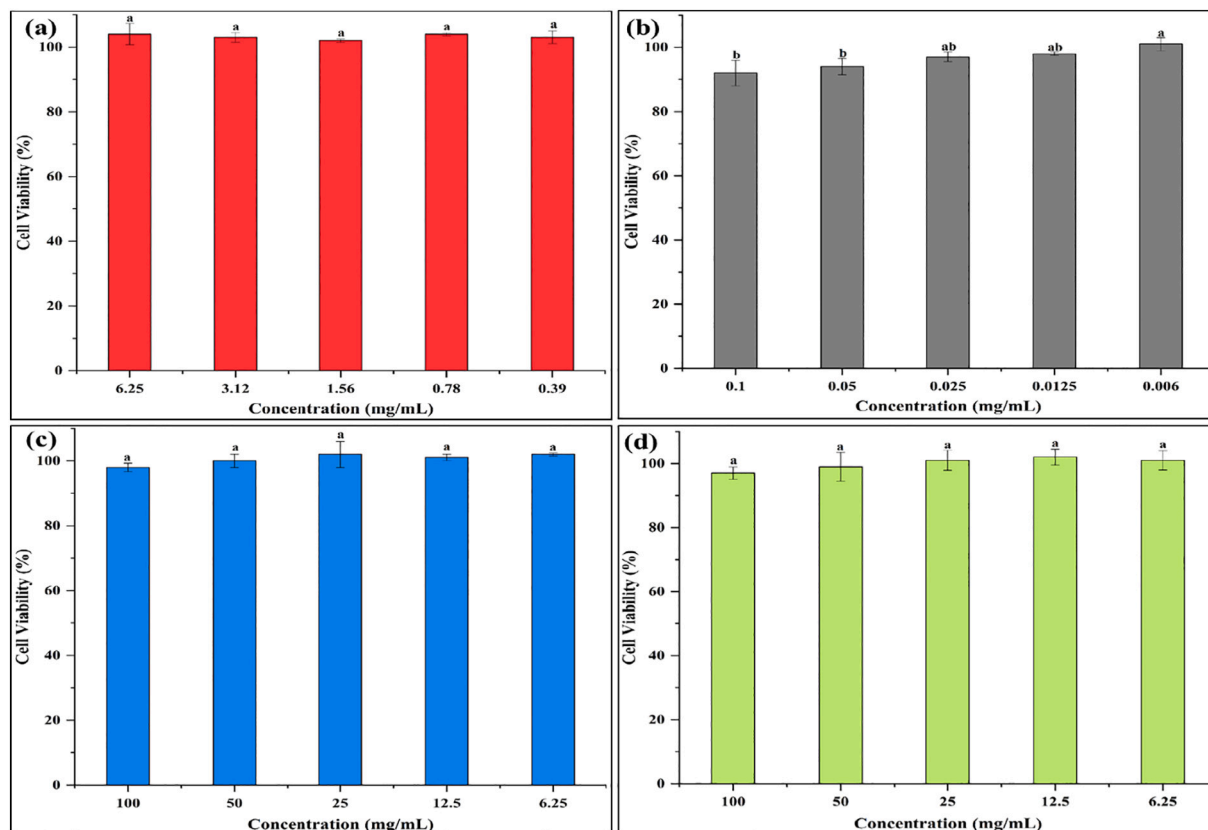


Fig. 5. Viability of WI-38 cells treated with ANT (a), MMT (b), PVA-HAS (c) and ANT/MMT/PVA-HAS (d) FFSs.

smart film in line with Yun, et al. [63].

3.2.7. Antioxidant and antimicrobial activity

The radical scavenging activity of prepared films were evaluated using DPPH assay (Table 2). ANT powder showed strong antioxidant activity with a low IC_{50} value of 1.92 mg/mL. IC_{50} value for ANT was lower than that reported by Wu, et al. [67] but tenfold higher than another report [68], due to differences in extraction conditions such as temperature, pH, and solvents [3]. PVA-HAS film showed the lowest scavenging activity of 2.80 % (Table 2), in agreement with Qin, et al. [69], which increased insignificantly ($P > 0.05$) after the addition of MMT. ANT conferred a strong antioxidant activity as demonstrated by high (63.51 %) scavenging activity of the smart film in agreement with other findings [20,63].

As shown in Table 2, PVA-HAS and MMT/PVA-HAS films had no antimicrobial activity against all the tested pathogenic strains [12,61]. On the other hand, the smart film showed significant antimicrobial efficacy (Fig. S2) against the studied strains, due to the high phenolic content of anthocyanins-rich hibiscus extract, which disrupts the cell membrane of bacteria and interferes with the bacterial metabolisms [20]. The effect was more pronounced against gram-positive than other gram-negative species, where the highest inhibition zone diameter was recorded against *S. aureus* (25 ± 1.0 mm), which could be related to the structural differences in cell wall composition between gram-positive and negative bacteria [31].

3.2.8. Colorimetric parameters and pH response

Effects of MMT and ANT on color parameters of films are summarized in Table 3. PVA-HAS film had the highest L^* (lightness) value of 94.26, which decreased upon increasing the concentration of MMT, together with an increase in the b^* value indicating the yellowness of films [70]. Among all films, the smart film showed the highest a^* (redness) and ΔE values as a result of ANT incorporation, and a low L^*

value (27.27) inferring an increased film opacity. In different pH solutions, the smart film exhibited obvious color changes, which was consistent with the measured color parameters (Table 3) and with those of ANT colors (Fig. 1a). Moreover, significant differences were observed in all color parameters with increasing the pH value, where, the L^* parameter significantly increased, resulting in light-colored films. The a^* value was high in acidic pH range (2–4) and decreased in alkaline pH, while the b^* value decreased and became negative at pH 7, tending to originate a blue color. At higher pH (10 and 13), the b^* value increased to 10.15 and 13.41, respectively, which contributed to the film appearing more yellowish. This color trend underlines the suitability of the halochromic smart film to be used as a pH indicator in food packaging. In addition, the smart film displayed a short response time in acidic pHs (2 and 4) of 2 and 6 min, respectively, while the color change in alkaline pHs was noted after 8–10 min (Fig. S3). This finding could be used as a rationale for estimating the time taken for the film to change color in the stored samples in real time.

3.2.9. Release study

Direct contact between synthesized packaging films with foods necessitate the determination of active ingredients release [20]. Fig. 4b showed that ANT release was faster in water than in 50 % and 95 % ethanol, owing to the low or insolubility of the film in ethanol [71]. The cumulative release of ANT in water, 50 % ethanol, and 95 % ethanol was 12.21, 6.51, and 2.48 %, respectively, after 270 min. The release of ANT depends on many factors, such as the type of food simulants, solubility, and diffusion rate of the ANT from the film into the solvent [72]. These results were in agreement with those obtained for ANT release from methylcellulose/chitosan and starch films [73,74].

3.2.10. Cytotoxicity evaluation

Cytotoxicity of packaging materials is an important safety parameter, especially for nanocomposites that may be a source of migratable

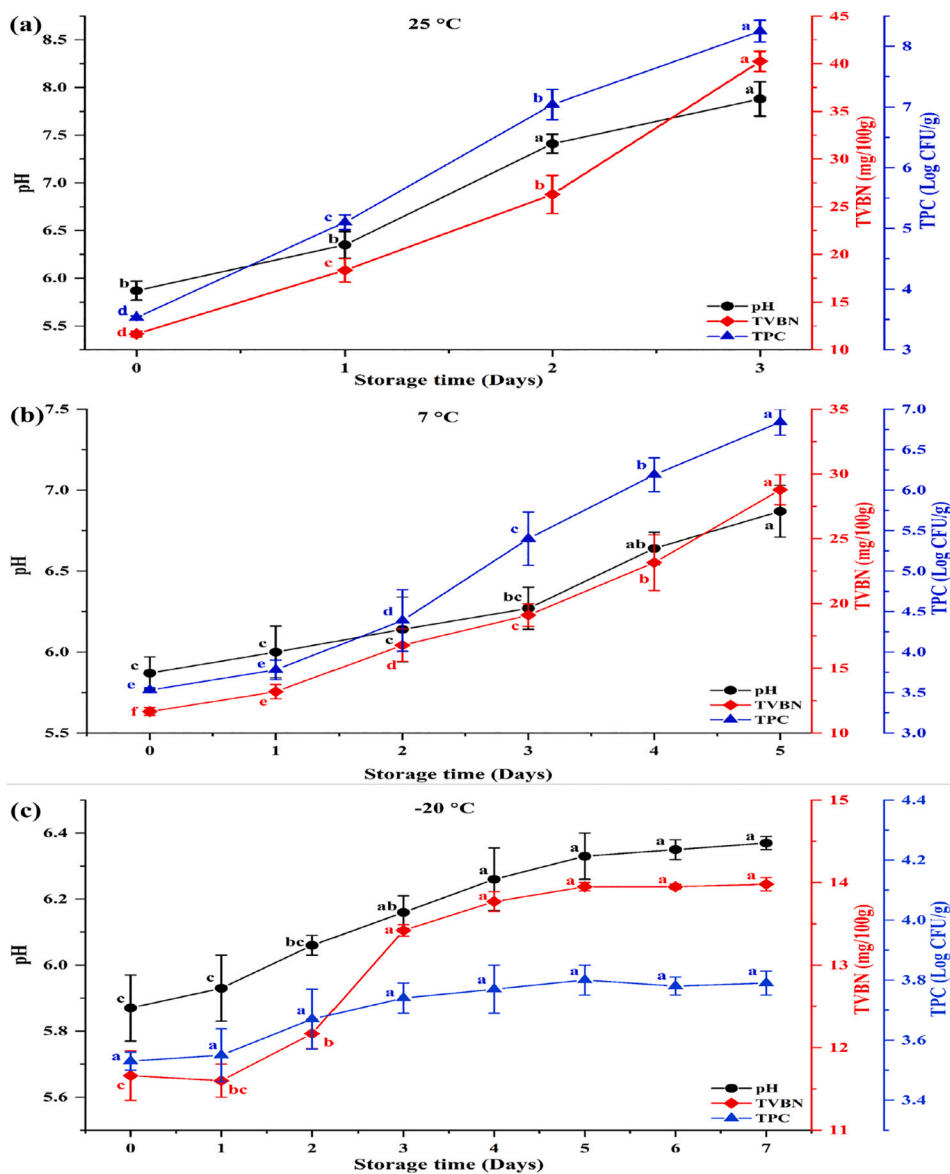


Fig. 6. pH, TVBN, and TPC values of chicken samples stored at 25 °C (a), 7 °C (b), and -20 °C (c).

components to food matrices. Cell viability of normal WI-38 cells after treatment with different concentrations of ANT, MMT and FFSs is presented in Fig. 5. ANT of roselle calyx was reported to possess selective toxicity against cancerous cell lines only [75,76]. Accordingly, ANT roselle calyx used in the study did not show any cytotoxic activity against WI-38 cells, with viability of 104% attained after treatment with 6.25 mg/mL. Similar evidence on normal skin fibroblasts and Vero kidney cells was reported [77,78]. WI-38 cell viability was not highly affected upon increasing the concentration of MMT (Fig. 5b). This may be due to the unmodified form of MMT K-10 that did not exert high cytotoxic activity [79]. Similar findings were recorded by García-Guzmán, et al. [80] against fibroblast NIH3T3 cells in presence of double the MMT concentration used in our study. For cells treated with PVA-HAS and ANT/MMT/PVA-HAS FFSs (Fig. 5c & d), no cytotoxic activity was recorded, where the cell viability ranged from 97 to 102% [81,82].

3.3. Chicken freshness monitoring

The smart film applicability to monitor chicken breast freshness was studied at three different temperatures. In this study, TPC, pH, and

TVBN were used being the most reliable indicators for evaluating chicken meat quality [1,17], coupled with observing the film color change throughout the storage period. As a rich source of proteins and other nutrients, chicken meat deteriorate due to microbial growth and enzymatic hydrolysis resulting in the formation of nitrogenous compounds such as amines and ammonia. Initially, fresh chicken samples had a pH value of 5.87 and a TVBN value of 11.66 mg/100 g, and the TPC was 3.53 log CFU/g. After 1 day of storage at 25 °C, the film's color changed from red to pink, with increasing the pH, TVBN, and TPC values to 6.40, 18.34 mg/100 g and 5.11 log CFU/g, respectively. At day 2, the pH increased to 7.41, TVBN to 26.29 mg/100 g, and the TPC to 7.04 log CFU/g (Fig. 6a), associated with remarkable color change of the smart film to light purple (Fig. S4). These previous values exceeded the acceptable limits set by the Egyptian organization of standardization for chicken meat quality (1090/2005) for pH (5.5–6.4), TVBN (20 mg/100 g), and TPC (6 log CFU/g) [83]. The color response of the film as a result of chicken deterioration can be easily perceived after one day of abusive storage even by inexpert consumers.

For samples stored at 7 °C, pH, TVBN, and TPC values exhibited a gradual increase over time and exceeded the acceptable limits on day 4 (Fig. 6b), with a visible change in film's color from red (days 1–2) to pink

(day 3), then light blue (day 4), and finally blue color on day 5 (Fig. S3). Our results fit with reports of Zhao, et al. [84] who determined the shelf life of chicken meat stored at 25 and 4 °C for 2 and 4–7 days, respectively. At –20 °C, there was no observed color change of films and pH, TVBN, and TPC values were below the safety standards throughout the 7 days storage period, possibly due to microbial growth inhibition at the freezing temperatures. The results of this study prove that the colorimetric pH indicator film developed (ANT/MMT/PVA-HAS) has a good color response to an amine-rich environment even after only one day, highlighting its efficiency to be potentially applied for monitoring of the freshness of meat products.

4. Conclusion

To the best of our knowledge, this is the first report on the fabrication of a halochromic smart and active film based on PVA and high amylose starch, reinforced with MMT and activated with ANT. Addition of MMT significantly increased TS, thermal stability, water resistance, color parameters and reduced the WVP of films. No significant changes in mechanical, barrier, or hydration properties were demonstrated by ANT incorporation into the optimal nanocomposite (MMT/PVA-HAS II), however, the smart film showed strong antioxidant, antibacterial and pH-responsive properties. FTIR, XRD and SEM analyses confirmed the interactions of film ingredients and their even distribution into the film matrix. MTT assay inferred the non-toxicity of the films' components using normal WI-38 cell lines. The work was extrapolated for the application of the novel film to monitor freshness of chicken breasts stored at different storage temperatures based on color response that can be perceived easily by consumers. The promising attributes warrant establishing the feasibility of larger scale film production to verify its efficiency for industrial applications. Investigating the film's response time in the stored food should be addressed in futures studies for increasing the consumers' confidence in food freshness and safety before consumption.

CRedit authorship contribution statement

Muhammed R. Sharaby: Writing – original draft, Visualization, Validation, Software, Methodology, Investigation, Funding acquisition, Formal analysis, Data curation, Conceptualization. **Emad A. Soliman:** Writing – review & editing, Validation, Supervision, Conceptualization. **Rowaida Khalil:** Writing – review & editing, Validation, Supervision, Resources, Funding acquisition, Conceptualization.

Declaration of competing interest

The authors declare the following financial interests/personal relationships which may be considered as potential competing interests: Rowaida Khalil reports financial support was provided by Academy for Scientific Research and Technology (ASRT). Rowaida Khalil reports financial support was provided by Partnership for Research and Innovation in the Mediterranean Area (PRIMA). Muhammed Sharaby reports financial support was provided by Egyptian Ministry of Higher Education.

Data availability

Data will be made available on request.

Acknowledgments

The authors acknowledge the Mission Sector-Ministry of Higher Education-Egypt (MOHE) for funding the Ph.D. scholarship of the first author at Egypt-Japan University of Science and Technology (E-JUST). This work was also supported by a project (Sustainable technologies and methodologies to improve quality and extend product shelf life in the

Mediterranean agro-food supply chain “FRUALGAE”) in the period July 2020–2023, funded by Partnership for Research and Innovation in the Mediterranean Area (PRIMA) and Academy for Scientific Research and Technology (ASRT)-Egypt.

Appendix A. Supplementary data

Supplementary data to this article can be found online at <https://doi.org/10.1016/j.ijbiomac.2023.128910>.

References

- [1] S.B.H. Hashim, H.E. Tahir, L. Lui, J. Zhang, X. Zhai, A.A. Mahdi, N.A. Ibrahim, G. K. Mahunu, M.M. Hassan, Z. Xiaobo, S. Jiyong, Smart films of carbohydrate-based/sunflower wax/purple Chinese cabbage anthocyanins: a biomarker of chicken freshness, *Food Chem.* 399 (2023), 133824.
- [2] D. Liu, C. Zhang, Y. Pu, S. Chen, H. Li, Y. Zhong, Novel colorimetric films based on polyvinyl alcohol/sodium carboxymethyl cellulose doped with anthocyanins and betacyanins to monitor pork freshness, *Food Chem.* 404 (2023), 134426.
- [3] N. Oladzadabbasabadi, A. Mohammadi Nafchi, M. Ghasemlou, F. Ariffin, Z. Singh, A.A. Al-Hassan, Natural anthocyanins: Sources, extraction, characterization, and suitability for smart packaging, *Food Packag. Shelf Life* 33 (2022).
- [4] M. Lu, Q. Zhou, H. Yu, X. Chen, G. Yuan, Colorimetric indicator based on chitosan/gelatin with nano-ZnO and black peanut seed coat anthocyanins for application in intelligent packaging, *Food Res. Int.* 160 (2022).
- [5] A. Sadi, H. Ferfera-Harrar, Cross-linked CMC/Gelatin bio-nanocomposite films with organoclay, red cabbage anthocyanins and pistacia leaves extract as active intelligent food packaging: colorimetric pH indication, antimicrobial/antioxidant properties, and shrimp spoilage tests, *Int. J. Biol. Macromol.* 242 (2023), 124964.
- [6] L. García-Guzmán, G. Cabrera-Barjas, C.G. Soria-Hernández, J. Castaño, A. Y. Guadarrama-Lezama, S. Rodríguez Llamazares, Progress in starch-based materials for food packaging applications, *Polysaccharides* 3 (1) (2022) 136–177.
- [7] B. Debnath, P. Duarah, D. Haldar, M.K. Purkait, Improving the properties of corn starch films for application as packaging material via reinforcement with microcrystalline cellulose synthesized from elephant grass, *Food Packag. Shelf Life* 34 (2022).
- [8] Y.-H. Yun, S.-D. Yoon, Effect of amylose contents of starches on physical properties and biodegradability of starch/PVA-blended films, *Polym. Bull.* 64 (6) (2009) 553–568.
- [9] M. Li, P. Liu, W. Zou, L. Yu, F. Xie, H. Pu, H. Liu, L. Chen, Extrusion processing and characterization of edible starch films with different amylose contents, *J. Food Eng.* 106 (1) (2011) 95–101.
- [10] S. Kang, H. Wang, L. Xia, M. Chen, L. Li, J. Cheng, X. Li, S. Jiang, Colorimetric film based on polyvinyl alcohol/okra mucilage polysaccharide incorporated with rose anthocyanins for shrimp freshness monitoring, *Carbohydr. Polym.* 229 (2020), 115402.
- [11] P.K. Panda, K. Sadeghi, J. Seo, Recent advances in poly (vinyl alcohol)/natural polymer based films for food packaging applications: a review, *Food Packag. Shelf Life* 33 (2022).
- [12] D. Liu, S. Dang, L. Zhang, K. Munsop, X. Li, Corn starch/polyvinyl alcohol based films incorporated with curcumin-loaded Pickering emulsion for application in intelligent packaging, *Int. J. Biol. Macromol.* 188 (2021) 974–982.
- [13] G. Yurong, L. Dapeng, Preparation and characterization of corn starch/PVA/glycerol composite films incorporated with ϵ -polylysine as a novel antimicrobial packaging material, *e-Polymers* 20 (1) (2020) 154–161.
- [14] S. Tunç, O. Duman, Preparation and characterization of biodegradable methyl cellulose/montmorillonite nanocomposite films, *Appl. Clay Sci.* 48 (3) (2010) 414–424.
- [15] H. Almasi, B. Ghanbarzadeh, A.A. Entezami, Physicochemical properties of starch-CMC-nanoclay biodegradable films, *Int. J. Biol. Macromol.* 46 (1) (2010) 1–5.
- [16] Y.Y. Qin, Z.H. Zhang, L. Li, M.L. Yuan, J. Fan, T.R. Zhao, Physio-mechanical properties of an active chitosan film incorporated with montmorillonite and natural antioxidants extracted from pomegranate rind, *J. Food Sci. Technol.* 52 (3) (2015) 1471–1479.
- [17] A.N. Ahmad, S. Abdullah Lim, N. Navaranjan, Development of sago (*Metroxylon sagu*)-based colorimetric indicator incorporated with butterfly pea (*Clitoria ternatea*) anthocyanin for intelligent food packaging, *J. Food Saf.* 40 (4) (2020).
- [18] X. Lin, N. Li, Q. Xiao, Y. Guo, J. Wei, T. Jiao, Q. Chen, Q. Chen, X. Chen, Polyvinyl alcohol/starch-based film incorporated with grape skin anthocyanins and metal-organic framework crystals for colorimetric monitoring of pork freshness, *Food Chem.* 395 (2022), 133613.
- [19] L. Liu, W. Wu, L. Zheng, J. Yu, P. Sun, P. Shao, Intelligent packaging films incorporated with anthocyanins-loaded ovalbumin-carboxymethyl cellulose nanocomplexes for food freshness monitoring, *Food Chem.* 387 (2022), 132908.
- [20] M. Alizadeh-Sani, M. Tavassoli, S.A. Salim, M. Azizi-lalabadi, D.J. McClements, Development of green halochromic smart and active packaging materials: TiO₂ nanoparticle- and anthocyanin-loaded gelatin/ κ -carrageenan films, *Food Hydrocoll.* 124 (2022).
- [21] L. Meng, J. Zhu, Y. Ma, X. Sun, D. Li, L. Li, H. Bai, G. Xin, X. Meng, Composition and antioxidant activity of anthocyanins from *Aronia melanocarpa* cultivated in Haicheng, Liaoning, China, *Food Biosci.* 30 (2019).

- [22] H. Yong, X. Wang, X. Zhang, Y. Liu, Y. Qin, J. Liu, Effects of anthocyanin-rich purple and black eggplant extracts on the physical, antioxidant and pH-sensitive properties of chitosan film, *Food Hydrocoll.* 94 (2019) 93–104.
- [23] Z.W. Abdullah, Y. Dong, N. Han, S. Liu, Water and gas barrier properties of polyvinyl alcohol (PVA)/starch (ST)/glycerol (GL)/halloysite nanotube (HNT) bionanocomposite films: experimental characterisation and modelling approach, *Compos B: Eng.* 174 (2019).
- [24] C.L. Luchese, N. Sperotto, J.C. Spada, I.C. Tessaro, Effect of blueberry agro-industrial waste addition to corn starch-based films for the production of a pH-indicator film, *Int. J. Biol. Macromol.* 104 (2017) 11–18.
- [25] ASTM, Standard Test Methods for Tensile Properties of Thin Plastic Sheeting D882-02 Annual Book of ASTM Standards, American Society for Testing and Materials, Philadelphia, PA, USA, 2007.
- [26] M. Aitboulahsen, H. Chairi, A. Laglaoui, S. Zantar, A. Abdelhay, M. Bakkali, M. H. Zerrouk, Gelatin/pectin-based film incorporated with essential oils: functional characteristics and shelf life extension of tilapia fillets under refrigeration, *J. Food Saf.* 40 (3) (2020).
- [27] ASTM, Standard Test Methods for Water Vapor Transmission of Materials E96 – 00, Annual Book of ASTM, American Society for Testing and Materials, Philadelphia, PA, USA, 2000.
- [28] R.K.S. Khalil, M.R. Sharaby, D.S. Abdelrahim, Novel active edible food packaging films based entirely on citrus peel wastes, *Food Hydrocoll.* 134 (2023).
- [29] Y. Li, K. Wu, B. Wang, X. Li, Colorimetric indicator based on purple tomato anthocyanins and chitosan for application in intelligent packaging, *Int. J. Biol. Macromol.* 174 (2021) 370–376.
- [30] J. Liu, H. Wang, M. Guo, L. Li, M. Chen, S. Jiang, X. Li, S. Jiang, Extract from *Lycium ruthenicum* Murr. Incorporating κ-carrageenan colorimetric film with a wide pH-sensing range for food freshness monitoring, *Food Hydrocoll.* 94 (2019) 1–10.
- [31] M.R. Sharaby, E.A. Soliman, A.B. Abdel-Rahman, A. Osman, R. Khalil, Novel pectin-based nanocomposite film for active food packaging applications, *Sci. Rep.* 12 (1) (2022), 20673.
- [32] Y. Cao, W. Gu, J. Zhang, Y. Chu, X. Ye, Y. Hu, J. Chen, Effects of chitosan, aqueous extract of ginger, onion and garlic on quality and shelf life of stewed-pork during refrigerated storage, *Food Chem.* 141 (3) (2013) 1655–1660.
- [33] J. Huang, J. Liu, M. Chen, Q. Yao, Y. Hu, Immobilization of roselle anthocyanins into polyvinyl alcohol/hydroxypropyl methylcellulose film matrix: study on the interaction behavior and mechanism for better shrimp freshness monitoring, *Int. J. Biol. Macromol.* 184 (2021) 666–677.
- [34] S.A. Amer, H.S. Al-Khalaifah, A. Gouda, A. Osman, N.I.A. Goda, H.A. Mohammed, M.I.M. Darwish, A.M. Hassan, S.K.A. Mohamed, Potential effects of anthocyanin-rich roselle (*Hibiscus sabdariffa* L.) extract on the growth, intestinal histomorphology, blood biochemical parameters, and the immune status of broiler chickens, *Antioxidants (Basel)* 11 (3) (2022).
- [35] K.H. Erna, W.X.L. Felicia, J.M. Vonnice, K. Rovina, K.W. Yin, M.N. Nur'Aqilah, Synthesis and physicochemical characterization of polymer film-based anthocyanin and starch, *Biosensors (Basel)* 12 (4) (2022).
- [36] X. Zhai, J. Shi, X. Zou, S. Wang, C. Jiang, J. Zhang, X. Huang, W. Zhang, M. Holmes, Novel colorimetric films based on starch/polyvinyl alcohol incorporated with roselle anthocyanins for fish freshness monitoring, *Food Hydrocoll.* 69 (2017) 308–317.
- [37] P. Zeng, X. Chen, Y.R. Qin, Y.H. Zhang, X.P. Wang, J.Y. Wang, Z.X. Ning, Q. J. Ruan, Y.S. Zhang, Preparation and characterization of a novel colorimetric indicator film based on gelatin/polyvinyl alcohol incorporating mulberry anthocyanin extracts for monitoring fish freshness, *Food Res. Int.* 126 (2019), 108604.
- [38] M. Vishnuvarthanan, M.F. Al Shahidah, N.R. Gobika, B. Priyadarshini, B. Basika, Effect of alumina silicate (MMT K10) nanoclay on adhesion and barrier properties of corn starch-based bioadhesive, *Silicon* 13 (12) (2020) 4315–4322.
- [39] N. Tahari, P.L. de Hoyos-Martinez, N. Izaguirre, N. Houwaida, M. Abderrabba, S. Ayadi, J. Labidi, Preparation of chitosan/tannin and montmorillonite films as adsorbents for Methyl Orange dye removal, *Int. J. Biol. Macromol.* 210 (2022) 94–106.
- [40] S. Kang, H. Wang, M. Guo, L. Zhang, M. Chen, S. Jiang, X. Li, S. Jiang, Ethylene-vinyl alcohol copolymer-montmorillonite multilayer barrier film coated with mulberry anthocyanin for freshness monitoring, *J. Agric. Food Chem.* 66 (50) (2018) 13268–13276.
- [41] R. Tanwar, V. Gupta, P. Kumar, A. Kumar, S. Singh, K.K. Gaikwad, Development and characterization of PVA-starch incorporated with coconut shell extract and sepiolite clay as an antioxidant film for active food packaging applications, *Int. J. Biol. Macromol.* 185 (2021) 451–461.
- [42] R. Kong, J. Wang, M. Cheng, W. Lu, M. Chen, R. Zhang, X. Wang, Development and characterization of corn starch/PVA active films incorporated with carvacrol nanoemulsions, *Int. J. Biol. Macromol.* 164 (2020) 1631–1639.
- [43] D.S. Naidu, M.J. John, Effect of clay nanofillers on the mechanical and water vapor permeability properties of xylan-alginate films, *Polymers (Basel)* 12 (10) (2020).
- [44] O. Alekseeva, A. Noskov, E. Grishina, L. Ramenskaya, N. Kudryakova, V. Ivanov, A. Agafonov, Structural and thermal properties of montmorillonite/ionic liquid composites, *Materials (Basel)* 12 (16) (2019).
- [45] M.U. Trivedi, C.K. Patlolla, N.M. Misra, M.K. Pandey, Cucurbit[6]uril glued magnetic clay hybrid as a catalyst for nitrophenol reduction, *Catal. Lett.* 149 (9) (2019) 2355–2367.
- [46] A. Hassani, A. Khataee, S. Karaca, C. Karaca, P. Gholami, Sonocatalytic degradation of ciprofloxacin using synthesized TiO₂ nanoparticles on montmorillonite, *Ultrason. Sonochem.* 35 (2017) 251–262.
- [47] E.A. Soliman, M. Furuta, Influence of phase behavior and miscibility on mechanical, thermal and micro-structure of soluble starch-gelatin thermoplastic biodegradable blend films, *Food Nutr. Sci.* 05 (11) (2014) 1040–1055.
- [48] N. Hammoudi, H. Ziani Cherif, F. Borsali, K. Benmansour, A. Meghezzi, Preparation of active antimicrobial and antifungal alginate-montmorillonite/lemon essential oil nanocomposite films, *Mater. Technol.* 35 (7) (2019) 383–394.
- [49] M. Alboofetileh, M. Rezaei, H. Hosseini, M. Abdollahi, Effect of montmorillonite clay and biopolymer concentration on the physical and mechanical properties of alginate nanocomposite films, *J. Food Eng.* 117 (1) (2013) 26–33.
- [50] B. Rohini, S. Padma Ishwarya, R. Rajasekharan, A.K. VijayaKumar, *Ocimum basilicum* seed mucilage reinforced with montmorillonite for preparation of bionanocomposite film for food packaging applications, *Polym. Test.* 87 (2020).
- [51] S. Pourjavaher, H. Almasi, S. Meshkini, S. Pirs, E. Parandi, Development of a colorimetric pH indicator based on bacterial cellulose nanofibers and red cabbage (*Brassica oleracea*) extract, *Carbohydr. Polym.* 156 (2017) 193–201.
- [52] Z.W. Abdullah, Y. Dong, Preparation and characterisation of poly(vinyl) alcohol (PVA)/starch (ST)/halloysite nanotube (HNT) nanocomposite films as renewable materials, *J. Mater. Sci.* 53 (5) (2017) 3455–3469.
- [53] B. Liu, H. Xu, H. Zhao, W. Liu, L. Zhao, Y. Li, Preparation and characterization of intelligent starch/PVA films for simultaneous colorimetric indication and antimicrobial activity for food packaging applications, *Carbohydr. Polym.* 157 (2017) 842–849.
- [54] S.D. Sadhu, A. Soni, S.G. Varmani, M. Garg, Preparation of starch-poly vinyl alcohol (PVA) blend using potato and study of its mechanical properties, *Int. J. Pharm. Sci. Invent.* 3 (3) (2014) 33–37.
- [55] H.L. Calambas, A. Fonseca, D. Adames, Y. Aguirre-Loredo, C. Caicedo, Physical-mechanical behavior and water-barrier properties of biopolymers-clay nanocomposites, *Molecules* 26 (21) (2021).
- [56] R. Arjmandi, A. Hassan, S.J. Eichhorn, M.K. Mohamad Haafiz, Z. Zakaria, F. A. Tanjung, Enhanced ductility and tensile properties of hybrid montmorillonite/cellulose nanowhiskers reinforced poly(lactic acid) nanocomposites, *J. Mater. Sci.* 50 (8) (2015) 3118–3130.
- [57] K. Zhang, T.S. Huang, H. Yan, X. Hu, T. Ren, Novel pH-sensitive films based on starch/polyvinyl alcohol and food anthocyanins as a visual indicator of shrimp deterioration, *Int. J. Biol. Macromol.* 145 (2020) 768–776.
- [58] K.K. Gaikwad, S. Singh, Y.S. Lee, A pyrogallol-coated modified LDPE film as an oxygen scavenging film for active packaging materials, *Prog. Org. Coat.* 111 (2017) 186–195.
- [59] T.R. Crompton, Physical Testing of Plastics, Smithers Rapra Technology, USA, 2012.
- [60] Z. Wu, J. Wu, T. Peng, Y. Li, D. Lin, B. Xing, C. Li, Y. Yang, L. Yang, L. Zhang, R. Ma, W. Wu, X. Lv, J. Dai, G. Han, Preparation and application of starch/polyvinyl alcohol/citric acid ternary blend antimicrobial functional food packaging films, *Polymers (Basel)* 9 (3) (2017).
- [61] E.M.C. Alexandre, R.V. Lourenço, A.M.Q.B. Bittante, I.C.F. Moraes, P.J.d.A. Sobral, Gelatin-based films reinforced with montmorillonite and activated with nanoemulsion of ginger essential oil for food packaging applications, *Food Packag. Shelf Life* 10 (2016) 87–96.
- [62] M. Koosha, S. Hamed, Intelligent Chitosan/PVA nanocomposite films containing black carrot anthocyanin and bentonite nanoclays with improved mechanical, thermal and antibacterial properties, *Prog. Org. Coat.* 127 (2019) 338–347.
- [63] D. Yun, H. Cai, Y. Liu, L. Xiao, J. Song, J. Liu, Development of active and intelligent films based on cassava starch and Chinese bayberry (*Myrica rubra* Sieb. et Zucc.) anthocyanins, *RSC Adv.* 9 (53) (2019) 30905–30916.
- [64] Y. Kasirga, A. Oral, C. Caner, Preparation and characterization of chitosan/montmorillonite-K10 nanocomposites films for food packaging applications, *Polym. Compos.* 33 (11) (2012) 1874–1882.
- [65] C. Yu, Y. Ke, Q. Deng, S. Lu, J. Ji, X. Hu, Y. Zhao, Synthesis and characterization of polystyrene-montmorillonite nanocomposite particles using an anionic-surfactant-modified clay and their friction performance, *Appl. Sci.* 8 (6) (2018).
- [66] B. Pantelic, M. Ponjavic, V. Jankovic, I. Aleksic, S. Stevanovic, J. Murray, M. B. Fournet, J. Nikodinovic-Runic, Upcycling biodegradable PVA/starch film to a bacterial biopigment and biopolymer, *Polymers (Basel)* 13 (21) (2021).
- [67] H.Y. Wu, K.M. Yang, P.Y. Chiang, Roselle anthocyanins: antioxidant properties and stability to heat and pH, *Molecules* 23 (6) (2018).
- [68] W. Widowati, A.P. Rani, R.A. Hamzah, S. Arumwardana, E. Afifah, H.S.W. Kusuma, D.D. Rihibiha, H. Nufus, A. Amalia, Antioxidant and antiaging assays of *Hibiscus sabdariffa* extract and its compounds, *Nat. Prod. Sci.* 23 (3) (2017).
- [69] Y. Qin, Y. Liu, X. Zhang, J. Liu, Development of active and intelligent packaging by incorporating betalains from red pitaya (*Hylocereus polyrhizus*) peel into starch/polyvinyl alcohol films, *Food Hydrocoll.* 100 (2020).
- [70] R. Sothornvit, S.-I. Hong, D.J. An, J.-W. Rhim, Effect of clay content on the physical and antimicrobial properties of whey protein isolate/organo-clay composite films, *LWT Food Sci. Technol.* 43 (2) (2010) 279–284.
- [71] M. Cheng, X. Yan, Y. Cui, M. Han, Y. Wang, J. Wang, R. Zhang, X. Wang, Characterization and release kinetics study of active packaging films based on modified starch and red cabbage anthocyanin extract, *Polymers (Basel)* 14 (6) (2022).
- [72] P. Ezati, J.-W. Rhim, pH-responsive chitosan-based film incorporated with alizarin for intelligent packaging applications, *Food Hydrocoll.* 102 (2020).
- [73] M. Sohany, I. Tawakkal, S.H. Ariffin, N. Shah, Y.A. Yusof, Characterization of anthocyanin associated purple sweet potato starch and peel-based pH indicator films, *Foods* 10 (9) (2021).
- [74] M. Alizadeh-Sani, M. Tavassoli, E. Mohammadian, A. Ehsani, G.J. Khaniki, R. Priyadarshi, J.W. Rhim, pH-responsive color indicator films based on

- methylcellulose/chitosan nanofiber and barberry anthocyanins for real-time monitoring of meat freshness, *Int. J. Biol. Macromol.* 166 (2021) 741–750.
- [75] S. Khaghani, F. Razi, M.M. Yajloo, M. Paknejad, A. Shariftabrzi, P. Pasalar, Selective cytotoxicity and apoptogenic activity of *Hibiscus sabdariffa* aqueous extract against MCF-7 human breast cancer cell line, *J. Cancer Ther.* 02 (03) (2011) 394–400.
- [76] L.G. Maciel, M.A.V. do Carmo, L. Azevedo, H. Daguer, L. Molognoni, M.M. de Almeida, D. Granato, N.D. Rosso, *Hibiscus sabdariffa* anthocyanins-rich extract: chemical stability, in vitro antioxidant and antiproliferative activities, *Food Chem. Toxicol.* 113 (2018) 187–197.
- [77] N.H.I. Bakar, T.C. Lee, A.R. Mohd-Hairul, R.A. Raus, D.F. Basri, N.S. Adzahar, Real-time cytotoxicity assay of water extracts *Hibiscus rosa-sinensis*, *Mater. Sci. Forum* 981 (2020) 265–270.
- [78] D. Wang, M. Nagata, M. Matsumoto, Y. Amen, D. Wang, K. Shimizu, Potential of *Hibiscus sabdariffa* L. and Hibiscus acid to reverse skin aging, *Molecules* 27 (18) (2022).
- [79] T.J. Gutierrez, I.E. Leon, A.G. Ponce, V.A. Alvarez, Active and pH-sensitive nanopackaging based on polymeric anthocyanin/natural or organo-modified montmorillonite blends: characterization and assessment of cytotoxicity, *Polymers (Basel)* 14 (22) (2022).
- [80] P. García-Guzmán, L. Medina-Torres, F. Calderas, M.J. Bernad-Bernad, J. Gracia-Mora, X. Marcos, J. Correa-Basurto, D.M. Núñez-Ramírez, O. Manero, Rheological mucoadhesion and cytotoxicity of montmorillonite clay mineral/hybrid microparticles biocomposite, *Appl. Clay Sci.* 180 (2019).
- [81] S. Lee, M. Zhang, G. Wang, W. Meng, X. Zhang, D. Wang, Y. Zhou, Z. Wang, Characterization of polyvinyl alcohol/starch composite films incorporated with p-coumaric acid modified chitosan and chitosan nanoparticles: a comparative study, *Carbohydr. Polym.* 262 (2021), 117930.
- [82] N. Gürlür, S. Paşa, Ö. Erdoğan, O. Cevik, Physicochemical properties for food packaging and toxicity behaviors against healthy cells of environmentally friendly biocompatible starch/citric acid/polyvinyl alcohol biocomposite films, *Starch - Stärke* 75 (2021) 2100074.
- [83] M.A. Hussein, W.R. El-Ghareeb, M.A.F. Nasr, The effect of rosemary extract and lactic acid on the quality of refrigerated broiler fillets, *J. Food Sci. Technol.* 55 (12) (2018) 5025–5034.
- [84] M. Zhao, M. Nuerjiang, X. Bai, J. Feng, B. Kong, F. Sun, Y. Li, X. Xia, Monitoring dynamic changes in chicken freshness at 4 degrees C and 25 degrees C using pH-sensitive intelligent films based on sodium alginate and purple sweet potato peel extracts, *Int. J. Biol. Macromol.* 216 (2022) 361–373.


ARTICLES FOR FACULTY MEMBERS

ROSELLE (HIBISCUS SABDARIFFA) ANTHOCYANIN USE IN MONITORING MEAT FRESHNESS

Title/Author	Inkjet-printed pH-sensitive QR code labels for real-time food freshness monitoring / Xu, Y., Liu, Z., Liu, R., Luo, M., Wang, Q., Cao, L., & Ye, S.
Source	<i>Journal of Materials Science</i> Volume 56 Issue 33 (2021) Pages 18453–18462 https://doi.org/10.1007/s10853-021-06477-x (Database: Springer Nature)



Inkjet-printed pH-sensitive QR code labels for real-time food freshness monitoring

Yuan Xu¹, Zhangming Liu¹, Rui Liu¹, Mengxue Luo¹, Qi Wang¹, Liqin Cao^{1,*}, and Shuangli Ye^{1,*} 

¹ School of Printing and Packaging, Wuhan University, Wuhan 430072, Hubei Province, People's Republic of China

Received: 20 May 2021

Accepted: 24 August 2021

Published online:

7 September 2021

© The Author(s), under exclusive licence to Springer Science+Business Media, LLC, part of Springer Nature 2021

ABSTRACT

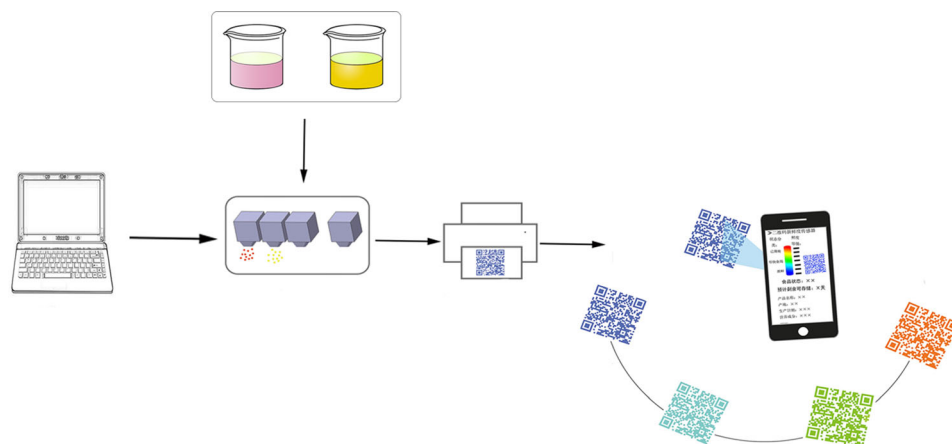
In this work, dynamic pH-sensitive quick response code (QR code) labels have been successfully fabricated by inkjet-printing technology. Inks with roselle anthocyanins and curcumin natural dye are prepared, respectively. The rheological property, contact angle, and surface tension of the prepared inks are tested. Both inks show good printability with Newtonian fluid property. The QR code labels with different ratios of inks are fabricated, in which the ink ratio is controlled by automatic computer program. It can be seen that the color of all printed QR code labels is sensitive to the concentrations of ammonia solutions, demonstrating that the pH-sensitive QR code labels are achieved. The ammonia-dependent color difference is analyzed by $L^*a^*b^*$ digital images. It can be found that the color difference strongly depends on the ink ratio, which suggests that the QR code labels with different ink ratios can be applied for diverse food freshness monitoring in real time. Therefore, in future, combined with the QR code application program (QR code APP) of intelligent devices, the developed QR code labels can be used as data carrier and freshness sensor as well, which provides a convenient method to get comprehensive food information, including freshness, expected storage time, date and identification of product, etc.

Handling Editor: Maude Jimenez.

Address correspondence to E-mail: clq@whu.edu.cn; slye@whu.edu.cn

<https://doi.org/10.1007/s10853-021-06477-x>

GRAPHICAL ABSTRACT



Introduction

As a key issue in the food industry, ensuring the quality and safety of foods is of utmost importance [1, 2]. Currently, consumers generally evaluate the freshness of foods by the “Best Before” or “Expiry date” on the package. However, if the storage or transportation environment could not meet the requirements, it may cause the “Best Before” or “Expiry date” to be of little practical value [3]. Consequently, based on these dates, food waste [4, 5] or safety problems [6] can be produced. Therefore, the real-time assessing of freshness information has to be concerned. In recent years, extensive efforts have been taken to estimate the freshness of foods, such as electronic nose [7], near-infrared spectroscopy [8], liquid chromatography [9], freshness indicator film/arrays [10–14], and metal–organic framework (MOF) [15]. Nevertheless, there are some disadvantages with these approaches. For example, high-cost equipment, complicated preparation process, and the inability to get freshness information conveniently can be the problems to consumers.

The pH-sensitive colorimetric indicator presents distinct color change by interacted with compounds (e.g., CO_2 , total volatile basic nitrogen (TVB-N), peroxide, aldehydes) produced by food spoilage [16–19]. TVB-N caused by protein destruction is mainly composed of alkaline gases, including ammonia

(NH_3), trimethylamine ($\text{C}_3\text{H}_9\text{N}$), and dimethylamine ($\text{C}_2\text{H}_7\text{N}$) [18, 20, 21], which has a great influence on the pH value of headspace atmosphere of package. Therefore, visual colorimetric pH indicator has been prepared for nondestructively detecting the freshness of food. On the other hand, due to the development of intelligent packaging, quick response (QR) code, as a data carrier has been studied [22], especially in the field of traceability [23–25], anti-counterfeiting [26–28], and sensing [29–32]. Compared with one-dimensional bar code, QR code has advantages of high information storage capacity, diverse coding language (numeric data, alphanumeric data, 8-bit byte data, and Kanji characters), in-plane omnidirectional identification and the ability to correct errors in the damage zones [23, 26, 33, 34]. During the process of transportation, sales and storage, the static information can be acquired by scanning the QR code on the package, including the production date, shelf life, and other information of the food. With the improvement of people’s living standards, it’s very critical to acquire the real-time quality of foods (especially for the food which has to be stored under certain conditions) [35]. Therefore, it is particularly important to develop a real-time, simple, low-cost, reliable, and non-destructive detection method or technology to obtain the food freshness.

In this study, novel QR code labels with tuned color by the ammonia concentration have been

explored, which can offer a dual function of real-time freshness monitoring and static information storage of packaged foods. Inks with roselle anthocyanins and curcumin natural dye are applied for the designed QR code labels. The pH sensitivity of roselle anthocyanins and curcumin and the printability of prepared inks are investigated. The ink ratio-dependent color differences of QR code labels to ammonia are demonstrated as well. The developed colorimetric QR code labels can store both static information and dynamic information, which significantly enhances the functions of QR code labels in the field of Internet of Things.

Materials and methods

Materials

Roselles were purchased from a farm in Jiangxi Province, China. Curcumin, ethanol, disodium hydrogen phosphate dodecahydrate ($\text{Na}_2\text{HPO}_4 \cdot 12\text{H}_2\text{O}$), citric acid monohydrate ($\text{C}_6\text{H}_8\text{O}_7 \cdot \text{H}_2\text{O}$), sodium carbonate (Na_2CO_3), sodium bicarbonate (NaHCO_3), and ammonia were all purchased from Sinopharm Chemical Reagent Co., Ltd. All materials were of analytical quality and used directly after purchase.

Ink preparation

The fabrication procedure of pH-sensitive QR code labels is presented in Fig. 1. The preparation process of QR code labels mainly includes roselle anthocyanins extraction, ink preparation, and label printing. Firstly, roselle anthocyanins were extracted by the method of Chen et al. [36] with a slight modification. Fresh roselles were dried in an electric thermostatic drying oven at 40–60 °C and then crushed and sieved to get roselle powders. 1 g roselle powder was added to 20 mL 70% (v/v) ethanol aqueous solution and extracted for 101 min with a constant temperature water bath at 54 °C. Then, the centrifugation (9000 rmin^{-1} , 20 min) process was performed, and the supernatant was concentrated by a rotary evaporator (RE-52AAA, Shanghai Jiapeng Technology Co., Ltd., China) at 40 °C to remove the solvent. After that, the solution was freeze-dried, and the roselle anthocyanins were obtained. Secondly, roselle anthocyanins were dissolved in 50% (v/v) ethanol aqueous solution to prepare 30 gL^{-1} roselle anthocyanins solution and curcumin in ethanol to prepare 0.3 gL^{-1} curcumin solution, respectively. In the meanwhile, 5% (w/w) glycerin was added as well. Two kinds of natural dye inks were achieved with ultrasonic stirring, respectively, as shown in Fig. 1a.

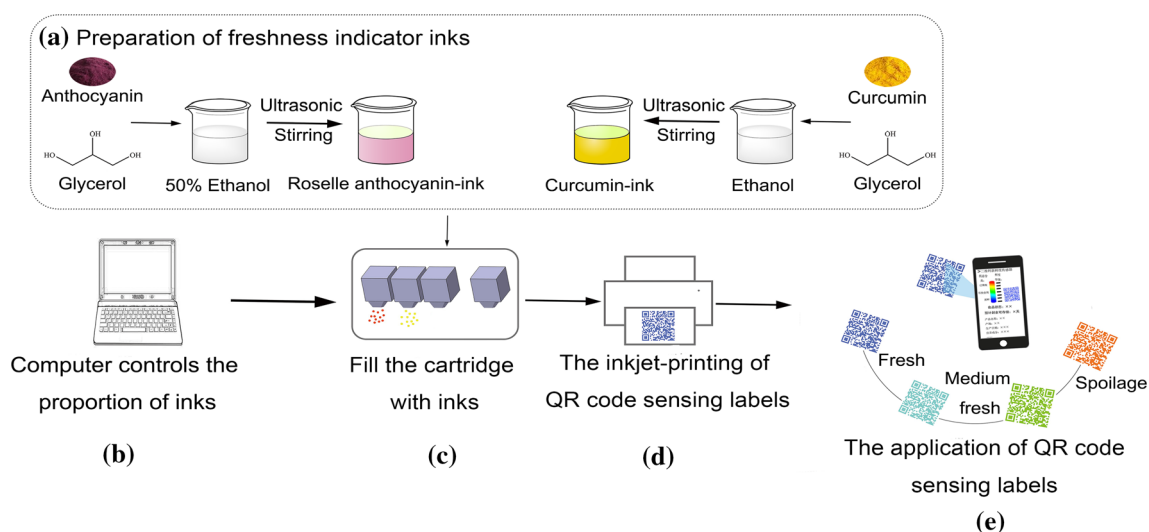


Figure 1 A schematic representation of the fabrication procedure for the pH-sensitive QR code labels. Preparation procedure of roselle anthocyanins and curcumin inks, respectively (a), QR code labels were fabricated by inkjet printing with controlled ink ratio

(b–d), comprehensive food information including real-time freshness is acquired by QR code application program (QR code APP) (e).

Fabrication of QR code labels

For QR code labels fabrication, a thermal inkjet printer (HP DeskJet2628, Hewlett-Packard Co., Ltd., China) was used for the inkjet printing of QR code labels, as shown in Fig. 1b–d. The original magenta (M) and yellow (Y) inks in the 803 tri-color cartridge were replaced by prepared roselle anthocyanins ink and curcumin ink, respectively. Adobe Photoshop software was used to design QR code labels with different M: Y ratios (pure Y, 1:4, 1:1, 4:1, pure M). In order to increase the color contrast between QR codes and white paper (120 gm^{-2}) substrates, 15 times inkjet printing were performed [37]. Finally, printed QR code labels were put into a vacuum oven and dried for 24 h at $15 \text{ }^\circ\text{C}$ to remove the solvent, and five kinds of QR code labels were prepared. QR code label with roselle anthocyanins ink to curcumin ink volume ratio of pure Y, 1:4, 1:1, 4:1, pure M was named as CR, 1 ATH-4 CR, 1 ATH-1 CR, 4 ATH-1 CR, and ATH, respectively. Figure 1e demonstrates the application of QR code labels. By scanning the label on package, detailed food information including real-time freshness and expected storage time can be acquired conveniently.

Characterization and measurements

The spectra of prepared solutions with different volume ratios of roselle anthocyanins to curcumin at pH (4–11) were obtained by a spectrophotometer (UV-3600, Shimadzu Incorporation, Japan) in the range of 400–800 nm. Dynamic viscosity of inks was determined by a 40.0 mm-diameter Peltier stainless steel parallel plate with a shear rate range of $10\text{--}500 \text{ s}^{-1}$ using a rheometer (Discovery HR10, TA Instruments, America). The contact angle of prepared inks on substrates (120 gm^{-2} white printing paper) was measured by a contact angle measuring instrument (SL200, KINO Industry Co., Ltd., America) by shoot 50 frames continuously at the rate of 10 frames^{-1} . The surface tension was checked by a bubble pressure tension meter (HZ-800A, Zibo Boshan Haifen Instrument Co., Ltd., Shandong, China), and the experiments were performed in triplicate for each ink. After the fabrication of QR code labels, formulated labels were placed on the top of different concentrations of ammonia solutions (200 mL 1 gL^{-1} , 2 gL^{-1} , 3.5 gL^{-1} , 5 gL^{-1} and 7.5 gL^{-1} in 250 mL glass beaker) for 2 min to observe the color

variations, and a spectro-densitometer (Spectro Eye, X-Rite Incorporation, America) was applied to measure the L^* , a^* , and b^* of QR code labels before and after ammonia exposure. All measurements were conducted in room temperature.

Results and discussion

Figure 2a–e presents the pH-dependent color and absorption spectra of prepared solutions with different volume ratios of roselle anthocyanins to curcumin. Roselle anthocyanins solution was prepared by mixing $0.5 \text{ mL } 10 \text{ gL}^{-1}$ 50% (v/v) roselle anthocyanins aqueous ethanol and 10 mL pH (4–11) buffer reagents. Curcumin solution was the mixture of $0.5 \text{ mL } 0.1 \text{ gL}^{-1}$ curcumin ethanol and 10 mL pH (4 ~ 11) buffer reagents. The mixed solutions were the mixture of the roselle anthocyanins solution and curcumin solution with different volume ratio of 4:1, 1:1 and 1:4, respectively. It can be seen that the color of the prepared natural roselle anthocyanins and curcumin solutions is sensitive to the pH value. And the initial color of mixed solutions gradually changes from purple to yellow with decreasing content of roselle anthocyanins solution from 100 to 0%. Due to chemical structure transformation [38], the color of roselle anthocyanins appears light purple at pH 4–5, purple at pH 6 and changed to blue when pH arrives at 7–9, and then yellow-green at pH 10–11. Consequently, the maximum of absorption wavelength shifts from 517 to 590 nm, as shown in Fig. 2a. For curcumin solution, because of the transformation of molecular structure [39], the colors change from yellow to orange with increasing pH value, and the maximum of absorption wavelength shifts from 428 nm ($\text{pH} \leq 8$) to 464 nm ($\text{pH} > 8$), as shown in Fig. 2b. For the mixed solutions with roselle anthocyanins to curcumin volume ratio of 4:1 (Fig. 2c) and 1:1 (Fig. 2d), there are two characteristic absorption peaks, which are close to the characteristic absorption peaks of roselle anthocyanins and curcumin, respectively. For the mixed solution with roselle anthocyanins to curcumin of volume ratio 4:1, the color change is similar to that of roselle anthocyanins with increasing pH value. The maximum of the absorption peak appears at 428 nm ($\text{pH} \leq 7$) and 580 nm ($\text{pH} \geq 8$), respectively, as presented in Fig. 2c. For the mixed solution with roselle anthocyanins to curcumin volume ratio of 1:1, the maximum of the

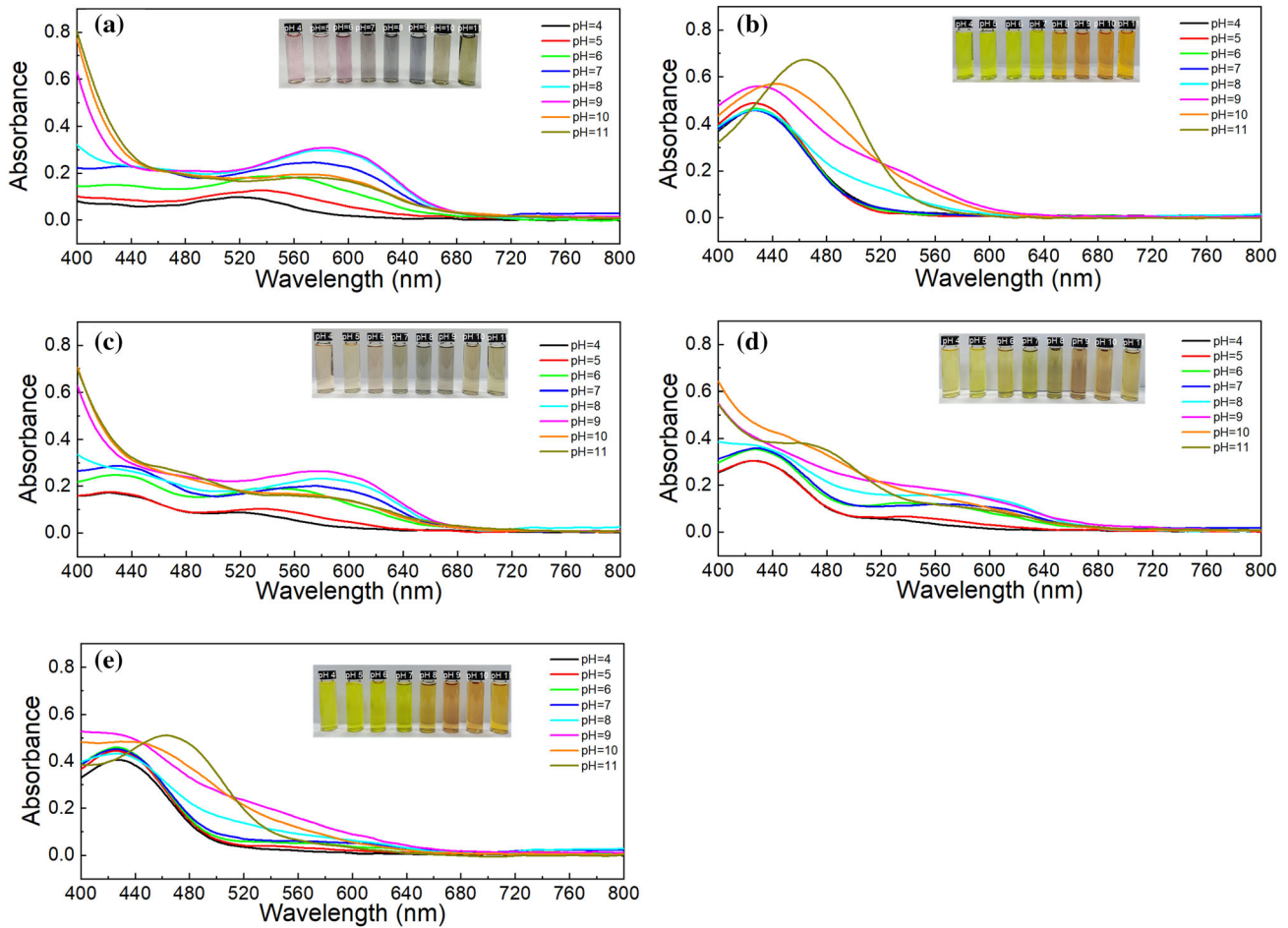


Figure 2 The pH-dependent color and absorption spectra of mixed solutions with roselle anthocyanins to curcumin volume ratio of pure roselle anthocyanins (a), pure curcumin (b), 4:1 (c), 1:1 (d), and 1:4 (e), respectively.

absorption wavelength shifts from 428 to 465 nm with increasing pH value, as shown in Fig. 2d. By decreasing the volume ratio of roselle anthocyanins to 1:4, the color change of mixed solutions and the maximum of the absorption peaks are similar to that of curcumin solution, respectively, as shown in Fig. 2e.

The printability of prepared inks has to be investigated, which is responsible for the quality of the QR code labels [3, 37]. The dynamic viscosity, contact angle, and surface tension of the prepared inks at room temperature are tested, respectively. Figure 3 shows the dynamic viscosity of the prepared inks at the shear rate of 10–500 s⁻¹. It can be found that the viscosity of both prepared inks remains constant with the increasing of shear rate, indicating the Newtonian behavior in the tested shear range. The prepared roselle anthocyanins ink shows higher viscosity

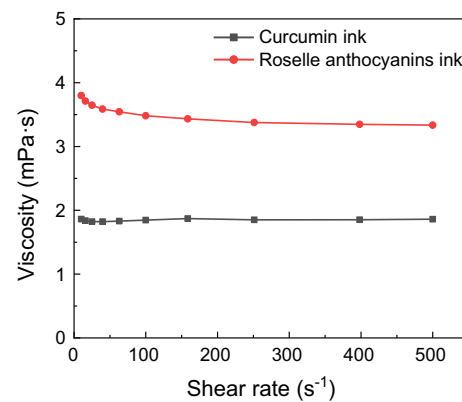


Figure 3 Shear rate-dependent dynamic viscosity of prepared roselle anthocyanins and curcumin inks, respectively.

values than that of curcumin ink, both meet the basic requirements for inkjet printing (QB/T 2730.1-2013).

Figure 4 Time-dependent contact angle of prepared roselle anthocyanins ink (a) and curcumin ink (b), respectively.

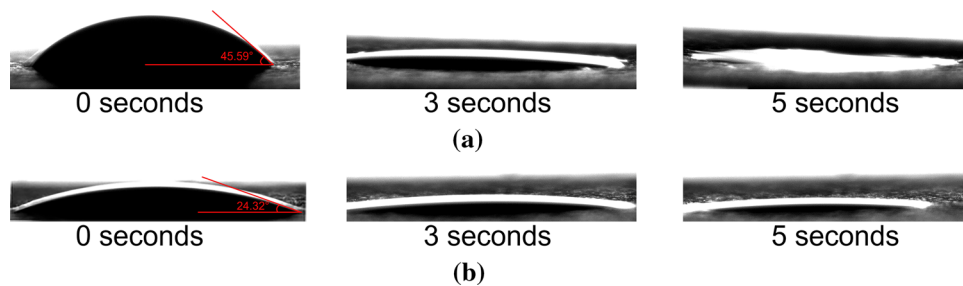
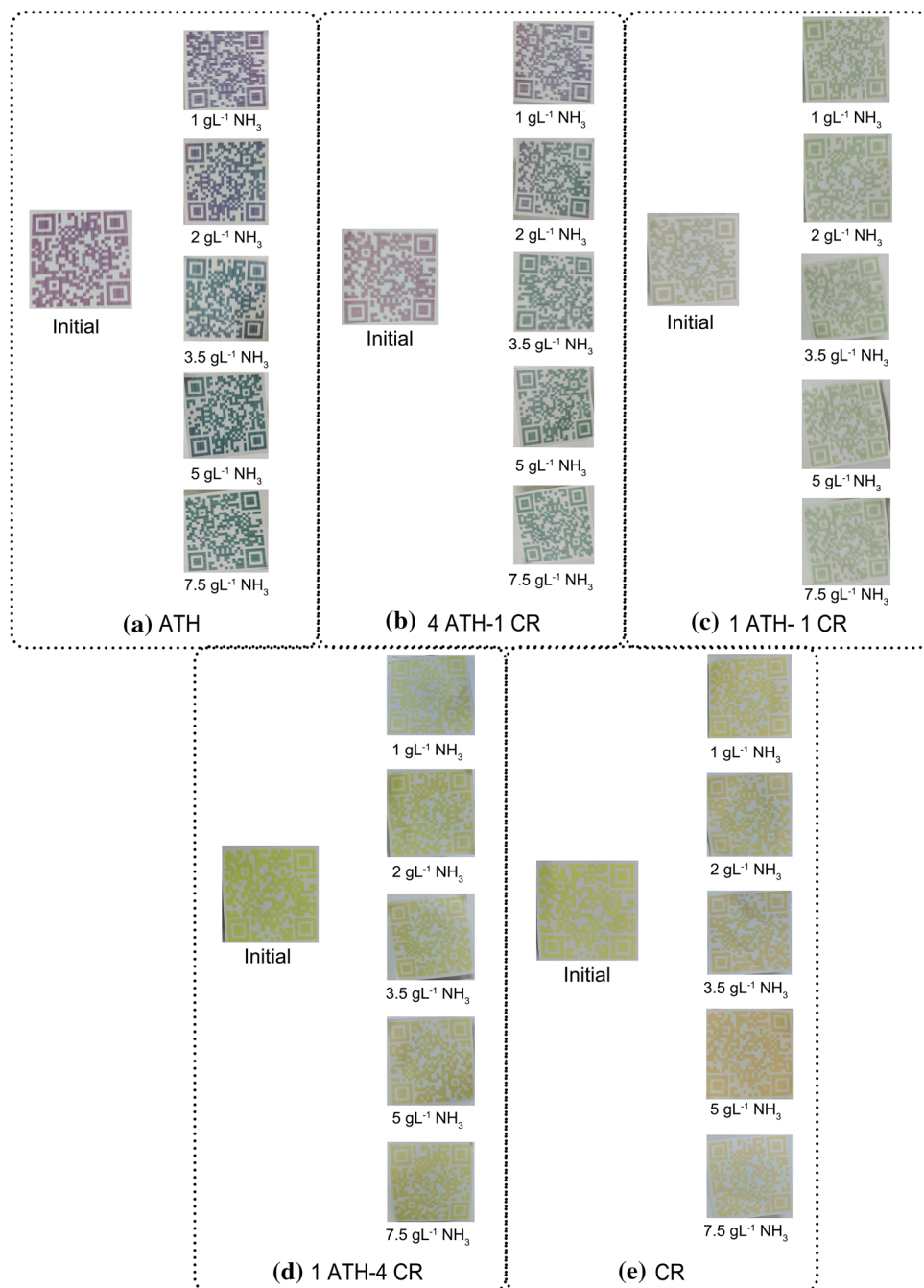


Figure 5 The color changes of the colorimetric QR code labels [(a) ATH, (b) 4 ATH-1 CR, (c) 1 ATH-1 CR, (d) 1 ATH-4 CR, and (e) CR] to different concentrations of ammonia solutions, respectively.



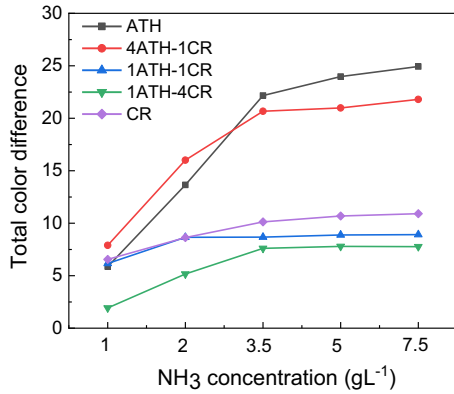


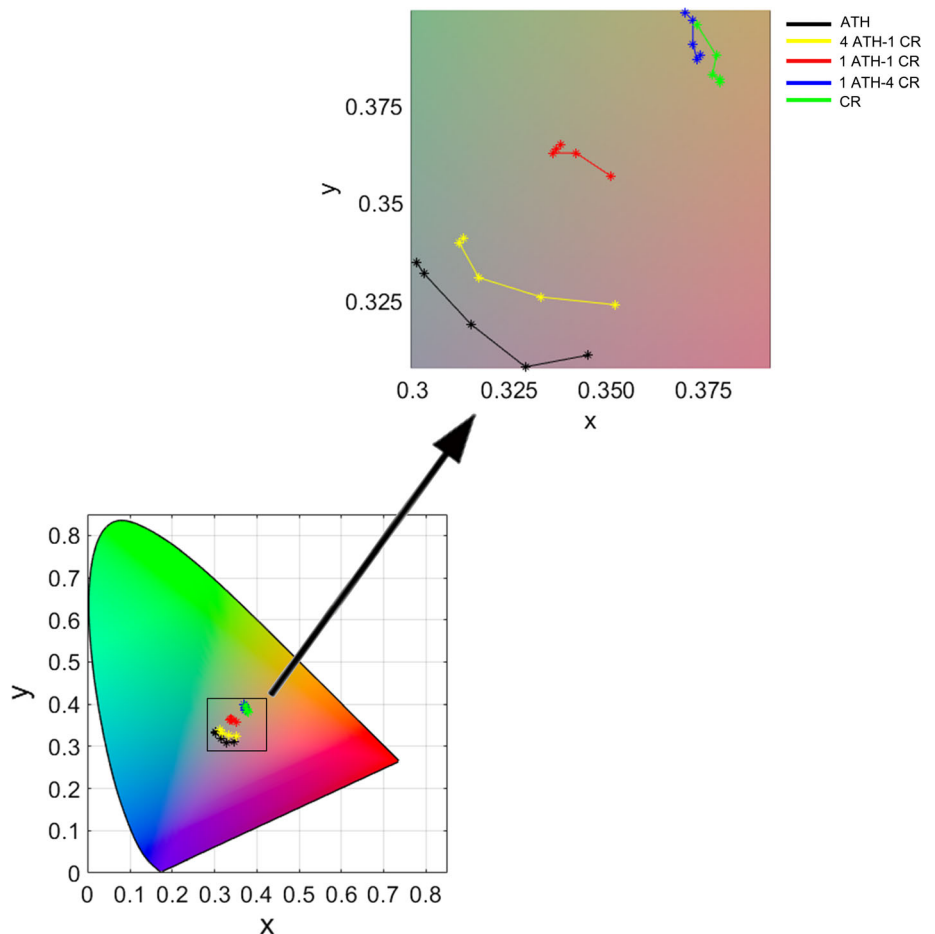
Figure 6 The total color difference of colorimetric QR code labels against different concentrations of ammonia solutions, respectively.

Contact angle is an important parameter to evaluate the wettability of the prepared inks on the substrate, and the smaller the contact angle between ink and substrate, the better the ink spreading on the substrate. As shown in Fig. 4, it can be found that the

primitive contact angle of roselle anthocyanins ink and curcumin ink on white paper substrate is 45.59° and 24.32°, respectively. Both inks can infiltrate into paper after 5 s, suggesting good wettability of the prepared inks on substrates. The surface tension for roselle anthocyanins ink and curcumin ink is $2.70 \times 10^{-2} \text{ Nm}^{-1}$ and $2.09 \times 10^{-2} \text{ Nm}^{-1}$, respectively, which is suitable for inkjet printing [40]. Therefore, both prepared inks have good printability and excellently meet the requirements of inkjet printing. No clogging of the ink cartridge nozzle was found, which also confirmed the printability of these inks.

After fabrication, the responses of QR code labels to ammonia solutions were analyzed, as illustrated in Figs. 5, 6, and 7. Figure 5 presents the color changes against different concentrations of ammonia solutions for the fabricated QR code labels with different volume ratios of roselle anthocyanins ink to curcumin ink. The colors of all QR code labels strongly depend on the concentrations of ammonia solutions.

Figure 7 The variations of QR code labels in the Y chromaticity diagram. For ATH (black line), the concentrations of ammonia solutions from right to left and bottom to top are 1 gL⁻¹, 2 gL⁻¹, 3.5 gL⁻¹, 5 gL⁻¹, and 7.5 gL⁻¹, respectively, and the same for 4 ATH-1 CR (yellow line) and 1 ATH-1 CR (red line). For 1 ATH-4 CR (blue line) and CR (green line), the concentrations of ammonia solutions from top to bottom are 1 gL⁻¹, 2 gL⁻¹, 3.5 gL⁻¹, 5 gL⁻¹, and 7.5 gL⁻¹, respectively.



With increasing the concentrations of ammonia solutions, the color of the ATH and 4 ATH-1 CR labels gradually turns to green, and 1 ATH-1 CR label transforms from brown to light green, while the color of the 1 ATH-4 CR and CR labels changes from yellow to orange. The total color difference (ΔE) can be used to quantitatively evaluate the color changes of QR code labels before and after ammonia solutions exposure, which can be calculated by [41]

$$\Delta E = \sqrt{(L_1^* - L_0^*)^2 + (a_1^* - a_0^*)^2 + (b_1^* - b_0^*)^2}$$

where the subscripts “0” and “1” represent the samplings before and after the ammonia solutions exposure, respectively. The colorimetric data of L^* , a^* , and b^* values are the average of three position detection patterns of QR codes. Generally, a ΔE value greater than 5 can be observed by the naked human eyes, while a ΔE greater than 12 indicates the color difference is extremely significant and the absolute difference in color, which can be easily observed via the unaided eyes. The greater the ΔE value, the greater the color differences [11, 42]. As demonstrated in Fig. 6, when the concentration of ammonia solution is 1 gL^{-1} , it can be found that the ΔE values of four QR code labels are greater than 5 except for 1 ATH-4 CR label. When the ammonia increases to 2 gL^{-1} , the ΔE values of all fabricated labels are greater than 5. Moreover, for ATH and 4 ATH-1 CR labels, the ΔE values are even greater than 12, which means the color of these two labels changes greatly after 2 gL^{-1} ammonia exposure. The concentration of ammonia solution for the maximum ΔE value of the labels of ATH and 4 ATH-1 CR is 7.5 gL^{-1} , 2 gL^{-1} for 1 ATH-1 CR, 3.5 gL^{-1} for 1 ATH-4 CR, and 5 gL^{-1} for CR, respectively. Figure 7 illustrates the color variations of QR code labels exposed to different concentrations of ammonia solutions in the Y chromaticity diagram. These results demonstrate that the color of all fabricated QR code labels, especially for ATH and 4 ATH-1 CR, can display a good response to ammonia which is a main product of meat spoilage.

The stability of roselle anthocyanins can be influenced by environmental factors easily, for instance, temperature, light and metal ion [43, 44]. The curcumin has antioxidant, antibacterial, and anti-inflammatory properties [45, 46] even though it shows smaller ΔE value to ammonia exposure than that of roselle anthocyanins. As a result, the curcumin has been widely used in food freshness indication and

preservation [35, 47]. Therefore, the volume ratios of inks of prepared QR code labels, which can be automatically tuned by the computer program, can be manipulated according to the food type, storage condition, and storage time.

Conclusion

In this work, colorimetric QR code labels have been fabricated successfully. Inks with roselle anthocyanins and curcumin natural dye are applied for the designed QR code labels. Both inks show good printability with Newtonian fluid property. It can be found that the color of all printed QR code labels is sensitive to the concentrations of ammonia solutions, which suggests the pH-sensitive QR codes are prepared. Moreover, the ammonia-dependent color differences analysis shows that the color differences strongly depend on the ink ratios. Therefore, by adjusting the proportion of different inks, “One thing, One code” of freshness may be achieved. In future, the developed colorimetric QR code labels have a promising application in the field of Internet of Things with dual functions of data carrier and freshness sensor.

Acknowledgements

The authors gratefully appreciate financial support offered by the National Natural Science Foundation of China (Grant Nos. 51371129 and 11174226).

Declarations

Conflict of interest The authors declare that they have no conflicts of interest.

References

- [1] He J, Yap RCC, Wong SY, Li X (2015) Polymer composites for intelligent food packaging. *J Mol Eng Mater*. <https://doi.org/10.1142/s2251237315400055>
- [2] Kalpana S, Priyadarshini SR, Leena MM, Moses JA, Anandharamkrishnan C (2019) Intelligent packaging: trends and applications in food systems. *Trends Food Sci Technol* 93:145–157. <https://doi.org/10.1016/j.tifs.2019.09.008>

- [3] Luo X, Lim L-T (2020) An inkjet-printed sulfonephthalein dye indicator array for volatile amine detection. *J Food Sci* 85(2):442–454. <https://doi.org/10.1111/1750-3841.15020>
- [4] Newsome R, Balestrini CG, Baum MD, Corby J, Fisher W, Goodburn K, Labuza TP, Prince G, Thesmar HS, Yiannas F (2014) Applications and perceptions of date labeling of food. *Compr Rev Food Sci Food Saf* 13(4):745–769. <https://doi.org/10.1111/1541-4337.12086>
- [5] Williams H, Wikstrom F, Otterbring T, Lofgren M, Gustafsson A (2012) Reasons for household food waste with special attention to packaging. *J Clean Prod* 24:141–148. <https://doi.org/10.1016/j.jclepro.2011.11.044>
- [6] Sharp JCM, Reilly WJ (1994) Recent trends in foodborne infections in Europe and North America. *Br Food J* 96(7):25–34. <https://doi.org/10.1108/00070709410076333>
- [7] Chen HZ, Zhang M, Bhandari B, Guo ZM (2018) Evaluation of the freshness of fresh-cut green bell pepper (*Capsicum annuum* var. *grossum*) using electronic nose. *LWT-Food Sci Technol* 87:77–84. <https://doi.org/10.1016/j.lwt.2017.08.052>
- [8] Qiao L, Tang XY, Dong J (2017) A feasibility quantification study of total volatile basic nitrogen (TVB-N) content in duck meat for freshness evaluation. *Food Chem* 237:1179–1185. <https://doi.org/10.1016/j.foodchem.2017.06.031>
- [9] Qiu WQ, Chen SS, Xie J, Qu YH, Song X (2016) Analysis of 10 nucleotides and related compounds in *Litopenaeus vannamei* during chilled storage by HPLC-DAD. *LWT-Food Sci Technol* 67:187–193. <https://doi.org/10.1016/j.lwt.2015.11.047>
- [10] Liu B, Xu H, Zhao HY, Liu W, Zhao LY, Li Y (2017) Preparation and characterization of intelligent starch/PVA films for simultaneous colorimetric indication and antimicrobial activity for food packaging applications. *Carbohydr Polym* 157:842–849. <https://doi.org/10.1016/j.carbpol.2016.10.067>
- [11] Huang SY, Xiong YB, Zou Y, Dong QF, Ding FY, Liu XH, Li HB (2019) A novel colorimetric indicator based on agar incorporated with *Arnebia euchroma* root extracts for monitoring fish freshness. *Food Hydrocolloids* 90:198–205. <https://doi.org/10.1016/j.foodhyd.2018.12.009>
- [12] Guo LL, Wang T, Wu ZH, Wang JW, Wang M, Cui ZQ, Ji SB, Cai JF, Xu CL, Chen XD (2020) Portable food-freshness prediction platform based on colorimetric barcode combinatorics and deep convolutional neural networks. *Adv Mater* 32(45):202004805. <https://doi.org/10.1002/adma.202004805>
- [13] Lee K, Baek S, Kim D, Seo J (2019) A freshness indicator for monitoring chicken-breast spoilage using a Tyvek (R) sheet and RGB color analysis. *Food Packaging Shelf Life* 19:40–46. <https://doi.org/10.1016/j.fpsl.2018.11.016>
- [14] Zhang JJ, Zou XB, Zhai XD, Huang XW, Jiang CP, Holmes M (2019) Preparation of an intelligent pH film based on biodegradable polymers and roselle anthocyanins for monitoring pork freshness. *Food Chem* 272:306–312. <https://doi.org/10.1016/j.foodchem.2018.08.041>
- [15] Wang J, Li DQ, Ye YX, Qiu Y, Liu JW, Huang L, Liang B, Chen BL (2021) A fluorescent metal-organic framework for food real-time visual monitoring. *Adv Mater* 33(15):2008020. <https://doi.org/10.1002/adma.202008020>
- [16] Nopwinyuwong A, Trevanich S, Suppakul P (2010) Development of a novel colorimetric indicator label for monitoring freshness of intermediate-moisture dessert spoilage. *Talanta* 81(3):1126–1132. <https://doi.org/10.1016/j.talanta.2010.02.008>
- [17] Lee GY, Shin HS (2016) Development of freshness indicator for quality of skate (*Raja kenoei*) during storage. *Food Sci Biotechnol* 25(5):1485–1489. <https://doi.org/10.1007/s10068-016-0230-4>
- [18] Lee GY, Lee S, Shin HS (2016) Evaluation of gas freshness indicator for determination of skate (*Raja kenoei*) quality during storage. *Food Sci Biotechnol* 25(5):1497–1500. <https://doi.org/10.1007/s10068-016-0232-2>
- [19] Kulchan R, Boonsupthip W, Jinkarn T, Suppakul P (2016) Developing a novel colorimetric indicator for monitoring rancidity reaction and estimating the accelerated shelf life of oxygen-sensitive dairy products. *Int Food Res J* 23(3):1092–1099
- [20] Loughran M, Diamond D (2000) Monitoring of volatile bases in fish sample headspace using an acidochromic dye. *Food Chem* 69(1):97–103. [https://doi.org/10.1016/s0308-8146\(99\)00224-1](https://doi.org/10.1016/s0308-8146(99)00224-1)
- [21] Bekhit A, Holman BWB, Giteru SG, Hopkins DL (2021) Total volatile basic nitrogen (TVB-N) and its role in meat spoilage: a review. *Trends Food Sci Technol* 109:280–302. <https://doi.org/10.1016/j.tifs.2021.01.006>
- [22] Ghaani M, Cozzolino CA, Castelli G, Farris S (2016) An overview of the intelligent packaging technologies in the food sector. *Trends Food Sci Technol* 51:1–11. <https://doi.org/10.1016/j.tifs.2016.02.008>
- [23] Ramalho JFCB, Correia SFH, Fu LS, Dias LMS, Adao P, Mateus P, Ferreira RAS, Andre PS (2020) Super modules-based active QR codes for smart trackability and IoT: a responsive-banknotes case study. *NPJ Flex Electron* 4(1):48–54. <https://doi.org/10.1038/s41528-020-0073-1>
- [24] Peng YQ, Zhang LX, Song ZX, Yan J, Li XX, Li ZB (2018) A QR code based tracing method for fresh pork quality in cold chain. *J Food Process Eng* 41(4):e12685. <https://doi.org/10.1111/jfpe.12685>
- [25] Qian JP, Xing B, Zhang BH, Yang H (2021) Optimizing QR code readability for curved agro-food packages using

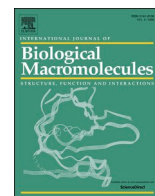
- response surface methodology to improve mobile phone-based traceability. *Food Packaging Shelf Life* 28:100638. <https://doi.org/10.1016/j.foodpack.2021.100638>
- [26] Han S, Bae HJ, Kim J, Shin S, Choi SE, Lee SH, Kwon S, Park W (2012) Lithographically encoded polymer microtaggant using high-capacity and error-correctable QR code for anti-counterfeiting of drugs. *Adv Mater* 24(44):5924–5929. <https://doi.org/10.1002/adma.201201486>
- [27] Sun J, Shrestha K, Park H, Yadav P, Parajuli S, Lee S, Shrestha S, Koirala GR, Kim Y, Marotrao KA, Maskey BB, Olaoluwa OC, Park J, Jang H, Lim N, Jung Y, Cho G (2020) Bridging R2R printed wireless 1 bit-code generator with an electrophoretic QR code acting as WORM for NFC carrier enabled authentication label. *Adv Mater Technol* 5(2):1900935. <https://doi.org/10.1002/admt.201900935>
- [28] Kennedy ZC, Stephenson DE, Christ JF, Pope TR, Arey BW, Barrett CA, Warner MG (2017) Enhanced anti-counterfeiting measures for additive manufacturing: coupling lanthanide nanomaterial chemical signatures with blockchain technology. *J Mater Chem C* 5(37):9570–9578. <https://doi.org/10.1039/c7tc03348f>
- [29] Ramalho J, Correia SFH, Fu LS, Antonio LLF, Brites CDS, Andre PS, Ferreira RAS, Carlos LD (2019) Luminescence thermometry on the route of the mobile-based internet of things (IoT): how smart QR codes make it real. *Adv Sci* 6(19):1900950. <https://doi.org/10.1002/advs.201900950>
- [30] Burklund A, Saturley-Hall HK, Franchina FA, Hill JE, Zhang JXJ (2019) Printable QR code paper microfluidic colorimetric assay for screening volatile biomarkers. *Biosens Bioelectron* 128:97–103. <https://doi.org/10.1016/j.bios.2018.12.026>
- [31] Katoh A, Maejima K, Hiruta Y, Citterio D (2020) All-printed semiquantitative paper-based analytical devices relying on QR code array readout. *Analyst* 145(18):6071–6078. <https://doi.org/10.1039/d0an00955e>
- [32] Engel L, Benito-Altamirano I, Tarantik KR, Pannek C, Dold M, Prades JD, Wollenstein J (2021) Printed sensor labels for colorimetric detection of ammonia, formaldehyde and hydrogen sulfide from the ambient air. *Sens Actuator B-Chem* 330:129281. <https://doi.org/10.1016/j.snb.2020.129281>
- [33] Tarjan L, Senk I, Tegeltija S, Stankovski S, Ostojic G (2014) A readability analysis for QR code application in a traceability system. *Comput Electron Agric* 109:1–11. <https://doi.org/10.1016/j.compag.2014.08.015>
- [34] Abdolahi M, Jiang H, Kaminska B (2019) Structural colour QR codes for multichannel information storage with enhanced optical security and life expectancy. *Nanotechnology* 30(40):405301. <https://doi.org/10.1088/1361-6528/ab2d3b>
- [35] Kuswandi B, Jayus LTS, Abdullah A, Heng LY (2012) Real-time monitoring of shrimp spoilage using on-package sticker sensor based on natural dye of curcumin. *Food Anal Meth* 5(4):881–889. <https://doi.org/10.1007/s12161-011-9326-x>
- [36] Chen HZ, Zhang M, Bhandari B, Yang CH (2020) Novel pH-sensitive films containing curcumin and anthocyanins to monitor fish freshness. *Food Hydrocolloids* 100:105438. <https://doi.org/10.1016/j.foodhyd.2019.105438>
- [37] Zhang Y, Lim L-T (2016) Inkjet-printed CO₂ colorimetric indicators. *Talanta* 161:105–113. <https://doi.org/10.1016/j.talanta.2016.08.014>
- [38] Grajeda-Iglesias C, Figueroa-Espinoza MC, Barouh N, Barea B, Fernandes A, de Freitas V, Salas E (2016) Isolation and characterization of anthocyanins from *Hibiscus sabdariffa* flowers. *J Nat Prod* 79(7):1709–1718. <https://doi.org/10.1021/acs.jnatprod.5b00958>
- [39] Esatbeyoglu T, Huebbe P, Ernst IMA, Chin D, Wagner AE, Rimbach G (2012) Curcumin: from molecule to biological function. *Angew Chem-Int Edit* 51(22):5308–5332. <https://doi.org/10.1002/anie.201107724>
- [40] Magdassi S (2010) *The chemistry of inkjet inks*. World Scientific Publishing Company, Singapore
- [41] Ohta N (1977) Correspondence between CIELAB and CIELUV color differences. *Color Res Appl* 2(4):178–182. <https://doi.org/10.1002/col.5080020407>
- [42] Chen HZ, Zhang M, Bhandari B, Yang CH (2019) Development of a novel colorimetric food package label for monitoring lean pork freshness. *LWT-Food Sci Technol* 99:43–49. <https://doi.org/10.1016/j.lwt.2018.09.048>
- [43] Giusti MM, Wrolstad RE (2003) Acylated anthocyanins from edible sources and their applications in food systems. *Biochem Eng J* 14(3):217–225. [https://doi.org/10.1016/s1369-703x\(02\)00221-8](https://doi.org/10.1016/s1369-703x(02)00221-8)
- [44] He Z, Xu M, Zeng M, Qin F, Chen J (2016) Interactions of milk alpha- and beta-casein with malvidin-3-O-glucoside and their effects on the stability of grape skin anthocyanin extracts. *Food Chem* 199:314–322. <https://doi.org/10.1016/j.foodchem.2015.12.035>
- [45] Khorasani MY, Langari H, Sany SBT, Rezayi M, Sahebkar A (2019) The role of curcumin and its derivatives in sensory applications. *Mater Sci Eng C-Mater Biol Appl* 103:109792. <https://doi.org/10.1016/j.msec.2019.109792>
- [46] Zheng DT, Huang CX, Huang HH, Zhao Y, Khan MRU, Zhao H, Huang LJ (2020) Antibacterial mechanism of curcumin: a review. *Chem Biodivers* 17(8):e2000171. <https://doi.org/10.1002/cbdv.202000171>
- [47] Ma QY, Du L, Wang LJ (2017) Tara gum/polyvinyl alcohol-based colorimetric NH₃ indicator films incorporating curcumin for intelligent packaging. *Sens Actuator B Chem* 244:759–766. <https://doi.org/10.1016/j.snb.2017.01.035>

Publisher's Note Springer Nature remains neutral with regard to jurisdictional claims in published maps and institutional affiliations.

ARTICLES FOR FACULTY MEMBERS

ROSELLE (HIBISCUS SABDARIFFA) ANTHOCYANIN USE IN MONITORING MEAT FRESHNESS

Title/Author	Intelligent food tag: A starch-anthocyanin-based pH-sensitive electrospun nanofiber mat for real-time food freshness monitoring / Lv, H., Wang, C., He, D., Zhao, H., Zhao, M., Xu, E., Jin, Z., Yuan, C., Guo, L., Wu, Z., Liu, P., & Cui, B.
Source	<i>International Journal of Biological Macromolecules</i> Volume 256 Part 1 (2024) 128384 Pages 1-12 https://doi.org/10.1016/j.ijbiomac.2023.128384 (Database: ScienceDirect)



Intelligent food tag: A starch-anthocyanin-based pH-sensitive electrospun nanofiber mat for real-time food freshness monitoring

Haowei Lv^{a,1}, Chenxi Wang^{a,1}, Deyun He^a, Haibo Zhao^a, Meng Zhao^a, Enbo Xu^b, Zhengyu Jin^c, Chao Yuan^a, Li Guo^a, Zhengzong Wu^{a,*}, Pengfei Liu^{a,*}, Bo Cui^{a,*}

^a State Key Laboratory of Biobased Material and Green Papermaking, School of Food Science and Engineering, Qilu University of Technology, Shandong Academy of Sciences, Jinan 250353, China

^b College of Biosystems Engineering and Food Science, Zhejiang University, Hangzhou 310058, China

^c State Key Laboratory of Food Science and Technology, Jiangnan University, Wuxi 214122, China

ARTICLE INFO

Keywords:

Natural polymer
Starch
Anthocyanins

ABSTRACT

A starch-based nanofiber mat was prepared for real-time monitoring of food freshness for the first time. UV–vis results showed that roselle anthocyanins (RS) conferred a wide pH sensing range on the nanofiber mat. The prepared nanofiber mats demonstrated good color visibility (total color difference value (ΔE) increased to 56.4 ± 0.7) and a reversible response (within 120 s). Scanning electron microscopy and Fourier transform infrared spectroscopy results suggested that the nanofibers had smooth surfaces without beaded fibers and that RS was well embedded into the nanofibers. The introduction of RS improved the thermal stability of the nanofibers. Color stability tests revealed that the nanofibers exhibited excellent color stability (maximum change $\Delta E = 1.57 \pm 0.03$) after 14 days of storage. Pork and shrimp freshness tests verified that the nanofibers could effectively reflect the dynamic freshness of pork and shrimp. Nontoxic, degradable and responsive characteristics make the pH-sensitive nanofiber mat a smart food label with great application potential.

1. Introduction

Due to the frequent occurrence of modern food “safety” and “waste” problems, there is a growing interest in developing smart food label (SFL), and they have become a hot research topic. SFL is a material and item that can realize real-time monitoring of the condition of packaged food or the environment around food [1]. Providing consumers with information about the freshness of the food they purchase, SFL have great potential to replace the concept of “shelf life” for food packaging based on a dynamic labeling system. The main cause of deterioration of animal foods is the degradation of their proteins and other nitrogenous compounds by microorganisms and endogenous enzymes. The whole process is accompanied by the generation of large quantities of volatile base nitrogen (e.g., ammonia, dimethylamine, trimethylamine, etc.) [2], resulting in elevated pH levels in food packaging environment. Consequently, it is necessary and feasible to develop a pH-sensitive SFL to monitor the freshness and quality of food products to “improve food safety and prevent food waste”.

Many studies have been conducted on the application of pH-sensitive

dyes in SFL. However, the majority of the currently reported pH-sensitive SFLs use chemical chromogenic formulation indicators (e.g., bromothymol blue, dimethylphenol, bromocresol green, methyl red, cresol red, chlorophenol, etc.) [3], which may migrate into food during the monitoring process and result in toxicity or carcinogenicity problems [4]. This drawback ultimately led to limitations in the commercialization of these SFLs. Using natural pH-sensitive dyes for SFL preparation has been recommended as the best option thus far. Roselle anthocyanins (RS), a water-soluble edible and natural pigment that mainly exists in the form of cyanidine and delphinidine [5–7], are ideal for use as a pH colorimetric indicator due to their wide range of sources, safety, nonpollution and high pH sensitivity.

To date, various methods have been applied for anthocyanin encapsulation, including emulsion, casting, extrusion, cohesion, molecular encapsulation, etc. [8–10]. Although these strategies are usually highly effective, they have different shortcomings, such as extreme temperature, the use of organic solvents and complex steps, which limit their practical applications. Therefore, it is of great interest to find alternative methods for immobilizing anthocyanins into SFL.

* Corresponding authors.

E-mail addresses: wzzqlu@hotmail.com (Z. Wu), zxliupf@163.com (P. Liu), cuib@qlu.edu.cn (B. Cui).

¹ These authors contributed equally to the work and should be regarded as co-first authors.

Electrospinning is an electrohydrodynamic processing technique in which a high potential electric field is applied to a polymer solution or melt to form Taylor cones (electrically charged conical droplets), which are ultimately stretched into fibers [11]. Currently, it has become an effective method to prepare nanofibers in a direct and continuous manner. Compared with traditional encapsulation techniques, nanofiber mats prepared by electrospinning have the advantages of a large specific surface area, high porosity, adjustable fiber size and morphology, light weight, superior mechanical properties, simplicity of operation, mild conditions, low cost, etc. and has emerged as an attractive method for encapsulating active substances in recent years. Based on its appealing properties, electrospinning is an ideal technology for immobilizing RS into SFL.

Notably, the pH sensitivity of most natural dyes is slightly lower than that of their chemical counterparts [12]. Interestingly, electrospinning technology can bridge this gap remarkably well. The high porosity and high specific surface area of the electrospun nanofibers led to an increase in the number of interaction sites between the immobilized anthocyanins and the volatile base nitrogen released from meat spoilage [6]. The higher porosity provides a lower resistance to transfer and ultimately increases the sensitivity of the fiber membrane to changes in ambient pH, improving the accuracy of SFL in detecting the freshness level of meat products. In addition, electrospinning is a nonthermal process, so its preparation process is extremely friendly to anthocyanins, which are heat-sensitive [13].

Due to their excellent biocompatibility, biodegradability and recyclability, natural biopolymers are preferable for use as matrix carriers for preparing SFL [14,15]. To date, a variety of pH-sensitive SFL based on natural biopolymers have been successfully developed. For example, Jang, Kang, Adedeji, Kim, Lee, Kim and Jung [16] developed a cellulose/red radish color extract film through casting technology. In the

study of Cao, Wang, Wang, Lin, Niu, Guo, Yan and Wang [17], anthocyanins were successfully doped into a membrane matrix of chitosan (CS)/sodium alginate (SA) by a casting technique. Among the natural polymers used to develop eco-friendly SFL, starch is by far one of the most promising [18]. Owing to its cost-effective, nontoxic and renewable properties, starch is considered as an ideal material for constructing green SFL, which can not only be in direct contact with food but also provide food freshness information to consumers when doped with pH-sensitive dyes. In recent years, several studies have reported the use of starch to encapsulate anthocyanins. For example, Bao, Cui, Tian, Ding, Tian, Zhang, Wang, Zang, Sun, Li, Si and Li [19] reported a potato starch/chondroitin sulfate/blueberry anthocyanin film that can achieve real-time monitoring of shrimp freshness. However, most currently reported starch-based SFL are usually based on casting techniques, no research has yet prepared natural polymers-based SFL by electrospinning techniques.

In this study, we developed a green pH-responsive electrospun nanofiber mats for food freshness monitoring. For the novel SFL, octenyl succinic anhydride starch (OSA) was used as a film-forming material while RS was used as a pH-sensitive dye, and starch electrospinning properties were improved and increased by the addition of nontoxic, biodegradable polyvinyl alcohol (PVA). The environmental pH level of protein-based foods increases due to the release of volatile base nitrogen (TVB-N) during the spoilage process, thus new SFLs with high porosity and high surface area containing RS-sensitive dyes can respond quickly with color changes to provide consumers with information about the freshness of food (Fig. 1). The structural, physical, and optical properties of the electrospinning solutions and nanofiber mats with different RS concentration gradients were systematically characterized by ultraviolet-visible spectroscopy (UV-vis), scanning electron microscopy (SEM), Fourier transform infrared spectroscopy (FTIR), X-ray diffraction

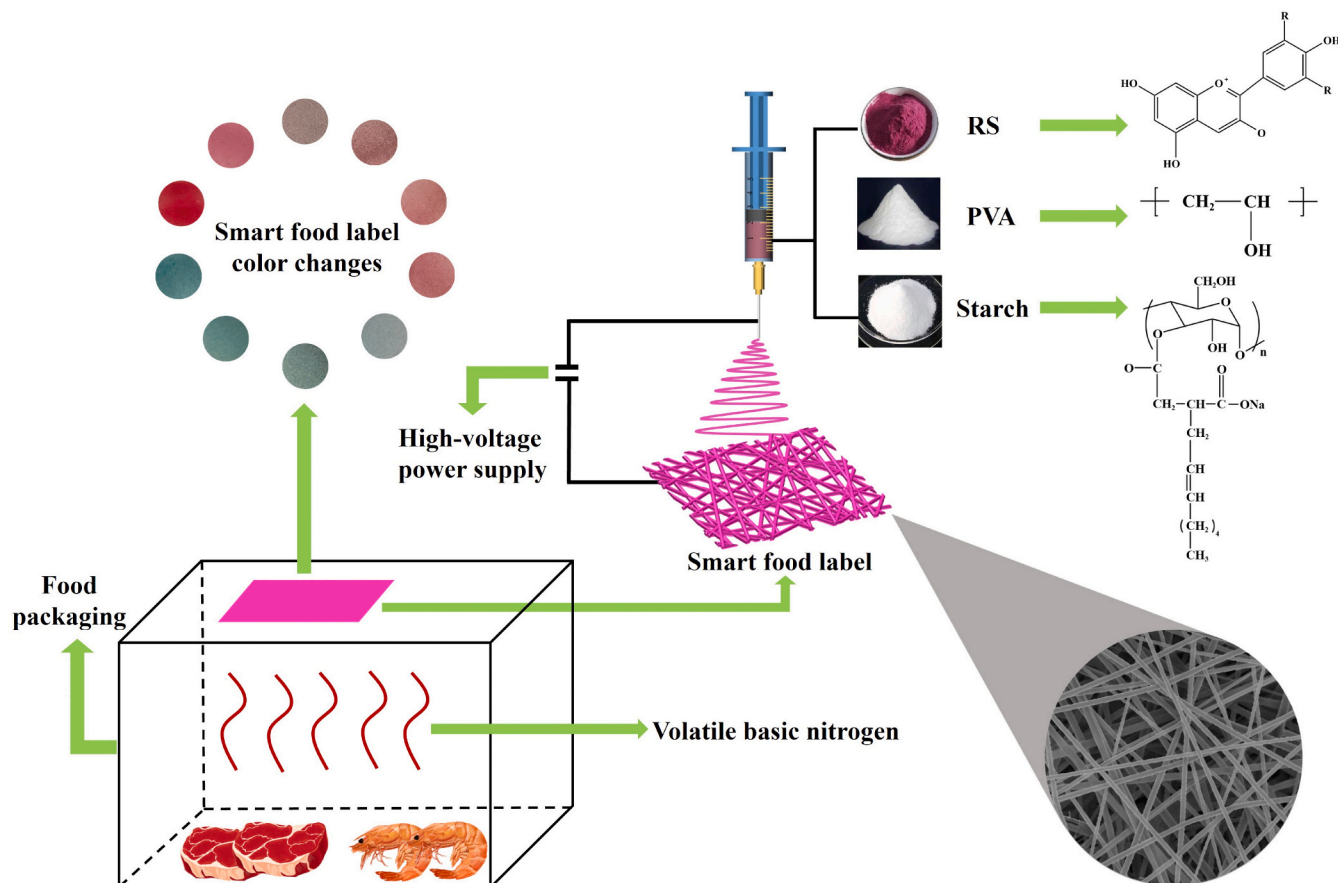


Fig. 1. Schematic representation of the electrospinning process and operation principle of OPRNFs.

(XRD), thermogravimetric analysis (TGA) and water contact angle (WCA). In addition, the application potential and reliability of the novel SFL was confirmed by real-time monitoring of the deterioration of pork and shrimp during storage. To the best of our knowledge, this is the first report in which starch-based nanofibers were prepared for real-time monitoring of food freshness.

2. Materials and methods

2.1. Materials

OSA was purchased from Shanghai Yuanye Bio-Technology Co., Ltd. (Shanghai, China). PVA was supplied by Macklin Biochemical CO., Ltd. (Shanghai, China). The RS with 25 % total anthocyanin content was obtained from Yizimin Plant Technology Co., Ltd. (Shaanxi, China). Fresh pork was sourced from local markets. The sodium hydroxide, hydrochloric acid and ammonia were got from Fuyu Fine Chemical Co., Ltd. (Tianjin, China). All other agents used were of analytical grade and used without further purification. Deionized water with a resistivity of 18.2 M Ω purified by Milli-Q system from Millipore (Bedford, MA, USA) was used for this study.

2.2. Preparation of electrospinning solutions

To prepare the electrospinning solution with a total concentration of 10 % (w/v), 0.5 g OSA and 0.5 g PVA (mass ratio = 1:1) were dissolved in a vessel and deionized water was added until the volume of the solution reached 10 mL. The mixed solutions were magnetically stirred at 95 °C for 3 h. The mixed solution was cooled to ambient temperature (25 °C) until ready for further use. Based on the experimental results, the RS concentration gradient is set to OSA/PVA mixed solutions of 1.2 %, 1.6 %, 2.0 % and 2.4 % (w/v). After the addition of RS, the four resulting mixed solutions were stirred at 30 °C for 4 h using a magnetic stirrer. Then, they were placed in an ultrasonic processor for 5 min to remove air bubbles. As a final step, electrospinning solutions with different RS concentrations (0 %, 1.2 %, 1.6 %, 2.0 % and 2.4 % (w/v)) were separately electrospun to obtain nanofiber mats. The corresponding mats were denoted as OPNFs, OPRNFs-1.2 %, OPRNFs-1.6 %, OPRNFs-2.0 % and OPRNFs-2.4 %.

2.3. Solution properties

Prior to electrospinning, the surface tension values of all electrospinning solutions (OPNFs, OPRNFs-1.2 %, OPRNFs-1.6 %, OPRNFs-2.0 % and OPRNFs-2.4 %) were determined using a DSA25 drop shape analyzer (KRÜSS, Hamburg, Germany). The conductivities were determined at room temperature using a DDS-307A conductivity meter (Shanghai Yifen, China). The viscosity properties were measured using an MCR 302 rheometer (Anton Paar, Stuttgart, Germany) equipped with a cone/plate spindle diameter of 50 mm and a cone angle of 1°. The viscosities (Pa·s) were recorded at shear rates ranging from 0.1 to 100 s⁻¹.

2.4. Electrospinning process

As shown in Fig. 1, the prepared OSA/PVA/RS mixed electrospinning solutions were loaded into a 5 mL disposable plastic syringe with a 22 G blunt needle. Nanofibers were then prepared by using a NANON-03 electrospinning unit (MECC Co., Ltd., Fukuoka, Japan), which consists of a high-voltage power supply (0.5–30 kV), a syringe pump and a grounded stainless steel rotating drum (diameter of the rotating drum is 200 mm) containing conductive aluminum foil used as a collector for fiber deposition. The electrostatic spinning parameters for all gradients of the blended solutions were set as follows: a voltage of 20 kV was applied at 30 °C and the spinning solutions were pumped into the needle tip at a flow rate of 0.3 mL/h using a precision syringe pump. Nanofibers

were formed and deposited on the rotating drum with a distance of 15 cm between the rotating drum and the needle tip. The rotation speed was 200 rpm and the humidity was limited to 30 %. Afterward, the collected nanofiber mats were separated from the collector and placed in a desiccator for further analysis. For comparison, pure OPNFs without RS addition were also prepared under the same electrospinning conditions.

2.5. UV-vis absorption spectra analysis

UV-vis spectra of RS solutions at different pH (2.0–12.0) were measured using a TU-1900 commercial spectrometer (Purkinje General Corporation, Beijing, China). The wavelength range for scanning is set to 400–800 nm. RS solutions at different pH values were prepared using 0.1 mol/L HCL and 0.1 mol/L NaOH solutions. The pH values were measured using an S210-B pH meter (Mettler Toledo, Schwerzenbach, Switzerland), while color changes at different pH values were recorded using a digital camera.

2.6. Morphology analysis

The microstructures of the prepared nanofibers with different RS concentrations were observed using a SU3500 scanning electron microscope (Hitachi, Tokyo, Japan). The nanofibers were immobilized using conductive adhesive and sputtered with gold under vacuum conditions at 15 mA for 60 s. SEM images of each sample were taken at an accelerating voltage of 5 kV and the magnification of the SEM images was set to 5000 \times and 10,000 \times , respectively. The average diameter (AD) of the nanofibers was calculated using an imageJ2X software (National Institutes of Health, Bethesda, Maryland, USA). At least 100 nanofibers were randomly selected for each sample.

2.7. FT-IR

FT-IR was carried out to investigate the intermolecular interactions of OSA, PVA, RS and the prepared nanofibers (OPNFs, OPRNFs-1.2 %, OPRNFs-1.6 %, OPRNFs-2.0 % and OPRNFs-2.4 %) using a Nicolet iS10 Fourier transform infrared spectrometer equipped with a Smart iTX ATR sampling accessory (Thermo Fisher Scientific, Madison, WI, USA) in the spectral range of 4000–600 cm⁻¹ for 64 scans at a spectral resolution of 4 cm⁻¹ (scanner velocity, 7.5 kHz; background, 64 scans; sample, 64 scans; temperature controllable, (25 \pm 1) °C). The infrared spectrometer is equipped with an interferometer, KBr beam splitter and deuterated triglycine sulfate (DTGS) detector. Spectral acquisition was accomplished by using OMSNIC software (Thermo Electron Corp., Madison, WI, USA). Spectra were collected in triplicate for each sample and the average values were calculated for subsequent data analysis.

2.8. XRD

The crystal structures of OSA, PVA, RS and the prepared nanofibers (OPNFs, OPRNFs-1.2 %, OPRNFs-1.6 %, OPRNFs-2.0 % and OPRNFs-2.4 %) were characterized using a D2 PHASER X-ray diffractometer (Bruker AXS Ltd., Karlsruhe, Germany) equipped with Cu-K α radiation. The diffractometer was operated at 40 kV and 40 mA and the XRD spectra were recorded in the scattering range of 2 θ (5°–30°) at a rate of 30°/min and a step size of 0.02° under room temperature.

2.9. Thermal stability analysis

The TGA of OSA, PVA, RS and prepared nanofibers (OPNFs, OPRNFs-1.2 %, OPRNFs-1.6 %, OPRNFs-2.0 % and OPRNFs-2.4 %) were carried out using an STA 6000 thermogravimetric analyzer (PerkinElmer Inc., Shelton, CT, USA) under a nitrogen atmosphere with a flow rate of 50 mL/min. The samples were heated from 30 °C to 600 °C at a rate of 20 K/min. The mass of each sample was approximately 5 mg.

2.10. WCA

The WCA values of OPNFs and OPRNFs with different RS concentrations (0 %, 1.2 %, 1.6 %, 2.0 % and 2.4 %) were measured by a DSA25 drop shape analyzer (KRÜSS, Hamburg, Germany). For all samples, the contact angle was analyzed for the surface of contact air during the drying step of the nanofiber mats. Prior to the experiment, the samples were cut to 30 mm × 50 mm and adhered to slides. The WCA value of each sample was measured by dropping 2 μL of distilled water onto the surface of the fiber membrane and photographing it. Digital pictures were recorded after 10 s of deposition and were analyzed by ADVANCE software (KRÜSS, Hamburg, Germany) to calculate the contact angle. The WCA value was averaged by taking three measurements at different locations on the surface of the fiber membrane.

2.11. Colorimetric response testing of OPRNFs to pH and ammonia vapor

To assess ammonia sensitivity, OPRNFs-2.4 % was immobilized in the mouth part of a conical flask (100 mL) containing ammonia (5 %, v/v) and then covered by a piece of clear glass. After OPRNFs-2.4 % reached the color change endpoint in ammonia, they were then exposed to acetic acid (10 %, v/v) for color reversibility testing. The order of exposure was alternated to ensure the integrity of the test. In addition, with reference to the method of Goudarzi, Moshtaghi and Shahbazi [20], the colorimetric response of OPRNFs-2.4 % at different pH values was tested. The pH sensitivity of OPRNFs-2.4 % to volatile ammonia was evaluated using an ammonia solution (0.8 M) kept at 25 ± 1 °C for 30 min. Due to the rapid progression of color change of OPRNFs-2.4 %, the color change of the fiber mats was captured by a camera and analyzed colorimetrically using Adobe Photoshop CS5 software (the colorimeter was unable to capture the colorimetric information in time). The total color difference value (ΔE) was calculated based on the obtained parameters L (lightness), a (redness/greenness, ±) and b (yellowness/blueness, ±) as follows:

$$\Delta E = \sqrt{(\Delta L^*)^2 + (\Delta a^*)^2 + (\Delta b^*)^2} \quad (1)$$

where $\Delta L^* = L^* - L_0^*$; $\Delta a^* = a^* - a_0^*$; $\Delta b^* = b^* - b_0^*$. L^* , a^* and b^* represent the color of the fiber mats after storage, and L_0^* , a_0^* and b_0^* represent the initial gray values of the fiber membrane. The reference standard for color analysis is set as white board ($L_0^* = 51.10$, $a_0^* = 38.07$, $b_0^* = 7.87$) [21]. Each measurement was recorded using the camera under the same light conditions.

2.12. Color stability of OPRNFs

The color stability of the nanofiber mats was characterized based on color change. To simulate a commercial storage environment, the prepared OPRNFs-2.4 % were stored separately in a thermostatic incubator at different temperature conditions (4 °C and 25 °C) with humidity controlled at 75 %. The color of the nanofiber mats was collected every two days within 14 days. The color indices were calculated according to the CIE $L^* a^* b^*$ color system by using an ADCI-60-C colorimeter (Chen Taike Instruments Co., Ltd., Beijing, China). The ΔE values of the nanofiber mats during storage were calculated to evaluate their color stability according to Eq. (1).

2.13. Application of nanofiber mats for pork freshness monitoring

Pork (30.0 g ± 0.5 g) and shrimp (30.0 g ± 0.5 g) were placed in sterilized petri dishes (d = 120 mm). OPNFs and OPRNFs-2.4 % samples were cut into rectangular strips (15 mm × 30 mm) and attached to the top of the petri dish and sealed. After that, the petri dishes were stored in a thermostatic incubator at 25 °C and 75 % RH. The color changes of OPRNFs-2.4 % was observed at 0 h, 24 h, 36 h, 48 h, 60 h and 72 h during the storage of pork and captured with a camera. The color change

of OPRNFs-2.4 % was recorded by photography at 0 h, 6 h, 12 h, 24 h and 36 h during the storage of fresh shrimp. Total volatile base nitrogen (TVB-N) levels and pH values of the pork were measured using a K9860 Kjeldahl nitrogen analyzer (Jinan Hannon Instrument Co., Ltd., Shandong, China) and a S210—B pH meter (Mettler Toledo, Schwerzenbach, Switzerland) at 0 h, 24 h, 36 h, 48 h, 60 h and 72 h, respectively. In addition, TVB-N levels and pH values of the fresh shrimp were measured at 0 h, 6 h, 12 h, 24 h and 36 h. Based on the determination method described in Goudarzi, Moshtaghi and Shahbazi et al. [20], total viable counts (TVC) of bacteria were determined in pork and shrimp during the storage period, and their ΔE values at the corresponding time points were determined by using an ADCI-60-C colorimeter (Chen Taike Instruments Co., Ltd., Beijing, China).

2.14. Statistical analysis

All experiment data were measured three times and their means with standard deviations were obtained for statistical analysis. Significant differences ($p < 0.05$ were considered statistically significant) between data were processed using one-way analysis of variance (ANOVA) in SPSS statistics version 17.0 software (SPSS Inc., Chicago, IL, USA).

3. Results and discussions

3.1. UV-vis spectra and color changes of RS at different pH values

The color variation of RS buffer solutions with pH 2–12 was measured with UV-vis spectra to verify the usefulness of the RS as a sensitive indicator dye. As shown in Fig. 2a, the color of RS solution changed from bright red to yellow with increasing pH from 2.0 to 12.0. The RS solution appears bright red at pH 2.0–3.0, pink at pH 4.0–6.0, gradually changing from pink to purple at pH 7.0–9.0, and the yellow color gradually changes to brown at pH 10.0–12.0. Fig. 2b shows the trend of the absorption spectrum of RS with increasing pH. In the pH range of 2–4, the maximum absorption wavelength appeared at approximately 526 nm, and the absorbance decreased with increasing pH. With increasing alkaline conditions, the maximum absorption in the pH 7–11 range shows a bathochromic shift at around 584 nm. The abovementioned color changes in RS and peak shifts in the UV-visible spectra are both due to the transformation of the chemical structure of RS in different pH environments [19]. The structural changes of RS during the color shift are shown in Fig. 2c. In the pH range of 2.0–3.0, red flavylium cations were the main constituent elements when the solution was bright red. At pH 4.0–6.0, the red color started to diminish and the anthocyanin mechanism was transformed to quinone type, which appeared pink. With increasing alkalinity, at pH 7.0–9.0, the deprotonation of hydroxyl groups led to red flavylium cations forming a colorless methanolic pseudobase and the color gradually changed to purple. In a strongly alkaline environment at pH > 9, the pyran ring of anthocyanin was opened and transformed to a chalcone structure, which eventually changed to yellow [22]. The above results prove that RS anthocyanins can be used as a natural pH indicator in SFL by continuously transforming their structures under different pH environmental conditions.

3.2. Morphology characterization

The surface morphologies of nanofiber mats with different RS concentrations were observed by SEM. The corresponding SEM images and diameter distribution histograms are shown in Figs. 3 and S1. Sufficient molecular entanglement is a critical prerequisite for obtaining electrospun nanofibers [23]. However, previous results have shown that the viscoelastic jets generated by pure OSA solutions during electrospinning are highly unstable, which ultimately leads to difficulties in achieving the stacking of nanofibers into mats [24]. As shown in Fig. 3, all five samples have a clear nanofiber structure after SEM magnification of

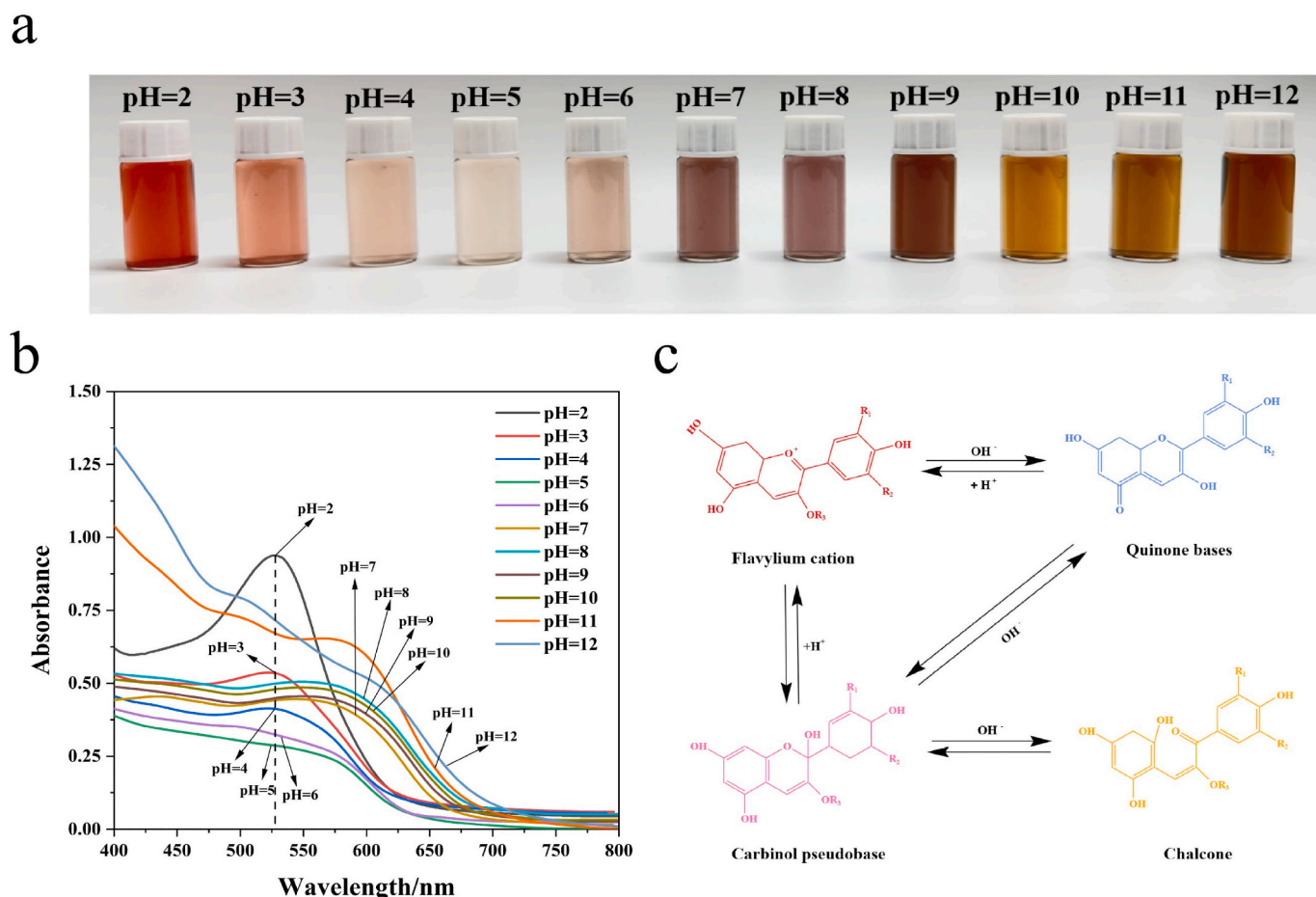


Fig. 2. (a) Color changes and (b) UV-vis spectra of RS solutions at pH 2–12. (c) Structural transformations of RS during the color change. (For interpretation of the references to color in this figure legend, the reader is referred to the web version of this article.)

5000 times. The resulting nanofibers have smooth cylindrical surfaces and randomly formed interwoven network structures, are well dispersed and do not have any beads or defects. This indicated that the incorporation of PVA promoted the molecular entanglement of OSA and improved the electrospinning property of OSA, which eventually led to the successful electrospinning of OSA starch into nanofibers.

Conductivity and viscosity properties are critical factors in determining the diameter of electrospun nanofibers. Table 1 summarizes the viscosity, conductivity, surface tension and AD values of the corresponding electrospinning solutions of OPNFs, OPRNFs-1.2 %, OPRNFs-1.6 %, OPRNFs-2.0 % and OPRNFs-2.4 % nanofiber mats. Typically, solution jets with high conductivity and low viscosity have a richer charge on the surface and are more likely to stretch into fibers with smaller diameters during the electrospinning process [25]. Compared to OPNFs, the AD value of OPRNFs decreased after doping with a small amount of RS anthocyanins. As shown in Fig. 3a and b, the AD value of the nanofibers significantly decreased from (408 ± 72) nm (OPNFs) to (276 ± 69) nm (OPRNFs-1.2 %) ($p < 0.05$). This was because the addition of small amounts of anthocyanins caused the conductivity of the electrospinning solution of the OPNFs to increase from (648.8 ± 2.4) $\mu\text{S}/\text{cm}$ to (656.2 ± 1.7) $\mu\text{S}/\text{cm}$ (OPRNFs-1.2 %) (Table 1), resulting in the formation of nanofibers with smaller AD value. However, as shown in Fig. 3b–e, the AD values of OPRNFs climbed stepwise with a further increase in RS concentration: (276 ± 69) nm (OPRNFs-1.2 %), (322 ± 70) nm (OPRNFs-1.6 %), (434 ± 74) nm (OPRNFs-2.0 %) and (490 ± 88) nm (OPRNFs-2.4 %). The continuous addition of RS resulted in a significant increase in the viscosity (from (0.46 ± 0.02) Pa·s of OPRNFs-1.2 % to (0.94 ± 0.01) Pa·s of OPRNFs-2.4 %) ($p < 0.05$) of the

electrospinning solution. With the increase in viscosity, the jet was less easily stretched during the electrospinning process, leading to the generation of nanofibers with larger AD values [26]. The hydrogen bonding generated between RS and the OSA/PVA matrix is also one of the main factors contributing to the increase in solution viscosity and the larger AD of the nanofibers [27].

In addition, Table 1 shows that the addition of RS has little effect on the surface tension of the electrospinning solution. The maximum electrospinnable concentration of RS is approximately 2.4 % with constant matrix concentration, the electrospinnability of the blended solution will be significantly decreased when the concentration of RS continues to increase (>2.4 %). The RS particles were not observed in the SEM images, suggesting that RS were well embedded into the OSA/PVA matrix and distributed inside the nanofibers in small size.

3.3. FT-IR analysis

FT-IR spectroscopy reveals the position and intensity of the absorption peaks of samples and can be used to determine the chemical group and structural composition of a substance by reflecting molecular structural features [28,29]. The FT-IR spectra of OSA starch, PVA powder, OPNFs and OPRNFs with different RS concentrations (OPRNFs-1.2 %, OPRNFs-1.6 %, OPRNFs-2.0 % and OPRNFs-2.4 %) are presented in Fig. 4a. The stretching vibration of the O–H bond resulted in the presence of an obvious absorption peak at approximately 3300 cm^{-1} , which was attributed to the inclusion of hydroxyl groups in all materials [29]. For OSA, PVA, OPNFs, OPRNFs-1.2 %, OPRNFs-1.6 %, OPRNFs-2.0 % and OPRNFs-2.4 %, two strong absorption bands were observed at

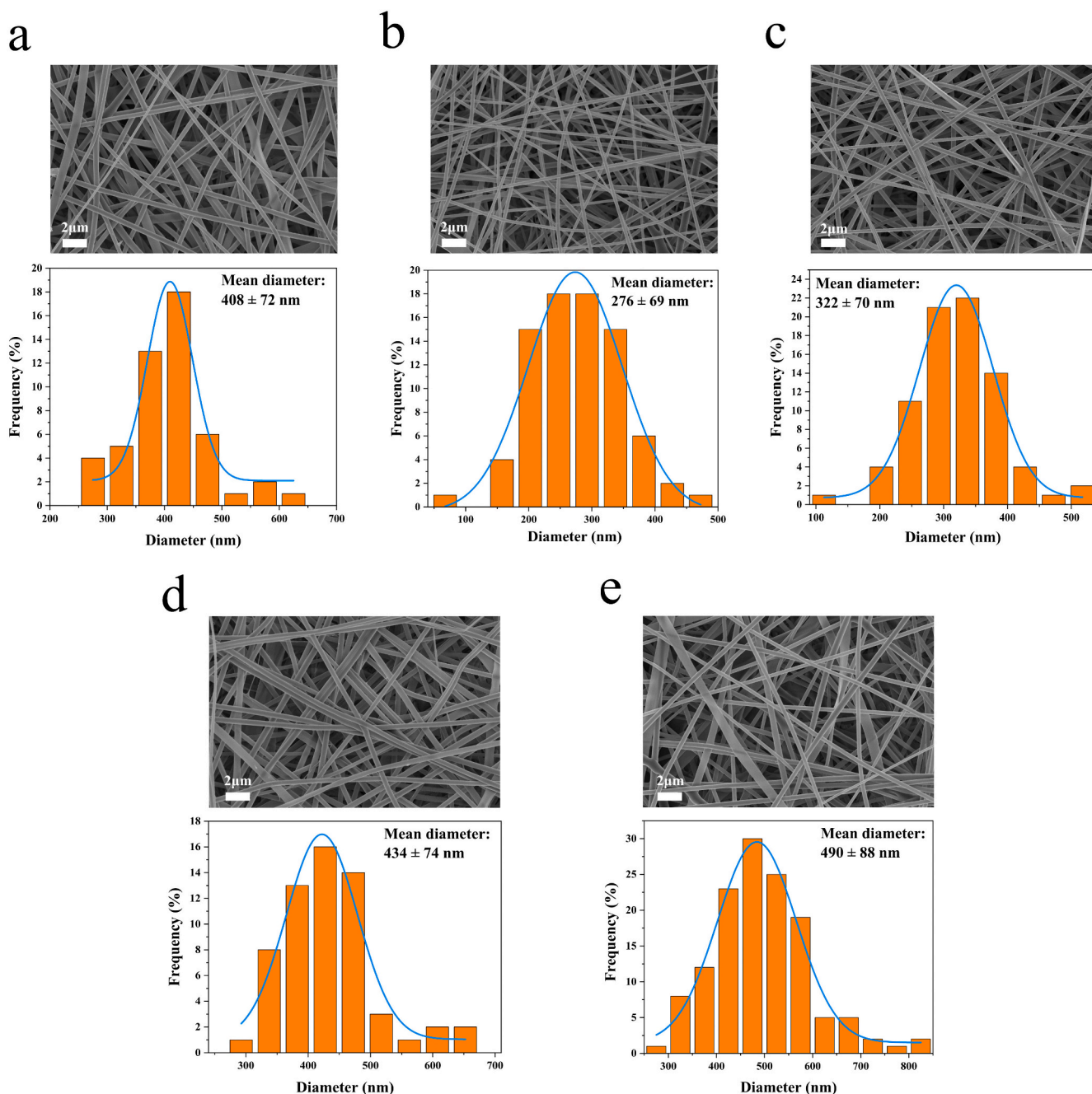


Fig. 3. SEM images and diameter distributions of (a) OPNFs, (b) OPRNFs-1.2 %, (c) OPRNFs-1.6 %, (d) OPRNFs-2.0 % and (e) OPRNFs-2.4 %. Magnification is 5000 \times .

approximately 2930 cm^{-1} and 1002 cm^{-1} , corresponding to the C–H and C–C stretching vibrations, respectively. In the spectrum of PVA, CH–CH₂ stretching located at 1435 cm^{-1} was found, which may be related to the basic carbon skeleton bending [30]. In accordance with that reported in previous studies, the FT-IR spectra of RS showed three characteristic absorption bands at 1736 cm^{-1} , 1610 cm^{-1} and 1078 cm^{-1} , corresponding to C–O, C=N and C–O stretching vibrations, respectively. The dominant absorption peak of RS was located at approximately 1020 cm^{-1} , which was associated with the deformation of the aromatic ring C–H [5]. Notably, a relatively weak absorption peak was observed at 1798 cm^{-1} , which can be explained by the stretching of the pyran ring of flavonoids from RS [31]. Typically, the small addition of RS resulted in negligible changes in the FT-IR spectra of the nanofiber mats. However, the positions of some absorption peaks

of the nanofiber mats changed after the addition of RS. As shown in Fig. 4a, the absorption peaks at approximately 3300 cm^{-1} and 2930 cm^{-1} of OPRNFs shifted to lower wavenumbers with increasing RS concentration compared to the control group (OPNFs). This phenomenon may be caused by the formation of new hydrogen bonds and electrostatic interactions between RS and the membrane matrix (OSA/PVA) [32], which is consistent with the conclusions obtained from SEM analyses. The above results indicate that RS was successfully immobilized in the OSA/PVA composite membrane matrix.

3.4. XRD analysis

XRD patterns of OSA, PVA, RS and electrospun fiber mats with different RS concentrations (OPNFs, OPRNFs-1.2 %, OPRNFs-1.6 %, OPRNFs-2.0 %, OPRNFs-2.4 %) were recorded to investigate the

Table 1

Physicochemical properties of electrospinning solutions and the AD values of the produced electrospun nanofibers.

Sample	Shear viscosity at 100 s ⁻¹ (Pa·s)	Surface tension (mN/m)	Conductivity (μS/cm)	AD (nm)
OPNFs	0.38 ± 0.03 ^a	36.04 ± 0.11 ^a	648.8 ± 2.4 ^a	408 ± 72 ^c
OPRNFs-1.2 %	0.46 ± 0.02 ^b	36.34 ± 0.36 ^a	656.2 ± 1.7 ^b	276 ± 69 ^a
OPRNFs-1.6 %	0.55 ± 0.04 ^c	36.78 ± 0.07 ^b	660.3 ± 2.8 ^b	322 ± 70 ^b
OPRNFs-2.0 %	0.79 ± 0.03 ^d	37.68 ± 0.16 ^c	674.6 ± 2.1 ^c	434 ± 74 ^d
OPRNFs-2.4 %	0.94 ± 0.01 ^e	38.03 ± 0.18 ^c	681.3 ± 2.6 ^c	490 ± 88 ^e

Note: significant differences ($p < 0.05$) are reflected by different superscripts on the same row of data. Data (mean ± SD) are results from three independent experiments.

OPRNFs-2.0 % and OPRNFs-2.4 %) are shown in Fig. 4b. In the XRD diffractogram of PVA, characteristic peaks related to its crystal structure were present at 11.5°, 19.4°, 22.7° and 40.5°, which were in good agreement with the results in the study of Zhai, Shi, Zou, Wang, Jiang, Zhang, Huang, Zhang and Holmes [5]. Compared to PVA, no significant sharp peaks appeared in the XRD patterns of OSA and RS, and only broad peaks centered at $2\theta = 19.0^\circ$ were observed. This is attributed to the fact that OSA and RS presented an amorphous pattern, which is consistent with previous reports [33]. With OSA doped into PVA and electrospun into nanofiber mats, the diffraction peaks of OPNFs at $2\theta = 19.0^\circ$ were attenuated compared to PVA and the OPNFs also showed no characteristic peaks of PVA at 11.5°, 22.7° and 40.5°. This indicates that the addition of OSA starch disrupted the crystallinity of PVA, while the disappearance of the characteristic PVA peaks indirectly illustrated the excellent compatibility of the OSA/PVA matrix [34]. As shown in Fig. 4b, the diffraction peak intensity of OPRNFs at $2\theta = 19.0^\circ$ climbs with increasing addition amount of RS in OPNFs. The phenomenon of increased crystallinity of OPRNFs nanofiber mats may be due to the enhancement of crystalline regions and molecular interactions (hydrogen bonding and electrostatic interactions) between RS, OSA and PVA [32]. Notably, the XRD patterns of the prepared OPRNFs nanofiber mats were almost identical to those of the OPNFs, which demonstrated that RS was successfully immobilized in the OSA/PVA membrane matrix

through hydrogen bonding and exhibited good compatibility. This result is consistent with the conclusions drawn from FT-IR and SEM analyses [35].

3.5. Thermal stability analysis

The thermal stability profiles of RS and prepared nanofiber mats (OPNFs, OPRNFs-1.2 %, OPRNFs-1.6 %, OPRNFs-2.0 % and OPRNFs-2.4 %) obtained by a thermogravimetric analyzer are shown in Fig. 5a and b. The TGA curves indicate the relationship between the mass of the nanofiber mats and the temperature while the differential thermogravimetric curve (DTG) curves reveal the variation profile of the maximum mass loss rate temperature for different nanofiber mats. As shown in Fig. 5a, OPRNFs nanofiber mats (OPRNFs-1.2 %, OPRNFs-1.6 %, OPRNFs-2.0 % and OPRNFs-2.4 %) showed similar trends in mass change. Slight loss of quality occurred in OPRNFs between 30 °C and 120 °C, which was mainly attributed to the evaporation of physically adsorbed water. The rapid evaporation of water molecules might be related to the high porosity and low densification of electrospun nanofiber mats [36]. Two different weight loss steps occurred after thermal degradation, which could be supported by the appearance of different reaction peaks in the DTG curves. The thermal decomposition temperature ranges for the first stage of OPRNFs-1.2 %, OPRNFs-1.6 %, OPRNFs-2.0 % and OPRNFs-2.4 % nanofibers were 225 °C–302 °C, 230 °C–320 °C, 233 °C–325 °C and 240 °C–330 °C, respectively ($T_{\text{dmax}} = 270.42^\circ\text{C}$ – 283.41°C). This is due to the thermal degradation of OSA, PVA and RS in the nanofiber mats, which is the main mass loss stage of OPRNFs nanofibers (weight loss rate: 20.89 %–59.68 %). The temperature range for the second weight loss step is 400 °C–500 °C ($T_{\text{dmax}} = 409.09^\circ\text{C}$ – 433.39°C , weight loss rate: 16.12 %–28.58 %). The complete degradation of PVA and its byproducts and the final decomposition of ash are the main causes of weight loss at this stage [37]. As shown in Fig. 5a, the onset temperature of weight loss of RS in the first stage was 190 °C. However, OPRNFs nanofibers prepared by the electrospinning technique had weight loss initiation temperatures (the first stage) in the range of 225 °C–240 °C, which indicated that the electrospinning technique was effective in encapsulating and enhancing the thermal stability of RS, which was consistent with the results observed by SEM. Meanwhile, as shown in Fig. 5b, the maximum mass loss rate temperature values (i.e., peak decomposition temperatures) of OPRNFs increased from 270.42 °C and 409.09 °C (OPRNFs-1.2 %) to 283.41 °C and 433.39 °C (OPRNFs-2.4 %), respectively, with the increase in the

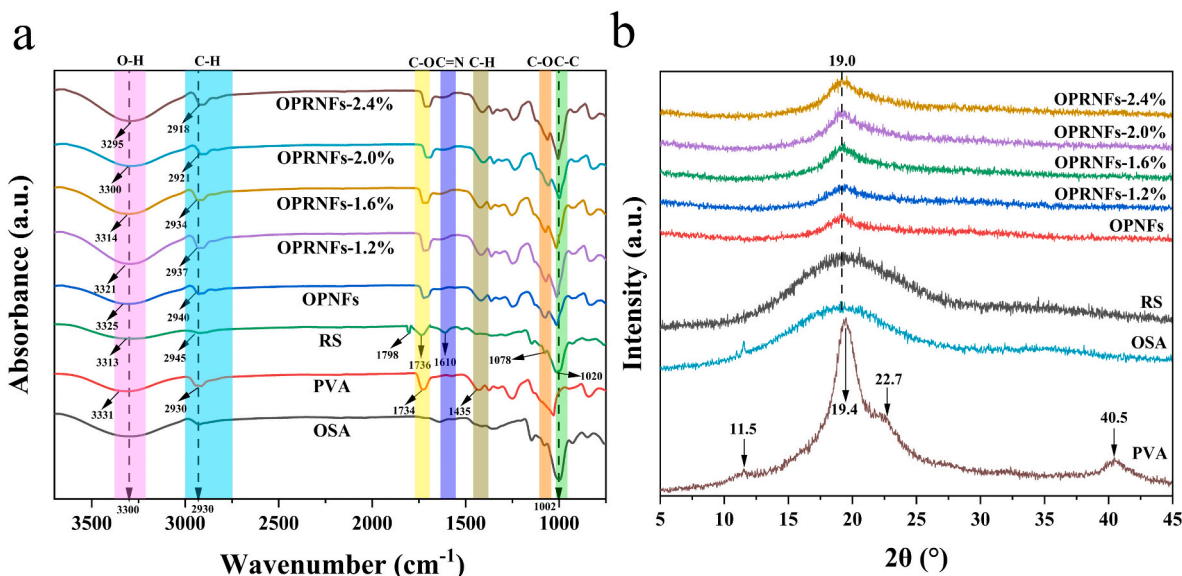


Fig. 4. (a) FTIR spectra and (b) XRD patterns of OSA, PVA, RS, OPNFs and OPRNFs.

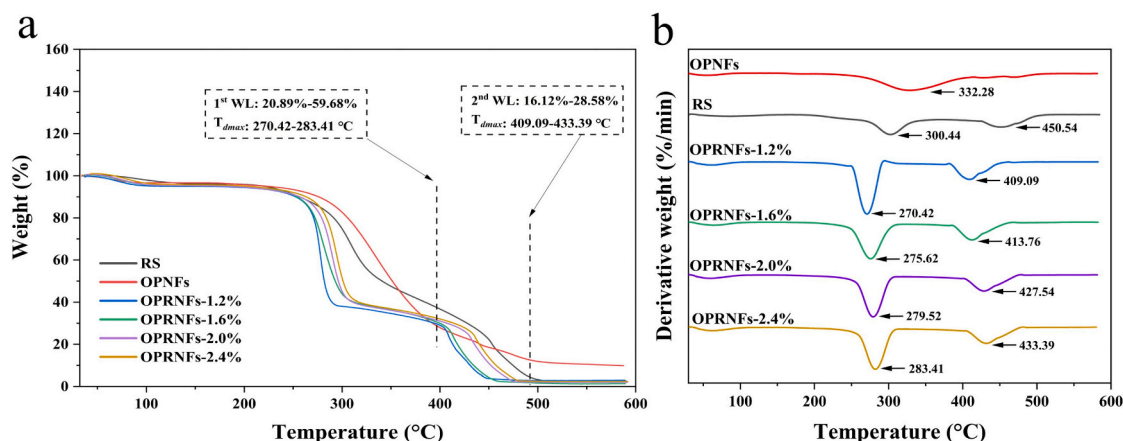


Fig. 5. (a) TGA and (b) DTG curves of RS powder, OPNFs and OPRNFs.

proportion of RS in the blends. A higher concentration of RS exists in the nanofiber mats exhibit higher stability, revealing the presence of interactions (hydrogen bonding) between RS and the OSA/PVA matrix, which is in accordance with the results obtained from the SEM, FT-IR, XRD and TGA analyses.

3.6. WCA analysis

WCA is considered to be a visual indicator for evaluating the wettability of a film surface. In general, the higher the contact angle, the more hydrophobic it is. When the WCA value is lower than 90° , the film is considered hydrophilic. As shown in Fig. 6, as the RS content increased from 0 % to 2.4 % (w/v), the WCA values of the fiber membranes decreased from $(62.6 \pm 1.0)^\circ$ (0 %) to $(58.2 \pm 1.5)^\circ$ (1.2 %), $(58.6 \pm 1.1)^\circ$ (1.6 %), $(53.4 \pm 0.8)^\circ$ (2.0 %) and $(50.2 \pm 1.3)^\circ$ (2.4 %), respectively. There is a large number of hydrophilic hydroxyl groups on the molecular chain of RS, thus the doping of RS has a certain enhancing effect on the hydrophilicity of the membrane. The same results were obtained for hydroxypropyl cellulose smart monitoring membranes doped with RS prepared by the casting method reported by Huang, Liu, Chen, Yao and Hu [38]. The amines produced during pork spoilage will provide $-OH$ groups when contacting the H_2O molecule, hence a certain degree of hydrophilicity is conducive to improving the sensitivity of SFL.

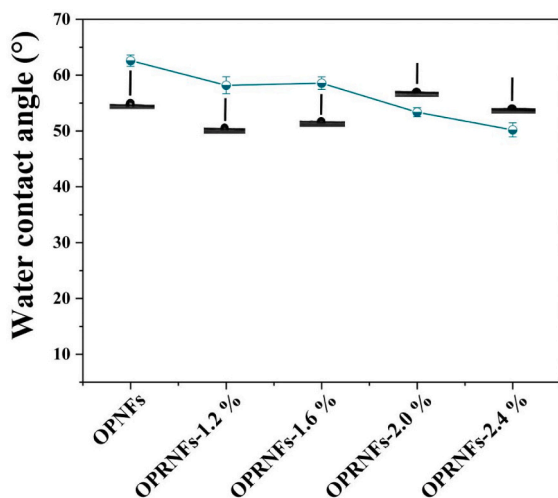


Fig. 6. (a) Water contact angle values of OPNFs and OPRNFs.

3.7. Colorimetric response tests for pH and ammonia vapor of OPRNFs

As shown in Fig. 7a, OPRNFs-2.4 % exhibited a similar trend of color change as RS solution at different pH values: pH 1–2 = dark red; pH 3–4 = light red; pH 5–7 = purple; pH 8 = light green; pH 9–10 = dark green; and pH 11–12 = yellow. The color parameters (L, a, b and ΔE) corresponding to OPRNFs-2.4 % at each pH stage are given in Table S2. The significant change in ΔE makes the process from pH 1 to 12 observable to the naked eye. In addition, the ΔE of OPRNFs-2.4 % showed a good linear relationship with pH in the range of 2–12 ($y = 4.0475x + 0.253$, $R^2 = 0.9632$). Referring to the methodology in the study of Goudarzi, Moshtaghi and Shahbazi et al. [20], the limit of detection (LOD) of 0.8 for OPRNFs-2.4 % was calculated by $LOD = 3.3 K/N$, where K represents the standard deviation of the blank measurement and N represents the slope of the calibration curve. As shown in Fig. 7c, OPRNFs-2.4 % underwent a continuous series of color changes (red \rightarrow green \rightarrow brown \rightarrow yellow) under continuous fumigation (within 30 min) with volatile ammonia. The sensitivity of OPRNFs-2.4 % to ammonia vapors increased significantly over time from $(11.7 \pm 1.5) \%$ at 5 min to $(34.7 \pm 2.5) \%$ at 15 min and reached $(81.7 \pm 1.5) \%$ at 30 min. The ΔE of OPRNFs-2.4 % also showed a good linear relationship ($y = 0.2502x + 31.039$, $R^2 = 0.9645$) with the concentration of ammonia (10–100 μM), which was symbolized by an LOD of 1.18 μM for ammonia with high sensitivity to ammonia vapor.

As shown in Tables 2 and 3, the color response and reversibility of OPRNFs-2.4 % were analyzed by exposing them successively to volatile ammonia (5 %) and acetic acid (10 %) with an exchange of order. Since ΔE is detectable by the naked eye at >5 [39], the color change made by OPRNFs-2.4 % in response to ambient pH changes was distinguishable. As shown in Table 2, within 35 s of exposure of OPRNFs-2.4 % to volatile ammonia, a significant color change occurred (red \rightarrow blue \rightarrow green), and the a and b values of OPRNFs-2.4 % changed from 38.1 ± 1.8 and 7.9 ± 0.3 to -16.9 ± 0.3 and -4.3 ± 0.3 , respectively. After that, OPRNFs-2.4 % were exposed to acetic acid and completed the color reversal process within 120 s (Table 2). During the colorimetric response test, ΔE increased sharply to 56.4 ± 0.7 and then decreased rapidly to 10.0 ± 0.7 (Table 2). This phenomenon indicates that OPRNFs-2.4 % can react with ammonia in the environment relatively quickly and return to normal rapidly after ammonia disappears, which proves that OPRNFs-2.4 % possesses a high color response sensitivity. In addition, color change reversibility is also an important factor affecting the intelligent detection performance of SFL. To test the reversibility of the color change of OPRNFs-2.4 %, the order of exposure was further exchanged. The color change and response sensitivity of OPRNFs-2.4 % was once again confirmed (Table 3). It is concluded that OPRNFs-2.4 % has the potential to be used as a pH-sensitive SFL for food freshness monitoring.

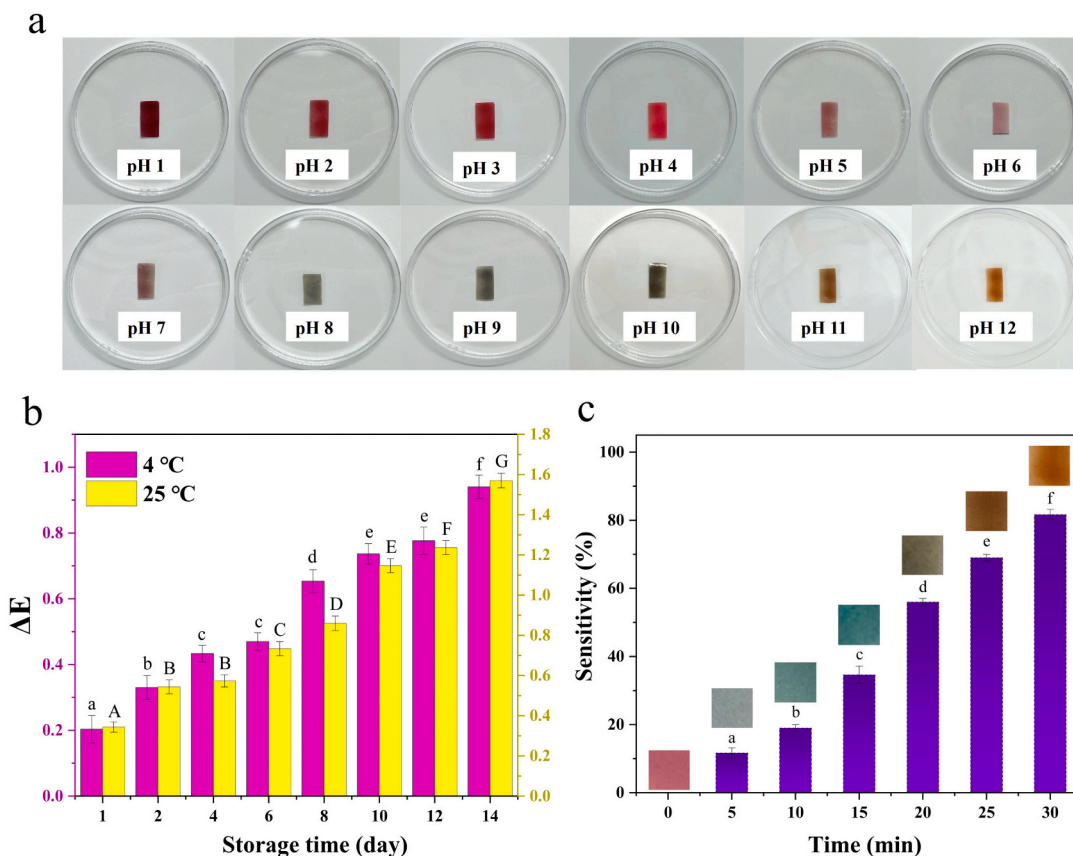


Fig. 7. (a) The color change of OPRNFs-2.4 % in the range of pH 1–12. (b) Color stability (ΔE values) of OPRNFs-2.4 % stored at 4 °C and 25 °C. (c) The sensitivity of OPRNFs-2.4 % to ammonia vapor. (For interpretation of the references to color in this figure, the reader is referred to the web version of this article.)

Table 2

Color response and corresponding parameters of OPRNFs-2.4 % after exposure to volatile ammonia and then acetic acid.

Times (s)	0	3	9	20	35 (0)	14	25	54	120
	Volatile ammonia (5%)					Acetic acid (10%)			
L	51.1 ± 0.4 ^b	62.5 ± 0.8 ^f	54.9 ± 2.3 ^d	52.1 ± 1.0 ^{bc}	48.1 ± 1.7 ^a	53.4 ± 0.5 ^{cd}	54.1 ± 0.5 ^{cd}	58.1 ± 0.4 ^c	54.7 ± 1.3 ^d
a	38.1 ± 1.8 ⁱ	-4.6 ± 0.5 ^d	-9.2 ± 0.4 ^c	-15.1 ± 0.4 ^b	-16.9 ± 0.3 ^a	10.1 ± 0.2 ^c	21.1 ± 0.4 ^f	27.2 ± 1.0 ^e	29.8 ± 1.0 ^b
b	7.9 ± 0.3 ^d	0.43 ± 0.1 ^c	1.5 ± 0.4 ^c	-1.9 ± 0.2 ^b	-4.3 ± 0.3 ^a	7.4 ± 0.2 ^d	10.9 ± 1.3 ^e	13.2 ± 0.5 ^f	12.0 ± 0.6 ^{ef}
ΔE	-----	47.9 ± 1.1 ^c	48.6 ± 0.9 ^c	54.1 ± 1.7 ^f	56.4 ± 0.7 ^f	28.1 ± 1.3 ^d	17.6 ± 0.9 ^c	14.1 ± 0.9 ^b	10.0 ± 0.7 ^a

Note: significant differences ($p < 0.05$) are reflected by different superscripts on the same row of data. Data (mean ± SD) are results from three independent experiments.

3.8. Color stability analysis

Color stability of OPRNFs is directly related to whether accurate information about the food being monitored is reflected. Thus, it is a key metric for evaluating the applicability of SFL in food freshness testing. Fig. 7b demonstrates the change in ΔE of OPRNFs-2.4 % after 14 days of storage at 4 °C and 25 °C, respectively. The test results show that the color difference value of the film at 4 °C ($\Delta E = 0.94 \pm 0.03$) is lower than that at 25 °C ($\Delta E = 1.57 \pm 0.03$), proving that OPRNFs-2.4 % possesses better color stability at 4 °C. Due to the hydrophilic nature of

RS, dehydration under storage conditions at 25 °C decreases the color stability of the indicator, causing OPRNFs-2.4 % to show higher ΔE values at 25 °C. As previously reported, the naked eye will not be able to catch the color change when ΔE is < 5 [40], as the maximum change in the ΔE value of OPRNFs-2.4 % during 14 days of storage at 4 °C and 25 °C was only 1.57, therefore, OPRNFs-2.4 % presented excellent color stability and can be used as a good medium to monitor whether spoilage of meat products occurs.

Table 3

Color response and corresponding parameters of OPRNFs-2.4 % after exposure to acetic acid and then volatile ammonia.

Times (s)	0	60	140	270 (0)	18	32	49	78	210
	Acetic acid (10%)				Volatile ammonia (5%)				
L	52.2 ± 0.8 ^a	40.1 ± 0.3 ^c	30.1 ± 0.2 ^b	17.2 ± 0.2 ^a	44.9 ± 0.5 ^d	60.6 ± 0.7 ⁱ	58.5 ± 0.5 ^h	50.0 ± 0.1 ^f	46.4 ± 0.5 ^e
a	36.6 ± 0.5 ^a	50.0 ± 0.1 ⁱ	35.0 ± 0.3 ^f	38.0 ± 0.8 ^b	20.5 ± 0.3 ^c	-3.6 ± 0.5 ^d	-11.6 ± 0.5 ^e	-12.6 ± 0.6 ^b	-18.5 ± 0.2 ^a
b	8.3 ± 0.1 ^d	16.3 ± 0.8 ^f	11.7 ± 0.4 ^e	24.1 ± 0.3 ^a	8.4 ± 0.1 ^d	-1.2 ± 0.1 ^b	3.4 ± 0.5 ^c	-1.7 ± 0.1 ^b	-3.5 ± 0.3 ^a
ΔE	-----	66.2 ± 1.2 ^f	47.7 ± 0.8 ^a	48.1 ± 0.7 ^a	50.2 ± 0.6 ^b	60.7 ± 0.4 ^c	59.8 ± 0.9 ^d	51.7 ± 0.5 ^c	50.2 ± 0.7 ^b

Note: significant differences ($p < 0.05$) are reflected by different superscripts on the same row of data. Data (mean ± SD) are results from three independent experiments.

3.9. Application for pork freshness monitoring

Volatile nitrogen compounds produced by the breakdown of its proteins during storage of pork and shrimp samples can lead to a rise in pH in the package. To test the potential of OPRNFs-2.4 % smart fiber mats in monitoring the freshness of meat and seafood products, the relationship between the color change of OPRNFs-2.4 % and freshness was expressed by measuring TVB-N levels, pH, TVC and ΔE values

during storage (Fig. 8a–d). As shown in Fig. 9, the OPNFs group experienced no color changes throughout the storage period. Notably, OPRNFs-2.4 % group showed a series of significant color changes throughout the deterioration of meat: red (0 h), light red (24 h), pink (36 h), purple (48 h), light green (60 h) and dark green (72 h). The light red color of OPRNFs-2.4 % corresponded to a TVB-N of (14.5 ± 0.3) mg/100 g (pH = 5.95 ± 0.03, TVC = 4.09 ± 0.06, ΔE = 17.04 ± 0.63), indicating that the meat was in a fresh state (TVB-N < 15 mg/100 g,

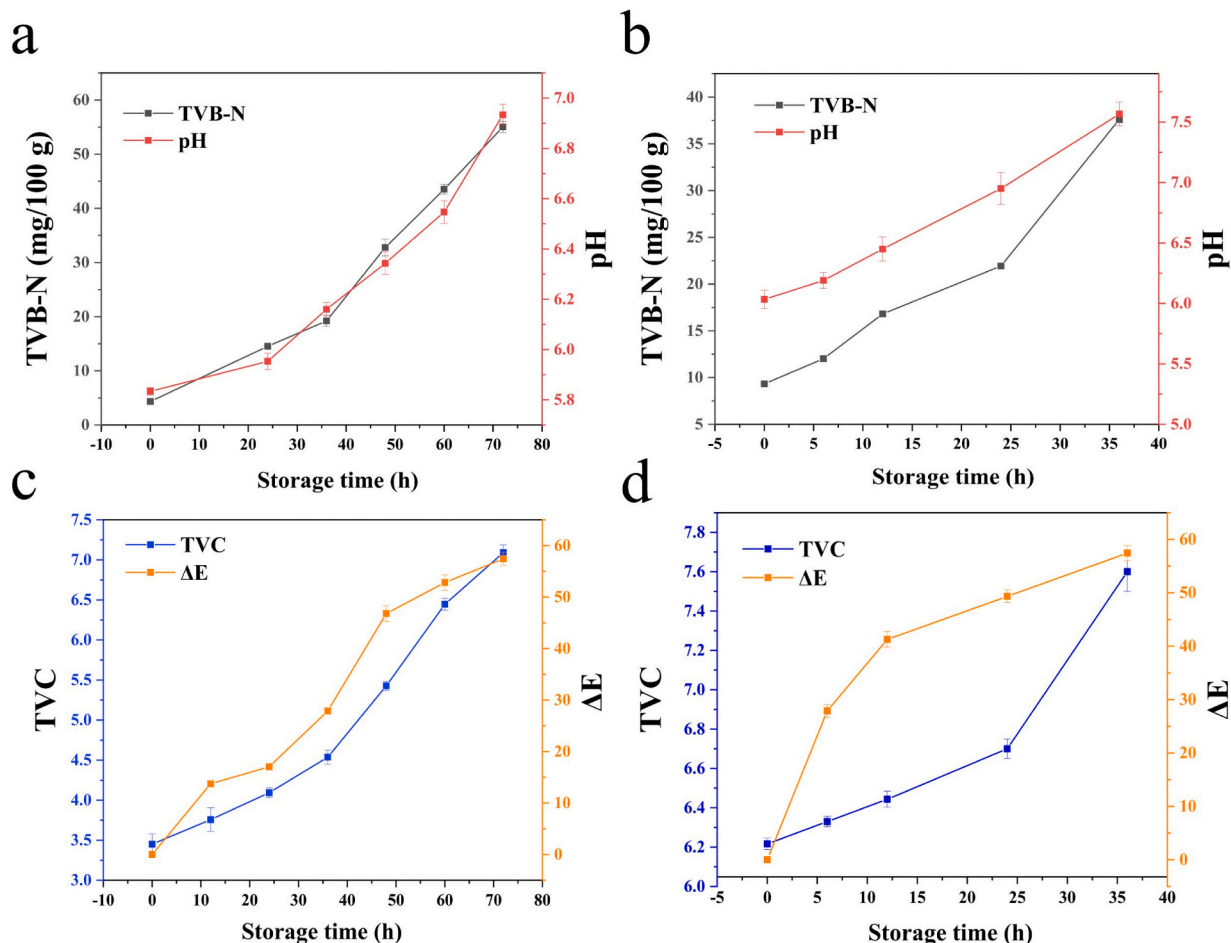


Fig. 8. TVB-N and pH values of (a) pork and (b) shrimp during storage. TVC and ΔE values of (c) pork and (d) shrimp during storage.

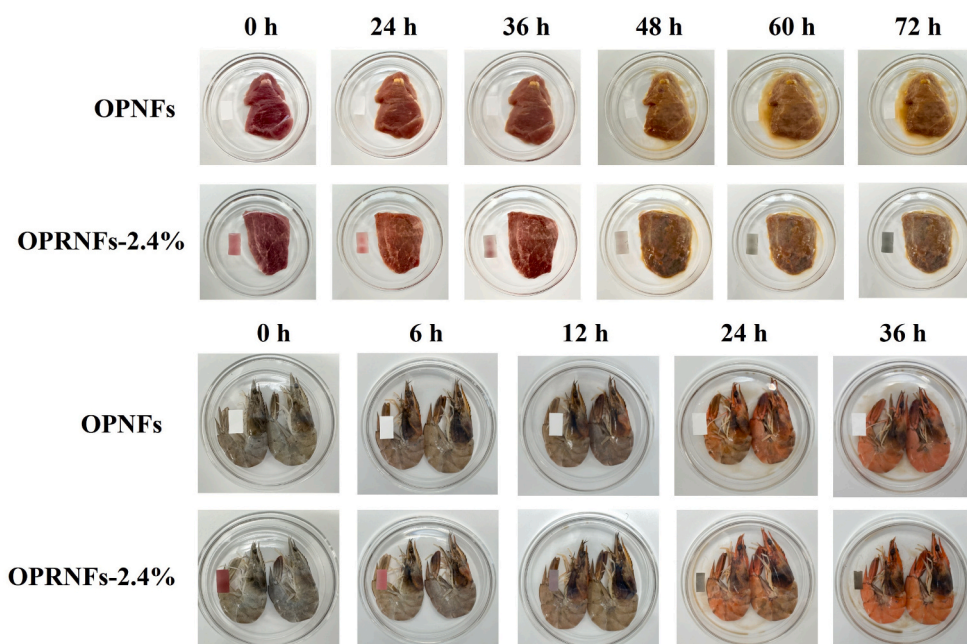


Fig. 9. Photographs of OPNFs and OPRNFs-2.4 % for freshness monitoring of pork and shrimp at 25 °C. (For interpretation of the references to color in this figure, the reader is referred to the web version of this article.)

Chinese standard GB 2707-2016). The pink color of OPRNFs-2.4 % corresponded to a TVB-N of (19.2 ± 1.0) mg/100 g ($\text{pH} = 6.16 \pm 0.02$, $\text{TVC} = 4.54 \pm 0.08$, $\Delta E = 27.88 \pm 0.48$), indicating that the pork had begun to deteriorate. During the transformation of OPRNFs-2.4 % from pink to dark green color, the TVB-N increased from (19.2 ± 1.0) mg/100 g to (55.0 ± 1.0) mg/100 g and the environmental pH increased from 6.16 ± 0.02 to 6.93 ± 0.04 owing to the accumulation of volatile ammonia, which indicated that the pork had been completely spoiled.

Concerning the monitoring of fresh shrimp, significant color responses also occurred for OPRNFs-2.4 %: red (0 h), pink (6 h), purple (12 h), light green (24 h) and dark green (36 h). The light green color of OPRNFs-2.4 % corresponded to a TVB-N of (21.9 ± 0.1) mg/100 g ($\text{pH} = 6.95 \pm 0.13$, $\text{TVC} = 6.70 \pm 0.05$, $\Delta E = 54.08 \pm 0.91$). According to the Chinese standard (GB 2733-2015), the retention limit of TVB-N in seawater shrimp is 30 mg/100 g. Therefore, the light green color of OPRNFs-2.4 % indicated that the shrimp were in a fresh state ($\text{TVB-N} < 30$ mg/100 g, Chinese standard GB 2733-2015). When OPRNFs-2.4 % changed into dark green color, the corresponding TVB-N was (37.6 ± 0.4) mg/100 g ($\text{pH} = 7.57 \pm 0.09$, $\text{TVC} = 7.60 \pm 0.05$, $\Delta E = 57.43 \pm 1.42$), which indicated that the shrimp had been completely spoiled.

According to the results, the RS indicating activity in the matrix of OPNFs was well maintained. During the storage process, a significant change in ΔE occurred which was highly positively correlated with TVB-N, TVC and pH. Therefore, OPRNFs-2.4 % could achieve the efficacy of monitoring the freshness of pork.

4. Conclusions

In this study, a pH-sensitive SFL based on OSA/PVA/RS was developed by electrospinning technology. Good morphology, thermal stability, pH sensitivity and color stability of the novel SFL were obtained. In addition, by using a colorimetric film, the naked eye can visually distinguish the freshness, sub-freshness and spoilage of pork (red \rightarrow light red \rightarrow pink \rightarrow purple \rightarrow light green \rightarrow dark green) and shrimp (red \rightarrow pink \rightarrow purple \rightarrow light green \rightarrow dark green) based on the color of the film. Therefore, the OSA/PVA/RS nanofiber mats can be used as an intelligent SFL for reminding consumers of the best eating period of the food they purchased and providing early warning of food spoilage. The natural biopolymer and natural colorant-based SFL developed in this

study has great potential for application in improving food safety and reducing food waste, which has profound implications for the development of a safer and more sustainable food supply chain. However, it is difficult to realize the full encapsulation of anthocyanins by a single electrospinning technique, thus its stability will be somewhat reduced and may affect the color rendering of SFL, which is detrimental to the widespread commercialization of OPRNFs-2.4 %. How to further improve the stability of anthocyanins will be the focus of the research in the future. For example, the preparation of electrospun nanofibers with a core-shell structure is one of the possibly advanced strategies to improve the stability of encapsulated anthocyanin. In addition, screening modified starch with lower cost and higher electrospinnability as raw material, and developing smart APP for mobile are also effective measures that can accelerate the realization of commercial application of OPRNFs-2.4 %.

CRediT authorship contribution statement

Haowei Lv: Investigation, Writing – original draft. **Chenxi Wang:** Investigation, Writing – original draft. **Deyun He:** Funding acquisition, Investigation, Writing – original draft. **Haibo Zhao:** Funding acquisition, Investigation, Methodology, Writing – review & editing. **Meng Zhao:** Formal analysis, Writing – review & editing. **Enbo Xu:** Formal analysis, Writing – review & editing. **Zhengyu Jin:** Visualization, Writing – review & editing. **Chao Yuan:** Formal analysis, Writing – review & editing. **Li Guo:** Formal analysis, Funding acquisition. **Zhengzong Wu:** Conceptualization, Funding acquisition, Project administration, Supervision, Writing – review & editing. **Pengfei Liu:** Formal analysis, Funding acquisition, Writing – review & editing. **Bo Cui:** Funding acquisition, Project administration, Supervision, Writing – review & editing.

Declaration of competing interest

The authors declare that they have no known competing financial interests or personal relationships that could have appeared to influence the work reported in this paper.

Acknowledgements

This research was supported by the Key Research and Development Program of Shandong Province (2022TZXD0028, 2021CXGC010808, 2022TZXD0021 and 2023CXGC010708), “Youth Innovation Team Program” of Colleges and Universities in Shandong Province (2022KJ129), Natural Science Foundation of Shandong Province (ZR2021QC011), Research Leader Workshop of Jinan (2021GXRC101), Major Innovation Pilot Project of Integration of Science, Education and Industry of Qilu University of Technology (Shandong Academy of Sciences) (No. 2022JBZ01-08) and Innovation Pilot Project of Integration of Science, Education and Industry of Qilu University of Technology (2022PY010, 2022PY014 and 2023PX018) and Special Funds for Taishan Scholars Project.

Appendix A. Supplementary data

Supplementary data to this article can be found online at <https://doi.org/10.1016/j.ijbiomac.2023.128384>.

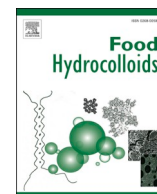
References

- J.M. Dages, Active and intelligent packaging materials chapter for global legislation for food contact materials book, in: J.S. Baughan (Ed.), *Global Legislation for Food Contact Materials*, Second edition, Woodhead Publishing, 2022, pp. 203–209.
- L. Shao, S. Chen, H. Wang, J. Zhang, X. Xu, H. Wang, Advances in understanding the predominance, phenotypes, and mechanisms of bacteria related to meat spoilage, *Trends Food Sci. Technol.* 118 (2021) 822–832.
- Q. Tang, J. Hu, S. Li, S. Lin, Y. Tu, X. Gui, Y. Dong, Preparation of an aramid nanofiber-reinforced colorimetric hydrogel employing natural anthocyanin as an indicator for shrimp and fish spoilage monitoring, *Eur. Polym. J.* 187 (2023), 111889.
- P. Amchova, H. Kotolova, J. Ruda-Kucerova, Health safety issues of synthetic food colorants, *Regul. Toxicol. Pharmacol.* 73 (3) (2015) 914–922.
- X. Zhai, J. Shi, X. Zou, S. Wang, C. Jiang, J. Zhang, X. Huang, W. Zhang, M. Holmes, Novel colorimetric films based on starch/polyvinyl alcohol incorporated with rosele anthocyanins for fish freshness monitoring, *Food Hydrocoll.* 69 (2017) 308–317.
- N. Echeagaray, N. Guzel, M. Kumar, M. Guzel, A. Hassoun, J.M. Lorenzo, Recent advancements in natural colorants and their application as coloring in food and in intelligent food packaging, *Food Chem.* 404 (2023), 134453.
- J.A. Valencia-Arredondo, G.I. Hernández-Bolio, G.I. Cerón-Montes, R. Castro-Muñoz, J. Yáñez-Fernández, Enhanced process integration for the extraction, concentration and purification of di-acylated cyanidin from red cabbage, *Sep. Purif. Technol.* 238 (2020).
- X. Peng, M. Umer, M.N. Pervez, K.M.F. Hasan, M.A. Habib, M.S. Islam, L. Lin, X. Xiong, V. Naddeo, Y. Cai, Biopolymers-based microencapsulation technology for sustainable textiles development: a short review, *Case Stud. Chem. Environ. Eng.* 7 (2023), 100349.
- P. Saini, Kamalesu, Lalita, Manikanika, Review on nanotechnology “Impact on the food services industry”, *Mater. Today Proc.* (2023).
- L. Liu, W. Wu, L. Zheng, J. Yu, P. Sun, P. Shao, Intelligent packaging films incorporated with anthocyanins-loaded ovalbumin-carboxymethyl cellulose nanocomplexes for food freshness monitoring, *Food Chem.* 387 (2022), 132908.
- Z. Du, H. Lv, C. Wang, D. He, E. Xu, Z. Jin, C. Yuan, L. Guo, Z. Wu, P. Liu, B. Cui, Organic solvent-free starch-based green electrospun nanofiber mats for curcumin encapsulation and delivery, *Int. J. Biol. Macromol.* 232 (2023), 123497.
- H. Cheng, H. Xu, D. Julian McClements, L. Chen, A. Jiao, Y. Tian, M. Miao, Z. Jin, Recent advances in intelligent food packaging materials: principles, preparation and applications, *Food Chem.* 375 (2022), 131738.
- T. Min, L. Zhou, X. Sun, H. Du, Z. Zhu, Y. Wen, Electrospun functional polymeric nanofibers for active food packaging: a review, *Food Chem.* 391 (2022), 133239.
- H. Lu, Q. Wang, G. Li, Y. Qiu, Q. Wei, Electrospun water-stable zein/ethyl cellulose composite nanofiber and its drug release properties, *Mater. Sci. Eng. C* 74 (2017) 86–93.
- G. Liu, Z. Gu, Y. Hong, L. Cheng, C. Li, Electrospun starch nanofibers: recent advances, challenges, and strategies for potential pharmaceutical applications, *J. Control. Release* 252 (2017) 95–107.
- J.H. Jang, H.J. Kang, O.E. Adedeji, G.Y. Kim, J.K. Lee, D.H. Kim, Y.H. Jung, Development of a pH indicator for monitoring the freshness of minced pork using a cellulose nanofiber, *Food Chem.* 403 (2023).
- S. Cao, S. Wang, Q. Wang, G. Lin, B. Niu, R. Guo, H. Yan, H. Wang, Sodium alginate/chitosan-based intelligent bilayer film with antimicrobial activity for pork preservation and freshness monitoring, *Food Control* 148 (2023), 109615.
- C. Cui, N. Ji, Y. Wang, L. Xiong, Q. Sun, Bioactive and intelligent starch-based films: a review, *Trends Food Sci. Technol.* 116 (2021) 854–869.
- Y. Bao, H. Cui, J. Tian, Y. Ding, Q. Tian, W. Zhang, M. Wang, Z. Zang, X. Sun, D. Li, X. Si, B. Li, Novel pH sensitivity and colorimetry-enhanced anthocyanin indicator films by chondroitin sulfate co-pigmentation for shrimp freshness monitoring, *Food Control* 131 (2022), 108441.
- J. Goudarzi, H. Moshtaghi, Y. Shahbazi, Kappa-carrageenan-poly(vinyl alcohol) electrospun fiber mats encapsulated with *Prunus domestica* anthocyanins and epigallocatechin gallate to monitor the freshness and enhance the shelf-life quality of minced beef meat, *Food Packag. Shelf Life* 35 (2023).
- C. Zhang, W. Chi, T. Zhou, Y. Wang, J. Li, L. Wang, Fabricating a visibly colorimetric film via self-releasing of anthocyanins from distributed mulberry pomace particles in hydrophilic sodium carboxymethyl starch-based matrix to monitor meat freshness, *Int. J. Biol. Macromol.* 246 (2023), 125617.
- C. Grajeda-Iglesias, E. Salas, N. Barouh, B. Baréa, M.C. Figueroa-Espinoza, Lipophilization and MS characterization of the main anthocyanins purified from hibiscus flowers, *Food Chem.* 230 (2017) 189–194.
- A.P.R. Charles, T.Z. Jin, R. Mu, Y. Wu, Electrohydrodynamic processing of natural polymers for active food packaging: a comprehensive review, *Compr. Rev. Food Sci. Food Saf.* 20 (6) (2021) 6027–6056.
- S. Li, L. Kong, G.R. Ziegler, Electrospinning of octenylsuccinylated starch-pullulan nanofibers from aqueous dispersions, *Carbohydr. Polym.* 258 (2021), 116933.
- A. Doderio, G. Schlatter, A. Hébraud, S. Vicini, M. Castellano, Polymer-free cyclodextrin and natural polymer-cyclodextrin electrospun nanofibers: a comprehensive review on current applications and future perspectives, *Carbohydr. Polym.* 264 (2021), 118042.
- M. Duan, J. Sun, Y. Huang, H. Jiang, Y. Hu, J. Pang, C. Wu, Electrospun gelatin/chitosan nanofibers containing curcumin for multifunctional food packaging, *Food Sci. Human Wellness* 12 (2) (2023) 614–621.
- Z. Aghaei, B. Ghorani, B. Emadzadeh, R. Kadkhodae, N. Tucker, Protein-based halochromic electrospun nanosensor for monitoring trout fish freshness, *Food Control* 111 (2020), 107065.
- Y. Liu, D. Wang, Z. Sun, F. Liu, L. Du, D. Wang, Preparation and characterization of gelatin/chitosan/3-phenylacetic acid food-packaging nanofiber antibacterial films by electrospinning, *Int. J. Biol. Macromol.* 169 (2021) 161–170.
- C. Wu, Y. Li, Y. Du, L. Wang, C. Tong, Y. Hu, J. Pang, Z. Yan, Preparation and characterization of konjac glucomannan-based bionanocomposite film for active food packaging, *Food Hydrocoll.* 89 (2019) 682–690.
- J.N.N. Bueno, E. Corradini, P.R. de Souza, V.d.S. Marques, E. Radovanovic, E. C. Muniz, Films based on mixtures of zein, chitosan, and PVA: development with perspectives for food packaging application, *Polym. Test.* 101 (2021), 107279.
- J. Zhang, X. Zou, X. Zhai, X. Huang, C. Jiang, M. Holmes, Preparation of an intelligent pH film based on biodegradable polymers and rosele anthocyanins for monitoring pork freshness, *Food Chem.* 272 (2019) 306–312.
- J. Sun, Y. Du, J. Ma, Y. Li, L. Wang, Y. Lu, J. Zou, J. Pang, C. Wu, Transparent bionanocomposite films based on konjac glucomannan, chitosan, and TEMPO-oxidized chitin nanocrystals with enhanced mechanical and barrier properties, *Int. J. Biol. Macromol.* 138 (2019) 866–873.
- Z. Li, W. Weng, Z. Ren, Y. Zhang, S. Li, L. Shi, Electrospun octenylsuccinylated starch-pullulan nanofiber mats: adsorption for the odor of oyster peptides and structural characterization, *Food Hydrocoll.* 133 (2022), 107992.
- J. Zheng, Y. Hu, C. Su, W. Liang, X. Liu, W. Zhao, Z. Sun, X. Zhang, Y. Lu, H. Shen, X. Ge, G. Ospankulova, W. Li, Structural, physicochemical and biodegradable properties of composite plastics prepared with polyvinyl alcohol (PVA), OSA potato starch and gliadin, *J. Food Eng.* 339 (2023), 111278.
- A. Celebioglu, T. Uyar, Fast-dissolving antioxidant curcumin/cyclodextrin inclusion complex electrospun nanofibrous webs, *Food Chem.* 317 (2020), 126397.
- M.S. Enayati, T. Behzad, P. Sajkiewicz, R. Bagheri, L. Ghasemi-Mobarakeh, W. Łojkowski, Z. Pahlevanneshan, M. Ahmadi, Crystallinity study of electrospun poly(vinyl alcohol) nanofibers: effect of electrospinning, filler incorporation, and heat treatment, *Iran. Polym. J.* 25 (7) (2016) 647–659.
- J. Huang, M. Chen, Y. Zhou, Y. Li, Y. Hu, Functional characteristics improvement by structural modification of hydroxypropyl methylcellulose modified polyvinyl alcohol films incorporating rosele anthocyanins for shrimp freshness monitoring, *Int. J. Biol. Macromol.* 162 (2020) 1250–1261.
- J. Huang, J. Liu, M. Chen, Q. Yao, Y. Hu, Immobilization of rosele anthocyanins into polyvinyl alcohol/hydroxypropyl methylcellulose film matrix: study on the interaction behavior and mechanism for better shrimp freshness monitoring, *Int. J. Biol. Macromol.* 184 (2021) 666–677.
- L. Prietto, T.C. Mirapalhete, V.Z. Pinto, J.F. Hoffmann, N.L. Vanier, L.-T. Lim, A. R. Guerra Dias, E. da Rosa Zavareze, pH-sensitive films containing anthocyanins extracted from black bean seed coat and red cabbage, *LWT* 80 (2017) 492–500.
- D. Liu, S. Dang, L. Zhang, K. Munsop, X. Li, Corn starch/polyvinyl alcohol based films incorporated with curcumin-loaded Pickering emulsion for application in intelligent packaging, *Int. J. Biol. Macromol.* 188 (2021) 974–982.

ARTICLES FOR FACULTY MEMBERS

ROSELLE (HIBISCUS SABDARIFFA) ANTHOCYANIN USE IN MONITORING MEAT FRESHNESS

Title/Author	<p>Multifunctional halochromic packaging materials: Saffron petal anthocyanin loaded-chitosan nanofiber/methyl cellulose matrices / Alizadeh-Sani, M., Tavassoli, M., McClements, D. J., & Hamishehkar, H.</p>
Source	<p><i>Food Hydrocolloids</i> Volume 111 (2021) 106237 Pages 1-13 https://doi.org/10.1016/J.FOODHYD.2020.106237 (Database: ScienceDirect)</p>



Multifunctional halochromic packaging materials: Saffron petal anthocyanin loaded-chitosan nanofiber/methyl cellulose matrices

Mahmood Alizadeh-Sani^a, Milad Tavassoli^b, David Julian McClements^{c,*},
Hamed Hamishehkar^{d,**}

^a Student's Scientific Research Center, Department of Food Safety and Hygiene, School of Public Health, Tehran University of Medical Sciences, Tehran, Iran

^b Student Research Committee, Department of Food Science and Technology, Faculty of Nutrition and Food Sciences, Tabriz University of Medical Sciences, Tabriz, Iran

^c Department of Food Science, University of Massachusetts Amherst, Amherst, MA, 01003, USA

^d Drug Applied Research Center, Tabriz University of Medical Sciences, Tabriz, Iran

ARTICLE INFO

Keywords:

Halochromic material
Colorimetric indicator
Natural colorants
Smart packaging
Saffron anthocyanins

ABSTRACT

A new generation of eco-friendly packaging materials is required to improve food quality, safety, nutritional value, shelf-life, and sustainability. In this study, a novel multifunctional halochromic packaging material was fabricated by immobilizing saffron petal anthocyanins within a biopolymer matrix consisting of chitosan nanofibers and methyl cellulose. The gas barrier, light screening, physico-mechanical, and optical properties of the films were then characterized. The color of the multifunctional films depended on pH and ammonia gas levels as a result of changes in the molecular structure of the anthocyanins. The films changed from reddish/pink to violet to green to yellow as the pH was increased from 1 to 14, and went from violet to green/yellow when the ammonia vapor concentration was increased. Incorporation of the anthocyanins into the films also increased their tensile strength, light screening properties, antimicrobial activity (*E. coli* & *S. aureus*), and antioxidant activity (DPPH radical scavenging). Analysis of the microstructure and spectroscopic properties of the films showed that the anthocyanins were compatible with the surrounding biopolymer matrix. Finally, we showed that the anthocyanin-loaded films could be used as smart packaging materials for monitoring changes in the freshness of a model meat product (lamb) during storage.

1. Introduction

Recently, there has been interest in the development of a new generation of active and smart food packaging materials with enhanced functional properties (Rai et al., 2019). Active packaging materials contain additives that improve the chemical or microbial stability of foods, such as antioxidants and antimicrobials (Alizadeh-Sani, Mohammadian, & McClements, 2020). Smart packaging materials are designed to monitor the environmental conditions foods experience throughout their lifetime, as well as to detect changes in their chemical composition, and then provide a readable response, such as a color change (Biji, Ravishankar, Mohan, & Gopal, 2015; Kerry & Butler, 2008). As a result, they can be used to provide manufacturers, suppliers, and consumers with information about the quality and microbial contamination of foods, which can help reduce food waste and improve food safety. Ideally, it would be advantageous to create smart and active

packaging materials that can also perform a multitude of other functions. For instance, they should have good mechanical properties, the ability to control the flow of gas and water, and the ability to control exposure to damaging ultraviolet or visible radiation. The purpose of the current study was therefore to create smart and active packaging materials from natural biodegradable components, which also had many of these other desirable attributes.

There are numerous substances in nature that can be used as sensors in smart packaging materials because they give measurable changes in their properties in response to alterations in their environment (Pereira, de Arruda, & Stefani, 2015; Wang, Xia, et al., 2019; Yong, Wang, Bai, et al., 2019). For instance, they may respond to alterations in temperature, pressure, electrical conductivity, gas concentrations, or pH, which can provide valuable information about the quality status of a food product (Biji et al., 2015). Ideally, smart food packaging systems should monitor the quality status of foods in real-time, which can be achieved

* Corresponding author.

** Corresponding author.

E-mail addresses: mccllements@foodsci.umass.edu (D.J. McClements), Hamishehkar.hamed@gmail.com (H. Hamishehkar).

<https://doi.org/10.1016/j.foodhyd.2020.106237>

Received 6 May 2020; Received in revised form 27 July 2020; Accepted 1 August 2020

Available online 7 August 2020

0268-005X/© 2020 Elsevier Ltd. All rights reserved.

by emitting a signal (colorimetric, optical, chemical, electric, etc.) in response to alterations in specific conditions (Biji et al., 2015; Liang, Sun, Cao, Li, & Wang, 2019). Several types of smart packaging materials have recently been developed based on colorimetric sensors, which may be natural or synthetic (Ma, Du, & Wang, 2017; Saliu & Della Pergola, 2018; Sun, Ye, Xia, Zhao, & Wang, 2016; Zhang, Zou, et al., 2019). Recently, however, there has been growing interest in the utilization of natural colorants for this purpose so as to make more sustainable and environmentally-friendly foods and packaging materials (Feketea & Tsabouri, 2017; Pereira Jr, de Arruda, & Stefani, 2015).

Another important focus of modern food packaging research is the replacement of synthetic materials (such as plastics) with natural ones (such as proteins and polysaccharides) so as to increase their sustainability and reduce their negative environmental impacts (Alizadeh-Sani, Ehsani, Kia, & Khezerlou, 2019; Alizadeh-Sani, Rhim, Azizi-Lalabadi, Hemmati-Dinarvand, & Ehsani, 2020; Yong, Wang, Bai, et al., 2019; Zhai et al., 2017). Chitosan nanofibers (CNFs) and methyl cellulose (MC) are biodegradable, non-toxic, and eco-friendly polysaccharides that are particularly suitable for the creation of eco-friendly packaging materials due to their film-forming properties (Wu et al., 2019; Yong, Wang, Bai, et al., 2019). However, the functional attributes of the films formed by these polysaccharides are often unsuitable for commercial applications and so they must be extended by using them in combination with other functional materials, such as natural fillers, antioxidants, antimicrobials, or optical modifiers (de Dicastillo, Bustos, Guarda, & Galotto, 2016a; De Dicastillo, Rodríguez, Guarda, & Galotto, 2016b; Kurek et al., 2018; Liu, Meng, Liu, Kan, & Jin, 2017). Previous studies have shown that incorporating chitosan nanofibers into methyl cellulose matrices can improve the moisture barrier and mechanical resistance of the composite materials, which was mainly attributed to the formation of strong hydrogen bonds between the biopolymers (Buraidah & Arof, 2011). As a result, the films were more stable to disintegration when exposed to the high relative humidity conditions found in high water activity foods.

Past research have shown that anthocyanins are suitable as natural pigments, colorimetric indicators, and antioxidants in films (Kang et al., 2020; Liang et al., 2019; Zhang, Liu, et al., 2019). Anthocyanins isolated from a wide range of fruits and vegetables can be used for this purpose (Pereira et al., 2015; Wang, Yong, et al., 2019; Zhai et al., 2017). The visible absorption spectrum, and therefore color, of anthocyanins varies with pH, temperature, and the presence of certain gasses in the environment, which means that they can be used as sensors of their environment. Saffron (*Crocus sativus* L.), also known as “red gold”, contains high levels of anthocyanins and other phenolic compounds (Ahmad, Ashraf, Gani, & Gani, 2018; Da Porto & Natolino, 2018). As a result, it can be used as a natural pigment, colorimetric sensor, and antioxidant in active and smart packaging materials (Ahmad et al., 2018; Da Porto et al., 2018). As a sensor, it can be used to visually detect food spoilage by undergoing a color change in response to an alteration in the pH or other properties of a food product.

In this study, we focus on the development of smart eco-friendly packaging materials that are sensitive to food spoilage indicators, with the aim of applying them to improve the quality and shelf-life of meat and seafood products. Moreover, these packaging materials were also designed so that they provided good barrier, mechanical, and preservative properties. A novel halochromic film was fabricated by trapping saffron petal extracts in composite biopolymer films fabricated from chitosan nanofibers and methylcellulose using a casting method. The optical, mechanical, transport, thermal, spectroscopic, release, ammonia-sensitivity, antioxidant, and antimicrobial properties of the films was measured. In addition, the ability of the halochromic smart films to enhance and detect the freshness of lamb meat during storage was evaluated.

2. Chemicals and experiments

2.1. Reagents

Methyl cellulose (MC) was obtained from the Henkel company, (Düsseldorf, Germany). Chitosan nanofibers (CNFs) (purity > 99%; width ~20–50 nm; de-acetylation degree ~80–85%; and, MW ~50–80 kDa) was supplied by the Nano-Novin polymer company (Mazandaran, Iran). Saffron flowers were collected to extract saffron petal anthocyanins from a farm near Kashmar city (Khorasan-Razavi, Iran). Initially, the stigmas and anthers were removed from the saffron plant and then the saffron petals were air dried at ambient temperature in a dark place and then powdered. DPPH (2, 2-diphenyl-1-picrylhydrazyl) and BHT (Butylated hydroxytoluene) standards were purchased from Sigma-Aldrich (St. Louis, MO). Medium cultures (Mueller Hinton agar and Nutrient broth) were purchased from Quelab (Montreal, Canada). Bacterial strains, *Escherichia coli* (ATCC-25922) and *Staphylococcus aureus* (ATCC-33591), were obtained from the Biological and Genetic Resources Center (Tehran, Iran). Deionized water was utilized for all tests and sample preparation. All reagents were of analytical grade and used without further purification.

2.2. Extraction of saffron petal anthocyanins (SPAs)

To extract the anthocyanins from the saffron petals, a percolation (soaking) method was used. The dried saffron petals were milled and sieved and then mixed with an appropriate solvent (distilled water/ethanol; 80/20 v/v) at a ratio of 1: 20 (w/v), and then gently shaken for 24 h at room temperature in the dark place. After extraction, the sample was passed through filter paper (Whatman No. 1) using a vacuum and then centrifuged at 5000×g for 10 min. The anthocyanins were concentrated by removal of the organic solvent using a rotary evaporator (37 °C and 25 mmHg). Finally, the total anthocyanin content (based on cyanidin-3-glucoside) in the samples was calculated using the pH differential method (Kang et al., 2020). The saffron petal anthocyanin content of the solution was determined to be 1.994 ± 0.005 mg/mL.

2.3. UV-vis spectroscopy analysis of saffron anthocyanin solutions

Changes in the color of the saffron anthocyanin solution with pH were measured using a UV-visible spectrophotometer (Ultrospec 2000, Scintec, UK). The spectra of the anthocyanin solutions were scanned from 400 to 800 nm at pH values ranging from 1.0 to 14.0.

2.4. Fabrication of MC-based composite films

The pH-sensitive composite biopolymer films were prepared using a casting method. Initially, a methylcellulose solution (3% w/v) was prepared by adding powdered polysaccharide into distilled water and magnetically stirring at 50 °C for 2 h. Subsequently, a chitosan nanofiber solution, which consisted of 70% w/v of chitosan nanofiber solution (1 or 3% w/v dissolved in 1% v/v acetic acid) and glycerol (30% w/v) as a plasticizer, were added to the methylcellulose solution, and then the mixture was magnetically stirred. The mixed polysaccharide solution was then cooled and saffron anthocyanins (3% w/v) were added with continual stirring. Finally, the biopolymer films were spread and cast on a Petri dish (8 cm internal diameter) and then dried at ambient temperature for 24–48 h. The resulting films were stored in the dark at a relative humidity of $50 \pm 2\%$ before analysis. The concentrations of each material were based on the methylcellulose weight.

2.5. Antimicrobial resistance activity of MC-based films

The antibacterial activity of the films was investigated using a disc diffusion method against *Escherichia coli* (Gram-negative) and

Staphylococcus aureus (Gram-positive), which were selected because of their importance in food spoilage and safety. The films were aseptically cut into discs (10 mm) and then laid onto the surface of Mueller Hinton agar plates with a bacterial density of about 1.5×10^6 CFU/mL. The plates were then incubated at 37 °C for 24 h and the inhibitory zone around the discs was measured using a caliper.

2.6. Antioxidant quenching activity of MC-based films

The antioxidant activity of the films (50 mg) was tested using the 2,2-Diphenyl-1-picrylhydrazyl (DPPH) method using a UV-visible spectrophotometer (Ultrospec 2000, Scintec, UK) (Liu et al., 2017). For comparison, the radical scavenging activity of aqueous solutions containing different concentrations of the test antioxidant (anthocyanin) or a standard antioxidant (Butylated hydroxytoluene, BHT) were also measured (10, 20, 40, 80, 160, and 200 µL/mL). The test was performed by adding 3.8 mL of a DPPH methanol solution (0.004%) to 0.2 mL of the sample's solution. Afterward, the samples were incubated at 25 °C in the dark for 30 min. The absorbance (Ab) values of the samples were determined at 517 nm and the DPPH radical quenching activity was calculated:

$$AA (\%) = \frac{Ab_{DPPH} - Ab_{sample}}{Ab_{DPPH}} \times 100 \quad (1)$$

2.7. Optical properties of MC-based films

2.7.1. Transparency

The transparency of the films was determined from optical transmittance at 600 nm (T_{600} , cm^{-1}) and film thickness (D, mm) measurements. The transmittance of the films was measured using a UV-vis spectrophotometer (Ultrospec 2000, Scintec, UK). The transparency was then estimated using the following equation:

$$\text{Transparency} = \frac{\log T_{600}}{D} \quad (2)$$

The transparency of the film samples was determined using a standard ASTM method (D1746-09).

2.7.2. Appearance

The pH-sensitivity of the color of the composite films was investigated using a method described previously (Choi, Lee, Lacroix, & Han, 2017) with some modifications. The films were immersed in buffer solutions with different pH values (2–14) and then the color of the films was recorded using digital photography.

2.7.3. UV-vis absorbance and transmittance

The light absorbance and transmittance spectra of the films were analyzed using a UV-visible spectrophotometer (Ultrospec 2000, Scintec, UK). The films were cut into rectangular pieces that were placed into a magnetic holder of a spectrophotometer cell. The optical properties of the films were then recorded from 200 to 800 nm. Air was used as a blank sample.

2.7.4. Instrumental color coordinates

The color coordinates of the films were determined using a Hunter lab colorimeter (Konica Minolta, Japan): L = lightness; a = greenness/redness; and, b = blueness/yellowness. The total color difference (ΔE) was then calculated as follows:

$$\Delta E = \sqrt{(L_s - L)^2 + (a_s - a)^2 + (b_s - b)^2} \quad (3)$$

Here, L_s (93.44), a_s (-0.04), and b_s (1.66) are the color coordinates of the standard white screen used. All analyses were carried out in three replicates.

The chromaticity of the films, which was determined by computing Chroma (C^*_{ab}) and Hue-angle (h_{ab}), was determined using the following

expressions:

$$C^*_{ab} = \sqrt{(a^*)^2 + (b^*)^2} \quad (4)$$

$$h_{ab} = \tan^{-1}(b^*/a^*) \rightarrow (\text{if } a^* \text{ and } b^* \text{ are positive}) \quad (5)$$

$$h_{ab} = 180 + \tan^{-1}(b^*/a^*) \rightarrow (\text{if } a^* \text{ and } b^* \text{ are negative or if } a^* \text{ is negative and } b^* \text{ is positive}) \quad (6)$$

$$h_{ab} = 360 + \tan^{-1}(b^*/a^*) \rightarrow (\text{if } a^* \text{ is positive and } b^* \text{ is negative}) \quad (7)$$

2.8. Ammonia vapor sensitivity test

Films were cut into disks (20 mm) and then held 1 cm above a vessel (80 mL) containing ammonia solution (8 mM) at 25 °C for 30 min (Kuswandi et al., 2012). The color of the films was recorded at 5 min intervals during this time. The film's sensitivity to volatile ammonia vapor was estimated as follows:

$$S_{RGB} (\%) = \frac{(R_i - R_f) + (G_i - G_f) + (B_i - B_f)}{R_i + G_i + B_i} \times 100 \quad (8)$$

Here, R_i , G_i , B_i and R_f , G_f , B_f represent the initial and final red, green, and blue values of the films, which were measured using the Pixie program for windows.

2.9. Anthocyanin release from the halochromic smart films

The release rate of anthocyanin from the halochromic films was measured after they were submerged in 25 mL of ethanol solution (10%, 50%, and 95%) or distilled water as model foodstuffs (Lee, Kim, & Park, 2018). Films were cut into squares (2 cm × 2 cm), then immersed in these model foodstuffs (25 °C), and then the system was gently shaken for 4 h. The absorbance of the solutions was recorded over time (30, 60, 90, 120, 180, and 240 min) at 520 nm (λ_{max}) using a UV-vis spectrophotometer (Ultrospec 2000, Scintec, UK). The pigment release rate was then expressed as the µg of saffron anthocyanins released per mm² of film using a standard curve.

2.10. Physical characterization of MC-based films

2.10.1. Film thickness

The thickness of the films was measured using a digital micrometer (Dial Thickness gauge 7301, Mitutoyo Corporation, Kanagawa, Japan) with an accuracy of 0.001 mm. The thickness was calculated from measurements made at six different locations on a film.

2.10.2. Film water-solubility

The water-solubility of the film was determined using a method described previously (Gontard, duchez, cuq, & guilbert, 1994) with some modifications. A disc of each film (2 cm diameter) was dried at 105 °C overnight in an oven, weighed (W_1), and immersed in 25 mL of distilled water while gently shaking for 24 h at room temperature. After this period, the films were collected and dried in a drying oven at 105 °C to determine the final weight (W_2) of dry matter. The water solubility (WS) was then calculated as follows:

$$WS (\%) = \frac{W_1 - W_2}{W_1} \times 100 \quad (9)$$

2.10.3. Film moisture content

Samples of the films were weighed before and after oven drying (105 ± 1 °C, 24 h) until a constant weight was achieved (dry sample weight). The moisture content (MC) was then determined from three replications for each film and calculated as the percentage of weight loss relative to the original weight:

$$MC = W_1 - W_2 \quad (10)$$

Here, W_1 and W_2 are the weights of the films before and after drying.

2.10.4. Film barrier properties

The water vapor permeability (WVP) and water vapor transmission rate (WVTR) of the films were measured using a standard method (ASTM-E96, 1995). The sample films were cut into a circular disc and sealed in a test glass cup with a 6 mm diameter. Cups filled with CaCl_2 granules as a desiccant (0% RH) and placed in a desiccator containing distilled water (100% RH). Cups were weighed every 3h over a 72h period. WVTR was determined from the WVP ($\text{g} \cdot \text{m}/\text{m}^2 \cdot \text{s} \cdot \text{Pa}$) using the following expression:

$$WVP = \frac{WVTR \times x}{\Delta P} \quad (11)$$

Where x and ΔP are the film thickness (mm) and water vapor pressure difference across the film (Pa), respectively.

2.10.5. Film mechanical properties

The mechanical properties of the films ($10 \text{ cm} \times 1 \text{ cm}$) was measured using a texture analyzer (Model DBBP-20, Bongshin, Korea). A cross-head speed of 10 mm/min and a 50 mm initial grip separation were used to measure the mechanical properties of the films at 25 °C (ASTM-D882-91, 1996). The MC-based films were conditioned at a relative humidity of $50 \pm 2\%$ before analysis. The stiffness (YM), strength (TS), and flexibility (EAB) of the films were then calculated as follows:

$$\text{Tensile stress (TS) (MPa)} = \frac{\text{Load at Break}}{\text{Original width} \times \text{Original thickness}} \quad (12)$$

$$\text{Elongation at break (EAB) (\%)} = \frac{\text{elongation at rupture}}{\text{initial gage length}} \times 100 \quad (13)$$

$$\text{Young's modulus (YM) (MPa)} = \frac{\text{Stress}}{\text{Strain}} \quad (14)$$

2.11. Films structure and interactions

2.11.1. Surface morphology

The surface morphology of the films ($2 \text{ cm} \times 2 \text{ cm}$) was characterized using field emission scanning electron microscopy (FE-SEM) at an accelerating voltage of 10 kV (TESCAN Mira3, Czech Republic). Film samples were sputter-coated with gold before testing and scanning.

2.11.2. Attenuated Total Reflectance Fourier Transform Infrared

Information about the interactions between the molecules within the composite films was obtained using Attenuated Total Reflectance Fourier Transform Infrared (ATR-FTIR) spectroscopy to measure the IR spectrum from 4000 to 400 cm^{-1} using 24 scans per sample at a resolution of 4 cm^{-1} (Bruker Tensor 27 FTIR spectrometer, Bruker, Germany).

2.11.3. X-ray diffraction (XRD)

Information about the crystallographic properties of the films was obtained from X-ray diffraction analysis. The X-ray diffraction patterns of the film samples ($2 \text{ cm} \times 2 \text{ cm}$) were acquired by passing an Ni-filtered $\text{Cu K}\alpha$ radiation beam (40 kV and 30 mA) through them and measuring the signal intensity in the angular range (2θ) from 5 to 80° using an X-ray diffractometer (Philips, PW1730 diffractometer, Amsterdam, Netherlands).

2.12. Thermal properties of MC-based films

A thermogravimetric analyzer was used to monitor the thermal properties of the films (Perkin Elmer TGA 4000 System, USA). The film

samples ($2 \text{ cm} \times 2 \text{ cm}$) were heated from 20 to 600°C at a heating rate of $10^\circ\text{C}/\text{min}$ under a nitrogen flow of $50 \text{ cm}^3/\text{min}$ in a standard aluminum pan and changes in their mass with temperature were recorded.

2.13. Food model packaging test

The potential of the colorimetric biopolymer films to monitor lamb meat spoilage during storage was assessed (72 h, 25°C). A rectangular ($3 \text{ cm} \times 4 \text{ cm}$) section of the halochromic smart film was placed inside a package containing 50 g of lamb meat (in contact with the meat). Changes in the color of the smart films were then observed and recorded using digital photography. At the same time, changes in the pH of the lamb meat samples were monitored using a method described previously (Alizadeh-Sani, Mohammadian, & McClements, 2020).

2.14. Statistical analysis

All films properties were measured in triplicate and the statistical significance was analyzed based on the mean \pm standard deviation values. Data were subjected to one-way analysis of variance (ANOVA) and Duncan's multiple range tests were carried out for comparison of the means at a significance level of $\alpha = 0.05$.

3. Results and discussion

3.1. Antimicrobial activity of films

An important attribute of active/smart packaging material is the ability to inhibit the growth of spoilage or pathogenic microorganisms on foods. For this reason, the antimicrobial activity of the various films was determined using model foodborne pathogenic and spoilage bacteria: *E. coli* & *S. aureus* (Table 1). The antimicrobial activity of films was performed using the disc diffusion method. The pure methylcellulose films did not exhibit any antimicrobial activity, since this polysaccharide is not known to be effective at killing microorganisms. All the other films did exhibit some antimicrobial activity against both bacteria, which suggests that both the chitosan nanofibers and saffron anthocyanins were effective antimicrobial agents. The mode of action of cationic chitosan nanofibers is generally ascribed to their interaction with cellular components and cell membranes, leading to an increase in membrane permeability (Genskowsky et al., 2015; Zhang, Liu, et al., 2019). The addition of the anthocyanins to the composite films increased their ability to inhibit bacterial growth, which may be due to the presence of high levels of antimicrobial phenolic groups in the anthocyanin molecules (Alizadeh-Sani, Khezerlou, & Ehsani, 2018; Zhang, Liu, et al., 2019). The antimicrobial activity of the films was stronger against *S. aureus* (Gram-positive) than against *E. coli* (Gram-negative) ($P < 0.05$). This effect can be attributed to differences in the physiological, metabolic, and structural characteristics of these two different groups of bacteria, particularly differences in their cell walls (Zhu, Cai, & Sun, 2018). The antimicrobial activity of phenolic compounds, such as anthocyanins, has been proposed to be due to various mechanisms, including their ability to increase cell membrane permeability, inhibit the uptake of vital substrates for cell growth, and interfere with key metabolic pathways (Genskowsky et al., 2015; Zhang, Liu, et al., 2019). Other researchers have reported that incorporation of anthocyanin-rich black plum peel extracts into chitosan-based films increased their antimicrobial activity (Zhang, Liu, et al., 2019).

3.2. Antioxidant activity of films

Lipid and protein oxidation often lead to quality deterioration of meat and fish products. For this reason, we measure the ability of the anthocyanins to inhibit oxidation in aqueous solutions and in films (Figs. 11 and 12, Table 2). A widely-used synthetic antioxidant activity (BHT) was used as a control.

Table 1

Physical, mechanical, optical, antibacterial and antioxidant properties of methylcellulose films loaded with chitosan nanofibers and saffron anthocyanins.

Physical properties	Film type			
	MC	MC ^{1%} CNFs	MC ^{3%} CNFs	MC ^{3%} CNFs/ 3%SPAs
Thickness (μm)	98 ± 12 ^a	108 ± 12 ^b	123 ± 10 ^c	125 ± 8 ^d
T (log T600/mm)	19.4 ± 1.5 ^b	17.56 ± 0.21 ^c	13.95 ± 1.90 ^f	13.0 ± 0.5 ^g
WVP (× 10 ⁻¹¹ g m/m ² s. Pa)	6.27 ± 0.01 ^{ae}	5.19 ± 0.05 ^{ac}	2.56 ± 0.04 ^m	2.42 ± 0.05 ^m
Water solubility (%)	45.7 ± 1.0 ^{bd}	44.7 ± 1.0 ^{bc}	42.5 ± 1.1 ^{cd}	42.7 ± 1.9 ^{cd}
Moisture content (%)	7.10 ± 0.14 ^e	6.00 ± 0.15 ^d	5.35 ± 0.21 ^c	2.80 ± 0.28 ^k
Mechanical properties				
Tensile strength (MPa)	38.6 ± 3.0 ^a	40.6 ± 2.6 ^b	62.6 ± 1.8 ^c	46.6 ± 1.6 ^d
Elongation at break (%)	38.2 ± 1.1 ^{ab}	9.86 ± 0.27 ^{ac}	4.26 ± 0.16 ^{bd}	11.51 ± 0.4 ^{ec}
Young modulus (MPa)	264.9 ± 3.4 ^e	287.7 ± 4.5 ^f	303.9 ± 6.1 ^g	288.5 ± 3.7 ^h
Color properties				
L value	89.5 ± 1.4 ^a	76.7 ± 2.5 ^b	67.3 ± 2.0 ^c	53.8 ± 5.0 ^d
a value	0.33 ± 0.12 ^{ab}	-0.66 ± 0.13 ^{ad}	-0.33 ± 0.08 ^{ad}	8.2 ± 1.2 ^{ae}
b value	2.66 ± 0.81 ^e	8.83 ± 0.75 ^f	9.16 ± 0.75 ^f	-7.66 ± 0.51 ^a
ΔE value	4.08 ± 0.05 ^{cd}	18.25 ± 0.13 ^{bd}	27.2 ± 1.3 ^{ab}	37.7 ± 1.7 ^{bc}
Chroma (C* _{ab})	2.68 ± 0.25 ^a	8.85 ± 0.78 ^b	9.16 ± 0.80 ^b	11.22 ± 0.66 ^c
Hue-angle (h _{ab})	82.92 ± 0.88 ^s	94.27 ± 1.11 ^d	92.06 ± 1.0 ^d	316.95 ± 0.95 ^f
Antimicrobial activity (Inhibition zone (mm))				
<i>E. coli</i>	-	10.4 ± 0.8 ^a	17.4 ± 0.5 ^b	20.2 ± 3.3 ^c
<i>S. aureus</i>	-	12.6 ± 0.8 ^m	19.7 ± 1.9 ⁿ	22.8 ± 1.5 ^k
Antioxidant activity				
DPPH radical scavenging (%)	-	13.1 ± 2.0 ^a	18.3 ± 0.2 ^b	83.6 ± 0.4 ^c

The data are presented as mean ± standard deviation. Any two means in the same row followed by the same letter are not significantly ($P > 0.05$) different from Duncan's multiple range tests. MC: Methyl cellulose, CNFs: Chitosan nanofibers, SPAs: Saffron petal's anthocyanins, WVP: Water vapor permeability, T: Transparency, DPPH: 2,2-diphenyl-1-picrylhydrazyl.

Analysis of the antioxidant activity of the saffron anthocyanins in aqueous solutions showed that they had a strong dose-dependent radical quenching activity (Fig. 1). This effect can be attributed to the presence of high level of phenolic groups in the structure of the anthocyanin molecules (Zhang, Liu, et al., 2019). It should be noted that the antioxidant activity of this natural compound was lower than that of BHT. Even so, it still had good antioxidant activity.

The pure methylcellulose film did not exhibit any antioxidant properties (Table 1), which was expected because this polysaccharide does not have any functional groups that are known to strongly inhibit oxidation. The composite films only exhibited mild DPPH radical quenching activity, which suggests that the chitosan nanofibers exhibited some antioxidant activity. This effect may have been due to the presence of free NH₂ groups on the chitosan chains that could interact with the DPPH free radical and a H⁺ ion from the surrounding solution to form a stable molecule (NH₃⁺) (Kurek et al., 2018; Yong, Wang, Bai, et al., 2019). In contrast, the anthocyanin-loaded halochromic smart films exhibited strong antioxidant activity (Table 1), which can be attributed to the radical quenching capacity of the polyphenolic hydroxyl groups on the anthocyanin molecule. Other researchers have reported that anthocyanins from various sources can increase the antioxidant activity of biopolymer films, including black soybean seed coat extract, purple-fleshed sweet potato extract, and

Table 2

Identification of key functional groups involved in molecular interactions in the films determined by FTIR analysis.

Origin	Wavenumber (cm ⁻¹)	Functional associated group	
Chitosan Nanofibers	~3500–3200	Amine, and hydroxyl, (H-bonded) O–H stretching -NH ₂ stretching -NH stretching	
	~2884	C–H stretching Aliphatic compound	
	~1700–1500	Amide I and amide II bands C=O stretching vibration N–H bending vibration C–N stretching vibration	
	~1640	Amide I C=O stretch	
	~1550	N–H bending Stretching of amide II	
	~1450	Bending vibration of O–H	
	~1371	C–H bending	
	~1020	C=O stretching Sugar ether C–O–C stretching	
	Methyl cellulose	~3397	O–H stretching
		~2883	C–H stretching
~1641		C–O stretching	
~1044		C–O–C stretching	
~660		Methoxyl and methyl groups C–H stretching vibration	
Saffron anthocyanin	~3500–3250	O–H stretching	
	~1771	C=O stretching of ring	
	~1650	Stretching vibration of the C=C	
	~1200	Aromatic ring	
	~1020	C–O stretching	
	~750–1000	Aromatic ring C–H deformation Aromatic rings	

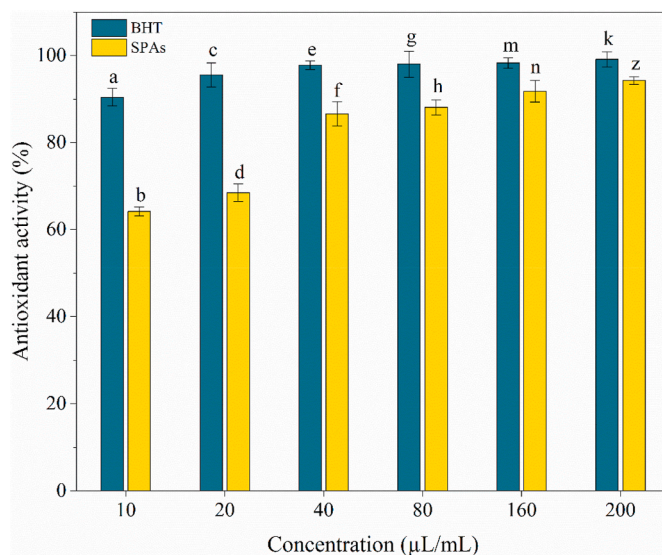


Fig. 1. Comparison of antioxidant quenching activity of anthocyanin solution with BHT as a standard sample.

murta fruit extract (De Dicastillo et al., 2016b; Wang, Yong, et al., 2019; Yong, Wang, Bai, et al., 2019).

3.3. Optical properties of films

The impact of the saffron anthocyanins on the optical properties of the composite films was characterized using a range of methods to assess their suitability as smart sensors.

3.3.1. Transparency

The transparency of packaging materials influences the overall appearance and acceptance of food products by consumers. It also influences their ability to protect food products from photo-degradation by selectively filtering out different light waves (Ezati and Rhim, 2020). The transparency of the various films was therefore measured at a wavelength of 600 nm (Table 1). The incorporation of chitosan nanofibers into these films led to an appreciable reduction in transparency, which is due to scattering of the light waves by the fibers. The subsequent incorporation of saffron anthocyanins into the films led to a further decrease in their transparency, which can be attributed to absorption of some of the light by this chromophore (Wang, Yong, et al., 2019; Yong, Wang, Zhang, et al., 2019).

3.3.2. Absorption spectrum

The ability of packaging materials to protect foodstuffs from photo-degradation is important to prevent discoloration and nutritional loss (Yong, Wang, Bai, et al., 2019). The UV-visible light absorbance and transmittance spectra of the various films was therefore measured as a function of wavelength (Fig. 2). Compared to the methylcellulose (Fig. 2 A) and methylcellulose/chitosan nanofiber films (Fig. 2 B), the ones containing the saffron anthocyanins (smart colorimetric film) (Fig. 2 C) had stronger UV light barrier properties ($\lambda < 370$ nm) and significantly reduced light transmittance. These light screening effects can again be attributed to the ability of the anthocyanins to absorb both UV and visible radiation (Yong, Wang, Zhang, et al., 2019). As expected, the transparency of the films was greater in the visible region of the electromagnetic spectrum in the absence of the anthocyanins because more light wave waves could penetrate through them. Previous researchers

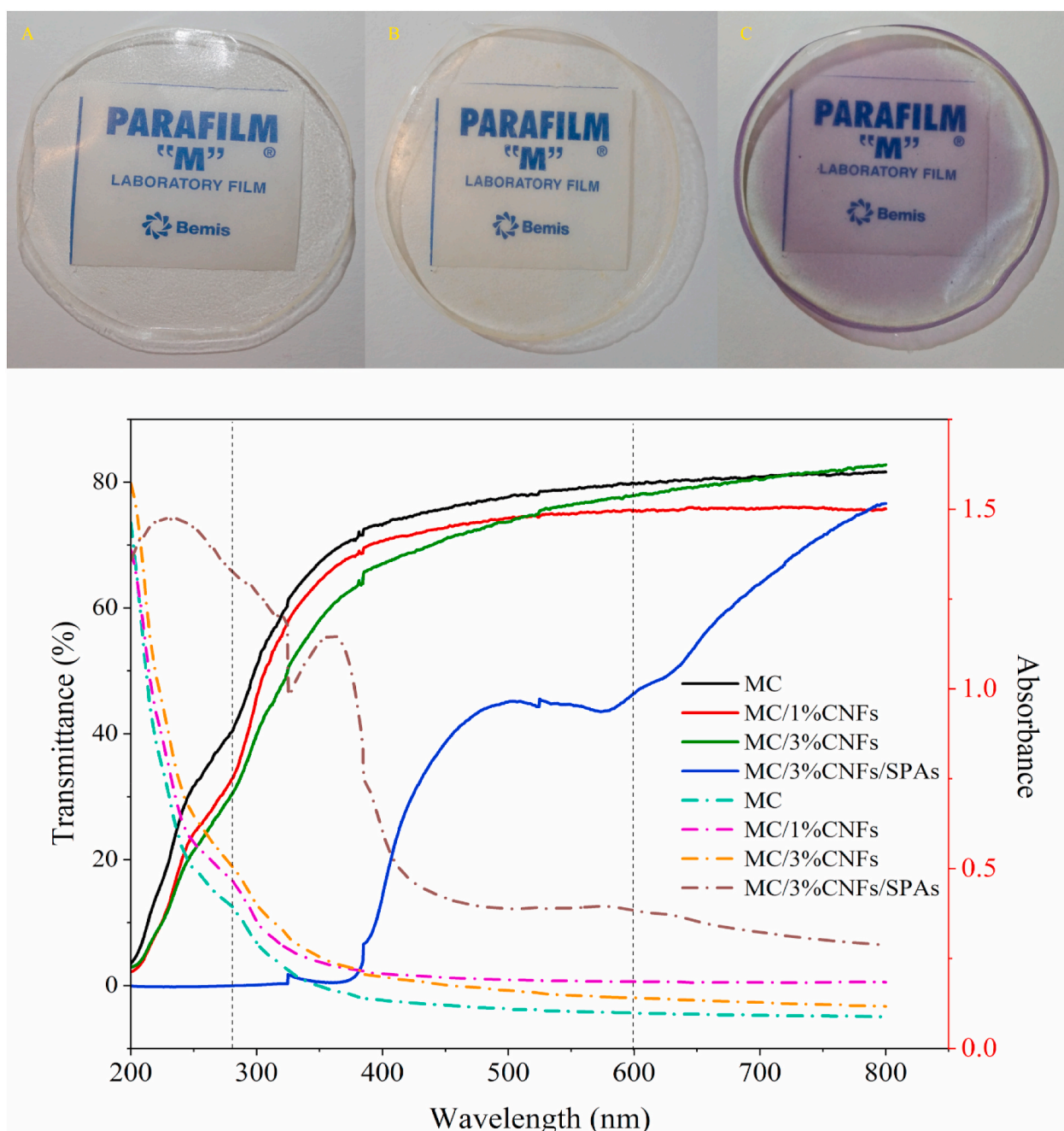


Fig. 2. Appearance of films (MC (A), MC/CNFs (B), and anthocyanin-loaded MC/CNFs (C)) and UV-visible absorbance and transmittance of MC-based films.

have also reported a reduced transmission of UV–visible radiation when anthocyanins are added to chitosan films (Ezati and Rhim, 2020; Yong, Wang, Bai, et al., 2019).

3.3.3. Color

Visually, the methylcellulose and methylcellulose/chitosan nanofiber films appeared transparent and colorless. In contrast, the films containing the saffron anthocyanins were bluish/violet in appearance. Instrumental colorimeter measurements were used to quantify the differences in the optical properties of the films (Table 1). The pure methylcellulose films had a relatively high lightness and low color because they were relatively transparent, so that the optical properties of the white plate behind the samples dominated the colorimeter measurements. The incorporation of chitosan nanofibers into these films led to a decrease in their lightness, which can be attributed to increased light scattering by the nanofibers (so less light reached the white back plate). The halochromic smart films containing saffron anthocyanins had the lowest lightness ($L = 53.8$, $C^*_{ab} = 11.2$) and yellowness ($b = -7.7$), but the highest blueness ($a = +8.2$), which is consistent with their bluish/violet color ($Hue-angle = 317.0$). As a result, there was a relatively large total color difference (ΔE) for this film compared to the other films ($P < 0.05$). The bluish/violet color in saffron anthocyanins is mainly the result of delphinidin 3,7-O-diglucoside, which is violet at mildly neutral pH values (Goupy, Vian, Chemat, & Caris-Veyrat, 2013). Other researchers have also reported color changes in packaging materials when anthocyanins from various natural sources are added, including mulberry (Ma, Liang, Cao, & Wang, 2018), black eggplant (Yong, Wang, Zhang, et al., 2019), blueberry, and blackberry (Kurek et al., 2018).

3.3.4. pH-dependence of anthocyanin color

Ultimately, we intended to use the pH-dependence of the color of anthocyanin to detect changes in the quality attributes of packaged meat products. For this reason, the change in the UV–visible absorption spectra and color of saffron anthocyanin solutions was measured over a range of pH values (Figs. 3 and 4). The color of the solutions changed from red to yellow as the pH was increased from 1 to 14, with a number of different colors being formed at intermediate pH values: red/pink (pH

1–4); violet/gray (pH 5–6); green (pH 7–9); and, yellow-green/yellow (pH 10–14). These color changes are due to pH-induced structural transformations of the anthocyanin molecules: flavylium cation (pH < 3); carbinol pseudo-base (pH 4–5); quinonoidal anhydro-base (pH 6–8); and, chalcone (pH > 10) (Zhang, Liu, et al., 2019).

The intensity and wavelength of the maximum absorption peak of the anthocyanin solutions depended on pH (Fig. 3). Under highly acidic conditions (pH < 4), a strong absorbance peak was observed around ~520 nm, whose height decreased as the pH was increased. A new peak then formed around 550 nm, whose intensity and position increased as the pH was raised from 5 to 9, which is a characteristic feature of anthocyanins (Luchese, Abdalla, Spada, & Tessaro, 2018). The intensity of this peak then diminished when the pH was raised further from 10 to 14. As mentioned earlier, the change in absorbance spectra and color of the saffron anthocyanin solutions can be attributed to changes in the molecular species present. Similar findings have been reported for anthocyanins isolated from black plum peel (Zhang, Zou, et al., 2019) and blueberry (Luchese et al., 2018).

3.4. Impact of ammonia vapor on halochromic smart film color

Ammonia is often generated when meat and fish products deteriorate and so it can be used as a marker of their freshness. The color of anthocyanins may change when they are exposed to certain gasses due to alterations in their molecular structures (Ezati and Rhim, 2020; Zhang, Zou, et al., 2019). For this reason, we examined the impact of ammonia gas on the color of the anthocyanin-loaded smart composite films to establish whether they could be used as indicators of meat quality. The color of the colorimetric films changed appreciably when they were exposed to ammonia vapor, changing from violet → bluish → green → green/yellow over time (Fig. 5). The color sensitivity (S_{RGB}) of the smart films increased rapidly over the first 15 min and then reached a constant value. These color changes are associated with structural transformations of the anthocyanin molecules when they are exposed to hydroxyl ions (Fig. 4). The establishment of an alkaline environment on the surface of the smart halochromic films is stimulated by the presence of ammonium ions (NH_4^+), which arise from hydration and hydrolysis of

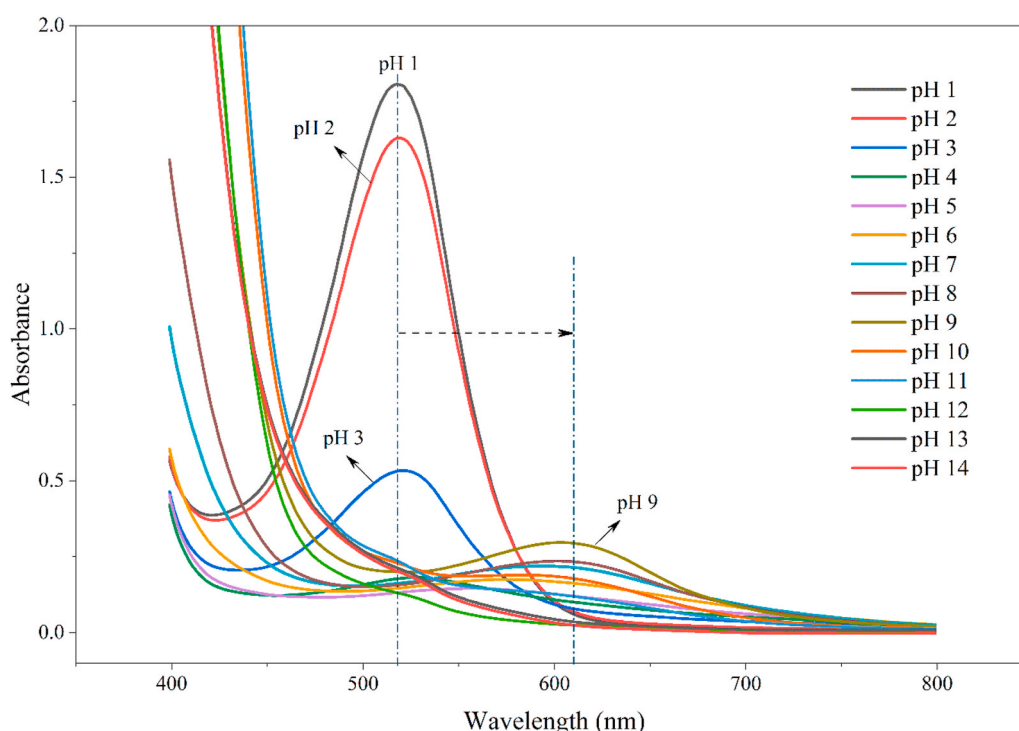


Fig. 3. The pH-dependence of the UV–visible spectra of saffron petal anthocyanin measured in various buffer solutions (pH 1 to 14).

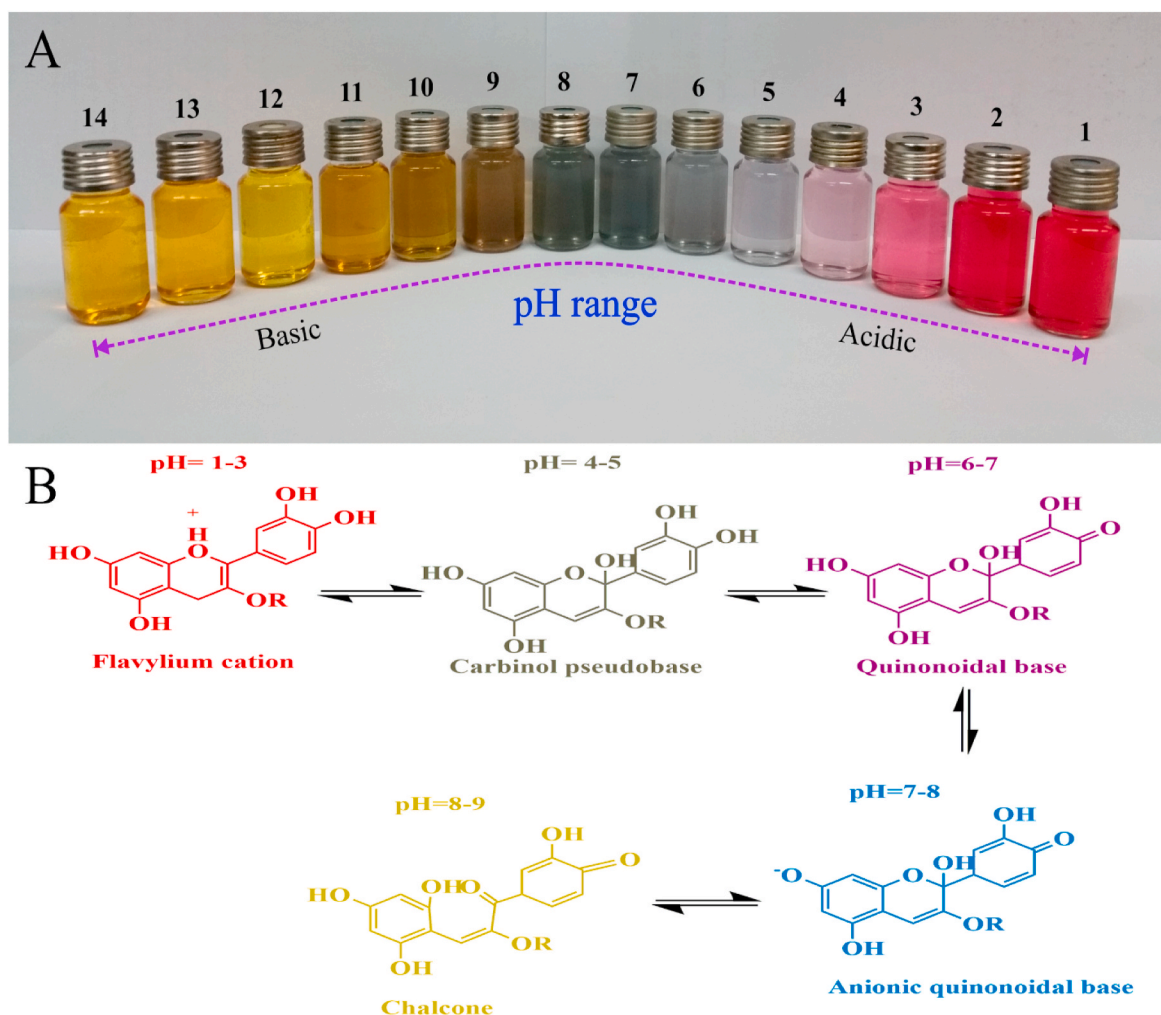


Fig. 4. (A): Solution color variations and (B): structural transformation of saffron petal anthocyanins in various buffer solutions. (For interpretation of the references to color in this figure legend, the reader is referred to the Web version of this article.)

the ammonia vapor (NH_3) inside the film (Ezati and Rhim, 2020). Overall, these results suggest that the anthocyanin-loaded composite films developed in our study are suitable for detection of ammonia gas, which means they should be sensitive to changes in meat or fish freshness.

3.5. Anthocyanin release from the halochromic smart films

The migration of a colorimetric indicator from a smart packaging material is undesirable because it may lose its efficacy or discolor the food. For this reason, rate of saffron anthocyanin release from the smart colorimetric films was determined using model food simulants: water and aqueous ethanol solutions (10, 50, or 95%). These solutions are designed to simulate foods with different polarities. The rate of anthocyanin release from the smart colorimetric films depended on the nature of the food simulant used: $\text{EtOH}_{10\%} > \text{Water} > \text{EtOH}_{50\%} > \text{EtOH}_{95\%}$ (Fig. 6). These results indicate that the anthocyanins are released most rapidly when the films are in contact with more polar fluids, which can be attributed to the high polarity of the anthocyanins, as well as the greater swelling of the biopolymer films in polar liquids (Ezati and Rhim, 2020; Lee et al., 2018). Other researchers have reported that the release of anthocyanins from biopolymer films increases as the polarity of the food simulant increases (Wang, Xia, et al., 2019).

3.6. pH-sensitivity of halochromic smart film

Deterioration in the freshness of meat and fish products during storage may also lead to appreciable pH changes in the muscle tissues (Ezati and Rhim, 2020; Ezati, Tajik, Moradi, & Molaei, 2019). For this reason, we measured the impact of pH on the color of the anthocyanin-loaded halochromic smart films (Fig. 7). The pH-dependence of the color of the films was similar to that of the saffron anthocyanin solutions (Fig. 4): red/pink ($\text{pH} < 4$); violet ($\text{pH} 5\text{--}6$); bluish/gray ($\text{pH} 7\text{--}8$); green ($\text{pH} 10\text{--}12$). These results were also consistent with the results from the ammonia testing under alkaline conditions, where the films went green (Fig. 5). Similar pH-induced color changes have been reported for rose anthocyanins incorporated within PVA/okra mucilage composite films (Kang et al., 2020).

3.7. Physical properties

3.7.1. Film thickness

The thickness of packaging materials affect their mechanical strength, light transmittance, and gas barrier properties (Zhang, Liu, et al., 2019). In this study, the thickness of the different films ranged from around 98 to 125 μm (Table 1). In general, the thickness of the films increased significantly ($P < 0.05$) as the concentration of additives was increased, which can be attributed to the fact that there was more solid matter remaining in the films after drying. Other researchers have

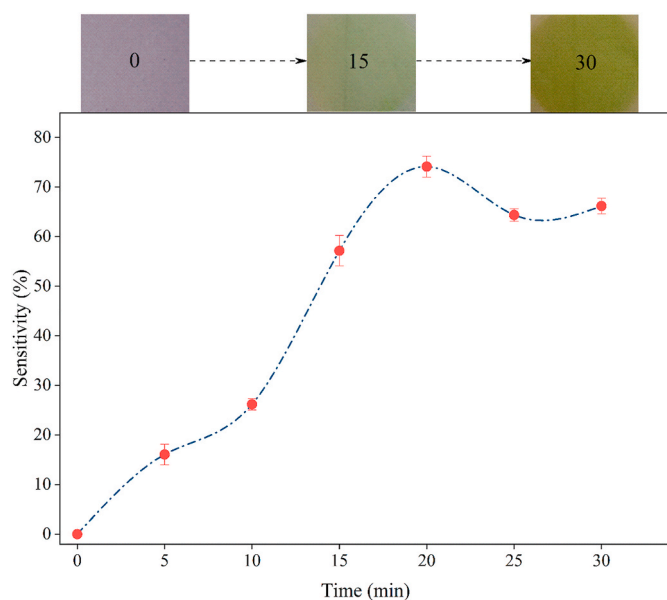


Fig. 5. The color sensitivity of the anthocyanin-loaded films changed appreciably when they were incubated in the presence of ammonia vapor. (For interpretation of the references to color in this figure legend, the reader is referred to the Web version of this article.)

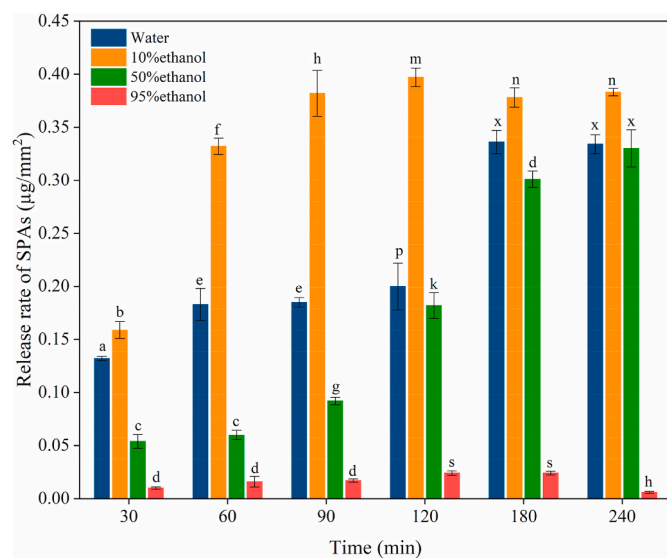


Fig. 6. Release of saffron petal anthocyanins from halochromic smart films incubated in water or ethanol solutions for different times.

reported that adding anthocyanin-rich purple and black eggplant extracts to chitosan films increased their thickness (Yong, Wang, Zhang, et al., 2019).

3.7.2. Moisture content

Typically, packaging materials consist of a network of polymers and/or particles with water molecules and other substances trapped within the pores between them (Alizadeh-Sani et al., 2018). The moisture content of the films decreased as the amounts of additives they contained increased (Table 1). For instance, the moisture content decreased significantly from 7.1% for the pure methylcellulose film to 2.8% for the saffron anthocyanin-loaded composite films ($P < 0.05$). This result suggests that some of the water molecules in the pores in the films were replaced with chitosan nanofibers and/or anthocyanin molecules. The

moisture content of a film is associated with their water vapor permeability: the higher the moisture content, the higher the WVP. This property is one of the common problems reported for films formed from biopolymers compared to those formed from synthetic polymers (Musso, Salgado, & Mauri, 2019). Thus, the ability of the anthocyanins to reduce the moisture content of the films may improve their barrier properties (see later). Other researchers have also reported that the moisture content of films decreases when anthocyanin-rich extracts are added (Yong, Wang, Bai, et al., 2019; Zhang, Liu, et al., 2019).

3.7.3. Film solubility

The water-solubility (WS) of packaging materials plays an important role in determining their functional performance (Huang et al., 2019). Ideally, a film should not dissolve when it is being used to protect food materials. The pure methylcellulose films had the highest water-solubility (Table 1). The addition of the chitosan nanofibers significantly reduced the water-solubility of the composite films in a dose-dependent manner ($P < 0.05$), which can be attributed to their water-insolubility. The incorporation of the saffron anthocyanins into these composite films did not significantly alter their water-solubility, despite their hydrophilic nature (Wang, Yong, et al., 2019; Zhang, Liu, et al., 2019). This is probably because the polar anthocyanins replaced some of the polar water molecules in the films. Other researchers have reported similar effects when anthocyanin-rich black plum peel extracts (Zhang, Liu, et al., 2019) and purple-fleshed sweet potato extracts (Yong, Wang, Bai, et al., 2019) are added to chitosan films.

3.7.4. Barrier properties of films

The water vapor permeability (WVP) of packaging materials is a key characteristic for maintaining the quality and safety of many foods. Typically, the WVP should be relatively low to prevent undesirable physical, chemical, or microbiological changes due to the migration of moisture into or out of the product. In our study, the WVP of the films decreased as the amounts of additives incorporated into them increased: methyl cellulose > composite > anthocyanin-loaded composite films (Table 1). This result suggests that the presence of the chitosan nanofibers and anthocyanins reduced the ability of the water molecules to diffuse through the films. Presumably, this occurred because there was a reduction in the pore size and/or an increase in the tortuosity of the polymer/particle network within the composite films after incorporation of the additives (Zhang, Liu, et al., 2019). Several other researchers have also reported reduction in the WVP of biopolymer films after introduction of various kinds of anthocyanins, including purple and black eggplant extracts (Yong, Wang, Zhang, et al., 2019), black plum peel extracts (Zhang, Liu, et al., 2019) and black soybean seed coat extracts (Wang, Yong, et al., 2019).

3.8. Mechanical resistance

The mechanical properties of packaging materials are particularly important for protecting foods from their environment. For this reason, we measured the tensile strength (TS: strength), elongation at break (EAB: flexibility), and Young's modulus (YM: stiffness) of the packaging materials (Table 1). Previous studies have shown that the structural organization and interactions of the components within composite films affects their mechanical characteristics (Ezati and Rhim, 2020). For this reason, we hypothesized that the addition of the chitosan nanofibers and anthocyanins would alter the mechanical properties of the methylcellulose films.

The pure methylcellulose films were relatively strong, stiff, and flexible: TS = 62.6 MPa; YM = 265 MPa; and, EAB = 38.2%. Incorporation of chitosan nanofibers (3%) significantly increased the strength and stiffness of the films but decreased their flexibility: TS = 62.6 MPa; YM = 304 MPa; and, EAB = 4.3%. Conversely, incorporation of saffron anthocyanins into the composite films, slightly reduced their strength, and stiffness, and increased their flexibility: TS = 46.6 MPa; YM = 288

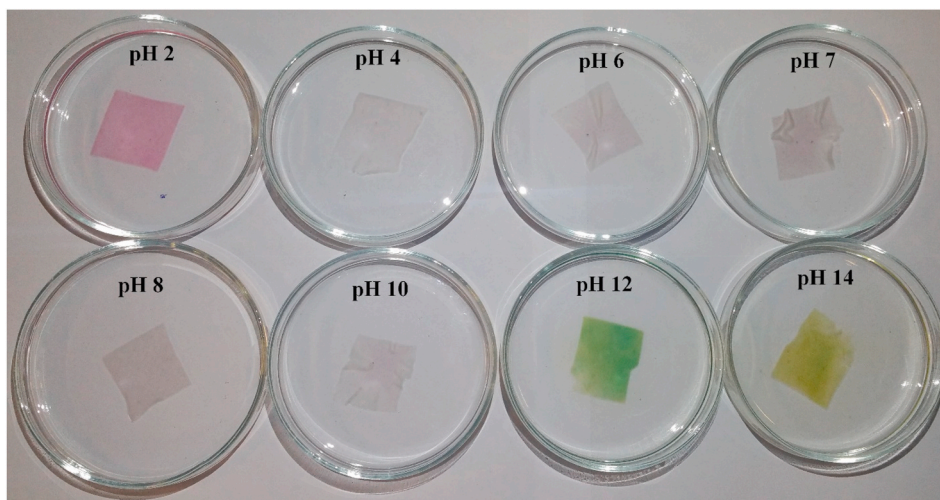


Fig. 7. Halochromic smart film color changes when incubated in various buffer solutions. (For interpretation of the references to color in this figure legend, the reader is referred to the Web version of this article.)

MPa; and, EAB = 11.5%. These results show that both the chitosan nanofibers and anthocyanins impacted the structural organization and/or interactions of the biopolymers and particles in the composite films. As mentioned earlier, there appeared to be extensive hydrogen bonding between the methylcellulose and chitosan nanofibers within the films, which would be expected to impact their rheological properties. The anthocyanins may act as plasticizers that increase the mobility of the biopolymer chains, thereby increasing film flexibility (Ezati and Rhim, 2020; Zhai et al., 2017). Researchers have reported that black plum peel anthocyanins increase the mechanical resistance and flexibility of chitosan films (Zhang, Liu, et al., 2019), whereas other researchers have reported that sweet potato anthocyanins decrease the strength and increase the flexibility of chitosan films (Yong, Wang, Bai, et al., 2019). Consequently, it appears that the impact of anthocyanins is system dependent.

3.9. Films structure and interactions

3.9.1. Surface morphology

The surface morphology of films with different compositions was determined using SEM images (Fig. 8). The films formed from only methyl cellulose had smooth and uniform surfaces, which can be attributed the fact that they contained no particular inclusions. The films containing chitosan nanofibers and methylcellulose had rougher surface morphologies, which can be attributed to the protuberance of some of

the nanofibers from their surfaces. Interestingly, the incorporation of the anthocyanins appeared to lead to a slightly smoother surface morphology, which may be due to their ability to interact with other structural components. Former researchers have reported similar findings after adding anthocyanins to biopolymer films (Liang et al., 2019; Wang, Yong, et al., 2019; Yong, Wang, Zhang, et al., 2019).

3.9.2. Molecular interactions

ATR-FTIR spectroscopy was used to provide insights into the molecular interactions present within the different kinds of films. The IR spectra obtained contained a number of characteristic peaks corresponding to specific functional groups within the films (Fig. 9). The major groups involved in the molecular interactions between the different constituents in the films were hydroxyl groups (anthocyanin, methyl cellulose, and chitosan nanofibers) and amine groups (chitosan nanofibers). The wavelength numbers for specific functional groups have been reported in the literature (Ezati and Rhim, 2020; Yong, Wang, Zhang, et al., 2019). This information was used to summarize the main functional groups involved in the molecular interactions within the films (Table 2).

The presence of the aromatic ring stretches in the IR spectra for the composite films provides strong evidence that the saffron anthocyanins were incorporated into the methyl cellulose/chitosan nanofiber matrix. Moreover, the ATR-FTIR analysis shows that the O-H groups on the saffron anthocyanins formed hydrogen bonds with the O-H and N-H

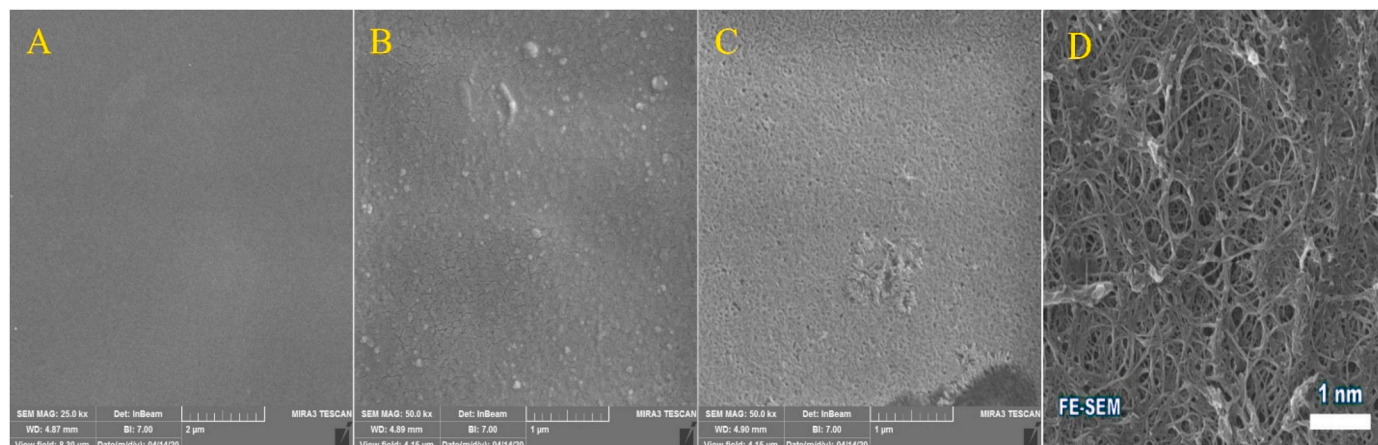


Fig. 8. Scanning electron microscopy images of MC films (A), MC/CNFs films (B), anthocyanin-loaded MC/CNFs films (C), and CNFs (D).

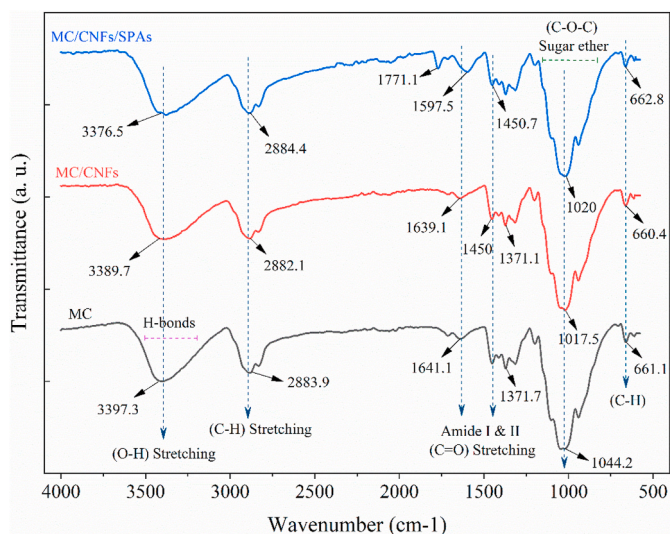


Fig. 9. ATR-FTIR spectra of MC, MC/CNFs, and anthocyanin-loaded MC/CNFs.

groups on the methyl cellulose and chitosan nanofibers, which is consistent with the findings of earlier studies on related materials (Ezati and Rhim, 2020; Yong, Wang, Bai, et al., 2019; Zhang, Liu, et al., 2019).

3.9.3. Film crystallinity

The crystallinity of biopolymer films is known to impact the mechanical and barrier properties of packaging materials (Zhai et al., 2017). For this reason, the crystallinity of different films was analyzed

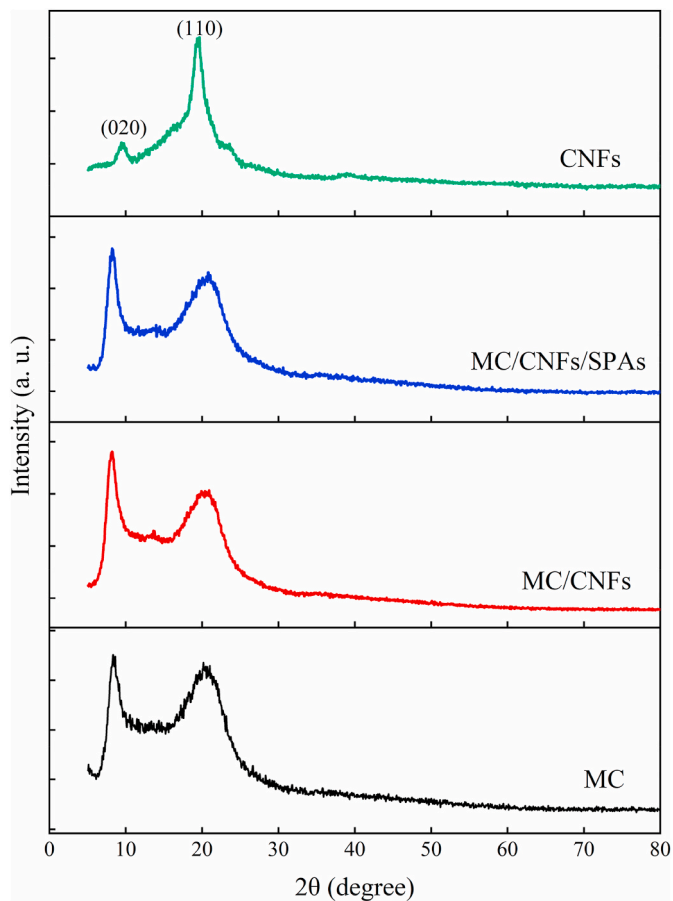


Fig. 10. X-ray diffraction patterns of MC, CNFs, MC/CNFs, and anthocyanin-loaded MC/CNFs films.

using X-ray diffraction (Fig. 10). The pure chitosan film had two distinct peaks at $2\theta = \sim 10^\circ$ and $\sim 20^\circ$, which is consistent with a crystalline structure that has (020), and (110) planes, respectively (Hai & Sugimoto, 2018). The pure methylcellulose film had a sharp peak at $\sim 8.5^\circ$ and a broad one at $\sim 21^\circ$, which is also indicative of a crystalline structure (Zhao et al., 2007). A weak peak was also observed at $\sim 13.3^\circ$ for the methylcellulose film, which is indicative of partial hydration of the polymers (Liebeck, Hidalgo, Roth, Popescu, & Böker, 2017). The addition of chitosan nanofibers or saffron anthocyanins to the methylcellulose films did not cause a major change in the X-ray diffraction pattern, suggesting that they did not greatly alter the structural organization of the molecules.

3.10. Thermal stability

The resistance of packaging materials to decomposition at elevated temperatures is another important attribute because it influences their resistance to environmental stresses, as well as their potential to be disposed of by incineration. The thermal stability of the methylcellulose films was therefore determined by thermogravimetric analysis and the resulting TGA and DTG profiles are shown in Fig. 11. The TGA profile represents the weight of the film versus temperature during heating, while the DTG profile represents the rate of weight change (dW/dT) versus temperature. The TGA profiles show that the thermal decomposition of all the films followed a fairly similar trend, involving three distinct stages of weight loss during heating. The first stage occurred around $170\text{--}200^\circ\text{C}$, due to evaporation of water and any other residual solvents. The second stage occurred around $230\text{--}250^\circ\text{C}$ due to evaporation and decomposition of glycerol. The third stage occurred around $460\text{--}480^\circ\text{C}$ due to decomposition of the polysaccharides and anthocyanins. The TGA profiles indicated that the addition of the anthocyanins to the composite films had a significant effect on their thermal stability, with a somewhat slower decomposition rate during heating. Moreover, the DTG profiles indicated that the anthocyanins caused the temperature where the maximum rate of thermal decomposition was observed to increase from 333 to 349°C . This effect is possibly because the anthocyanins are more heat-resistant than the polysaccharides. Similar results have been reported by other researchers when various kinds of anthocyanins have been incorporated into biopolymer films (Alizadeh-Sani, Rhim, et al., 2020; Liang et al., 2019; Wang, Yong, et al., 2019).

3.11. Application of halochromic smart films in monitoring meat freshness

Finally, we carried out a preliminary experiment to examine the potential application of our anthocyanin-loaded smart colorimetric films to protect and detect the freshness of a model meat product (lamb) (Fig. 12). The spoilage of meat and seafood products is typically caused by enzymes and microorganisms and is characterized by an increase in pH, as well as the formation of nitrogen-based volatile compounds (such as ammonia and amines) due to protein decomposition (Alizadeh-Sani, Mohammadian, & McClements, 2020). We therefore hypothesized that the ability of our halochromic smart films to change color in response to alterations in pH or ammonia levels could be used as an indicator/smart packaging material of meat quality.

Lamb meat samples were packaged in containers equipped with anthocyanin-loaded smart films and changes in their properties were monitored during storage. The lamb meat changed from pink to dark red during storage, and became considerably stiffer in texture, indicating that its quality had deteriorated. The pH of the lamb meat increased throughout storage, being 5.7, 6.0, 6.7 and 7.3 after 0, 24, 48, and 72 h storage, respectively, which was again an indication of its deterioration. The color of the films changed from violet to green/gray during storage, which may have been partly due to this rise in pH and partly due to the generation of volatile nitrogenous compounds associated with meat decomposition. Overall, our results show that the anthocyanin-loaded

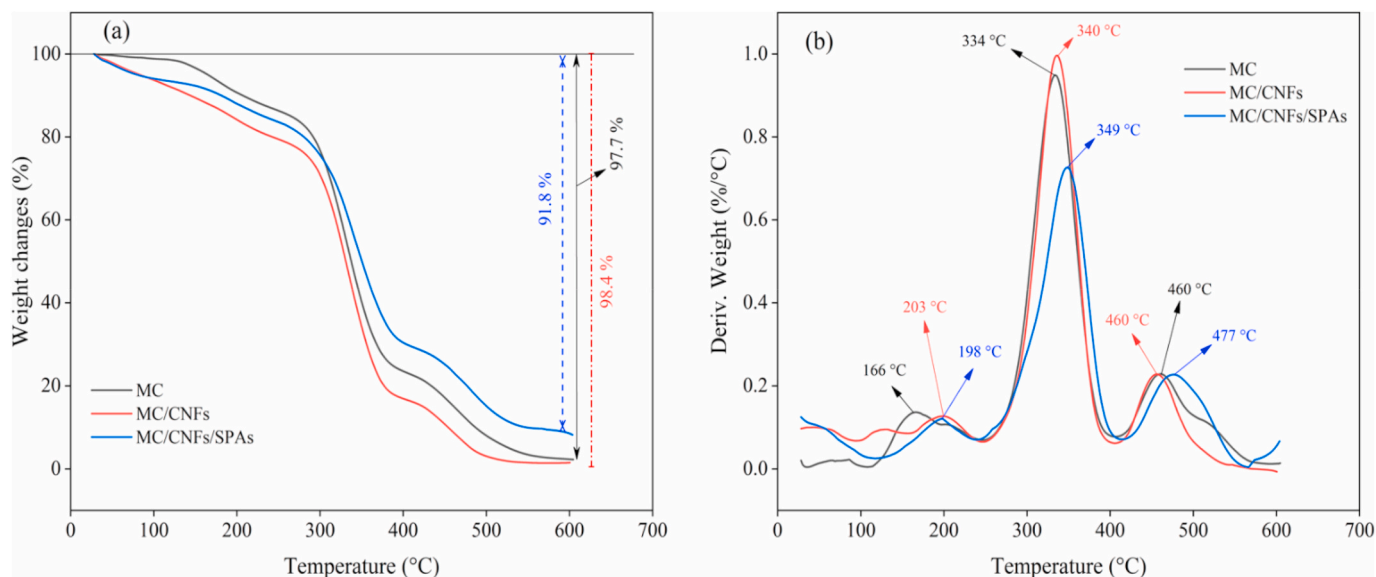


Fig. 11. TGA/DTG profile of MC, MC/CNFs, and anthocyanin-loaded MC/CNFs.

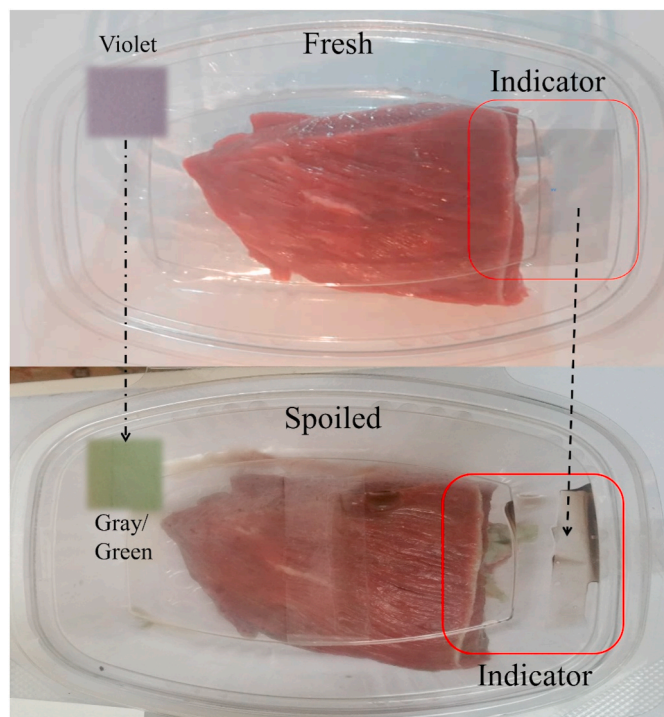


Fig. 12. Changes in the freshness of lamb meat during storage using halochromic smart films. These films were embedded in clear packaging material without anthocyanins.

halochromic films developed in this study have potential as smart packaging materials to protect and monitor meat freshness in real time. Other researchers have recently shown that rose anthocyanin-loaded PVA/okra mucilage films can be used to monitor the freshness of shrimp during storage (Kang et al., 2020). In future studies, it would be useful to quantify the pH changes, volatile nitrogen-based volatiles formation, and oxidation product concentrations throughout storage of the meat products to provide more detailed insights into the efficacy of the films.

4. Conclusion

In conclusion, a food-grade multifunctional packaging film was prepared and characterized, which consisted of saffron anthocyanins loaded into a methyl cellulose/chitosan nanofiber matrix. The incorporation of the anthocyanins into the composite films also notably improved their mechanical, moisture resistance, thermal, light-screening, gas barrier, antioxidant, and antimicrobial properties. Spectroscopic analysis indicated that the anthocyanin molecules interacted with the biopolymer matrix through hydrogen bonding. The color of the smart colorimetric films depended on the pH and ammonia gas content of their environment, which meant that the anthocyanin-loaded films could be used as smart packaging materials to protect and monitor the freshness of protein-rich foods, such as meat and seafood. Indeed, in a preliminary study we showed that these films were sensitive to changes in meat quality during storage. These halochromic films may therefore be useful for providing consumers with real-time information about the quality and safety of meat and seafood products, thereby reducing waste and improving the sustainability of the food supply.

CRediT authorship contribution statement

Mahmood Alizadeh-Sani: Conceptualization, Data curation, Formal analysis, Investigation, Methodology, Visualization, Writing - original draft, Writing - review & editing. **Milad Tavassoli:** Conceptualization, Data curation, Formal analysis, Investigation, Methodology, Visualization, Writing - original draft, Writing - review & editing. **David Julian McClements:** Writing - review & editing. **Hamed Hamishehkar:** Conceptualization, Data curation, Formal analysis, Funding acquisition, Investigation, Methodology, Project administration, Supervision, Visualization, Writing - original draft, Writing - review & editing.

Declaration of competing interest

The authors declare no conflict of interest.

Acknowledgements

This study was supported by Student Research Committee (Project No.64881), Tabriz University of Medical Sciences, Tabriz, Iran.

Appendix A. Supplementary data

Supplementary data to this article can be found online at <https://doi.org/10.1016/j.foodhyd.2020.106237>.

References

- Ahmad, M., Ashraf, B., Gani, A., & Gani, A. (2018). Microencapsulation of saffron anthocyanins using β glucan and β cyclodextrin: Microcapsule characterization, release behaviour & antioxidant potential during in-vitro digestion. *International Journal of Biological Macromolecules*, *109*, 435–442.
- Alizadeh-Sani, M., Ehsani, A., Kia, E. M., & Khezerlou, A. (2019). Microbial gums: Introducing a novel functional component of edible coatings and packaging. *Applied Microbiology and Biotechnology*, *103*(17), 6853–6866.
- Alizadeh-Sani, M., Khezerlou, A., & Ehsani, A. (2018). Fabrication and characterization of the bionanocomposite film based on whey protein biopolymer loaded with TiO₂ nanoparticles, cellulose nanofibers and rosemary essential oil. *Industrial Crops and Products*, *124*, 300–315.
- Alizadeh-Sani, M., Mohammadian, E., & McClements, D. J. (2020). Eco-friendly active packaging consisting of nanostructured biopolymer matrix reinforced with TiO₂ and essential oil: Application for preservation of refrigerated meat. *Food Chemistry*, *126782*.
- Alizadeh-Sani, M., Rhim, J.-W., Azizi-Lalabadi, M., Hemmati-Dinarvand, M., & Ehsani, A. (2020). Preparation and characterization of functional sodium caseinate/guar gum/TiO₂/cumin essential oil composite film. *International Journal of Biological Macromolecules*, *145*, 835–844.
- ASTM-D882-91. (1996). Annual Book of ASTM. *American Society for Testing and Materials*.
- ASTM-E96. (1995). Annual Book of ASTM. *American Society for Testing and Materials*. Philadelphia, PA.
- Bijji, K., Ravishankar, C., Mohan, C., & Gopal, T. S. (2015). Smart packaging systems for food applications: A review. *Journal of Food Science and Technology*, *52*(10), 6125–6135.
- Buraidah, M. H., & Arof, A. K. (2011). Characterization of chitosan/PVA blended electrolyte doped with NH₄. *Journal of Non-crystalline Solids*, *357*(16), 3261–3266.
- Choi, I. Lee, J. Y., Lacroix, M., & Han, J. (2017). Intelligent pH indicator film composed of agar/potato starch and anthocyanin extracts from purple sweet potato. *Food Chemistry*, *218*, 122–128.
- Da Porto, C., & Natolino, A. (2018). Extraction kinetic modelling of total polyphenols and total anthocyanins from saffron floral bio-residues: Comparison of extraction methods. *Food Chemistry*, *258*, 137–143.
- De Dicastillo, C. L., Rodríguez, F., Guarda, A., & Galotto, M. J. (2016b). Antioxidant films based on cross-linked methyl cellulose and native Chilean berry for food packaging applications. *Carbohydrate Polymers*, *136*, 1052–1060.
- de Dicastillo, C. L., Bustos, F., Guarda, A., & Galotto, M. J. (2016a). Cross-linked methyl cellulose films with murta fruit extract for antioxidant and antimicrobial active food packaging. *Food Hydrocolloids*, *60*, 335–344.
- Ezati, P., & Rhim, J.-W. (2020). pH-responsive chitosan-based film incorporated with alizarin for intelligent packaging applications. *Food Hydrocolloids*, *102*, 105629.
- Ezati, P., Tajik, H., Moradi, M., & Molaie, R. (2019). Intelligent pH-sensitive indicator based on starch-cellulose and alizarin dye to track freshness of rainbow trout fillet. *International Journal of Biological Macromolecules*, *132*, 157–165.
- Feketea, G., & Tsabouri, S. (2017). Common food colorants and allergic reactions in children: Myth or reality? *Food Chemistry*, *230*, 578–588.
- Genskowsky, E., Puente, L., Pérez-Álvarez, J., Fernández-Lopez, J., Muñoz, L., & Viuda-Martos, M. (2015). Assessment of antibacterial and antioxidant properties of chitosan edible films incorporated with maqui berry (*Aristotelia chilensis*). *LWT-Food Science and Technology*, *64*(2), 1057–1062.
- Gontard, n., duchez, c., cuq, j.-l., & guilbert, s. (1994). Edible composite films of wheat gluten and lipids: Water vapour permeability and other physical properties. *International Journal of Food Science and Technology*, *29*(1), 39–50.
- Goupy, P., Vian, M. A., Chemat, F., & Caris-Veyrat, C. (2013). Identification and quantification of flavonols, anthocyanins and lutein diesters in tepals of *Crocus sativus* by ultra performance liquid chromatography coupled to diode array and ion trap mass spectrometry detections. *Industrial Crops and Products*, *44*, 496–510.
- Hai, T. A. P., & Sugimoto, R. (2018). Fluorescence control of chitin and chitosan fabricated via surface functionalization using direct oxidative polymerization. *RSC Advances*, *8*(13), 7005–7013.
- Huang, S., Xiong, Y., Zou, Y., Dong, Q., Ding, F., Liu, X., et al. (2019). A novel colorimetric indicator based on agar incorporated with *Arnebium euromae* root extracts for monitoring fish freshness. *Food Hydrocolloids*, *90*, 198–205.
- Kang, S., Wang, H., Xia, L., Chen, M., Li, L., Cheng, J., et al. (2020). Colorimetric film based on polyvinyl alcohol/okra mucilage polysaccharide incorporated with rose anthocyanins for shrimp freshness monitoring. *Carbohydrate Polymers*, *229*, 115402.
- Kerry, J., & Butler, P. (2008). *Smart packaging technologies for fast moving consumer goods*. John Wiley & Sons.
- Kurek, M., Garofulić, I. E., Bakić, M. T., Šćetar, M., Uzelac, V. D., & Galić, K. (2018). Development and evaluation of a novel antioxidant and pH indicator film based on chitosan and food waste sources of antioxidants. *Food Hydrocolloids*, *84*, 238–246.
- Kuswandi, B., Jayus, Restyana, A., Abdullah, A., Heng, L. Y., & Ahmad, M. (2012). A novel colorimetric food package label for fish spoilage based on polyaniline film. *Food Control*, *25*(1), 184–189.
- Lee, M. H., Kim, S. Y., & Park, H. J. (2018). Effect of halloysite nanoclay on the physical, mechanical, and antioxidant properties of chitosan films incorporated with clove essential oil. *Food Hydrocolloids*, *84*, 58–67.
- Liang, T., Sun, G., Cao, L., Li, J., & Wang, L. (2019). A pH and NH₃ sensing intelligent film based on *Artemisia sphaerocephala* Krasch. gum and red cabbage anthocyanins anchored by carboxymethyl cellulose sodium added as a host complex. *Food Hydrocolloids*, *87*, 858–868.
- Liebeck, B. M., Hidalgo, N., Roth, G., Popescu, C., & Böker, A. (2017). Synthesis and characterization of methyl cellulose/keratin hydrolysate composite membranes. *Polymers*, *9*(3), 91.
- Liu, J., Meng, C.-g., Liu, S., Kan, J., & Jin, C.-h. (2017). Preparation and characterization of protocatechuic acid grafted chitosan films with antioxidant activity. *Food Hydrocolloids*, *63*, 457–466.
- Luchese, C. L., Abdalla, V. F., Spada, J. C., & Tessaro, I. C. (2018). Evaluation of blueberry residue incorporated cassava starch film as pH indicator in different simulants and foodstuffs. *Food Hydrocolloids*, *82*, 209–218.
- Ma, Q., Du, L., & Wang, L. (2017). Tara gum/polyvinyl alcohol-based colorimetric NH₃ indicator films incorporating curcumin for intelligent packaging. *Sensors and Actuators B: Chemical*, *244*, 759–766.
- Ma, Q., Liang, T., Cao, L., & Wang, L. (2018). Intelligent poly (vinyl alcohol)-chitosan nanoparticles-mulberry extracts films capable of monitoring pH variations. *International Journal of Biological Macromolecules*, *108*, 576–584.
- Musso, Y. S., Salgado, P. R., & Mauri, A. N. (2019). Smart gelatin films prepared using red cabbage (*Brassica oleracea* L.) extracts as solvent. *Food Hydrocolloids*, *89*, 674–681.
- Pereira, V. A., Jr., de Arruda, I. N. Q., & Stefani, R. (2015). Active chitosan/PVA films with anthocyanins from *Brassica oleracea* (Red Cabbage) as time-temperature indicators for application in intelligent food packaging. *Food Hydrocolloids*, *43*, 180–188.
- Rai, M., Ingle, A. P., Gupta, I., Pandit, R., Paralikar, P., Gade, A., et al. (2019). Smart nanopackaging for the enhancement of food shelf life. *Environmental Chemistry Letters*, *17*(1), 277–290.
- Saliu, F., & Della Pergola, R. (2018). Carbon dioxide colorimetric indicators for food packaging application: Applicability of anthocyanin and poly-lysine mixtures. *Sensors and Actuators B: Chemical*, *258*, 1117–1124.
- Sun, J., Ye, B., Xia, G., Zhao, X., & Wang, H. (2016). A colorimetric and fluorescent chemosensor for the highly sensitive detection of CO₂ gas: Experiment and DFT calculation. *Sensors and Actuators B: Chemical*, *233*, 76–82.
- Wang, S., Xia, P., Wang, S., Liang, J., Sun, Y., Yue, P., et al. (2019). Packaging films formulated with gelatin and anthocyanins nanocomplexes: Physical properties, antioxidant activity and its application for olive oil protection. *Food Hydrocolloids*, *96*, 617–624.
- Wang, X., Yong, H., Gao, L., Li, L., Jin, M., & Liu, J. (2019). Preparation and characterization of antioxidant and pH-sensitive films based on chitosan and black soybean seed coat extract. *Food Hydrocolloids*, *89*, 56–66.
- Wu, C., Sun, J., Zheng, P., Kang, X., Chen, M., Li, Y., et al. (2019). Preparation of an intelligent film based on chitosan/oxidized chitin nanocrystals incorporating black rice bran anthocyanins for seafood spoilage monitoring. *Carbohydrate Polymers*, *222*, 115006.
- Yong, H., Wang, X., Bai, R., Miao, Z., Zhang, X., & Liu, J. (2019). Development of antioxidant and intelligent pH-sensing packaging films by incorporating purple-fleshed sweet potato extract into chitosan matrix. *Food Hydrocolloids*, *90*, 216–224.
- Yong, H., Wang, X., Zhang, X., Liu, Y., Qin, Y., & Liu, J. (2019). Effects of anthocyanin-rich purple and black eggplant extracts on the physical, antioxidant and pH-sensitive properties of chitosan film. *Food Hydrocolloids*, *94*, 93–104.
- Zhai, X., Shi, J., Zou, X., Wang, S., Jiang, C., Zhang, J., et al. (2017). Novel colorimetric films based on starch/polyvinyl alcohol incorporated with rosele anthocyanins for fish freshness monitoring. *Food Hydrocolloids*, *69*, 308–317.
- Zhang, X., Liu, Y., Yong, H., Qin, Y., Liu, J., & Liu, J. (2019). Development of multifunctional food packaging films based on chitosan, TiO₂ nanoparticles and anthocyanin-rich black plum peel extract. *Food Hydrocolloids*, *94*, 80–92.
- Zhang, J., Zou, X., Zhai, X., Huang, X., Jiang, C., & Holmes, M. (2019). Preparation of an intelligent pH film based on biodegradable polymers and rosele anthocyanins for monitoring pork freshness. *Food Chemistry*, *272*, 306–312.
- Zhao, H., Kwak, J. H., Wang, Y., Franz, J. A., White, J. M., & Holladay, J. E. (2007). Interactions between cellulose and N-methylmorpholine-N-oxide. *Carbohydrate Polymers*, *67*(1), 97–103.
- Zhu, Z., Cai, H., & Sun, D.-W. (2018). Titanium dioxide (TiO₂) photocatalysis technology for nonthermal inactivation of microorganisms in foods. *Trends in Food Science & Technology*, *75*, 23–35.

ARTICLES FOR FACULTY MEMBERS

**ROSELLE (HIBISCUS SABDARIFFA) ANTHOCYANIN USE
IN MONITORING MEAT FRESHNESS**

Title/Author	Smart packaging for food spoilage assessment based on hibiscus sabdariffa l. anthocyanin-loaded chitosan films / Khezerlou, A., Tavassoli, M., Alizadeh Sani, M., Ehsani, A., & McClements, D. J.
Source	<i>Journal of Composites Science</i> Volume 7 Issue 10 (2023) 404 Pages 1-14 https://doi.org/10.3390/JCS7100404 (Database: MDPI)

Article

Smart Packaging for Food Spoilage Assessment Based on *Hibiscus sabdariffa* L. Anthocyanin-Loaded Chitosan Films

Arezou Khezerlou ^{1,†}, Milad Tavassoli ^{1,†}, Mahmood Alizadeh Sani ², Ali Ehsani ^{3,*}
and David Julian McClements ^{4,*}

¹ Student Research Committee, Department of Food Science and Technology, Faculty of Nutrition and Food Sciences, Tabriz University of Medical Sciences, Tabriz 5166614711, Iran

² Student's Scientific Research Center, Department of Food Safety and Hygiene, School of Public Health, Tehran University of Medical Sciences, Tehran 5166614711, Iran; saniam7670@gmail.com

³ Nutrition Research Center, Department of Food Science and Technology, Faculty of Nutrition and Food Sciences, Tabriz University of Medical Sciences, Tabriz 5166614711, Iran

⁴ Department of Food Science, University of Massachusetts Amherst, Amherst, MA 01003, USA

* Correspondence: ehsani@tbzmed.ac.ir (A.E.); mclclemetsdj@google.com (D.J.M.)

† These authors contributed equally to this work.

Abstract: An on-package colorimetric label was fabricated using *Hibiscus sabdariffa* L. anthocyanin as a freshness indicator because its color depends on pH. The anthocyanins were embedded within a chitosan matrix. The colorimetric labels were applied to estimate the spoilage of fish food during storage at 25 °C for 3 days. According to scanning electron microscopy results, the inclusion of the anthocyanins in chitosan matrix resulted in formation dense and uniform film. The chitosan colorimetric labels had acceptable thicknesses (78–85 μm), moisture contents (14–16%), swelling indices (84–102%), water vapor permeabilities ($3.0\text{--}3.2 \times 10^{-11}$ g m/m² s Pa), tensile strengths (11.3–12.3 MPa), and elongation at breaks (14–39%). It is noteworthy that the label can distinguish fish spoilage by color turn from light brown (fresh) to grayish (spoiled) by the naked-eye, due to alterations in the pH content and formation of volatile basic nitrogen during storage. Our results indicate that all-natural color labels can be an effective method to monitor the fish spoilage during storage, which may improve food quality and sustainability.

Keywords: color marker; fish freshness; Hibiscus tea anthocyanins; intelligent packaging; on package colorimetric label



Citation: Khezerlou, A.; Tavassoli, M.; Alizadeh Sani, M.; Ehsani, A.; McClements, D.J. Smart Packaging for Food Spoilage Assessment Based on *Hibiscus sabdariffa* L. Anthocyanin-Loaded Chitosan Films. *J. Compos. Sci.* **2023**, *7*, 404. <https://doi.org/10.3390/jcs7100404>

Academic Editor: Francesco Tornabene

Received: 5 August 2023

Revised: 1 September 2023

Accepted: 22 September 2023

Published: 24 September 2023



Copyright: © 2023 by the authors. Licensee MDPI, Basel, Switzerland. This article is an open access article distributed under the terms and conditions of the Creative Commons Attribution (CC BY) license (<https://creativecommons.org/licenses/by/4.0/>).

1. Introduction

Natural film-forming materials, like many proteins and polysaccharides, are being explored for their ability to construct more sustainable and green packaging materials to replace synthetic plastics [1,2]. The functional performance of these biopolymer-based packaging materials is often enhanced by incorporating additives that provide specific desirable functions, such as product monitoring (smart packaging) or product preservation (active packaging) [3,4]. Smart packaging materials include sensors that can monitor the food and/or environment inside the package and provide information about its freshness, quality, or safety [5,6]. The information provided by these sensors can be used by the food industry, retailers, and consumers to determine when a food should be sold, consumed, and discarded. Three major systems exist for intelligent packaging: data carriers, sensors, and indicators. There are many types of indicators that are categorized into three groups: freshness, Time-Temperature, and gas indicators. Colorimetric indicators based on pH changes are one of the most widely explored sensors in food packaging research because of their simplicity and non-invasive nature [7,8]. Color changes can easily be visually detected by food retailers and consumers [6,9]. Natural pigments isolated from botanical sources are being utilized for this purpose because they are sustainable, safe, and label

friendly, as well as exhibiting additional functional attributes, such as antioxidant and antimicrobial activity [10]. Plants contain a variety of pigments with the potential of being utilized as pH-sensitive sensors, especially anthocyanins [11]. Anthocyanins are extracted from many different types of spices, fruits, and vegetables, including saffron, rich black plum peel, red cabbage, red barberry, blueberry, purple sweet potato, and *cinnamomum camphora* fruit [12–16]. Anthocyanins with antimicrobial and antioxidant effect can improve the shelf life of foods by acting as natural preservatives in packaging materials [17]. Anthocyanins are water-soluble pigments whose color is strongly dependent on the pH of their surroundings [18], which is due to changes in their chemical structure [2].

One of the most widely used film-forming biopolymers for constructing sustainable packaging materials is chitosan, which is a cationic polysaccharide obtained from crab shells and some mushrooms [6,19]. In this study, we explored the possibility of using chitosan to construct biopolymer films that were loaded with anthocyanin-based color sensors. Several researchers have reported that chitosan can form films that are thin, flexible, translucent, and capable of incorporating functional additives [19–21]. The fact that chitosan can form clear films is important as it enables any color changes to be detected more easily [8].

Hibiscus sabdariffa L. (Roselle plant) is an annual herbaceous plant that belongs to the *Malvaceae* family [22]. It is widely cultivated around the world, including Asia, Central America, and Africa. *H. sabdariffa* has been shown to exhibit antioxidant, antibacterial, anti-inflammatory, cholesterol lowering, and hepatoprotective properties, which has been ascribed to the presence of anthocyanins and other bioactive phytochemicals [23]. The flowers of *H. sabdariffa* have a strong reddish color, which is due to the presence of a variety of anthocyanins, including delphinidin-3-sambubioside, cyanidin-3-sambubioside, cyanidin-3-glucoside, and delphinidin-3-glucoside [24]. In a recently published article, Toro-Márquez, Merino and Gutiérrez [25] developed composite films based on corn starch, montmorillonite, and anthocyanin-Jamaica (*Hibiscus sabdariffa*) flower extract. They studied the structural, thermal, and physicomechanical properties and color change of films at different pH conditions (1, 7, and 13). The objective of our study was to determine whether *H. sabdariffa* pigments could be used as natural labels to detect changes in food quality. Our hypothesis was that *H. sabdariffa* pigments in packaging materials can detect quality changes in fresh foods during storage because their deterioration leads to changes in pH.

In this study, *H. sabdariffa* anthocyanins (HSAs) were incorporated into chitosan-based on-package colorimetric labels to monitor fish spoilage. Initially, the structural, mechanical, optical, and barrier characteristics of the HSA-chitosan labels were characterized. Then, the response of these labels to changes in pH and ammonia levels was characterized. Finally, the potential of the HSA-chitosan labels for monitoring fish spoilage during room storage was evaluated.

2. Materials and Methods

2.1. Materials

Dried Hibiscus (*Hibiscus sabdariffa*) calyces were procured from the local market (Tabriz, Republic of Iran). Chitosan (low molecular weight, 50,000–190,000 Da (based on viscosity), 20–300 cP, 1 wt% in 1% acetic acid at 25 °C) and degree of deacetylation = 75–85%), ammonia solution, and sodium hydroxide (NaOH) pellets were bought from Sigma-Aldrich (St. Louis, MI, USA). Glycerol, hydrochloric acid (HCL), acetic acid, and anhydrous CaCl₂ were obtained from the Merck Co (Darmstadt, Germany). Ethanol (99.9%) was supplied by the Kimia Shimi Company (Tabriz, Iran). Fish meat was bought from the Fish Store (Tabriz, Iran). Analytical-grade reagents were used for all studies.

2.2. Anthocyanin Extraction

Anthocyanins were extracted from the *H. sabdariffa* calyces using a soaking method. Initially, the dried powder of *H. sabdariffa* was mixed with a blend of 70 mL distilled water and 30 mL ethanol and the mixture was gently agitated using a mechanical shaker (KS 130 Basic, IKA, Germany) at 50 rpm for 24 h. After filtration, the ethanol was evaporated

from the resulting HSA solution at 50 °C. The color change and UV–visible spectra of the HSA solutions obtained were then characterized after their pH values were adjusted [26].

2.3. Fabrication of Colorimetric Label

The colorimetric pH-sensitivity label was prepared by a casting method. Initially, a film-forming solution containing 3% chitosan (*w/v*) and 30 wt% glycerol (*w/v*) (on chitosan basis) in 100 mL of 1% acetic acid was prepared by vigorously stirring at 25 °C for 5 h. Following this, 3% HSAs (*w/v*) was added to the chitosan gel matrix, and the resulting mixture was stirred for 15 min and then degassed for 3 min to remove any air bubbles. Finally, the resulting solution was decanted into a plastic petri dish (8 cm diameter) and dried at 37 °C in a drying oven to obtain the colorimetric labels. Each components concentration was calculated according to the chitosan weight. For comparison, a control chitosan label was prepared without *H. sabdariffa*.

2.4. Structural Characterization of Label

The surface microstructure of the labels was monitored by the SEM instrument (TeScan-Mira 3xmu SEM, Czech Republic) at 25 kV accelerating voltage. The molecular structures of the chitosan and HAS-loaded chitosan labels were characterized using a Fourier transform infrared (FTIR) spectrometer (Tensor 27, Bruker, Billerica, MA, USA) over the wavenumber range from 4000 to 400 cm^{-1} with 4 cm^{-1} resolutions. The tensile strength (TS) and elongation at break (EAB) of the labels were measured using a tensile testing machine (Model DBBP-20, Republic of Korea). The sample dimensions used were 10 cm \times 1 cm, the maximum stretching distance was 30 mm, and the stretching speed was 10 mm/min.

2.5. Dimensions and Physical Properties of Labels

The thickness of the labels was measured at five randomly selected locations using a micrometer (Mitutoyo, Japan) and the average was calculated. The moisture content (MC) of the labels was computed by the difference in weight of the labels before and after drying at 110 °C for 24 h:

$$\text{MC (\%)} = \frac{W_{\text{before}} - W_{\text{after}}}{W_{\text{before}}} \times 100 \quad (1)$$

The swelling index (SI) of the labels was determined by measuring the weight of the label before (W_{Dry}) and after (W_{Wet}) they were soaked in 20 mL of distilled water for 24 h:

$$\text{SI (\%)} = \left[\frac{W_{\text{Wet}} - W_{\text{Dry}}}{W_{\text{Wet}}} \right] \times 100 \quad (2)$$

The water vapor permeability (WVP) was determined using a standardized gravimetric method (ASTM-E96-1995). First, the open tops of cylindrical cups containing 5 g anhydrous CaCl_2 (0% RH, 25 °C) were sealed using the label material. The cups were then placed within a desiccator containing distilled water (100% RH, 25 °C) and weighed every 3 h 6 times.

The water contact angle (WCA) was measured using a contact angle analyzer (Phonex 150, Republic of Korea): the sample size was 3 cm \times 6 cm, the test liquid was water, the drop size was 5 μL , and the equilibrium time was 20 s.

2.6. Color Characterization of Label

The transparency of the labels was determined by dividing the film transmission measured at 600 nm using a spectrophotometer by the label thickness measured by a digital micrometer. The optical properties (absorption and transmittance) of the film samples were also recorded from 200 to 800 nm using a UV–vis spectrophotometer (Unico, UV-2100, Dayton, USA).

A colorimeter (Hunter lab, Konica Minolta, Japan) was used to analyze the tristimulus color coordinates (L, a, b) of the labels. The color difference (ΔE) was also calculated from the color coordinates:

$$\Delta E = \sqrt{(L_s - L)^2 + (a_s - a)^2 + (b_s - b)^2} \quad (3)$$

The values from the white screen used as a back plate were: L_s (98.87), a_s (−2.54), and b_s (3.95).

2.7. Ammonia Vapor Sensitivity Test

The sensitivity of the labels to ammonia vapor was analyzed using a method described previously with slight modifications. Briefly, labels were cut into a circle (2 cm diameter) and then placed in 80 mL of NH_3 solution (0.8 M). Digital photographs of the samples were recorded every 5 min for 30 min. The sensitivity (S_{RGB}) of the labels was then calculated:

$$S_{RGB}(\%) = \frac{(R_i - R_f) + (G_i - G_f) + (B_i - B_f)}{R_i + G_i + B_i} \times 100 \quad (4)$$

2.8. Color Release Test

A color release test was used to evaluate the affinity for the anthocyanins for the chitosan-based labels. Each label was immersed in 30 mL of food simulants with different polarities (0%, 10%, 50%, or 95% ethanol in distilled water) and then gently shaken for 4 h. A UV–vis spectrophotometer was then used to measure the absorbance of the label solutions after predetermined times (15, 30, 60, 90, 120, 180, and 240 min). The pigment release rate was then calculated as anthocyanin/ mm^2 .

2.9. Fish Spoilage Test

Fish slices were placed in a plastic container and an HSA-loaded label was affixed to the inner side of the top of each container. The containers were then stored at 25 °C for three days. The pH values, TVB-N levels, and color of the labels were recorded every 12 h at 25 °C. The color changes of the labels were documented using digital photography.

2.10. Statistical Analysis

Means and standard deviations (SD) were calculated from repeated experiments. The experimental results were tested using a one-way analysis of variance (ANOVA) by Microsoft Excel 2016. A statistically significant result was defined as $p < 0.05$.

3. Results and Discussion

3.1. pH Response of Anthocyanin Solutions

The halochromic behavior of the HSA solutions were characterized by measuring the color and UV–visible spectra at different pH values (2–12) (Figure 1a,b). With increasing pH, the color of the HSA solutions changed from reddish to pink to olive to yellow. This color change can be ascribed to pH-induced changes in the molecular characteristics of the anthocyanins, from flavylium cation ($\text{pH} \leq 3$) to quinonoidal anhydro-base ($\text{pH} 6\text{--}7$) to chalcone ($\text{pH} \geq 8$) (Figure 1c) [15]. The color change pattern of HAS was similar to onion peel extract [27].

The maximum absorbance in the UV–visible spectra was around ~510 nm under highly acidic conditions, which corresponds to the flavylium cations. With increasing pH, the maximum absorbance gradually decreased and there was a slight bathochromic shift to higher wavelengths, which can be ascribed to the transition to a chalcone structure [28,29]. Similar findings have been reported for anthocyanins extracted from black plum peels [15] and blueberries [30]. The observed change in color of the HSA solutions with pH suggests that these anthocyanins might be suitable for application as natural halochromic indicators in the labels.

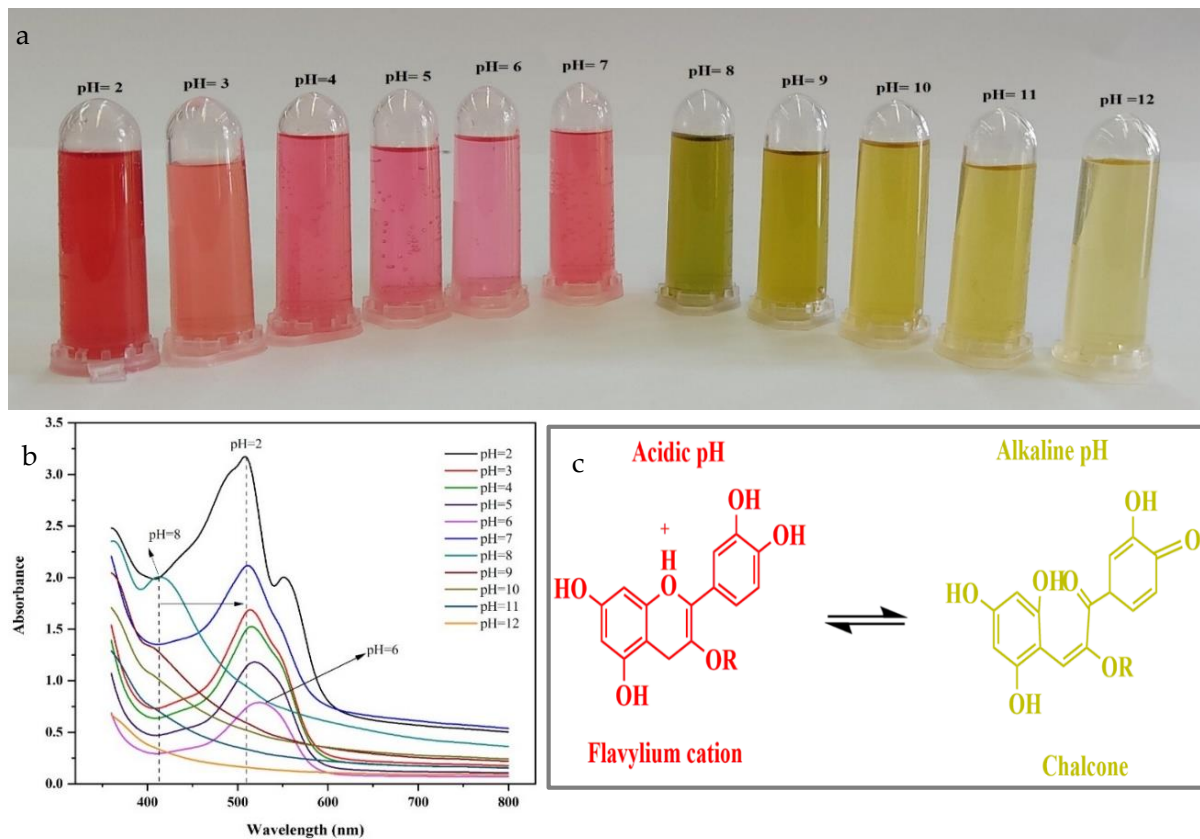


Figure 1. (a) The appearance of the HSA solutions; (b) UV-vis spectra of HSA solutions at different pH values; (c) Chemical structure of anthocyanins at different pH values.

3.2. Structural Characterization of Labels

SEM was used to provide insights into the morphology of the chitosan-based labels (Figure 2a,b). The labels formed from chitosan had smooth, homogeneous, and compact surfaces in both the presence and absence of the HSAs. There was no evidence of cracks or other irregularities in the films containing the HSAs, suggesting that the anthocyanins were well dispersed within the chitosan matrix. This phenomenon can be attributed to the existence of OH groups in the anthocyanins, which can form intramolecular H-bonds with the chitosan molecules [31,32].

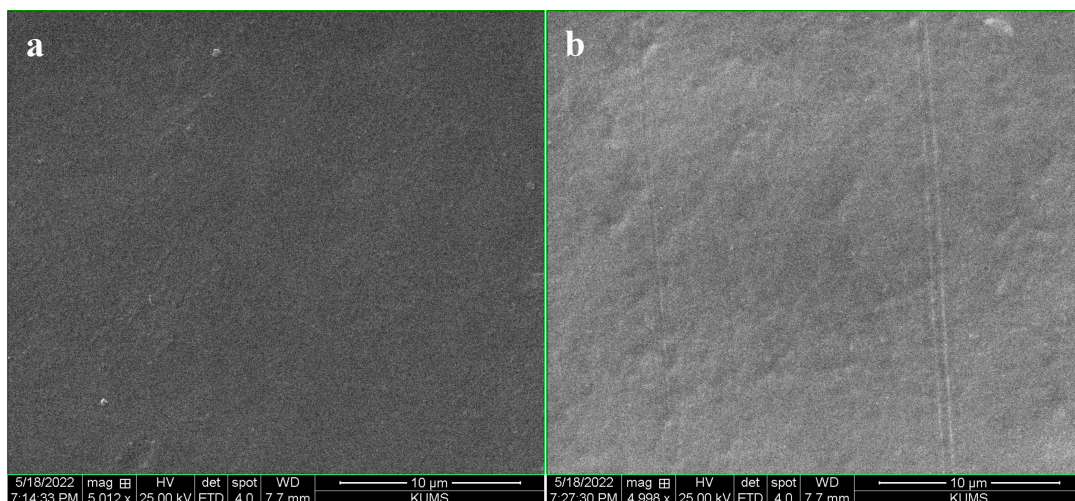


Figure 2. SEM images of (a) pure chitosan and (b) HSA-loaded chitosan labels.

FTIR analysis was conducted to provide information about the molecular interactions of the chitosan-based labels (Figure 3). The FTIR spectra show that there was a peak at 3240 cm^{-1} , which can be ascribed to O-H stretching vibrations caused by intramolecular and intermolecular hydrogen bonding, as well as N-H stretching vibrations caused by amino groups in the chitosan. The peak observed at 2895 cm^{-1} can be ascribed to the stretching vibration of C-H bonds in $-\text{CH}_2$ and $-\text{CH}_3$ groups. The peak observed at 1640 cm^{-1} refer to C=O stretching vibrations of Amide I groups. The absorption peak at 1010 cm^{-1} can be ascribed to C-O and C-N stretching vibrations molecules [1].

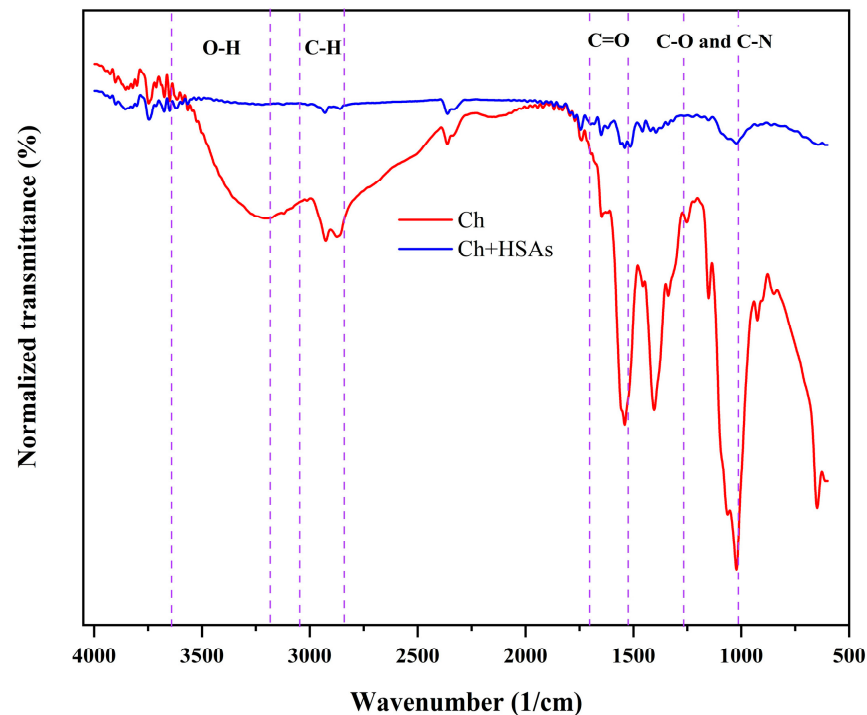


Figure 3. FTIR spectra of pure chitosan and HSA-loaded chitosan labels.

A comparison of the FTIR spectra of the pure chitosan and the HSA-loaded chitosan labels indicated that the immobilization of anthocyanins results in noteworthy changes in the spectra of the label, which is consistent with changes in the composition and molecular interactions of the labels. The increase in intensity of the peaks after incorporation of the HSA into the chitosan labels can be attributed to the formation of H-bonds between the O-H groups in the anthocyanins and the O-H groups in the chitosan. Overall, these observations suggest that the HSA were compatible with the chitosan matrix.

Compared with the pure chitosan labels, the ones containing the HSAs had higher tensile strength and lower elongation at break values (Table 1). This effect can be ascribed to the strong binding of anthocyanin molecules to multiple chitosan chains leading to increased crosslinking. [33]. As a result, the labels became stronger and less flexible, which is in agreement with other studies on the impact of anthocyanins on the mechanical properties of biopolymer films [34].

Table 1. Dimensions and physical properties of chitosan and HSA-loaded chitosan labels.

Labels	Thickness (μm)	MC (%)	SI (%)	WVP ($\text{g m}^{-2} \text{ s Pa}$)	TS (MPa)	EAB (%)	Transparency (%)
Chitosan	79.8 ± 0.1^a	16.3 ± 0.2^a	102.0 ± 0.6^a	3.2 ± 0.02^a	11.25 ± 0.14^a	38.76 ± 0.07^a	78.6 ± 0.6^a
HAS-chitosan	85.4 ± 0.6^b	14.3 ± 0.4^b	83.6 ± 0.4^b	2.99 ± 0.06^b	12.25 ± 0.16^b	13.87 ± 0.02^b	53.0 ± 0.4^b

MC: moisture content; SI: swelling index; WVP: water vapor permeability; TS: tensile strength; EAB: elongation at break. lowercase letters show significant differences between chitosan and HSA-loaded chitosan labels.

3.3. Dimensions and Physical Properties of Labels

The HAS-loaded chitosan label (85.4 μm) was significantly thicker than that of the pure chitosan label (79.8 μm) (Table 1), even though they were prepared under the same conditions. This effect can mainly be attributed to the increased solids content of the colorimetric labels caused by the presence of the anthocyanin additives. However, the crosslinking of the chitosan molecules by anthocyanin may also have altered the molecular organization of the biopolymer molecules in the labels, thereby rising their thickness. Other studies have also shown that adding anthocyanins to chitosan films increases their thickness [35].

The pure chitosan labels had a higher moisture content amount (16.3%) than the HSA-loaded ones (14.3%). This effect might have occurred because the interactions between the anthocyanin and chitosan molecules within the biopolymer matrix reduced the number of free hydroxyl groups available for water molecules to interact with [36,37]. The swelling index of the pure chitosan labels (102%) was significantly higher than that of the HSA-loaded ones (83.6%), which can be accredited to the fact that the crosslinking of the chitosan molecules in the biopolymer matrix by anthocyanins restricted their ability to swell in the presence of water [38].

Measurements of the WVP of packaging materials provide insights into their ability to resist the movement of water from inside to outside the packaging or vice versa, which has an important impact on food quality and shelf life. The WVP of the pure chitosan label ($3.2 \times 10^{-11} \text{ g m/m}^2 \text{ s Pa}$) was slightly more than the one that contained the HSAs ($2.99 \times 10^{-11} \text{ g m/m}^2 \text{ s Pa}$). This effect may have been for the reason that crosslinking of the chitosan molecules altered the microstructure of the biopolymer network (such as its porosity), which declined the ability of the water vapor molecules to travel through. Similar results have been found when another kind of anthocyanin was incorporated into polycaprolactone films [39].

The wettability of the labels was studied using a water contact angle test (Figure 4a,b). The wettability of the pure chitosan film (WCA = 63.7°) was greater than that of the one that contained the HSAs (57.8°). This result proposes that the presence of the anthocyanins in the labels reduced their hydrophobicity. This is probably because the anthocyanins are more hydrophilic than chitosan [40,41]. Other studies have also revealed that including anthocyanins to biopolymer-based packaging materials reduces their contact angle [19,41,42].

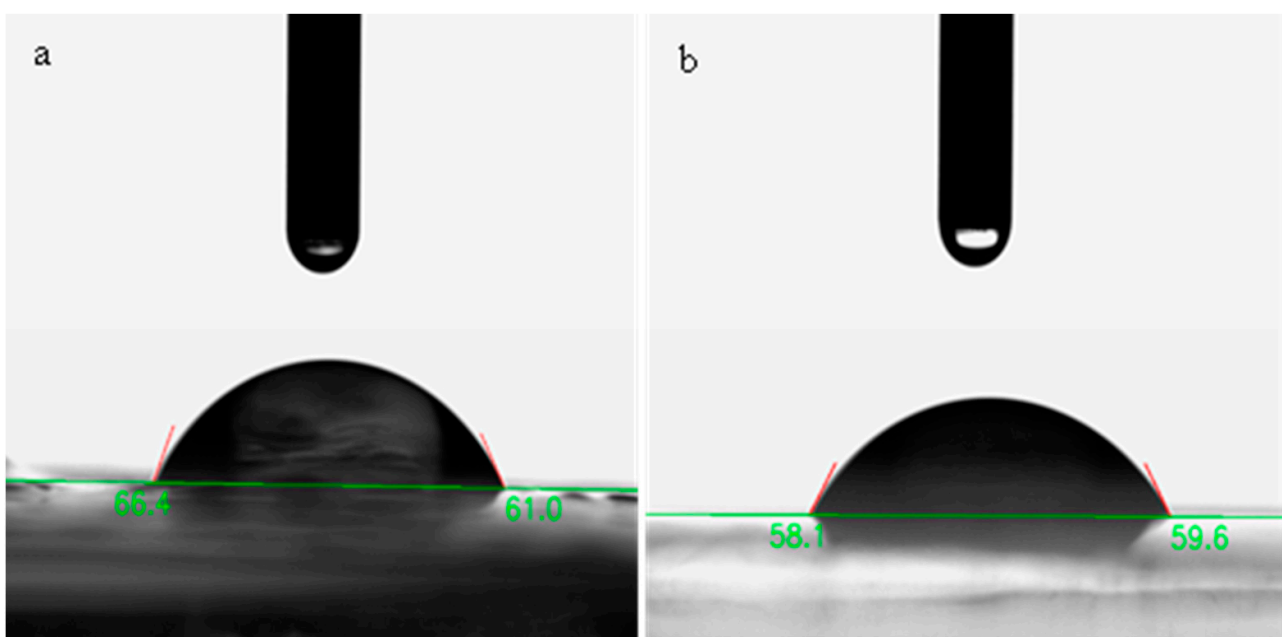


Figure 4. Schematic diagram of WCA of pure Ch (a) and Ch/HSAs label (b).

3.4. Color Characterization of Labels

The appearance and transparency of packaging materials is important because it impacts consumer perception of food products, as well as the susceptibility of foods to photodegradation reactions that can cause discoloration and nutritional loss [43]. Visually, the pure chitosan labels appeared colorless and highly transparent, whereas the ones containing the HSAs appeared light brown and slightly cloudy, which suggests that the existence of the anthocyanins caused selective light absorption and scattering.

The UV–visible light transmittance and absorbance spectra of the labels were recorded via a UV–visible spectrophotometer to provide further insights into their optical properties (Figure 5a,b). The HSA-loaded chitosan labels exhibited greater UV light barrier characteristics and declined light transmittance (especially around ~280 nm) than the pure chitosan ones. This effect can be ascribed to the capability of anthocyanins to absorb UV light, as well as to their ability to change the microstructure of the chitosan network in a way that increases light scattering [28,44]. For instance, crosslinking of the chitosan molecules by the anthocyanins may have led to the formation of heterogeneities with dimensions close to the wavelength of UV light. The fact that the transmittance of the labels containing the anthocyanins was less in the visible wavelength range is consistent with the visible observations that they were less clear and browner than the pure chitosan labels. Reduction in clarity and changes in color of biopolymer-based films has been reported after incorporating anthocyanins by [8,43].

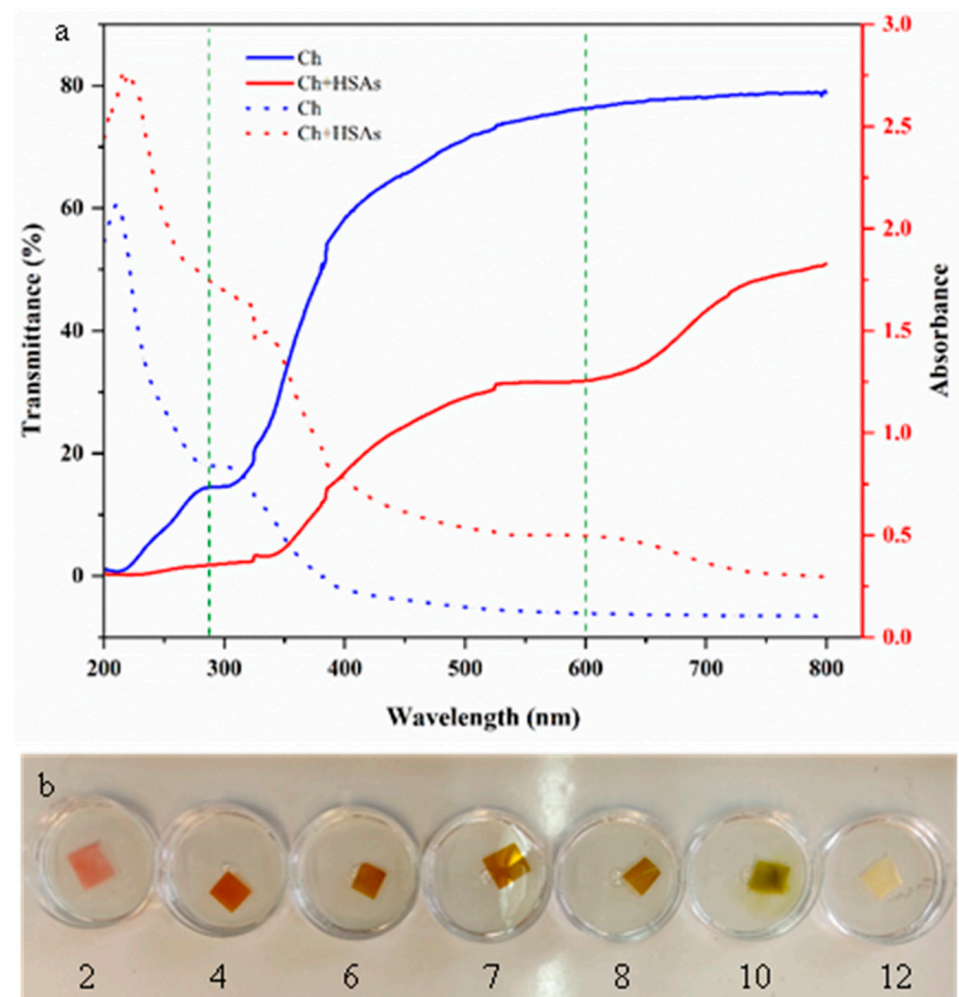


Figure 5. (a) Impact of wavelength on the UV–visible transmittance and absorbance of pure chitosan and HSA-loaded chitosan labels; (b) Photographs of the HSA-loaded chitosan labels at pH values ranging from 2 to 12.

3.5. Ammonia Test

Seafood products release volatile ammonia when they deteriorate due to the generation of nitrogenous products by microorganisms when they digest proteins. The release of these gases can cause color changes in anthocyanins, which can therefore be used as a halochromic sensor of food quality. In this study, the sensitivity of the HSA-loaded chitosan films to ammonia compounds released from fish samples was evaluated using a sensitivity test (SRGB). The sensitivity of the labels to volatile NH_3 was measured at 5-min intervals for 25 min. The color change and SRGB values of the labels are shown in Figure 6. Based on sensitivity results, the color of the labels changed from light brown to green and their SRGB value increased to 37.5% in the first 5 min. This color change can be ascribed to the fact that NH_3 reacts with H_2O in the labels, which results in the production of NH_4^+ and OH^- . The presence of the NH_4^+ changes the pH inside the labels, which promotes a structural transformation of the anthocyanins, leading to a color change from light brown to green. The color of the labels changed from green to dark green after about 10 min of exposure to the ammonia atmosphere, and the SRGB value increased to 42.3%. Upon further storage, the labels became darker green and the SRGB values increased. These results indicate that the HSA-loaded chitosan labels responded significantly to the presence of the volatile ammonia within the first 5 min, which indicates they had a relatively fast response time. Other researchers have also reported that biopolymer films containing other kinds of anthocyanins also exhibit this kind of behavior [7].

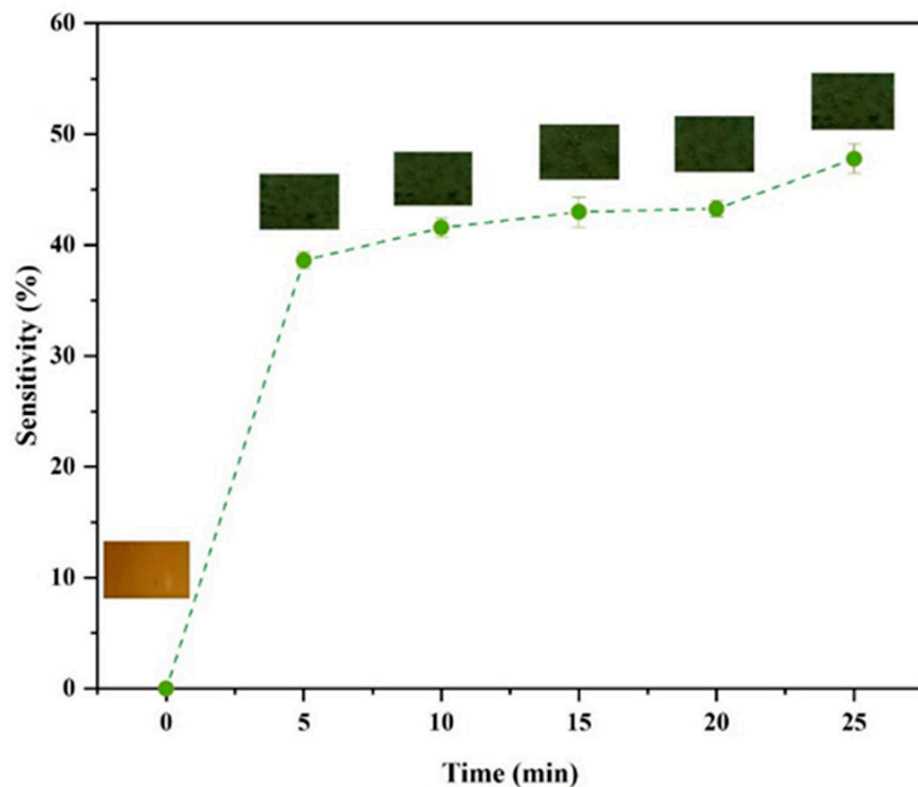


Figure 6. Impact of incubation time on the color and color sensitivity of HSA-loaded chitosan labels in the presence of ammonia gas.

3.6. Release of HSA from Labels into Food Simulants

The release of anthocyanins from chitosan films into four model food simulants with different polarities is shown in Figure 7. All samples exhibited a relatively fast release during the first 30 min (1.2–5%) followed by a slower release over the next 60 min, until a relatively constant value was reached. The release of the anthocyanins depended on the alcohol concentration in the food simulants. The release of HSAs from the labels was fairly similar when they were exposed to contact with food simulants containing relatively

low ethanol concentrations (0, 10, or 50%). However, the release rate was much smaller for the sample containing the highest ethanol concentration (95%). This effect may have been because high ethanol levels reduced the swelling of the labels, thereby inhibiting the diffusion of the anthocyanins out of the chitosan network. Similar findings have been reported by other researchers using different types of anthocyanins [6,45].

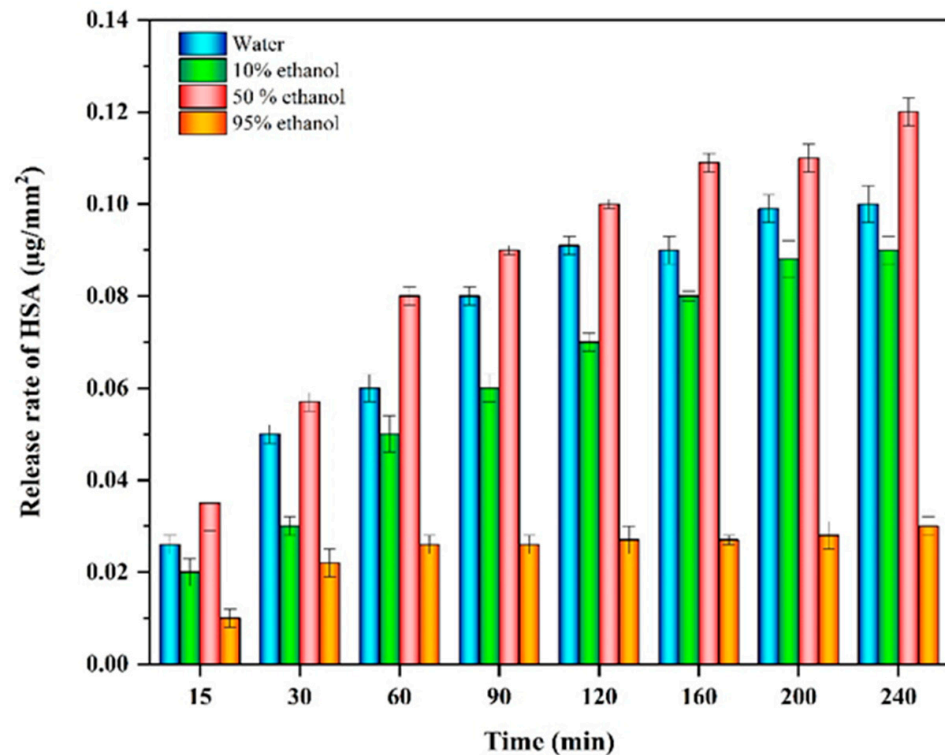


Figure 7. Release rate of anthocyanins from HSA-loaded chitosan labels when brought into contact with food simulants with different polarities.

3.7. Monitoring of Fish Spoilage

Finally, the HSA-loaded chitosan labels were used to monitor the spoilage of fish during storage at 25 °C (Figure 8a). Visibly, the color of the labels changed from light brown before storage to grayish after storage. This phenomenon can be attributed to the increase in TVB-N level and pH due to decomposition of the fish protein tissue by enzymes and microorganisms, leading to ammonia production (Figure 8b). Indeed, the pH of the samples increased from 6.8 to 8.4 and the TVB-N concentration increased from 6.7 to 53.3 mg/100 g after 72 h storage. These results suggest that the fish samples would be inedible after three days storage because they exceeded the safe consumption threshold [46]. Trials on fish show that HSA-loaded chitosan labels may be applied for spoilage monitoring of fish samples, due to their significant color change (ΔE) at storage time. There were good linear correlations between the pH value of the fish and the color change ($R^2 = 0.990$; Figure 8c), and between the TVB-N levels of the fish and the color change ($R^2 = 0.9909$; Figure 8d). Several other studies have shown the potential of anthocyanins as natural colorimetric sensors to monitor the freshness of foods. For instance, Wang et al. used a chitosan/chitin ester nanofiber film matrix and eggplant peel anthocyanins to distinguish pork freshness [47]. Their indicator films were also sensitive to NH_3 and pH and provided information about changes in the freshness of the pork after storage of 48 h. In another study, Alnadari et al. reported similar results for freshness monitoring of beef using a carboxymethyl cellulose based indicator imbued with *Cinnamomum camphora* fruit peel waste anthocyanins [16].

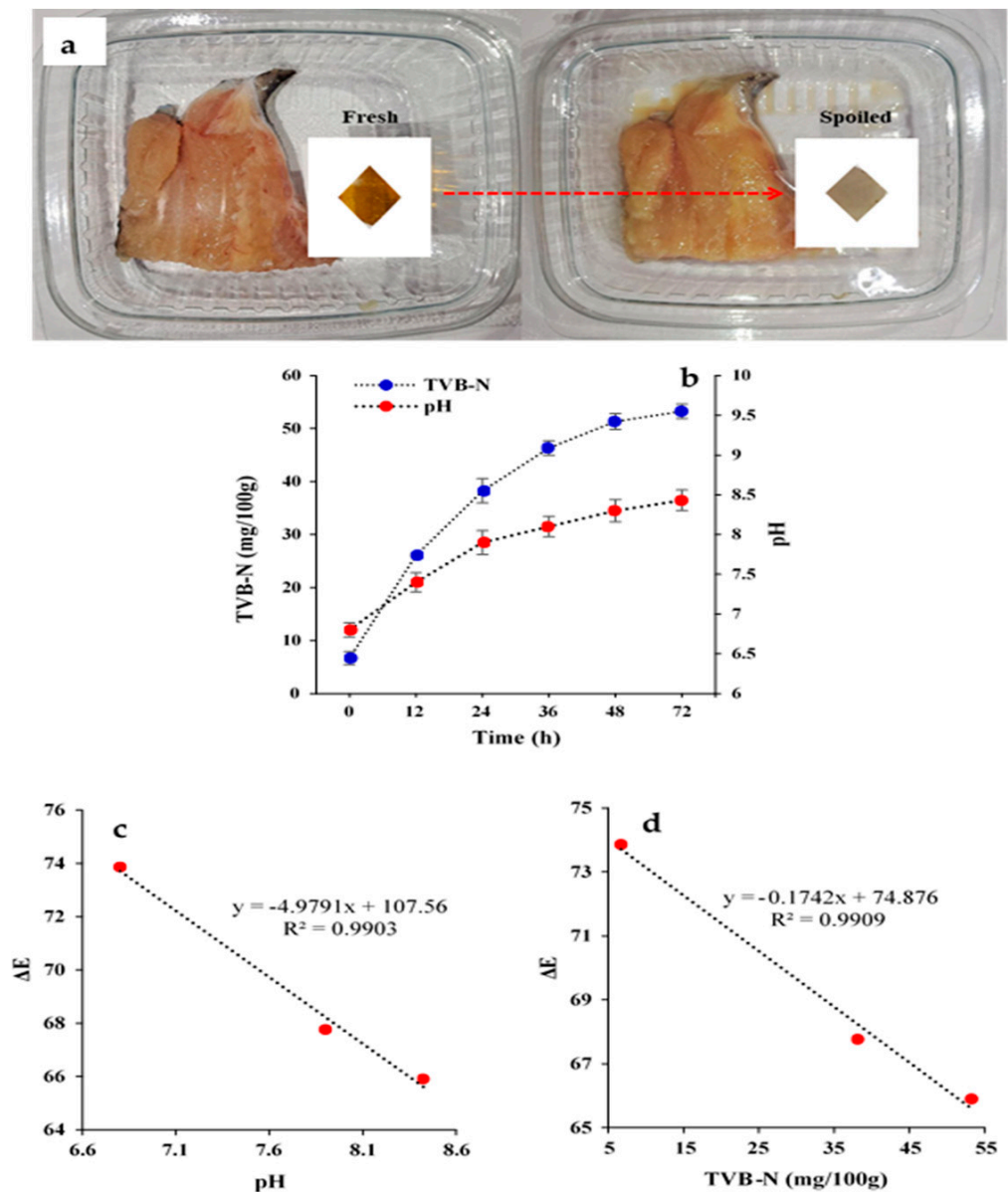


Figure 8. (a) Color changes of on-packaging HSA-loaded chitosan labels during fish storage; (b) Change in TVB-N and pH values of fish sample during storage; (c,d) correlation analysis of quality parameters (pH, and TVB-N) of fish and ΔE of the labels.

4. Conclusions

This study has shown that on-package colorimetric labels can be assembled from natural pigments (anthocyanins) and polymers (chitosan). As observed, these labels changed color, owing to the presence of ammonia gas inside packaging and alterations in pH and could therefore be used to monitor changes in the fish quality at duration of storage. Microscopy and spectroscopy analysis suggested that the HSAs were successfully integrated into the chitosan matrix within the labels. The incorporation of the anthocyanins increased their mechanical strength but made them more brittle, which was attributed to their ability to crosslink the chitosan molecules. Moreover, the anthocyanins reduced the swelling and WVP of the chitosan films, which was again attributed to their crosslinking effects. The color change of the anthocyanins are pH and volatile nitrogenous gas contents dependent, which suggested they would be suitable for monitoring the spoilage of meat products. This was confirmed by using the anthocyanin-loaded chitosan labels to monitor the freshness of fish during the duration of storage. The labels turned from light brown (fresh) to grey

(spoiled) after storage, with the magnitude of the color change being closely correlated to the pH and TVB-N levels.

These natural sensors could be utilized within the food industry to provide producers, retailers, and consumers with information about the freshness of foodstuffs in real time. In the food industry, the utilization of these smart packaging materials may boost sustainability and reduce environmental concerns.

Author Contributions: A.K.: conceptualization, data curation, formal analysis, funding acquisition, investigation, methodology, project administration, visualization, writing—original draft; M.T.: conceptualization, data curation, Formal analysis, funding acquisition, investigation, methodology, project administration, visualization, writing—original draft; M.A.S.: conceptualization, data curation, formal analysis, funding acquisition, investigation, methodology, project administration, visualization, writing—original draft; A.E.: conceptualization, funding acquisition, investigation, methodology, project administration, supervision, visualization, writing—original draft; D.J.M.: investigation, writing—review and editing. All authors have read and agreed to the published version of the manuscript.

Funding: The study was approved and supported by the Student Research Committee, Tabriz University of Medical Sciences, Tabriz, Iran [project no. 70155].

Data Availability Statement: Data will be made available on request.

Conflicts of Interest: The authors declare no competing interest.

References

- Alizadeh Sani, M.; Khezerlou, A.; Tavassoli, M.; Mohammadi, K.; Hassani, S.; Ehsani, A.; McClements, D.J. Bionanocomposite active packaging material based on soy protein Isolate/Persian Gum/Silver nanoparticles; fabrication and characteristics. *Colloids Interfaces* **2022**, *6*, 57. [[CrossRef](#)]
- Abedi-Firoozjah, R.; Salim, S.A.; Hasanvand, S.; Assadpour, E.; Azizi-Lalabadi, M.; Prieto, M.A.; Jafari, S.M. Application of smart packaging for seafood: A comprehensive review. *Compr. Rev. Food Sci. Food Saf.* **2023**, *22*, 1438–1461. [[CrossRef](#)]
- Kaur, G.; Sharma, S.; Mir, S.A.; Dar, B.N. Nanobiocomposite Films: A “Greener Alternate” for Food Packaging. *Food Bioprocess Technol.* **2021**, *14*, 1013–1027. [[CrossRef](#)]
- Milad, T.; Khezerlou, A.; Moghaddam, T.N.; Firoozy, S.; Bakhshizadeh, M.; Sani, M.A.; Hashemi, M.; Ehsani, A.; Lorenzo, J.M. Sumac (*Rhus coriaria* L.) anthocyanin loaded-pectin and chitosan nanofiber matrices for real-time monitoring of shrimp freshness. *Int. J. Biol. Macromol.* **2023**, *242*, 125044. [[CrossRef](#)]
- Cerqueira, M.A.; Costa, M.J.; Fuciños, C.; Pastrana, L.M.; Vicente, A.A. Development of Active and Nanotechnology-based Smart Edible Packaging Systems: Physical–chemical Characterization. *Food Bioprocess Technol.* **2014**, *7*, 1472–1482. [[CrossRef](#)]
- Arezou, K.; Tavassoli, M.; Alizadeh-Sani, M.; Hashemi, M.; Ehsani, A.; Bangar, S.P. Multifunctional food packaging materials: Lactoferrin loaded Cr-MOF in films-based gelatin/ κ -carrageenan for food packaging applications. *Int. J. Biol. Macromol.* **2023**, *251*, 126334. [[CrossRef](#)]
- Tavassoli, M.; Alizadeh Sani, M.; Khezerlou, A.; Ehsani, A.; Jahed-Khaniki, G.; McClements, D.J. Smart Biopolymer-Based Nanocomposite Materials Containing pH-Sensing Colorimetric Indicators for Food Freshness Monitoring. *Molecules* **2022**, *27*, 3168. [[CrossRef](#)]
- Ezati, P.; Rhim, J.-W. pH-responsive chitosan-based film incorporated with alizarin for intelligent packaging applications. *Food Hydrocoll.* **2020**, *102*, 105629. [[CrossRef](#)]
- Becerril, R.; Nerín, C.; Silva, F. Bring some colour to your package: Freshness indicators based on anthocyanin extracts. *Trends Food Sci. Technol.* **2021**, *111*, 495–505. [[CrossRef](#)]
- López-Cruz, R.; Sandoval-Contreras, T.; Iñiguez-Moreno, M. Plant Pigments: Classification, Extraction, and Challenge of Their Application in the Food Industry. *Food Bioprocess Technol.* **2023**, 1–17. [[CrossRef](#)]
- Qi, D.; Xiao, Y.; Xia, L.; Li, L.; Jiang, S.; Jiang, S.; Wang, H. Colorimetric films incorporated with nisin and anthocyanins of pomegranate/*Clitoria ternatea* for shrimp freshness monitoring and retaining. *Food Packag. Shelf Life* **2022**, *33*, 100898. [[CrossRef](#)]
- Zhang, J.; Zou, X.; Zhai, X.; Huang, X.; Jiang, C.; Holmes, M. Preparation of an intelligent pH film based on biodegradable polymers and roselle anthocyanins for monitoring pork freshness. *Food Chem.* **2019**, *272*, 306–312. [[CrossRef](#)] [[PubMed](#)]
- Liu, D.; Cui, Z.; Shang, M.; Zhong, Y. A colorimetric film based on polyvinyl alcohol/sodium carboxymethyl cellulose incorporated with red cabbage anthocyanin for monitoring pork freshness. *Food Packag. Shelf Life* **2021**, *28*, 100641. [[CrossRef](#)]
- Sohany, M.; Tawakkal, I.S.; Ariffin, S.H.; Shah, N.N.; Yusof, Y.A. Characterization of Anthocyanin Associated Purple Sweet Potato Starch and Peel-Based pH Indicator Films. *Foods* **2021**, *10*, 2005. [[CrossRef](#)] [[PubMed](#)]
- Zhang, X.; Liu, Y.; Yong, H.; Qin, Y.; Liu, J.; Liu, J. Development of multifunctional food packaging films based on chitosan, TiO₂ nanoparticles and anthocyanin-rich black plum peel extract. *Food Hydrocoll.* **2019**, *94*, 80–92. [[CrossRef](#)]

16. Alnadari, F.; Al-Dalali, S.; Pan, F.; Abdin, M.; Frimpong, E.B.; Dai, Z.; Al-Dherasi, A.; Zeng, X. Physicochemical Characterization, Molecular Modeling, and Applications of Carboxymethyl Chitosan-Based Multifunctional Films Combined with Gum Arabic and Anthocyanins. *Food Bioprocess Technol.* **2023**, 1–19. [\[CrossRef\]](#)
17. Fang, Z.; Zhao, Y.; Warner, R.D.; Johnson, S.K. Active and intelligent packaging in meat industry. *Trends Food Sci. Technol.* **2017**, *61*, 60–71. [\[CrossRef\]](#)
18. Zhang, X.; Lu, S.; Chen, X. A visual pH sensing film using natural dyes from *Bauhinia blakeana* Dunn. *Sens. Actuators B Chem.* **2014**, *198*, 268–273. [\[CrossRef\]](#)
19. Gasti, T.; Dixit, S.; D'Souza, O.J.; Hiremani, V.D.; Vootla, S.K.; Masti, S.P.; Chougale, R.B.; Malabadi, R.B. Smart biodegradable films based on chitosan/methylcellulose containing *Phyllanthus reticulatus* anthocyanin for monitoring the freshness of fish fillet. *Int. J. Biol. Macromol.* **2021**, *187*, 451–461. [\[CrossRef\]](#)
20. Chen, M.; Yan, T.; Huang, J.; Zhou, Y.; Hu, Y. Fabrication of halochromic smart films by immobilizing red cabbage anthocyanins into chitosan/oxidized-chitin nanocrystals composites for real-time hairtail and shrimp freshness monitoring. *Int. J. Biol. Macromol.* **2021**, *179*, 90–100. [\[CrossRef\]](#)
21. Tavassoli, M.; Khezerlou, A.; Firoozy, S.; Ehsani, A.; Punia Bangar, S. Chitosan-based film incorporated with anthocyanins of red poppy (*Papaver rhoeas* L.) as a colorimetric sensor for the detection of shrimp freshness. *Int. J. Food Sci. Technol.* **2023**, *58*, 3050–3057. [\[CrossRef\]](#)
22. Riaz, G.; Chopra, R. A review on phytochemistry and therapeutic uses of *Hibiscus sabdariffa* L. *Biomed. Pharmacother.* **2018**, *102*, 575–586. [\[CrossRef\]](#)
23. Nguyen, Q.-D.; Dang, T.-T.; Nguyen, T.-V.-L.; Nguyen, T.-T.-D.; Nguyen, N.-N. Microencapsulation of roselle (*Hibiscus sabdariffa* L.) anthocyanins: Effects of different carriers on selected physicochemical properties and antioxidant activities of spray-dried and freeze-dried powder. *Int. J. Food Prop.* **2022**, *25*, 359–374. [\[CrossRef\]](#)
24. Jabeur, I.; Pereira, E.; Barros, L.; Calhelha, R.C.; Soković, M.; Oliveira, M.B.P.P.; Ferreira, I.C.F.R. *Hibiscus sabdariffa* L. as a source of nutrients, bioactive compounds and colouring agents. *Food Res. Int.* **2017**, *100*, 717–723. [\[CrossRef\]](#) [\[PubMed\]](#)
25. Toro-Márquez, L.A.; Merino, D.; Gutiérrez, T.J. Bionanocomposite Films Prepared from Corn Starch with and Without Nanopackaged Jamaica (*Hibiscus sabdariffa*) Flower Extract. *Food Bioprocess Technol.* **2018**, *11*, 1955–1973. [\[CrossRef\]](#)
26. Huang, H.-L.; Tsai, I.L.; Lin, C.; Hang, Y.-H.; Ho, Y.-C.; Tsai, M.-L.; Mi, F.-L. Intelligent films of marine polysaccharides and purple cauliflower extract for food packaging and spoilage monitoring. *Carbohydr. Polym.* **2023**, *299*, 120133. [\[CrossRef\]](#)
27. Gulati, M.; Keshav Murthy, P.S.; Reddy, J.P. Effect of Onion Peel Extract on Structural, Mechanical, Thermal, and Antioxidant Properties of Methylcellulose Films. *Food Bioprocess Technol.* **2023**, *16*, 1–15. [\[CrossRef\]](#)
28. Wu, C.; Sun, J.; Zheng, P.; Kang, X.; Chen, M.; Li, Y.; Ge, Y.; Hu, Y.; Pang, J. Preparation of an intelligent film based on chitosan/oxidized chitin nanocrystals incorporating black rice bran anthocyanins for seafood spoilage monitoring. *Carbohydr. Polym.* **2019**, *222*, 115006. [\[CrossRef\]](#)
29. Luchese, C.L.; Sperotto, N.; Spada, J.C.; Tessaro, I.C. Effect of blueberry agro-industrial waste addition to corn starch-based films for the production of a pH-indicator film. *Int. J. Biol. Macromol.* **2017**, *104*, 11–18. [\[CrossRef\]](#)
30. Luchese, C.L.; Abdalla, V.F.; Spada, J.C.; Tessaro, I.C. Evaluation of blueberry residue incorporated cassava starch film as pH indicator in different simulants and foodstuffs. *Food Hydrocoll.* **2018**, *82*, 209–218. [\[CrossRef\]](#)
31. Amaregouda, Y.; Kamanna, K.; Gasti, T. Fabrication of intelligent/active films based on chitosan/polyvinyl alcohol matrices containing *Jacaranda cuspidifolia* anthocyanin for real-time monitoring of fish freshness. *Int. J. Biol. Macromol.* **2022**, *218*, 799–815. [\[CrossRef\]](#)
32. Lu, M.; Zhou, Q.; Yu, H.; Chen, X.; Yuan, G. Colorimetric indicator based on chitosan/gelatin with nano-ZnO and black peanut seed coat anthocyanins for application in intelligent packaging. *Food Res. Int.* **2022**, *160*, 111664. [\[CrossRef\]](#)
33. Jiang, G.; Hou, X.; Zeng, X.; Zhang, C.; Wu, H.; Shen, G.; Li, S.; Luo, Q.; Li, M.; Liu, X.; et al. Preparation and characterization of indicator films from carboxymethyl-cellulose/starch and purple sweet potato (*Ipomoea batatas* (L.) lam) anthocyanins for monitoring fish freshness. *Int. J. Biol. Macromol.* **2020**, *143*, 359–372. [\[CrossRef\]](#)
34. Halász, K.; Csóka, L. Black chokeberry (*Aronia melanocarpa*) pomace extract immobilized in chitosan for colorimetric pH indicator film application. *Food Packag. Shelf Life* **2018**, *16*, 185–193. [\[CrossRef\]](#)
35. Lan, W.; Wang, S.; Zhang, Z.; Liang, X.; Liu, X.; Zhang, J. Development of red apple pomace extract/chitosan-based films reinforced by TiO₂ nanoparticles as a multifunctional packaging material. *Int. J. Biol. Macromol.* **2021**, *168*, 105–115. [\[CrossRef\]](#) [\[PubMed\]](#)
36. Qin, Y.; Liu, Y.; Yong, H.; Liu, J.; Zhang, X.; Liu, J. Preparation and characterization of active and intelligent packaging films based on cassava starch and anthocyanins from *Lycium ruthenicum* Murr. *Int. J. Biol. Macromol.* **2019**, *134*, 80–90. [\[CrossRef\]](#)
37. You, P.; Wang, L.; Zhou, N.; Yang, Y.; Pang, J. A pH-intelligent response fish packaging film: Konjac glucomannan/carboxymethyl cellulose/blackcurrant anthocyanin antibacterial composite film. *Int. J. Biol. Macromol.* **2022**, *204*, 386–396. [\[CrossRef\]](#)
38. Liu, D.; Zhang, C.; Pu, Y.; Chen, S.; Li, H.; Zhong, Y. Novel colorimetric films based on polyvinyl alcohol/sodium carboxymethyl cellulose doped with anthocyanins and betacyanins to monitor pork freshness. *Food Chem.* **2023**, *404*, 134426. [\[CrossRef\]](#)
39. Liu, L.; Zhang, J.; Zou, X.; Arslan, M.; Shi, J.; Zhai, X.; Xiao, J.; Wang, X.; Huang, X.; Li, Z.; et al. A high-stable and sensitive colorimetric nanofiber sensor based on PCL incorporating anthocyanins for shrimp freshness. *Food Chem.* **2022**, *377*, 131909. [\[CrossRef\]](#)

40. Lavrič, G.; Oberlintner, A.; Filipova, I.; Novak, U.; Likozar, B.; Vrabič-Brodnjak, U. Functional Nanocellulose, Alginate and Chitosan Nanocomposites Designed as Active Film Packaging Materials. *Polymers* **2021**, *13*, 2523. [[CrossRef](#)]
41. Fernández-Marín, R.; Fernandes, S.C.M.; Sánchez, M.Á.A.; Labidi, J. Halochromic and antioxidant capacity of smart films of chitosan/chitin nanocrystals with curcuma oil and anthocyanins. *Food Hydrocoll.* **2022**, *123*, 107119. [[CrossRef](#)]
42. Sani, M.A.; Dabbagh-Moghaddam, A.; Jahed-Khaniki, G.; Ehsani, A.; Sharifan, A.; Khezerlou, A.; Tavassoli, M.; Maleki, M. Biopolymers-based multifunctional nanocomposite active packaging material loaded with zinc oxide nanoparticles, quercetin and natamycin; development and characterization. *J. Food Meas. Charact.* **2023**, *17*, 2488–2504. [[CrossRef](#)]
43. Yong, H.; Wang, X.; Bai, R.; Miao, Z.; Zhang, X.; Liu, J. Development of antioxidant and intelligent pH-sensing packaging films by incorporating purple-fleshed sweet potato extract into chitosan matrix. *Food Hydrocoll.* **2019**, *90*, 216–224. [[CrossRef](#)]
44. Yong, H.; Wang, X.; Zhang, X.; Liu, Y.; Qin, Y.; Liu, J. Effects of anthocyanin-rich purple and black eggplant extracts on the physical, antioxidant and pH-sensitive properties of chitosan film. *Food Hydrocoll.* **2019**, *94*, 93–104. [[CrossRef](#)]
45. Roy, S.; Rhim, J.-W. Preparation of gelatin/carrageenan-based color-indicator film integrated with shikonin and propolis for smart food packaging applications. *ACS Appl. Bio Mater.* **2020**, *4*, 770–779. [[CrossRef](#)]
46. Zhang, K.; Huang, T.-S.; Yan, H.; Hu, X.; Ren, T. Novel pH-sensitive films based on starch/polyvinyl alcohol and food anthocyanins as a visual indicator of shrimp deterioration. *Int. J. Biol. Macromol.* **2020**, *145*, 768–776. [[CrossRef](#)]
47. Wang, F.; Zhan, J.; Ma, R.; Tian, Y. Simultaneous improvement of the physical and biological properties of starch films by incorporating steviol glycoside-based solid dispersion. *Carbohydr. Polym.* **2023**, *311*, 120766. [[CrossRef](#)]

Disclaimer/Publisher’s Note: The statements, opinions and data contained in all publications are solely those of the individual author(s) and contributor(s) and not of MDPI and/or the editor(s). MDPI and/or the editor(s) disclaim responsibility for any injury to people or property resulting from any ideas, methods, instructions or products referred to in the content.

ARTICLES FOR FACULTY MEMBERS

ROSELLE (HIBISCUS SABDARIFFA) ANTHOCYANIN USE IN MONITORING MEAT FRESHNESS

Title/Author	<p>The highly stable indicator film incorporating roselle anthocyanin co-pigmented with oxalic acid: Preparation, characterization and freshness monitoring application /Huang, J., Hu, Z., Li, G., Chin, Y., Pei, Z., Yao, Q., Li, D., & Hu, Y.</p>
Source	<p><i>Food Research International</i> Volume 173 Part 2 (2023) 113416 Pages 1-10 https://doi.org/10.1016/j.foodres.2023.113416 (Database: ScienceDirect)</p>



The highly stable indicator film incorporating roselle anthocyanin co-pigmented with oxalic acid: Preparation, characterization and freshness monitoring application

Jiayin Huang^{a,b}, Zhiheng Hu^{b,c}, Gaoshang Li^{a,b}, Yaoxian Chin^a, Zhisheng Pei^a, Qian Yao^d, Dan Li^e, Yaqin Hu^{a,*}

^a College of Food Science and Engineering, Yazhou Bay Innovation Institute, Hainan Tropical Ocean University, Marine Food Engineering Technology Research Center of Hainan Province, Collaborative Innovation Center of Marine Food Deep Processing, Sanya, Hainan 572022, China

^b Institute of Food Engineering, College of Biosystems Engineering and Food Science, Zhejiang University, Hangzhou, Zhejiang 310058, China

^c Hainan Key Laboratory of Herpetological Research, College of Fisheries and Life Science, Hainan Tropical Ocean University, Sanya, Hainan 572022, China

^d Key Laboratory of Medicinal and Edible Plants Resources Development of Sichuan Education Department, Sichuan Industrial Institute of Antibiotics, School of Pharmacy, Chengdu University, Chengdu, Sichuan 610106, China

^e Department of Food Science & Technology, Faculty of Science, National University of Singapore, Singapore 117542, Singapore

ARTICLE INFO

Keywords:

Indicator film
Co-pigmentation
High stability
Roselle anthocyanin
Real-time monitoring

ABSTRACT

A novel stable PVA/HPMC/roselle anthocyanin (RAE) indicator film co-pigmented with oxalic acid (OA) was prepared, its properties, application effects and stability enhancement mechanism were investigated correspondingly. The structural characterization revealed that more stable network was formed due to the co-pigmentation facilitated generation of molecular interactions. Meanwhile, the co-pigmentation improved film mechanical and hydrophobic properties compared to both PVA/HPMC/RAE newly prepared (PHRN) or stored (PHRS) film, expressing as higher tensile strength values (12.25% and 14.44% higher than PHRN and PHRS), lower water solubility (7.22% and 10.09% lower than PHRN and PHRS) and water vapor permeability values (33.20% and 21.05% lower than PHRN and PHRS) of PVA/HPMC/RAE/OA newly prepared (PHON) or stored (PHOS) film. Compared with the PHRS film, the PHOS film still presented more distinguishable color variations when being applied to monitor shrimp freshness, owing to the stabilization behaviors of co-pigmentation in anthocyanin conformation. Hence, the co-pigmentation was an effective strategy to enhance film stability, physical and pH-responsive properties after long term storage, leading to better film monitoring effects when applied in real-time freshness monitoring.

1. Introduction

The constant demands for food safety and growing environmental awareness have driven the development of eco-friendly intelligent packaging. The pH-indicator packaging which can not only provide an effective boundary for food protection but also possess high capacities for real-time freshness monitoring has gotten a lot of attention as a form of intelligent packaging.

Among several types of pH-sensitive pigments, anthocyanins have been the most widely applied in pH-indicator packaging due to their diverse sources, non-toxic properties and multiple functions. Up to now, a considerable number of studies have validated the feasibility of anthocyanin-based packaging on food freshness monitoring. For

example, the *Oxalis triangularis* ssp. *papilionacea* anthocyanin-based film and raspberry anthocyanin-based film both exhibited their great potentials in freshness evaluation (Li et al., 2023; Duan et al., 2022). The pH-responsive abilities of anthocyanins which can exhibit obvious color changes under different pH values by owing to molecular conformation differences, are strongly connected with the freshness monitoring behaviors of pH-indicator packaging. According to its mechanism, the pH-responsive performance of anthocyanins is the key point for the monitoring effects. However, low stability of anthocyanins has hindered its further application in food packaging. Anthocyanins are thought to be sensitive to environment factors such as light, temperature, wet, etc., as well as are susceptible to degradation. As a result, their color will fade, causing insignificant color changes and interfering with the assessment

* Corresponding author.

E-mail address: 1004346262@qq.com (Y. Hu).

<https://doi.org/10.1016/j.foodres.2023.113416>

Received 17 May 2023; Received in revised form 15 August 2023; Accepted 28 August 2023

Available online 29 August 2023

0963-9969/© 2023 Elsevier Ltd. All rights reserved.

of food freshness degree (Fei et al., 2021). As reported by Qin et al., (2021), after 5 months of storage at 35 °C, the *Lycium ruthenicum* anthocyanin-based packaging film degraded quickly, and film functional properties were damaged to variable degrees. Hence, it is of vital importance to modify the stability of anthocyanin to develop the anthocyanin-based packaging that is resistant to harsh environmental factors.

Till now, several novel strategies have been introduced to enhance the stability of anthocyanin-based packaging, and most of them focus on physical modification. Specifically, two approaches, the layer-by-layer and encapsulation are studied widely. For example, Zhai et al., (2020) prepared a rose anthocyanin indicator film with a light barrier layer of gellan gum and TiO₂ nanoparticles, the double layer packaging exhibited good resistance towards illumination simulation and presented color changes in freshness monitoring of pork and silver carp. Meanwhile, a *Lycium ruthenicum* anthocyanin-loaded nanocomplexes intelligent packaging incorporating starch and PVA presented higher stability than indicator film incorporated with free anthocyanin, and remarkable color variations were observed when being applied in bass fillets freshness monitoring (Qin et al., 2021). Similar results were obtained in the indicator film containing blueberry anthocyanin nanocomplexes loaded with ovalbumin carboxymethyl cellulose (Liu et al., 2022), which demonstrated that the encapsulation could exert positive influences on film stability. Notably, the preceding researches mostly focus on film characteristics after modification rather than film properties after long-term storage, which is more crucial for evaluating the influences of approaches on film stability. In addition, while the approaches described above can prevent anthocyanin-based packaging from harsh environmental conditions, there are several concerns about their effects on film responsive efficiency. They can capture and protect natural anthocyanin well, nevertheless, this may make it hard for anthocyanin to detect pH changes, resulting in poorer sensitivity and responsiveness towards pH alterations of packaging film (Qin et al., 2021). As a result, the monitoring effects may be inaccurate when they are used in freshness monitoring.

Hence, co-pigmentation which can not only improve stability of anthocyanin, but also intensify colors of anthocyanin may be helpful for the development of anthocyanin-based film with high stability, optimal response rate and acute monitoring effects. Previous studies have demonstrated that the co-pigmentation can stabilize natural anthocyanin by forming stable supermolecular complex via molecular interaction, leading to the prevention of flavonoid cations from the nucleophilic attacks of water molecules (Nie et al., 2022; Molaeafard, Jamei, & Marjani, 2021). Cao et al., (2023) found that different kinds of flavanols improved stability of cyanidin-3-O-glucoside, and the main driving force for the complex generation was hydrogen bonds and van der Waals forces. Similarly, the higher total anthocyanin contents, larger A_{\max} and color density under 105 °C heating treatment were observed in anthocyanin co-pigmented with amino acids, indicating their higher stability and greater color intense (Bingöl et al., 2022). Despite the intriguing potentials of co-pigmentation in anthocyanin stability, only one relevant report has been published, focusing on blueberry anthocyanin (BA) indicator film co-pigmented by chondroitin sulfate (CS) (Bao et al., 2022). The results suggested that the BA indicator film co-pigmented by CS exhibited higher color stability, better mechanical properties and more effective pH responsiveness, and could be applied in freshness monitoring of shrimp successfully. However, it is far from enough to completely study the influences of co-pigmentation on anthocyanin intelligent packaging. It is unknown whether the film properties would be improved after co-pigmentation throughout long-term storage. Meanwhile, it is generally believed that the organic acid performs better stabilization effects on anthocyanin, because the acyl groups introduced can alter the spatial conformation of anthocyanin to a more stable state. However, due to limited reports, it is unclear whether the anthocyanin intelligent packaging co-pigmenting organic acid can still present excellent characteristics and promising application prospects.

The roselle anthocyanin has been applied as a natural pigment in food industry due to its wide sources, abundant contents in calyx as well as multiple functions. Hence, in this study, a highly stable indicator film based on roselle anthocyanin extracts (RAE) co-pigmented with oxalic acid (OA) was prepared. In our previous study, the RAE co-pigmented by OA was proved to exhibit better thermal stability and stronger color intensity than RAE co-pigmented by other co-pigments such as maleic acid, malic acid and ferulic acid (Huang et al., 2023). In order to identify the effects of co-pigmentation on RAE indicator film during a long storage period, several properties including structural, physical and indication characteristics of OA-RAE film (stored for 0 day (d) and 6 months, respectively) were evaluated, respectively. Furthermore, the OA-RAE films were applied in the freshness monitoring of *Penaeus vannamei* for investigating their monitoring effects.

2. Materials and methods

2.1. Materials

The roselle anthocyanin extracts (RAE) were obtained from the roselle purchased from a local market in Hangzhou, China, and extracted according to our previous study (Huang, Liu, Chen, Yao, & Hu, 2021). Also, fresh shrimp (*Penaeus vannamei*, 12 ± 1 g) were purchased from the same market. The co-pigmentation compound oxalic acid (OA) (with 98.5% purity) was purchased from Yuanye Bio-technology Co., Ltd (Shanghai, China). The film forming substrate polyvinyl alcohol (PVA) and hydroxypropyl methylcellulose (HPMC) as well as other reagents were bought from Sinopharm Chemical Reagent Co., Ltd. (Shanghai, China). All chemicals were analytical grade.

2.2. UV-vis spectra of RAE-OA solutions

The RAE co-pigmented by OA (RAE-OA, RO) was prepared by our previous study (Huang et al., 2023). The UV-vis spectra were determined to investigate the pH-response ability of RAE and RO solutions. The UV-vis spectrophotometer (UV-2600, Shimadzu Co., Ltd, Japan) was used to measure the UV-vis spectra of solutions at different pH values (from 2.0 to 12.0) in the range of 450–700 nm.

2.3. Preparation of PVA/HPMC/RAE/OA indicator film

The film fabrication procedure was conducted according to previous researches in our group (Chen, Yan, Huang, Zhou, & Hu, 2021; Huang et al., 2020). Initially, 1.0 g PVA was dissolved in distilled water (100 mL) with a continuous stirring at 75 °C for 30 min. Then, 3.0 g HPMC was added into the PVA solution for stirring at 30 °C (2 h). After that, the RAE-OA (0.24%, w/v, $m_{\text{RAE}}:m_{\text{OA}} = 2:1$) was introduced to the film forming solution, which continuously stirred for 2 h in order to mix thoroughly. Subsequently, the obtainable solution was degassed by ultrasonic treatment. The indicator films were developed by solvent casting in a culture dish (9 cm × 9 cm) and dried in an oven for 24 h (30 °C). Finally, the newly obtained PVA/HPMC/OA-RAE indicator film was termed as PHON, and the newly PVA/HPMC/RAE indicator film was labeled as PHRN. Meanwhile, in order to investigate the film properties after long storage, above PHON and PHRN films were stored in a desiccator (RH = 50% (kept by the Mg(NO₃)₂ solution), room temperature, natural light) for 6 months, and the corresponding indicator films were termed as PVA/HPMC/OA-RAE film after storage (PHOS) and PVA/HPMC/RAE film after storage (PHRS), respectively.

2.4. Structural characterization of indicator film

The surface morphology of indicator film was observed by a scanning electron microscope (SEM, SU-8010, HITACHI Co., Ltd., Japan) with an accelerating voltage of 3.0 kV. The intermolecular binding and functional groups contained in the composite film were identified via a

Fourier-transform infrared (FT-IR) spectrometer (AVA TAR370, NICOLET Co., Ltd., America) in the spectral range between 4000 and 500 cm^{-1} with a resolution of 2 cm^{-1} . In addition, the film crystallinity was analyzed with an X-ray diffractometer (XRD, D8 Advance, Bruker AXS Co., Ltd., Germany) in the range of 15 to 80° (2 θ) with steps of 5° (2 θ)/min.

2.5. Physical properties determination of indicator film

2.5.1. Mechanical properties

The mechanical properties can be characterized into tensile strength (TS) and elongation at break (EB). The determination of mechanical properties was performed by a tensile analyzer (XLW-M, Labthink Technology Co., Ltd., China). Briefly, the indicator film was cut into a strip (8 cm \times 1 cm) and fixed between two grips with an initial distance of 40 mm. The tensile speed was assigned as 25 mm/min, and five replications were taken. The TS and EB were calculated according to following equation (1) and (2).

$$\text{TS (MPa)} = F/S \quad (1)$$

$$\text{EB (\%)} = [(L_1 - L_0)/L_0] \times 100\% \quad (2)$$

In which, the F was the maximum force during stretching (N), S was the effective force area of film (m^2), L_1 was the film length at break (mm), L_0 was the initial film length (mm).

2.5.2. Hydrophobic properties

The moisture content (MC) and water solubility (WS) of indicator film was measured according to our previous study (Huang, Liu, Chen, Yao, & Hu, 2021).

In short, the film was subjected to the high-temperature drying (105 °C) and finally to a stable weight. The MC was calculated according to following equation (3).

$$\text{MC (\%)} = (M_1 - M_2)/M_1 \times 100 \quad (3)$$

In which, the M_1 was the initial film weight (g), and the M_2 was the final film weight (g).

To evaluate the WS values, the film was immersed into the distilled water (50 mL) for 24 h with the continuous shaking under room temperature. Subsequently, the film was dried at 105 °C until reached the stable weight. The WS was calculated according to following equation (4).

$$\text{WS (\%)} = (W_i - W_f)/W_i \times 100 \quad (4)$$

In which, the W_i was the initial film weight (g), and the W_f was the final film weight (g).

Meanwhile, the gravimetric method was applied to determine the water vapor permeability (WVP), which was in accordance with Huang, Chen, Zhou, Li, & Hu (2020).

2.5.3. Thermal stability

The film thermal degradation behavior was investigated with a thermogravimetric analyzer (TGA, TA-Q500, TA Instruments Co., Ltd., USA) in the range of heating temperature from 50 to 750 °C with the heating rate of 20 °C/min under N_2 .

2.5.4. Color stability

The color differences of PVA/HPMC/RAE/OA (PHO) and PVA/HPMC/RAE (PHR) indicator films at different days were calculated to identify their storage stability. The storage conditions were similar to which stated in the Method section. Film color parameters (L^* , a^* , b^*) were determined at 0 d, 5 d, 15 d, 30 d, 60 d, 90 d...180 d, and the determination was performed six times for each group. The color difference ΔE was calculated according to Eq (5).

$$\Delta E = \sqrt{(L_t^* - L_0^*) + (a_t^* - a_0^*) + (b_t^* - b_0^*)} \quad (5)$$

In which, the L_t^* , a_t^* and b_t^* were film color parameters at t d, while the L_0^* , a_0^* and b_0^* were film color parameters at 0 d.

2.6. pH response ability of indicator film

The indicator films were cut into small pieces (2 cm \times 2 cm) and immersed into different pH buffer solutions, respectively (pH 3, 5, 7, 9, 11, 13) for 3 min. Film color parameters were recorded by a portable colorimeter (CM-3500d, Konica Minolta Co., Ltd, Japan), and photos about film color changes were taken correspondingly. The color difference (ΔE) was calculated by Eq (3), in which the L_t^* , a_t^* and b_t^* were film color parameters at different pH solutions, while the L_0^* , a_0^* and b_0^* were original film color parameters.

2.7. Application of indicator film on shrimp freshness monitoring

The application test was performed by our previous studies (Huang, Liu, Chen, Yao, & Hu, 2021; Ge et al., 2020). Specifically, one shrimp sample was put into a sterilized cultural dish attached a small piece of indicator film (1 cm \times 1 cm) and stored at 4 °C for 10 d. The film color parameters were determined by a portable colorimeter (CM-3500d, Konica Minolta Co., Ltd, Japan). Meanwhile, the total volatile nitrogen compounds (TVB-N) and total viable counts (TVC) were measured according to Dong et al., (2023). Briefly, taking 10 g shrimp sample and mixed with 100 mL distilled water, and then the mixture was centrifuged at 3000 r/min for 10 min (4 °C). Adding 5 mL MgO (1%) into the obtainable supernatant (10 mL), and the steam distillation was performed for 5 min. Finally, the H_3BO_3 was applied to absorb the distillate, and the resulting solution was titrated with 0.01 M HCl. The TVB-N content was calculated and expressed as mg/100 g. Meanwhile, the TVC values were determined under sterile environment. Adding 90 mL physiological saline into 10 g shrimp sample, and after being mixed and homogenized, 100 μL dilution of the sample solution was introduced to petri dishes. Subsequently, the samples were incubated for 2 d (37 °C), and the results were expressed as lg CFU/g. Aforementioned indicators were determined every two days.

2.8. Statistical analysis

All measurements were carried out in triplicate at least except for structural characterization, and the results were expressed as mean \pm standard deviation. Data analysis including one-way analysis of variance (ANOVA) and Duncan test ($p < 0.05$) was performed by SPSS 20.0 (Statistics 20, SPSS Inc., Chicago, IL, US). The regression fitting mathematical model was established to investigate the relationship between film color and shrimp freshness.

3. Results and discussions

3.1. UV-vis spectra of RAE-OA and RAE solutions under different pH

The color changes and related absorption spectra of RAE and RAE-OA solutions under different pH solutions (2 ~ 12) were shown in the Fig. 1. The pH-dependent variations were highly associated with anthocyanin conformation as a result of protonation and deprotonation (Zia et al., 2021; Liang, Sun, Cao, Li, & Wang, 2019).

As shown in the Fig. 1(a), the RAE solution displayed red color at pH 2.0–3.0, corresponding to the flavylium cation, which was consistent with the absorption peak at 520 nm. Then, the solution color changed to pink and gradually to colorless at pH 4.0–5.0, due to the presence of carbinol pseudo base (Tang et al., 2019). Afterwards, when the pH was at the range of 6.0–7.0, the solution color changed to purple and green–blue color, which was attributed to formation of quinoidal base.

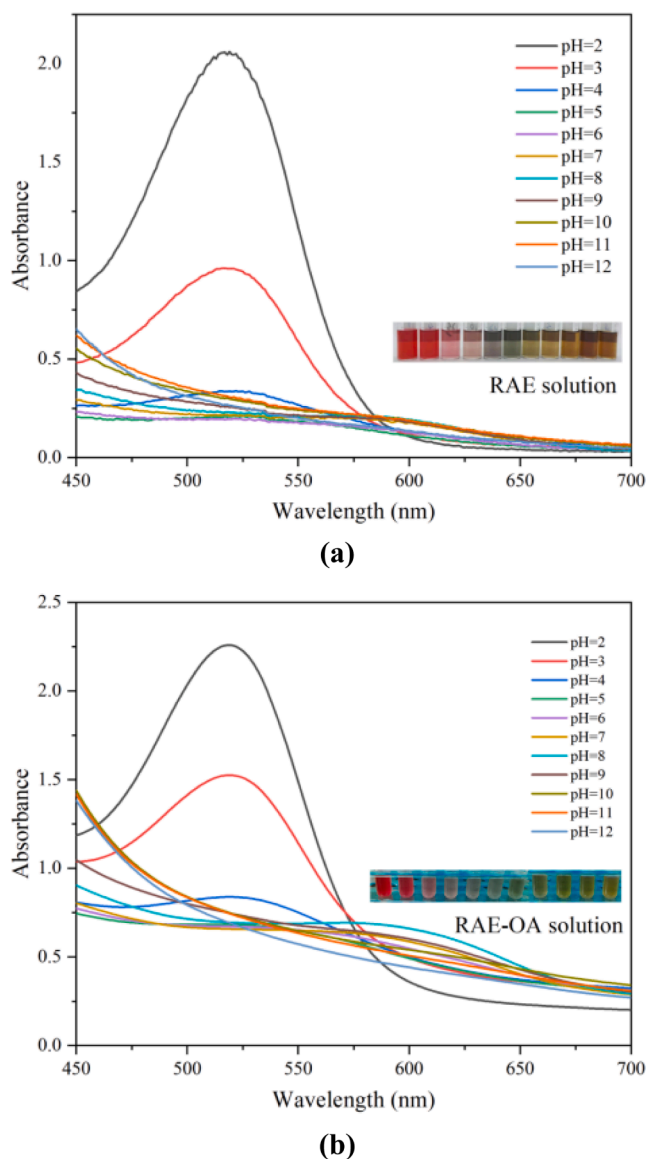


Fig 1. The UV-vis spectra of roselle anthocyanin (RAE) (a) and RAE-oxalic acid (OA) (b) solutions under different pH values (2 ~ 12).

Finally, the solution exhibited yellow color under the strong alkali environment ($\text{pH} > 8$), owing to the degradation of anthocyanin, resulting in the generation of chalcone (Li et al., 2023; Zhang et al., 2021; Franco, Cunha, & Bianchi, 2021).

The color change tendency of RAE co-pigmented with OA solution was comparable to that of RAE solution, however slight differences were observed (Fig. 1(b)). The maximum absorption peak in RAE-OA shifted to larger wavelengths (from 520 to 540 nm), and absorbance values under different pH increased significantly. The larger wavelength for maximum absorption peak and the enhanced color intensity was also reported in the blueberry anthocyanin solution co-pigmented with CS, which might be resulted from the new interaction formed between the anthocyanin and co-pigments (Bao et al., 2022). Surprisingly, the co-pigmentation might delay the color variations toward pH changes. For example, the RAE-OA solution retained a slight pink color at $\text{pH} = 6$, whereas the RAE solution had turned into colorless. Meanwhile, the yellow color in RAE-OA solution under extremely strong alkali environment was lighter than RAE solution. The above phenomenon could be due to the protection effects of co-pigmentation on conformation maintenance of anthocyanin, making it less sensitive to pH fluctuations.

However, the photographs of RAE-OA solution showed pH-dependent color changes, demonstrating its potentials in application of freshness monitoring.

3.2. The micro-structure properties of the indicator film

The SEM was applied to investigate the morphological properties of the indicator film, and the results were shown in Fig. 2(a). After preparation, both PHON and PHRN presented relatively compact surfaces, suggesting the well compatibility among PVA, HPMC, RAE and OA, which was associated with the plasticizing effect of anthocyanin, leading to the formation of intermolecular hydrogen bonds (Ge et al., 2020). However, owing to formation of RAE agglomerates at high concentrations, there were some minor uneven areas in the PHRN. Similar agglomerates were also reported in other studies (Chen, Yan, Huang, Zhou, & Hu, 2021; Zhang et al., 2019). By contrast, a smoother surface without significant cracks was obtained in the PHON, indicating that the co-pigmentation of RAE with OA might exert a positive influence on film uniformity. The phenomenon could be attributed to the interaction among OA and PVA/HPMC film matrix, facilitating the evenly distribution of RAE. Notably, after 6 months storage, considerable changes in morphology were identified, particularly for PHRS, with the surface becoming rough and porous with numerous pores. The breakdown of its molecular skeleton might be accounted for the disordered film structure. Meanwhile, the interaction binding between film matrix might weaken, allowing film components to migrate (Garalde, Thipmancee, Jarjyasakoolroj, & Sane, 2019). Surprisingly, the co-pigmentation of OA was able to stabilize the micro-structural network, inhibiting the degradation of anthocyanin as well as the precipitation and migration of compounds, as manifested by fewer pores and a more homogeneous surface in PHOS.

3.3. The molecular interactions of the indicator film

In order to investigate the functional groups and molecular interaction among film compounds, the FT-IR was applied, and the related spectra were shown in the Fig. 2(b). The broad peak around 3490 cm^{-1} could be attributed to O-H stretching vibration, while the characteristic peaks around 2900 cm^{-1} and 1435 cm^{-1} were corresponded to C-H and CH-CH₂ stretching vibration (Huang, Liu, Chen, Yao, & Hu, 2021). Meanwhile, the peaks around 1791 , 1633 , 1500 and 1070 cm^{-1} , which were assigned to pyran ring, aromatic ring, C = C and C-O-C stretching vibration of aromatic hydrocarbon skeleton, respectively, were the typical peaks of RAE (Zong et al., 2023). Those functional groups were identified in all experimental groups, indicating that the RAE was immobilized well into the film matrix, which agreed with the SEM results. Compared with PHRN film, the O-H stretching vibration in PHON film significantly shifted to high wavenumber (from 3479 to 3498 cm^{-1}), which was due to the formation of hydrogen bonds after the introduction of OA. In addition, the introduction of hydroxyl groups intensified the C = O stretching vibration (around 1750 cm^{-1}) and led to the re-organization of molecular binding. And the re-organization of interaction could be also accounted for the weakening and shift of typical peak around 1000 cm^{-1} (from 1070 to 1052 cm^{-1}).

After 6 months storage, several changes were observed in the FT-IR spectra, while the reason might be associated with the degradation of anthocyanin and the decomposition of film matrix, contributing to the breakdown of carbon skeleton and the generation of new small molecules. As a result, the molecular interactions undoubtedly changed (Fonseca-Garcia, Caicedo, Jiménez-Regalado, Morales, & Aguirre-Loredo, 2021). For example, the O-H stretching vibration attenuated and shifted to 3502 and 3511 cm^{-1} in PHRS and PHOS, respectively. Significant weakening in the intensity of typical peak for C-O-C stretching vibration (around 1015 cm^{-1}) was identified. Similarly, the C-H stretching vibration at 2900 cm^{-1} shifted toward higher wavenumber, and the strength decreased correspondingly with the extension

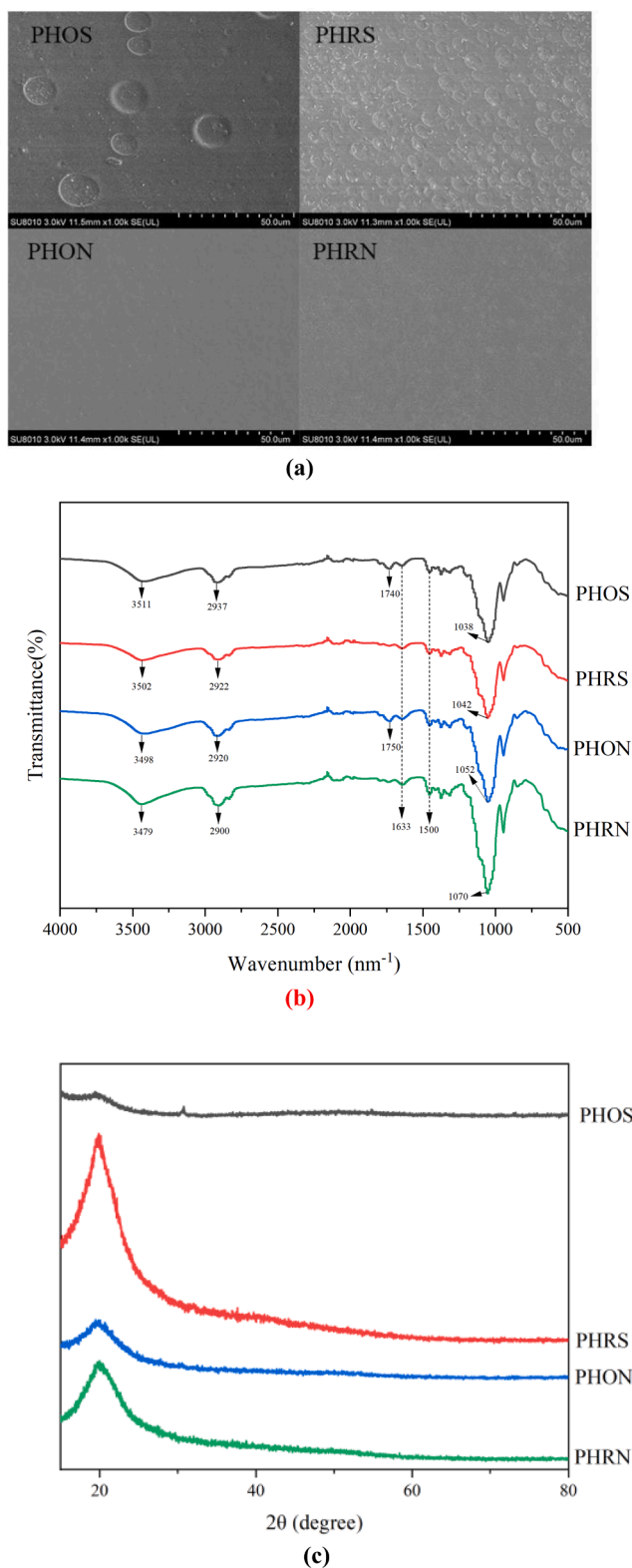


Fig 2. The structural characterization of the PVA/HPMC/OA-RAE (PHO) and PVA/HPMC/RAE (PHR) film. In which, the scanning electron microscope (SEM) photographs (a), Fourier-transform infrared (FT-IR) spectra (b) and X-ray diffractometer (XRD) spectra (c).

of storage time. Notably, the weakening and shift of characteristic peaks were slighter in PHOS film than PHRS, demonstrating that the co-pigmentation could prevent RAE from degradation effectively, resulting in a more stable molecular binding.

3.4. The crystalline structure of the indicator film

In order to identify the molecular interaction among film components further, the XRD was applied for investigation of crystalline structure, and the patterns were shown in the Fig. 2(c). An obvious diffraction peak at 19.33° was observed in all XRD patterns, which corresponded to the semi-crystalline property of PVA as reported by other studies (Qin et al., 2021; Boonsuk et al., 2020). Compared with XRD pattern of pure PVA obtained in our previous study (Huang, Liu, Chen, Yao, & Hu, 2021), the introduction of RAE significantly reduced intensity of crystalline peak, which was due to the amorphous structure of anthocyanin. Meanwhile, it was noticeable that this characteristic diffraction peak was dramatically weakened after the co-pigmentation of RAE with OA. The lower crystalline degree in the PHON film demonstrated that the co-pigmentation behavior could facilitate the film development with more regular molecular structure by generating stronger interactions. In addition, the typical diffraction peaks of the typeII amorphous peak in HPMC were not identified in either PHR or PHO film, which was resulted from the generation of electrostatic interactions among film matrix, resulting in improved film compatibility.

With the increase of storage time, the PHR and PHO film presented totally different XRD patterns. The anthocyanin degraded into several new compounds during storage, leading to the alignment of crystalline state. Besides that, the decomposition of film matrix (PVA and HPMC) could also affect the crystalline rearrangement. As a result, a sharper diffraction peak was observed in the PHRS film, suggesting the disruption of original polymer ordering. Similar results were obtained in Qin et al., (2021) and Hernandez (2021), in which both the *Lycium ruthenicum* anthocyanin-based film and the starch/polycaprolactone film exhibited a significant increase in the intensity of the typical diffraction peak during storage period. However, the diffraction peak in the PHOS film was less intense and broader in width, indicating that the co-pigmentation of RAE effectively prevented film retrogradation by forming tighter molecular interactions (Fonseca-Garcia, Caicedo, Jiménez-Regalado, Morales, & Aguirre-Loredo, 2021), which was in line with the SEM and FT-IR results.

3.5. The mechanical properties of the indicator film

Mechanical properties which could be characterized by TS and EB were associated with the structural network and molecular interactions of indicator film. The TS represented film fracture resistance, and its force depended on the density and distribution of molecular binding among the film components (Ezati, & Rhim, 2020). The PHRN film presented the TS value of 56.98 ± 0.24 MPa, which increased by $12.24 \pm 0.01\%$ when the RAE was co-pigmented by OA (Table 1). The generation of new hydrogen bonds was accounted for the increasing TS value, which might prompt the interaction of film components, thus strengthened the film resistance toward force. Similar results were obtained in the mulberry anthocyanin indicator film modified by TiO₂ nanoparticles, in which the TS exhibited the highest value of 30.0 ± 2.90 MPa. The authors investigated that the interfacial bonding was promoted via the addition of TiO₂, due to its large specific surface area (Li et al., 2022). However, after the incorporation of neem essential oil, the TS value of red radish anthocyanin film decreased significantly, owing to the hydrophobic properties of essential oil (Yang et al., 2022). Hence, the effects of modification materials on the tensile strength of anthocyanin-based film would be varied due to different properties of added component. With the extension of storage time, both PHOS and PHRS film presented declining TS tendencies, but the decrease was not significant. It was believed that the polymerization within the film

Table 1

The mechanical and hydrophobic properties of the PHO and PHR film.

	Tensile strength (MPa)	Elongation at break (%)	Moisture content (%)	Water solubility (%)	Water vapor permeability ($\text{g}\cdot\text{Pa}^{-1}\cdot\text{s}^{-1}\cdot\text{m}^{-1}\cdot 10^{-8}$)
PHOS	62.23 ± 1.47 ^a	16.13 ± 0.53 ^a	21.55 ± 3.47 ^a	27.46 ± 2.74 ^a	2.25 ± 0.25 ^b
PHRS	54.38 ± 1.09 ^b	16.00 ± 0.35 ^a	24.98 ± 3.99 ^a	30.54 ± 1.67 ^a	2.85 ± 0.29 ^a
PHON	63.96 ± 0.84 ^a	15.13 ± 0.18 ^a	11.60 ± 1.19 ^b	24.94 ± 3.27 ^a	1.65 ± 0.22 ^c
PHRN	56.98 ± 0.24 ^b	13.75 ± 1.77 ^a	15.69 ± 1.00 ^b	26.88 ± 3.91 ^a	2.47 ± 0.22 ^{ab}

matrix could be disrupted and rearranged during storage, leading to a disordered network. Meanwhile, the film might absorb water, resulting in the reduction of stiffness. However, the decline in the PHOS film was relatively slighter, demonstrating that the structural network was protected well after the co-pigmentation of RAE.

On the other hand, the EB value as the other indicator for mechanical property evaluation, was able to identify the freedom degree for movement of molecular chain. The EB value increased from 13.75 ± 1.77% to 15.13 ± 0.18% after the co-pigmentation of RAE, indicating the increase in flexibility, which might be attributed to the enhanced film compatibility after the addition of OA (Qin et al., 2021). After 6 months storage, the EB continuously increased to 16.00 ± 0.35% and 16.13 ± 0.53% for PHRS and PHOS, respectively. While the similar increasing trend was reported in the study of Qin et al., (2021), where the EB values of *Lycium ruthenicum* anthocyanin film increased by 23.80%-55.29% under different storage conditions after 5 months. The improved EB values were explained by the degradation of RAE, the rigidity of anthocyanin might weakened after storage. In addition, the decomposition products of anthocyanin exhibited strong plasticization effect, and the mobility of molecular chains was enhanced correspondingly (Liu et al., 2017).

3.6. The hydrophobic properties of the indicator film

Hydrophobic properties which were of vital importance for packaging application, could be evaluated by several indicators. For example, considering film system contained not only film components but also water molecules, the moisture content was applied to assess hydrophobicity. Meanwhile, the water solubility which measured the dissolve degree of film material also could be determined for hydrophobic property evaluation. As the Table 1 shown, the PHRN film exhibited relatively high MC and WS values of 15.69 ± 1.00% and 26.88 ± 3.91%, owing to the abundant hydroxyl groups contained in the RAE molecular chain. The co-pigmentation of RAE significantly decreased the MC value by 26.01 ± 7.38%, while the effect on WS was not significant (only decreased by 2.80 ± 0.02%), suggesting the introduction of OA improved film hydrophobicity to some extent. The enhancement effects could be explained by following reasons. Firstly, the RAE co-pigmented with OA generated stronger interactions with PVA/HPMC film matrix by the establishment of hydrogen bonds, contributing to a reduction in the available amount of hydroxyl groups. Secondly, it was commonly believed that the co-pigmentation behavior effectively protected the cationic chromophore of RAE from nucleophilic attack by water, resulting in greater resistance to water molecules. Additionally, as reported by Alizadeh-Sani, Tavassoli, McClements, & Hamishehkar, (2021), the decrease in MC might be also related to the replacement of water molecules in the film system by the introduction of OA-RAE molecules.

The WVP which represented film water blocking ability was also another usual indicator for evaluation of hydrophobic characteristics. The co-pigmentation of RAE enhanced film water barrier, as expressed by the reduction of WVP value from 2.47 ± 0.22 to 1.65 ± 0.22 $\text{g}\cdot\text{Pa}^{-1}\cdot\text{s}^{-1}\cdot\text{m}^{-1}\cdot 10^{-8}$ ($p < 0.05$). As previously stated, the stronger interaction of OA-RAE than natural RAE with film matrix could account for the reduction of WVP. In addition, the WVP was associated with the film inner structure. The more compact film structure network, the

fewer WVP value, because it was more difficult for water to permeate through the film matrix without apparent interfacial zones (Qin et al., 2021).

After 6 months of storage, the film hydrophobicity decreased, manifesting as higher MC, WS and WVP values. On the one hand, the enhanced hydrophilic properties might be due to the film's water absorption ability, which could absorb the water molecules in the storage environment. On the other hand, as demonstrated in the structural characterization, the inner structure would loosen during storage, thereby facilitating the film affinity toward water. Notably, the PHOS film experienced less hydrophilicity improvement, whose MC, WS and WVP values were 13.10 ± 12.29%, 10.11 ± 7.19% and 20.34 ± 15.13% lower than those of the PHRS film. The results revealed that the co-pigmentation of RAE had the potential to modify film water resistance.

3.7. The stability of the indicator film

As mentioned above, the film stability which could be characterized as color and thermal stability, was an important parameter for film actual application.

In this study, the PHO and PHR films were stored at the room temperature under natural light for 6 months, the color differences were calculated and the photos were taken (Fig. 3(a)). Initially, the PHR film exhibited a relatively dark purple-red color, while the PHO film presented a light rose-red color, which was due to the ability of oxalic acid to intensify color. After storage of 6 months, the film color showed totally different changes. The color of PHR film significantly faded and turned to light yellow/pink color at the sixth month, owing to the anthocyanin degradation. Similar results were reported by Qin et al., (2021) and Chen, Zhang, Bhandari, & Yang (2020), in which the significant color changes were identified in the sweet potato anthocyanin film and purple sweet potato anthocyanin film after the long-term storage. As the Fig. 3(a) shown, the ΔE value of PHR film increased with the extension of time, and a sharp increase was observed at 30 d (up to 22.48 ± 3.83). By contrast, the PHO film exhibited higher color stability with lower ΔE values of 6.52 ± 2.70 at the end of whole storage.

The TGA was applied to assess the thermal stability of the indicator film based on weight loss. The Fig. 3(b) presented 4 thermal degradation stages as follows: 1) 50–105 °C, resulted from evaporation of surface water; 2) 130–280 °C/320 °C (PHR/PHO), attributed to evaporation of intrinsic water; 3) 280/320 °C (PHR/PHO)-380 °C, caused by the decomposition of film components (RAE and film matrix); 4) above 380 °C, because of the decomposition of final residue (Yao, Wang, Zhou, Yang, & Pang, 2023; Sun et al., 2019; Zhang et al., 2019). It was noticeable that the largest weight loss occurred in the third stage, whose weight decreased by 65.67%, 69.17%, 66.81% and 71.95% for the PHOS, PHRS, PHON and PHRN, respectively. Meanwhile, the decomposition temperatures of both PHOS and PHON films were higher than PHR films in this stage, demonstrating that PHO films possessed stronger thermal stability. There were two factors could be accounted for the thermal stability enhancement of PHO films via co-pigmentation with OA. On the one hand, the formation of stronger hydrogen bonds following co-pigmentation resulted in a denser and more organized structure, contributing to good film compatibility. Thus the RAE could be well entrapped, and the film components were well protected too, allowing them to withstand considerably higher temperature. On the

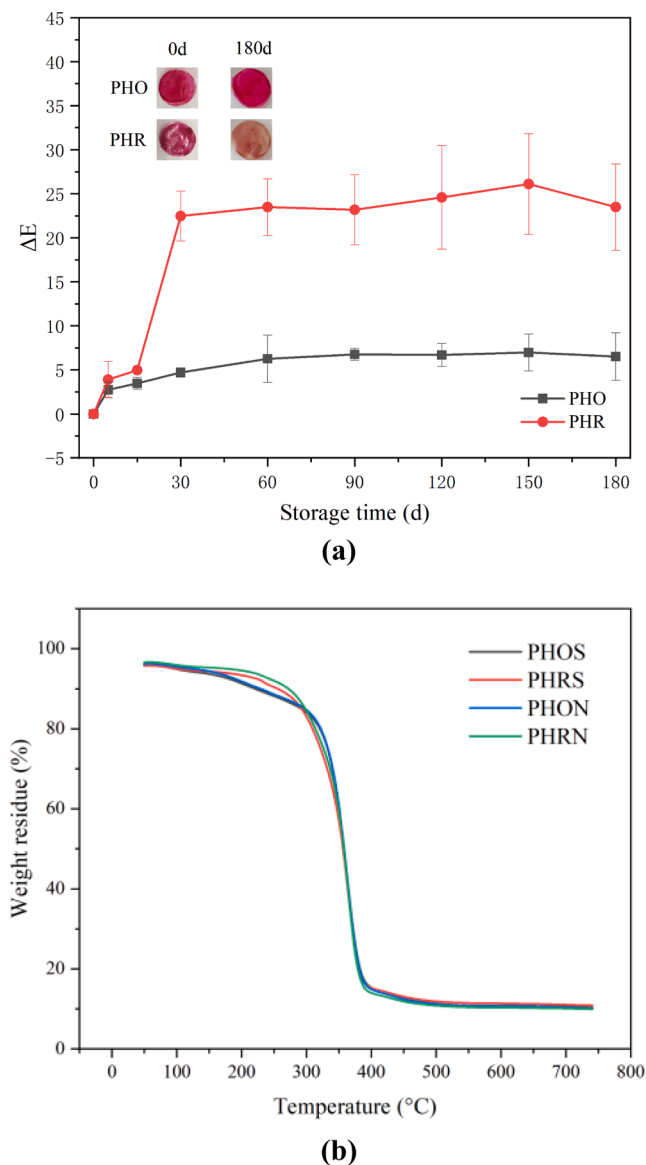


Fig 3. The stability of the PHO and PHR film. In which, the color differences during the long term storage (a) and the thermogravimetric analysis (TGA) spectra (b).

other hand, the co-pigmentation might protect cationic chromophore better, preventing the RAE from thermal degradation (Bao et al., 2022).

3.8. The pH-responsive ability of the indicator film

With the extension of storage time, the packaged food especially meat and aquatic products would produce large amounts of volatile nitrogen compounds, leading to variation of environment pH. Hence, the pH-responsive ability of indicator film was important for freshness monitoring, and the determination results were shown in the Table 2. The color changes of both PHON and PHRN films were similar to OARAE and RAE solution. With the increasing pH, the film changed from rose red to violet, light pink, colorless/blue, green and yellow, and the L* and a* values decreased while b* values fluctuated a lot accordingly. Notably, the ΔE values in the PHON were relatively higher than those in the PHRN, which might be due to the deeper and more intense color after co-pigmentation. Unsurprisingly, the hysteresis in color variations which was investigated in solution assay was also found in the indicator films. Specifically, the PHRS film color shifted to gray when the pH was

Table 2
The pH-responsive ability of the PHO and PHR film.

	pH	L*	a*	b*	ΔE	Color response	
PHOS	3	47.00 ± 0.00 ^c	45.67 ± 4.16 ^a	8.33 ± 0.53 ^d	22.56 ± 2.67 ^e		
	5	42.33 ± 0.58 ^d	45.33 ± 1.15 ^a	9.67 ± 1.15 ^c	18.93 ± 1.49 ^f		
	7	56.67 ± 1.53 ^{ab}	21.67 ± 0.58 ^b	3.00 ± 1.00 ^c	46.30 ± 1.16 ^d		
	9	57.33 ± 3.06 ^a	0.00 ± 0.00 ^d	1.00 ± 0.00 ^f	66.18 ± 0.89 ^b		
	11	54.00 ± 0.00 ^b	-23.67 ± 0.58 ^e	28.33 ± 0.58 ^a	85.59 ± 0.59 ^a		
	13	56.33 ± 1.53 ^{ab}	7.33 ± 0.58 ^c	25.33 ± 0.58 ^b	56.08 ± 1.00 ^c		
	PHRS	3	55.33 ± 1.53 ^{cd}	19.33 ± 1.15 ^b	9.67 ± 0.58 ^b	20.08 ± 1.78 ^d	
		5	56.33 ± 2.08 ^{bcd}	18.33 ± 2.31 ^a	9.67 ± 1.15 ^b	21.22 ± 3.17 ^d	
		7	59.33 ± 0.58 ^{ab}	11.67 ± 0.58 ^b	6.33 ± 0.58 ^{bc}	29.08 ± 0.23 ^c	
		9	53.33 ± 0.58 ^d	3.67 ± 0.58 ^c	2.67 ± 0.58 ^c	35.38 ± 0.51 ^a	
		11	62.00 ± 1.00 ^a	3.67 ± 0.58 ^c	15.67 ± 2.52 ^a	33.56 ± 1.40 ^{ab}	
		13	58.67 ± 3.79 ^{abc}	5.67 ± 1.53 ^c	19.67 ± 5.86 ^a	30.17 ± 3.60 ^{bc}	
		PHON	3	36.67 ± 1.15 ^d	57.67 ± 0.58 ^a	20.33 ± 1.53 ^b	38.0 ± 0.70 ^f
5			44.67 ± 1.53 ^c	45.33 ± 1.15 ^b	-17.00 ± 1.73 ^d	37.33 ± 1.59 ^e	
7			63.00 ± 2.00 ^b	14.67 ± 2.52 ^c	4.33 ± 0.58 ^c	49.65 ± 3.07 ^d	
9			38.33 ± 4.16 ^d	-2.33 ± 1.15 ^e	3.00 ± 1.73 ^c	59.46 ± 1.43 ^c	
11			39.67 ± 4.16 ^d	-29.33 ± 1.15 ^f	16.00 ± 1.73 ^b	84.47 ± 1.14 ^a	
13			69.00 ± 1.00 ^a	0.33 ± 0.58 ^d	46.33 ± 6.03 ^a	69.12 ± 1.59 ^b	
PHRN			3	34.00 ± 0.00 ^e	58.00 ± 0.00 ^a	34.67 ± 0.58 ^a	28.52 ± 0.50 ^e
	5		41.00 ± 1.73 ^d	55.67 ± 1.53 ^a	-11.67 ± 1.15 ^c	26.63 ± 1.04 ^e	
	7		55.33 ± 1.53 ^b	11.00 ± 2.00 ^b	3.00 ± 1.00 ^b	41.61 ± 2.39 ^d	
	9		47.33 ± 0.58 ^c	-10.33 ± 0.58 ^c	2.00 ± 0.00 ^b	57.30 ± 0.49 ^c	
	11		42.00 ± 1.00 ^d	-34.00 ± 4.36 ^d	25.33 ± 10.12 ^a	80.74 ± 1.79 ^a	
	13		62.33 ± 0.58 ^a	-6.67 ± 0.58 ^c	33.00 ± 7.94 ^a	64.16 ± 2.59 ^b	

9.0, while the PHOS film still remained colorless at that pH value, owing to the stabilization effects of co-pigmentation on the flavylum ion, resulting in its difficulty to react with environmental changes. Similarly, the retardation in pH-responsive efficiency of indicator film by the stabilization of anthocyanin was also reported in the blueberry anthocyanin film co-pigmented with chondroitin sulfate (Bao et al., 2022) and the *Lycium ruthenicum* anthocyanin encapsulated with chitosan hydrochloride/carboxymethyl chitosan nanocomplexes film (Qin et al., 2021). However, as the Table 2 shown, the ΔE values in each interval pH value of PHON were all > 5, indicating that obvious color changes could still be investigated, which would not exert negative effects when applied in freshness monitoring.

After storage, the PHRS film became light in color, and the color variations caused by pH changes could not be distinguished clearly. Qin et al., (2021) also reported that the *Lycium ruthenicum* film stored at 35 °C for one month would lose its pH-responsive capacity, due to the degradation of anthocyanin. By contrast, the pH-response ability of the PHOS film was not significantly affected, manifesting by obvious color variations and larger color difference values (from 18.93 ± 1.49 to 85.59 ± 0.59). The results above demonstrated that co-pigmentation

could maintain film response ability to pH changes even after long-term storage.

3.9. Application of indicator film on freshness monitoring of shrimp

In order to simulate the actual storage environment, the shrimp samples were stored at 4 °C for 10 d, and the photographs of indicator films during monitoring period were exhibited in the Fig. 4. According to our previous study, the freshness degree could be divided into 3 stages: fresh (0–2 d), onset of spoilage (4–6 d) and totally spoilage (8–10 d) (Huang, Liu, Chen, Yao, & Hu, 2021). The PHRN film changed its color correspondingly, from rose-red to gray green and yellow at the start point of each freshness stage with the increasing ΔE values from 7.08 ± 1.22 to 66.42 ± 1.62 . On the other hand, the PHON film exhibited similar consecutive color change tendency, varying from initial rose-red color to gray-green at 4 d, and further to gray-yellow at 8 d.

As the Fig. 4 shown, the PHRS film quickly shifted to light yellow at 2 d and then to yellow at 8 d, whose color changes were not consistent with the freshness degree classification. Meanwhile, the PHRS film exhibited relatively low color differences with the similar ΔE values in the range from 25.06 ± 1.00 to 27.44 ± 0.88 , which were hard to recognize by naked eyes, making it difficult to evaluate freshness changes of packaged shrimp. The loss of potentials in freshness monitoring of the PHRS film after long-term storage could be related to the degradation of anthocyanin, contributing to its faster decomposition under pH changes. As a result, its sensitivity to pH changes in the environment had accordingly diminished. Surprisingly, the monitoring effect of the PHOS film was not severely destroyed after long-term storage. Specifically, distinct color variations were observed, changing from rose-red to colorless (4–6 d) and gray yellow (8–10 d), and corresponding to the freshness degrees. Meanwhile, the color changes of the PHOS film at each freshness state could be intuitively perceived by naked eyes, because the internal ΔE values were all above 5.0 ($\Delta E_4-\Delta E_2 = 43.60$, $\Delta E_8-\Delta E_6 = 5.11$).

Furthermore, statistical analysis was performed to evaluate the correlation between film color and shrimp biochemical parameters (including TVB-N and TVC), and the results were shown in the Tab S1.

There were significantly positive correlations between ΔE and TVC in all prepared film, with the correlation coefficients of 0.899, 0.658, 0.845 and 0.931 in the PHOS, PHRS, PHON and PHRN film ($p < 0.05$). Regarding with the TVB-N, the PHOS, PHON and PHRN films presented strong correlations between ΔE and TVB-N ($p < 0.05$), while the ΔE value was less closely related to the TVB-N in the PHRS film ($p < 0.01$). Meanwhile, the predicted models of biochemical parameters based on ΔE values were established. Results suggested that freshness indicators of shrimp packaged by the PHOS, PHON and PHRN film could be predicted precisely, owing to their relatively higher R^2 . Hence, it could be inferred that both PHON and PHRN films had potentials in freshness monitoring. In addition, because of the protection behaviors of co-pigmentation in anthocyanin stabilization, the PHOS film suffered less than PHRS film, contributing the maintenance of film monitoring performances during long term storage. As a result, the PHOS film could still evaluate freshness degree both by naked eyes or with the help of established predicted model.

4. Conclusion

In this study, a novel highly stable indicator film incorporating roselle anthocyanin co-pigmented with oxalic acid was successfully developed. The structural characterization demonstrated that the co-pigmentation of RAE via OA resulted in the formation of molecular interaction, leading to the tighter structure network, which could be accounted for the improved stability. In addition, the co-pigmentation effectively enhanced film physical properties, the PHO films which were newly prepared or stored for a long term both exhibited higher TS and EB values, as well as stronger hydrophobic characteristics than the PHR films. However, the co-pigmentation would weaken the pH-responsive ability of the PHON film due to the protection of flavylum ion. But after long-term storage, the weakening behaviors would disappear, and the PHOS film responded to pH changes more efficiently, as manifesting by distinct color variations and intenser colors than the PHRS film. Furthermore, when it came to the application of shrimp freshness monitoring, PHR film could distinguish different freshness degrees only when it was newly prepared. By contrast, the PHO film which was stored for 6 months could still display visually color changes,

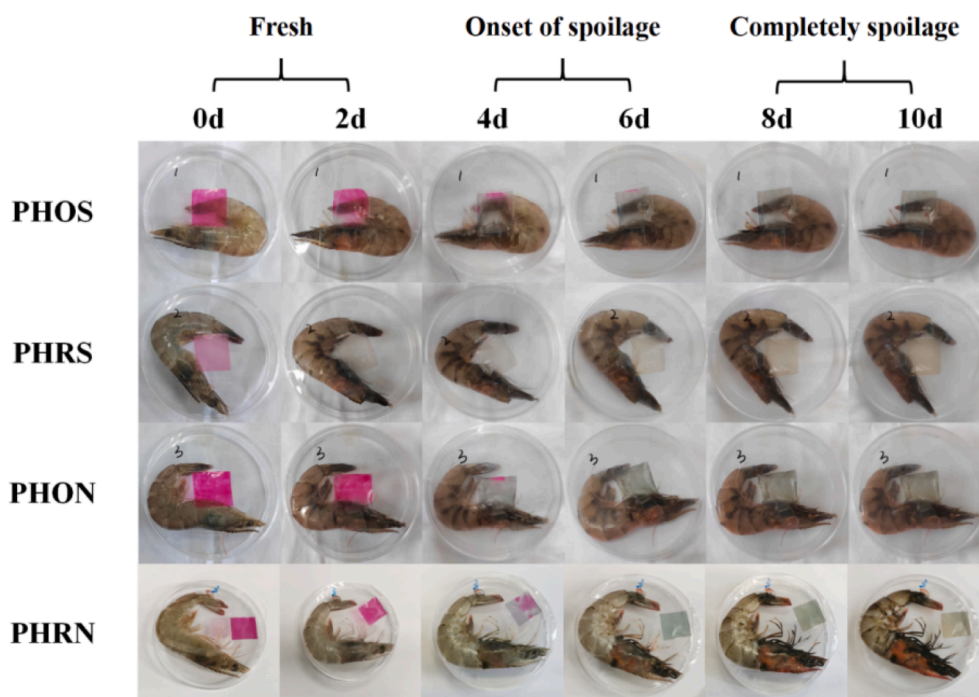


Fig. 4. The application of the PHO and PHR film in shrimp freshness monitoring.

and the film colors were strongly correlated to the biochemical parameters of shrimp (TVB-N and TVC). The results suggested that after 6 months of storage, the co-pigmentation could better maintain pH-responsive capacity of the PHOS film by the prevention of anthocyanin from degradation, leading to better monitoring effects than the PHRS film. Therefore, the roselle anthocyanin indicator film modified by co-pigmentation demonstrated great potentials in real-time freshness monitoring due to its improved stability, better physical properties and more efficient pH-response ability.

CRedit authorship contribution statement

Jiayin Huang: Writing – original draft, Investigation, Writing – review & editing. **Zhiheng Hu:** Data curation. **Gaoshang Li:** Formal analysis. **Yaoxian Chin:** Validation. **Zhisheng Pei:** Software. **Qian Yao:** Supervision. **Dan Li:** Supervision. **Yaqin Hu:** Funding acquisition.

Declaration of Competing Interest

The authors declare that they have no known competing financial interests or personal relationships that could have appeared to influence the work reported in this paper.

Data availability

The data that has been used is confidential.

Acknowledgement

This work was financially supported by Hainan Provincial Natural Science Foundation of China (321CXTD1012) and Scientific Research Foundation of Hainan Tropical Ocean University (RHDRC202117).

Appendix A. Supplementary material

Supplementary data to this article can be found online at <https://doi.org/10.1016/j.foodres.2023.113416>.

References

- Alizadeh-Sani, M., Tavassoli, M., McClements, D. J., & Hamishehkar, H. (2021). Multifunctional halochromic packaging materials: Saffron petal anthocyanin loaded-chitosan nanofiber/methyl cellulose matrices. *Food Hydrocolloids*, *111*, Article 106237. <https://doi.org/10.1016/j.foodhyd.2020.106237>
- Bao, Y. W., Cui, H. J., Tian, J. L., Ding, Y. M., Tian, Q. K., et al. (2022). Novel pH sensitivity and colorimetry-enhanced anthocyanin indicator films by chondroitin sulfate co-pigmentation for shrimp freshness monitoring. *Food Control*, *131*, Article 108441. <https://doi.org/10.1016/j.foodcont.2021.108441>
- Bingöl, A., Türkyılmaz, M., & Özkan, M. (2022). Increase in thermal stability of strawberry anthocyanins with amino acid copigmentation. *Food Chemistry*, *384*, 132518. <https://doi.org/10.1016/j.foodchem.2022.132518>
- Boonsuk, P., Sukolrat, A., Kaewtatip, K., Chantarak, S., Kelarakis, A., et al. (2020). Modified cassava starch/poly(vinyl alcohol) blend films plasticized by glycerol: Structure and properties. *Journal of Applied Polymer Science*, *137*, 48848. <https://doi.org/10.1002/app.48848>
- Cao, Y., Xia, Q. L., Ya, A., Chen, J. B., & Jin, Z. (2023). Copigmentation effect of flavonols on anthocyanins in black mulberry juice and their interaction mechanism investigation. *Food Chemistry*, *399*, Article 133927. <https://doi.org/10.1016/j.foodchem.2022.133927>
- Chen, H. Z., Zhang, M., Bhandari, B., & Yang, C. H. (2020). Novel pH-sensitive films containing curcumin and anthocyanins to monitor fish freshness. *Food Hydrocolloids*, *100*, Article 105438. <https://doi.org/10.1016/j.foodhyd.2019.105438>
- Chen, M. Y., Yan, T. Y., Huang, J. Y., Zhou, Y. Q., & Hu, Y. Q. (2021). Fabrication of halochromic smart films by immobilizing red cabbage anthocyanins into chitosan/oxidized-chitin nanocrystals composites for real-time hairtail and shrimp freshness monitoring. *International Journal of Biological Macromolecules*, *179*, 90–100. <https://doi.org/10.1016/j.ijbiomac.2021.02.170>
- Dong, S. Y., Zhang, Y. Q., Lu, D., Gao, W. L., Zhao, Q., et al. (2023). Multifunctional intelligent film integrated with purple sweet potato anthocyanin and quercetin-loaded chitosan nanoparticles for monitoring and maintaining freshness of shrimp. *Food Packaging and Shelf Life*, *35*, Article 101022. <https://doi.org/10.1016/j.fpsl.2022.101022>
- Duan, A. B., Yang, J., Wu, L. Y., Wang, T., Liu, Q. Y., et al. (2022). International Journal of Biological Macromolecules, *220*, 147–158. Preparation, physicochemical and application evaluation of raspberry anthocyanin and curcumin based on chitosan/starch/gelatin film. <https://doi.org/10.1016/j.ijbiomac.2022.08.053>
- Ezati, P., & Rhim, J. W. (2020). pH-responsive chitosan-based film incorporated with alizarin for intelligent packaging applications. *Food Hydrocolloids*, *102*, Article 105629. <https://doi.org/10.1016/j.foodhyd.2019.105629>
- Fei, P., Zeng, F. S., Zheng, S. Y., Chen, Q. L., Hu, Y. H., et al. (2021). Acylation of blueberry anthocyanins with maleic acid: Improvement of the stability and its application potential in intelligent color indicator packing materials. *Dyes and Pigments*, *184*, Article 108852. <https://doi.org/10.1016/j.dyepig.2020.108852>
- Fonseca-Garcia, A., Caicedo, C., Jiménez-Regalado, E. J., Morales, G., & Aguirre-Loredo, R. Y. (2021). Effects of poloxamer content and storage time of biodegradable starch-chitosan films on its thermal, structural, mechanical, and morphological properties. *Polymers*, *13*, 2341. <https://doi.org/10.3390/polym13142341>
- Franco, M. R., Cunha, L. R., & Bianchi, R. F. (2021). Janus principle applied to food safety: An active two-faced indicator label for tracking meat freshness. *Sensors and Actuators B: Chemical*, *333*, Article 129466. <https://doi.org/10.1016/j.snb.2021.129466>
- Galalde, R. A., Thipmancee, R., Jariyasakoolroj, P., & Sane, A. (2019). The effects of blend ratio and storage time on thermoplastic starch/poly(butylene adipate-co-terephthalate) films. *Heliyon*, *5*, e01251.
- Ge, Y. J., Li, Y., Bai, Y., Yuan, C. H., Wu, C. H., et al. (2020). Intelligent gelatin/oxidized chitin nanocrystals nanocomposite films containing black rice bran anthocyanins for fish freshness monitoring. *International Journal of Biological Macromolecules*, *155*, 1296–1306. <https://doi.org/10.1016/j.ijbiomac.2019.11.101>
- Hernandez, J. H. M. (2021). Effect of the incorporation of polycaprolactone (PCL) on the retrogradation of binary blends with cassava thermoplastic starch (TPS). *Polymers*, *13*, 38. <https://doi.org/10.3390/polym13010038>
- Huang, J. Y., Chen, M. Y., Zhou, Y. Q., Li, Y., & Ya, Q. H. (2020). Functional characteristics improvement by structural modification of hydroxypropyl methylcellulose modified polyvinyl alcohol films incorporating roselle anthocyanins for shrimp freshness monitoring. *International Journal of Biological Macromolecules*, *162*, 1250–1261. <https://doi.org/10.1016/j.ijbiomac.2020.06.156>
- Huang, J. Y., Hu, Z. H., Chin, Y. X., Pei, Z. S., Yao, Q., et al. (2023). Improved thermal stability of roselle anthocyanin by co-pigmented with oxalic acid: Preparation, characterization and enhancement mechanism. *Food Chemistry*, *410*, Article 135407. <https://doi.org/10.1016/j.foodchem.2023.135407>
- Huang, J. Y., Liu, J. L., Chen, M. Y., Yao, Q., & Hu, Y. Q. (2021). Immobilization of roselle anthocyanins into polyvinyl alcohol/hydroxypropyl methylcellulose film matrix: Study on the interaction behavior and mechanism for better shrimp freshness monitoring. *International Journal of Biological Macromolecules*, *184*, 666–677. <https://doi.org/10.1016/j.ijbiomac.2021.06.074>
- Li, L. L., Xiao, F., Xiao, Y. W., Liu, L. H., Jiang, S. T., et al. (2023). Colorimetric active carboxymethyl chitosan/oxidized sodium alginate-Oxalis triangularis ssp. papilionacea anthocyanins film@gelatin/zein-linalool membrane for milk freshness monitoring and preservation. *Food Chemistry*, *405*(Part B), Article 134994. <https://doi.org/10.1016/j.foodchem.2022.134994>
- Li, S. Q., Jiang, Y. L., Zhou, Y. T., Li, R. Z., Jiang, Y. F., et al. (2022). Facile fabrication of sandwich-like anthocyanin/chitosan/lemongrass essential oil films via 3D printing for intelligent evaluation of pork freshness. *Food Chemistry*, *370*, Article 131082. <https://doi.org/10.1016/j.foodchem.2021.131082>
- Liang, T., Sun, G., Cao, L., Li, J., & Wang, L. (2019). A pH and NH₃ sensing intelligent film based on Artemisia sphaerocephala Krasch. gum and red cabbage anthocyanins anchored by carboxymethyl cellulose sodium added as a host complex. *Food Hydrocolloids*, *87*, 858–868. <https://doi.org/10.1016/j.foodhyd.2018.08.028>
- Liu, J., Liu, S., Wu, Q. Q., Gu, Y. Y., Kan, J., et al. (2017). Effect of protocatechuic acid incorporation on the physical, mechanical, structural and antioxidant properties of chitosan film. *Food Hydrocolloids*, *73*, 90–100. <https://doi.org/10.1016/j.foodhyd.2017.06.035>
- Liu, L. M., Wu, W. N., Zheng, L. M., Yu, J. H., Sun, P. L., et al. (2022). Intelligent packaging films incorporated with anthocyanins-loaded ovalbumin-carboxymethyl cellulose nanocomplexes for food freshness monitoring. *Food Chemistry*, *387*, Article 132908. <https://doi.org/10.1016/j.foodchem.2022.132908>
- Molaeafard, S., Jamei, R., & Marjani, A. P. (2021). Co-pigmentation of anthocyanins extracted from sour cherry (*Prunus cerasus* L.) with some organic acids: Color intensity, thermal stability, and thermodynamic parameters. *Food Chemistry*, *339*, Article 128070. <https://doi.org/10.1016/j.foodchem.2020.128070>
- Nie, M., Wang, L., Lu, S. M., Wang, Y. G., Zheng, M. Y., et al. (2022). Protective effect of amino acids on the stability of bayberry anthocyanins and the interaction mechanism between l-methionine and cyanidin-3-O-glycoside. *Food Chemistry*, *396*, Article 133689. <https://doi.org/10.1016/j.foodchem.2022.133689>
- Qin, Y., Yun, D. W., Xu, F. F., Chen, D., Kan, J., et al. (2021). Smart packaging films based on starch/polyvinyl alcohol and Lycium ruthenicum anthocyanins-loaded nanocomplexes: Functionality, stability and application. *Food Hydrocolloids*, *119*, Article 106850. <https://doi.org/10.1016/j.foodhyd.2021.106850>
- Qin, Y., Yun, D. W., Xu, F. F., Li, C. C., Chen, D., et al. (2021). Impact of storage conditions on the structure and functionality of starch/polyvinyl alcohol films containing Lycium ruthenicum anthocyanins. *Food Packaging and Shelf Life*, *29*, Article 100693. <https://doi.org/10.1016/j.fpsl.2021.100693>
- Sun, J. S., Du, Y., Ma, J. Q., Li, Y. Z., Wang, L., et al. (2019). Transparent bionanocomposite films based on konjac glucomannan, chitosan, and TEMPO-oxidized chitin nanocrystals with enhanced mechanical and barrier properties. *International Journal of Biological Macromolecules*, *138*, 866–873. <https://doi.org/10.1016/j.ijbiomac.2019.07.170>
- Tang, B., He, Y., Liu, J., Zhang, J., Li, J. L., et al. (2019). Kinetic investigation into pH-dependent color of anthocyanin and its sensing performance. *Dyes and Pigments*, *170*, Article 107643. <https://doi.org/10.1016/j.dyepig.2019.107643>

- Yang, Z. K., Zhai, X. D., Zhang, C. C., Shi, J. Y., Huang, X. W., et al. (2022). Agar/TiO₂/radish anthocyanin/lemon essential oil bionanocomposite bilayer films with improved bioactive capability and electrochemical writing property for banana preservation. *Food Hydrocolloids*, 123, Article 107187. <https://doi.org/10.1016/j.foodhyd.2021.107187>
- Yao, P. Q., Wang, L., Zhou, N., Yang, Y., & Pang, J. (2023). A pH-intelligent response fish packaging film: Konjac glucomannan/carboxymethyl cellulose/blackcurrant anthocyanin antibacterial composite film. *International Journal of Biological Macromolecules*, 204, 386–396. <https://doi.org/10.1016/j.ijbiomac.2022.02.027>
- Zia, J., Mancini, G., Bustreo, M., Zych, A., Donno, R., et al. (2021). Porous pH natural indicators for acidic and basic vapor sensing. *Chemical Engineering Journal*, 403, Article 126373. <https://doi.org/10.1016/j.cej.2020.126373>
- Zhai, X. D., Zou, X. B., Shi, J. Y., Huang, X. W., Sun, Z. B., et al. (2020). Amine-responsive bilayer films with improved illumination stability and electrochemical writing property for visual monitoring of meat spoilage. *Sensors and Actuators B: Chemical*, 302, Article 127130. <https://doi.org/10.1016/j.snb.2019.127130>
- Zhang, J. J., Huang, X. W., Shi, J. Y., Liu, L., Zhang, X. N., et al. (2021). A visual bi-layer indicator based on roselle anthocyanins with high hydrophobic property for monitoring griskin freshness. *Food Chemistry*, 355, Article 129573. <https://doi.org/10.1016/j.foodchem.2021.129573>
- Zhang, X., Liu, Y. P., Yong, H. M., Qin, Y., Liu, J., et al. (2019). Development of multifunctional food packaging films based on chitosan, TiO₂ nanoparticles and anthocyanin-rich black plum peel extract. *Food Hydrocolloids*, 94, 80–92. <https://doi.org/10.1016/j.foodhyd.2019.03.009>
- Zong, Z. H., Liu, M., Chen, H. J., Farag, M. A., Wu, W. J., et al. (2023). Preparation and characterization of a novel intelligent starch/gelatin binary film containing purple sweet potato anthocyanins for *Flammulina velutipes* mushroom freshness monitoring. *Food Chemistry*, 405(Part B), Article 134839. <https://doi.org/10.1016/j.foodchem.2022.134839>

ABOUT UMT FACULTY

SDI

Selective Dissemination of Information (SDI) service is a current-awareness service offered by the PSNZ for UMT Faculty Members. The contents selection criteria include current publications (last 5 years), highly cited and most viewed/downloaded documents. The contents with pdf full text from subscribed databases are organized and compiled according to a monthly theme which is determined based on the topics of specified interest.

For more information or further assistance, kindly contact us at 09-6684185/4298 or email to psnz@umt.edu.my/sh_akmal@umt.edu.my

Thank you.

**Perpustakaan Sultanah Nur Zahirah
Universiti Malaysia Terengganu
21030 Kuala Nerus, Terengganu.**

Tel. : 09-6684185 (Main Counter)

Fax : 09-6684179

Email : psnz@umt.edu.my